CAPACI OCCASIO
FOUNDED 1894

SAIMM

THE SOUTHERN AFRICAN INSTITUTE OF MINING AND METALLURGY

125 YEARS 1894 - 2019

VOLUME 120 NO. 3 MARCH 2020

ELBROC
MINING PRODUCTS (PTY) LTD

TH ARCH SUPPORT SYSTEMS

PROFILE SETS

Ring Set

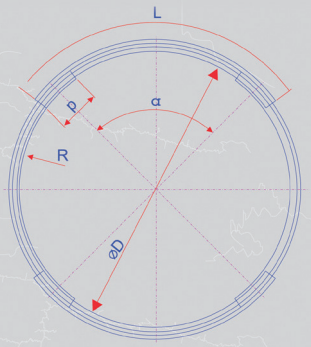

Semi Arch Set

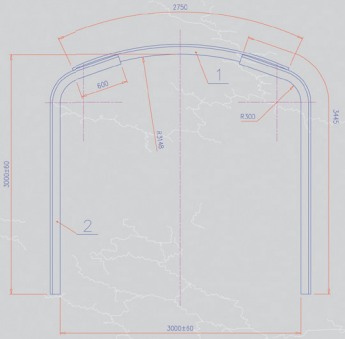

Half Arch Set

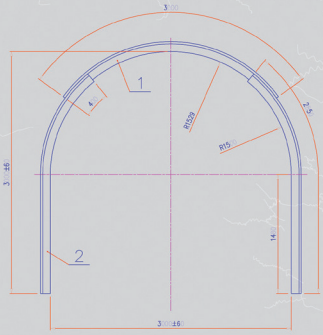

PRODUCTION CAPABILITIES:

- Standard arch lengths from 1.8m to 5.5m
- Minimal curvature R 1000mm, at R 1200mm at R 1600mm

APPLICATIONS

- Tunnel junctions
- Over and under ore passes
- Haulage
- Incline shaft portals
- Active support through bad ground conditions, dykes, faults, friable ground

BENEFITS

- Simple and fast installation
- High load carrying capacity
- Long operational life
- Suitable for tunnels from 4.15m to 5.5m wide
- Upright support beams cater for tunnel heights from 3.1 to 6.5m
- Cost effective
- Dimensional and design flexibility

OMNI 150

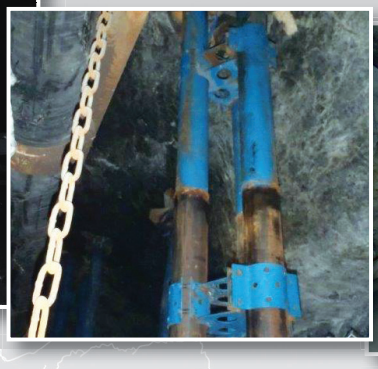

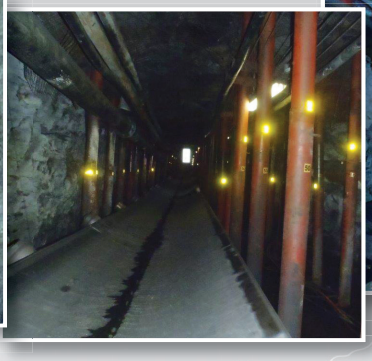

APPLICATIONS

- Tunnel support
- Pillar rehabilitation
- Set construction on friable ground
- Active blast on support
- Used with backfill
- Travelling ways, mono ways and winch chambers

BENEFITS AND FEATURES

- Provides active roof support with controlled yielding
- Working load set to customer requirements (8 to 45 ton)
- Resilient in rockburst conditions
- Superb energy absorption
- Can accommodate numerous seismic events
- Constant and consistent support resistance
- Light, easy and quick to install
- Safe remote installation
- Cannot be over extended
- Reusable versions available on request
- Standard lengths available to 6 meters
- Longer lengths available on request

SABS ISO 9001

a member of the rbh royal bafokeng holdings

TO VIEW OUR FULL RANGE OF TUNNEL SUPPORT PLEASE VISIT OUR WEBPAGE

Tel: +27 010 534 5174 • sales@elbroc.co.za
www.elbroc.co.za

mogs

OFFICE BEARERS AND COUNCIL FOR THE 2019/2020 SESSION

Honorary President

Mxolisi Mgojo
President, Minerals Council South Africa

Honorary Vice Presidents

Gwede Mantashe
Minister of Mineral Resources, South Africa

Ebrahim Patel
Minister of Trade and Industry, South Africa

Blade Nzimande
Minister of Science and Technology, South Africa

President

M.I. Mthenjane

President Elect

V.G. Duke

Senior Vice President

I.J. Geldenhuys

Junior Vice President

Z. Botha

Incoming Junior Vice President

W.C. Joughin

Immediate Past President

A.S. Macfarlane

Co-opted to Office Bearers

S. Ndlovu

Honorary Treasurer

V.G. Duke

Ordinary Members on Council

B. Genc
W.C. Joughin
G.R. Lane
E. Matinde
G. Njowa
B. Ntsoelengoe
S.M Rupprecht
N. Singh
A.G. Smith
M.H. Solomon
A.T. van Zyl
E.J. Walls

Co-opted Members

T. Makgala
R.C.W. Webber-Youngman

Past Presidents Serving on Council

N.A. Barcza
R.D. Beck
J.R. Dixon
H.E. James
R.T. Jones
C. Musingwini
S. Ndlovu
J.L. Porter
S.J. Ramokgopa
M.H. Rogers
D.A.J. Ross-Watt
G.L. Smith
W.H. van Niekerk

G.R. Lane–TPC Mining Chairperson
Z. Botha–TPC Metallurgy Chairperson

G. Dabula–YPC Chairperson
S. Manjengwa–YPC Vice Chairperson

Branch Chairpersons

Botswana	Vacant
DRC	S. Maleba
Johannesburg	D.F. Jensen
Namibia	N.M. Namate
Northern Cape	F.C. Nieuwenhuys
Pretoria	S. Uludag
Western Cape	A.B. Nesbitt
Zambia	D. Muma
Zimbabwe	C.P. Sadomba
Zululand	C.W. Mienie

PAST PRESIDENTS

*Deceased

* W. Bettel (1894–1895)
* A.F. Crosse (1895–1896)
* W.R. Feldtmann (1896–1897)
* C. Butters (1897–1898)
* J. Loevy (1898–1899)
* J.R. Williams (1899–1903)
* S.H. Pearce (1903–1904)
* W.A. Caldecott (1904–1905)
* W. Cullen (1905–1906)
* E.H. Johnson (1906–1907)
* J. Yates (1907–1908)
* R.G. Bevington (1908–1909)
* A. McA. Johnston (1909–1910)
* J. Moir (1910–1911)
* C.B. Saner (1911–1912)
* W.R. Dowling (1912–1913)
* A. Richardson (1913–1914)
* G.H. Stanley (1914–1915)
* J.E. Thomas (1915–1916)
* J.A. Wilkinson (1916–1917)
* G. Hildick-Smith (1917–1918)
* H.S. Meyer (1918–1919)
* J. Gray (1919–1920)
* J. Chilton (1920–1921)
* F. Wartenweiler (1921–1922)
* G.A. Watermeyer (1922–1923)
* F.W. Watson (1923–1924)
* C.J. Gray (1924–1925)
* H.A. White (1925–1926)
* H.R. Adam (1926–1927)
* Sir Robert Kotze (1927–1928)
* J.A. Woodburn (1928–1929)
* H. Pirow (1929–1930)
* J. Henderson (1930–1931)
* A. King (1931–1932)
* V. Nimmo-Dewar (1932–1933)
* P.N. Lategan (1933–1934)
* E.C. Ranson (1934–1935)
* R.A. Flugge-De-Smidt (1935–1936)
* T.K. Prentice (1936–1937)
* R.S.G. Stokes (1937–1938)
* P.E. Hall (1938–1939)
* E.H.A. Joseph (1939–1940)
* J.H. Dobson (1940–1941)
* Theo Meyer (1941–1942)
* John V. Muller (1942–1943)
* C. Biccard Jeppe (1943–1944)
* P.J. Louis Bok (1944–1945)
* J.T. McIntyre (1945–1946)
* M. Falcon (1946–1947)
* A. Clemens (1947–1948)
* F.G. Hill (1948–1949)
* O.A.E. Jackson (1949–1950)
* W.E. Gooday (1950–1951)
* C.J. Irving (1951–1952)
* D.D. Stitt (1952–1953)
* M.C.G. Meyer (1953–1954)
* L.A. Bushell (1954–1955)
* H. Britten (1955–1956)
* Wm. Bleloch (1956–1957)
* H. Simon (1957–1958)
* M. Barcza (1958–1959)
* R.J. Adamson (1959–1960)
* W.S. Findlay (1960–1961)
* D.G. Maxwell (1961–1962)
* J. de V. Lambrechts (1962–1963)
* J.F. Reid (1963–1964)
* D.M. Jamieson (1964–1965)
* H.E. Cross (1965–1966)
* D. Gordon Jones (1966–1967)
* P. Lambooy (1967–1968)
* R.C.J. Goode (1968–1969)
* J.K.E. Douglas (1969–1970)
* V.C. Robinson (1970–1971)
* D.D. Howat (1971–1972)
* J.P. Hugo (1972–1973)
* P.W.J. van Rensburg (1973–1974)
* R.P. Plewman (1974–1975)
* R.E. Robinson (1975–1976)
* M.D.G. Salamon (1976–1977)
* P.A. Von Wielligh (1977–1978)
* M.G. Atmore (1978–1979)
* D.A. Viljoen (1979–1980)
* P.R. Jochens (1980–1981)

G.Y. Nisbet (1981–1982)
A.N. Brown (1982–1983)

* R.P. King (1983–1984)

J.D. Austin (1984–1985)
H.E. James (1985–1986)
H. Wagner (1986–1987)

* B.C. Alberts (1987–1988)
* C.E. Fivaz (1988–1989)
* O.K.H. Steffen (1989–1990)
* H.G. Mosenthal (1990–1991)

R.D. Beck (1991–1992)

* J.P. Hoffman (1992–1993)
* H. Scott-Russell (1993–1994)

J.A. Cruise (1994–1995)
D.A.J. Ross-Watt (1995–1996)
N.A. Barcza (1996–1997)

* R.P. Mohring (1997–1998)

J.R. Dixon (1998–1999)
M.H. Rogers (1999–2000)
L.A. Cramer (2000–2001)

* A.A.B. Douglas (2001–2002)

S.J. Ramokgopa (2002-2003)
T.R. Stacey (2003–2004)
F.M.G. Egerton (2004–2005)
W.H. van Niekerk (2005–2006)
R.P.H. Willis (2006–2007)
R.G.B. Pickering (2007–2008)
A.M. Garbers-Craig (2008–2009)
J.C. Ngoma (2009–2010)
G.V.R. Landman (2010–2011)
J.N. van der Merwe (2011–2012)
G.L. Smith (2012–2013)
M. Dworzanowski (2013–2014)
J.L. Porter (2014–2015)
R.T. Jones (2015–2016)
C. Musingwini (2016–2017)
S. Ndlovu (2017–2018)
A.S. Macfarlane (2018–2019)

Honorary Legal Advisers
Scop Incorporated

Auditors
Genesis Chartered Accountants

Secretaries
The Southern African Institute of Mining and Metallurgy
Fifth Floor, Minerals Council South Africa
5 Hollard Street, Johannesburg 2001 • P.O. Box 61127, Marshalltown 2107
Telephone (011) 834-1273/7 • Fax (011) 838-5923 or (011) 833-8156
E-mail: journal@saimm.co.za

Typeset and Published by
The Southern African Institute of Mining and Metallurgy
P.O. Box 61127
Marshalltown 2107
Telephone (011) 834-1273/7
Fax (011) 838-5923
E-mail: journal@saimm.co.za

Printed by
Camera Press, Johannesburg

Advertising Representative
Barbara Spence
Avenue Advertising
Telephone (011) 463-7940
E-mail: barbara@avenue.co.za

ISSN 2225-6253 (print)
ISSN 2411-9717 (online)

Directory of Open Access Journals

INDEXED IN DOAJ

SAIMM
THE SOUTHERN AFRICAN INSTITUTE OF MINING AND METALLURGY
FOUNDED 1894
125 YEARS 1894 - 2019

VOLUME 120 NO. 3 MARCH 2020

Contents

PAPERS OF GENERAL INTEREST

An autoregressive integrated moving average (ARIMA) model was used in this study as a time series analysis (TSA) method for the prediction of slope failure. Data obtained from the movements of tension cracks at six out of ten established stations was used to predict future values. The results from the ARIMA method were compared with results from regression methods and were shown to be better in terms of the correlation coefficients and predicted mean square error values.

Point load index (PLI) value tests were performed using 15 different testing devices. The experiments were carried out on seven different rock types by the same operator. The sources of measurement error were identified, and additional experiments carried out in a modified device. The PLI values obtained from the modified PLI device were found to more reliable, with lower standard deviations than those obtained from other conventional testing devices.

The loading process in sublevel caving mines entails loading material from the drawpoint using load haul dump machines. When each bucket is drawn from the drawpoint, a decision must be made to continue loading or abandon the drawpoint and blast the next ring. It has been difficult to establish which specific factors manual drawpoint control is based on. This paper analyses the effect of operators' experience on the decision to abandon 'normal' rings, opening rings, and rings with loading issues at the Kiirunavaara and Malmberget iron ore mines.

Ethical research and scholarly publication in the mining and metallurgical community – A new era dawns

This commentary provides an overview of an important meeting between the SAIMM, ASSAf, and SciELO held during February 2020. The meeting arose as a result of new initiatives to ensure *integrity in 'research and scholarly publication'*, which have been agreed globally and have now been adopted by the departments of Science and Innovation and Higher Education, the National Foundation for Research, and the group representing the universities of South Africa, among others. The purpose of the meeting was to ensure that the SAIMM, and all South African scientific and professional institutions in general, will meet the global principles of ethical research and scholarly publication (ERSP) as adopted by South Africa.

The Institute is aware of these new ERSP 'rules of engagement', and as such, the relevant committees are now starting to work through the issues. Such matters will be published in due course. By way of example in the interim, two issues of direct relevance to the SAIMM include (i) the inability to publish papers that have previously been published in formal refereed conference proceedings, and (ii) a strict limit to the proportion of papers (and authors) sourced from any one institution in any specific journal edition. Such rules will undoubtedly impact upon the manner in which papers presented at conferences will be published in future, and on specific themed editions that include papers from a specific source or specific authors. For these reasons, the Publication and Technical Programme Committees are likely to enter into something akin to a new era of operation in order to meet these new principles while still continuing to provide enhanced knowledge and intellectual services to the mining and metallurgical industries and all the major allied disciplines.

Against the background above, it may be of interest to note that the SAIMM Journal is currently a proven and sought-after global publication. Investigations over the past two years have shown that approximately 70% of the papers submitted for publication arise from international sources and from universities and research institutions as geographically widespread as the USA, China, Japan, India, Russia, Pakistan, Turkey, Germany, the UK, Egypt, and Iran. Approximately 300–400 highly qualified and experienced academics and industrial practitioners, both local and international, are active on the panel of reviewers. Approximately 40 to 45 paper are submitted per month, all of which are pre-reviewed monthly prior to the selected ones entering the review process. Twelve journal editions (one each month) are published annually, with editorial and typesetting undertaken in-house.

In these matters, the Journal would appear to be meeting its current goals and the needs of many of its readers. This is best reflected by the *resolutions factor i.e.* the number of times a paper is electronically opened and read, known colloquially as the 'hits' on a paper. Such data is captured monthly by ASSAf and SciELO for all accredited journals in South Africa. Of specific interest to the SAIMM community is the fact that between 15 000 and 16 000 'hits' (*i.e.* opening and/or reading of papers) are being recorded for the SAIMM Journal per month, with the next accredited journal on the ASSAf list recording 7 000 hits and the remaining accredited journals recording hits in the mid- to lower hundreds. Such results suggest that the SAIMM *Journal* is widely read and is therefore of significant relevance to its professional community.

However, what remains to be done is to enhance the standing of the *Journal* to an even higher intellectual status by improving its *Impact Factor* (IF – *a measure reflecting the average number of citations to articles published in science and social journals*). This step would lead to enhanced accreditation for those in academe who, by having their research published and cited in the SAIMM *Journal*, would earn personal academic accreditation as well as acquire funds for their universities (approximately R120 000 per single Journal paper). It is this that the SAIMM seeks to improve in the short term – in addition to implementing the longer-term goals set by ASSAf and SciELO for proven integrity in research and scholarly publishing currently, as is currently being instituted in the country at present. There is much to be discussed and done in the near future. All will be reported in due course.

R.M.S. Falcon

President's Corner

I'll remember the month of March 2020 for two events that happened in tandem – the first one was my birthday on the 26th when I turned 50 years (half-century) old. Turning 50 years is significant in anyone's life and mine was no different. However, I did not expect it to be as dramatic as it turned out to be, which leads to the second event, the beginning of the country's 21-day lockdown from midnight on 26 March to midnight on 16 April.

At the time of writing this letter, we were on the third day of the lockdown where, other than persons involved in essential services, we are all in quarantine within our homes or isolated if we have been infected by the coronavirus disease, also known as COVID-19. Most industries remain closed during this three-week period – the South Africa's mining industry production levels are down to about 30% and globally, we are headed for a recession, the Global Covid-19 Recession (GCR). The impact of the pandemic is unprecedent in the modern world and its effects will be long-lasting in several ways; including, to name a few, how we work (and play), the nature of economic activity, and specifically for the SAIMM, how we pursue our primary objective of providing continuing education and skills for our members.

A fundamental and immediate change that has happened in how we work is the huge exodus to (home fitness and) digital platforms to continue with 'office work' (work from home – WFH). Work at the coal face (no pun intended) continues with minimal people resources to ensure the continued supply of coal for our electricity generation (imagine the double whammy of being isolated at home with intermittent electricity availability) – to prevent infections and transmission of the disease remains the primary objective. For those operations that are already digitalized, this period of lockdown, such as is prevalent in most countries where infections have been recorded, the transition to digital is vindicated. This is the beginning of the future of our lives and we need to adapt promptly or suffer the consequences.

The SAIMM, as with other organizations that convene conferences and meetings for learning, has postponed and will likely cancel some conferences during this year as a result of the lockdown and possible continuing consequences of the COVID-19 disease. Alternative and innovative avenues to continue to deliver our services, such as webcasts at scale' (*i.e.* for a large number of people), are being explored. This is the upside of the pandemic and we will take advantage of the opportunities presented to us to thrive in this new way of thinking and acting.

There's no telling whether the three weeks will be sufficient to arrest the spread of the disease in South Africa. It's the minimum and scientifically proven method of preventing further infections and we must adhere to this advice with military discipline for the sustainability of the nation. We are all under varying degrees of emotional and mental strain, the domestic economy is under recession, and as at Friday 27 March, Moody's Investor Service finally downgraded South Africa's sovereign credit rating to junk status with a negative outlook. Livelihoods are at stake - I dare say that we have reached the bottom in our social and economic development. It is now the time for leadership, not only as I have discussed in earlier letters, to rise up to this occasion – 'the greatest leader is not necessarily the one who does the greatest things. He is the one that gets the people to do the greatest things'[1]. Wishing you all safety, health and resolve. Please do take care.

M.I. Mthenjane
President, SAIMM

[1]Ronald Reagan

EVOLUTION ON THE OUTSIDE
REVOLUTION ON THE INSIDE

THE NEW SANDVIK 800i
CONNECTED CONE CRUSHER SERIES

These eight crushers maximize uptime and offer you the best possible solution for any mining or aggregate application. Connected 24/7 to the My Sandvik portal, and with the new generation Automation and Connectivity System (ACS) as standard, they boost productivity and help you predict performance. And with the option of Sandvik Reborn and overhaul kits, crushing has never been easier to upgrade, and as cost-efficient to operate.

Join the crusher revolution.
ROCKTECHNOLOGY.SANDVIK/800i

SANDVIK

Monitoring unstable slopes in an open pit lignite mine using ARIMA

H. Özşen[1]

Affiliation:
[1]Konya Teknik University, Department of Mining Engineering, Konya, Turkey.

Correspondence to:
H. Özşen

Email:
hozsen@ktun.edu.tr

Dates:
Received: 12 Mar. 2019
Revised: 24 Sep. 2019
Accepted: 28 Nov. 2019
Published: March 2020

How to cite:
Özşen, H.
Monitoring unstable slopes in an open pit lignite mine using ARIMA.
The Southern African Insitute of Mining and Metallurgy

DOI ID:
http://dx.doi.org/10.17159/2411-9717/665/2020

Synopsis

Slope stability is a widely studied area because of the significant consequences of slope failure. There are various factors affecting slope stability in open pit mines, and predicting the time of failure can be difficult due to the complex nature of the rock mass. Regression methods are often used in this prediction process, but they are limited in that they use a strict mathematical model. Therefore, possible future changes within the structure of a slope can be underestimated because once a mathematical model has been established to predict slope failure, it is then used indefinitely. For this reason, an autoregressive integrated moving average (ARIMA) model is used in this study as a time series analysis (TSA) method for the prediction of slope failure. Data obtained from the movements of tension cracks from six out of ten established stations in Ilgın open pit lignite mine of Turkish Coal Enterprises, West Lignite Enterprises (TKI-GLI) were used to predict future values. The prediction results from the ARIMA method were also compared with results from regression methods and were shown to be more successful.

Keywords
slope failure, open pit mining, time series analysis, autoregressive integrated moving average (ARIMA), regression.

Introduction

Slope stability is an important aspect in a broad range of areas, such as mining, geology, construction, and architecture. It is critical in open pit mines. Many factors such as geological structural properties, the geometry of the slope, the presence of underground water, the properties of materials used, and excavation methods affect slope stability. The consequences of a possible slope failure can be both fatal to personnel and damaging to the mine. Thus, the necessary calculations and analyses should be carried out within certain time intervals. However, this is a complex process which requires experienced professionals. For these reasons, many studies conducted to predict problems with slope stability have used methods other than the classical calculation methods. Regression-based methods are the most preferred because of their simple, explanatory structure and high suitability for measuring these kinds of problems.

Occhiena, Pirulli, and Scavia (2014) developed an analysis procedure to interpret data from a microseismic monitoring system. Gama *et al.* (2017) investigated small baseline subsets for measuring ground deformation and found that SBAS processing allowed the identification of a large number of widely distributed persistent scatters. Another example of a monitoring application relating to this area is from Carlà *et al.* (2017a), who used monitoring data from open pit mines to detect instabilities. There are other applications in which researchers have pursued the monitoring of deformations in the slopes (Fuhrmann *et al.*, 2013; Vanneschi *et al.* 2017). Some researchers have gone one step further in their follow-up studies and have tried to develop methods for estimating deformations that may arise from the available data using different methods (Carlà *et al.*, 2017b; Jibson, 2011; Song, Huang, and Cen, 2016; Khanlari, 2011).

Regression-based methods are among the most preferred modelling strategies used to predict deformation. The rationale behind using regression in predicting slope failure is that a mathematical model is constructed and parameters of that model are estimated using regression methods. However, although regression is a straightforward method, it does have drawbacks: each slope embodies its own characteristics; a mathematical model used for one slope would not fit another. Thus, the appropriate model should be selected first, and then its parameters found. Experience in model selection is, therefore, essential. The other limitation of regression lies in its dependence on strict mathematical formulae. Once a mathematical model by regression is built up to model the structure of a slope, it is used for all future estimates of slope condition. However, several factors, which are expressed as

shock effects, can occur and change the structure of the slope. These include heavy rainfall and earth tremors. In that case, the modelled mathematical expressions lose their validity.

For the abovementioned reasons, researchers have started to experiment with other methods of slope stability analysis. Wu *et al.* (2015) successfully used an improved fractal prediction model in forecasting mine slope deformation. Tan *et al.* (2011) utilized artificial neural networks (ANNs) and particle swarm optimization to predict deformation in a deep open pit mine. They showed the applicability of these methods by calculating RMSE (root mean square error) and MAVE (mean average value error). These values for two measurement points were found between 3% and 6%. Lian *et al.* (2013) conducted a landslide prediction by using an ensemble extreme learning machine (ELM) based on TSA. They used 38 groups of data from June 2004 to July 2007 and their relative errors in seven test data were between 0.03 and 3.17%. Liu *et al.* (2014) compared three state-of-the-art techniques for nonlinear displacement analysis – support vector machine (SVM), relevance vector machine (RVM), and Gaussian process (GP) – using 11 observations from September 2006 to July 2007. They recorded approximate average percentage errors in these methods of between 0.4% and 0.8%. Another ANN application in this area was conducted by Chen and Zeng (2013), who used an improved back-propagation ANN and obtained relative errors between 0.05% and 3.83%.

As mentioned above, regression-based methods have some significant drawbacks. ANNs and other state-of-the-art methods also have their own disadvantages. For example, they require a greater amount of data than that collected in the cited studies for statistically meaningful results in training. Furthermore, as with the regression methods, they can be affected by shock effects. Thus, a time series method, ARIMA, is the preferred method of prediction in this study. ARIMA is based on the autoregressive moving average (AR-MA) process and predicts a new value by using 'some' previous values of a time series data group. It also relies on a mathematical model, but that model does not cover all of the data. It stands for 'some' previous data to predict a new future value. By this aspect, it can cope with shock effects. In addition to this, the only thing that should be found is the model order and not what kind of mathematical model fits the data. Therefore it is easier than regression in that less experience is needed.

Data obtained from six stations in TKI-Ilgın open pit lignite mine was used in this study to predict future deformation values. The ARIMA model was created with 50 deformation data values and six data values were used to validate the prediction capability of the model. The correlation coefficient (R^2) and root mean square error (RMSE) of fits were calculated to compare different ARIMA models. RMS and predicted MSE (PMSE) in validation were also recorded to gauge the effectiveness of the models. To compare ARIMA with regression, the regression models of all six stations were also established. In addition to this, a manually created shock effect was also analysed for station-1 to show the deficiency of regression in incorporating that phenomena. The results give comparatively fewer errors in ARIMA models.

Materials and methods

Problem definition

The tension cracks on the west slope of TKI-GLI Çavuşçugöl open pit mine were observed with a tracking system (Özşen, Özkan, and Mesutoğlu, 2019; Özşen and Özkan, 2013). Çavuşçugöl is located in central Anatolia, 13 km from Ilgın and 80 km from Konya. In the west slopes of the site, there were tension cracks approximately 10 m in length, 20 cm wide, and 50 cm in height as seen in Figure 1 (Özşen and Özkan, 2013). To track these cracks, 10 measurement stations were established. The measurement equipment and method are shown in Figure 2a. A plan view of the mine site and the measurement directions are shown in Figure 2b. Here, the horizontal deformations towards the pit are defined by the Y direction while deformations parallel to the pit are defined by the X direction. Vertical deformations are defined by Z direction. Readings were taken with a precision of 0.01 mm in the Z direction and 0.1 mm in the X and Y directions.

The readings were taken over a period of 56 days and the deformation values relative to the first reading were recorded in the X, Y, and Z directions. The model in this study was constructed for the Y-direction deformations. That is, the amounts of deformation towards and away from the mine were modelled and predictions of possible deformations in that direction were attempted. Also, data from six stations of the ten established stations was used in the study because of its suitability for the ARIMA model.

ARIMA as a TSA method

In TSA, the intention is to predict unobserved data by using observed data that changes with time. A time series data group can be defined as:

$$\boldsymbol{z}_T = (z_1, z_2, \ldots z_T) \quad [1]$$

Here, predictions of T observed values of the data and unobserved data values in time $T + k$ were attempted: z_{T+k}. Let $\widehat{z_T}(k)$ be a predictor of z_{T+k} and be defined as:

Figure 1—Tension cracks formed in the field

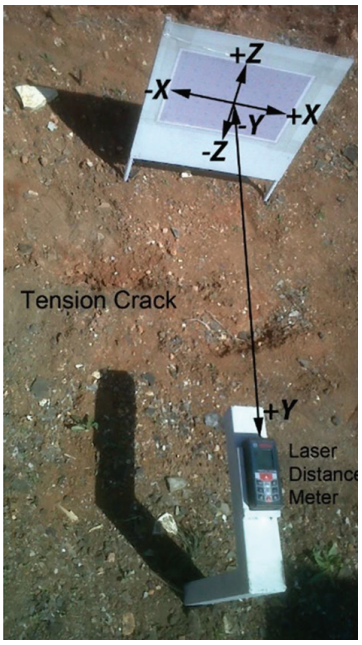

Figure 2a—Equipment and method of measurement system

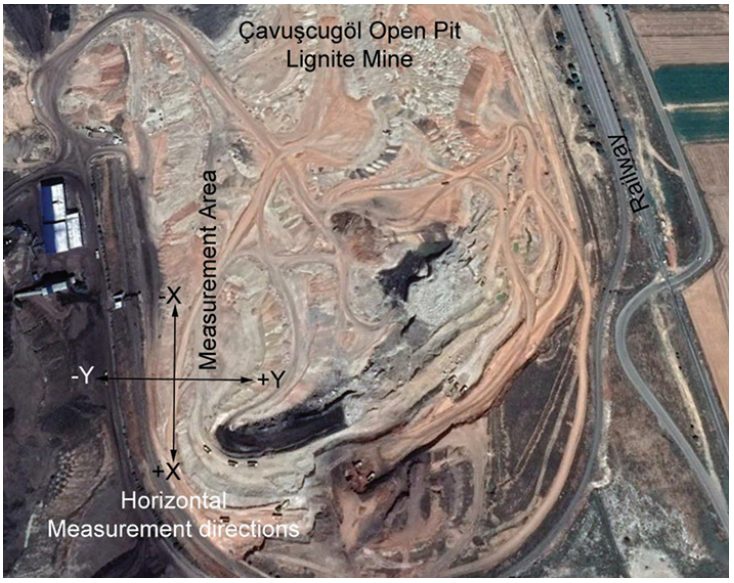

Figure 2b—Plan view of the open pit and the horizontal directions defined in the measurement system for monitoring movements on the tension cracks

$$\widehat{z_T}(k) = \alpha_1 z_T + \alpha_2 z_{T-1} + \cdots + \alpha_T z_1 \quad [2]$$

If $e_T(k)$ is defined as the error of this prediction, it can be defined as:

$$e_T(k) = z_{T+k} - \widehat{z_T}(k) \quad [3]$$

The aim is to minimize error functions which depend on $e_T(k)$. The most used error function is the mean square prediction error (MSPE), which is defined as:

$$MSPE(z_{T+k}|\boldsymbol{z}_T) = E[(z_{T+k} - \widehat{z_T}(k))^2|\boldsymbol{z}_T)] = E[e_T^2(k)|\boldsymbol{z}_T] \quad [4]$$

There are many methods in TSA, such as moving average, random walk, exponential smoothers. and ARIMA models.

Especially for stochastic modelling of time series data, ARIMA could be the best choice. Generally, moving average (MA) models can define trends in data while autoregressive (AR) models are well suited for periodicity such as seasonal variances. An AR model of a time series data group x can be defined as (Kaiser and Maravall, 2000):

$$x_t = \alpha_1 x_{t-1} + \alpha_2 x_{t-2} + \cdots + \alpha_p x_{t-p} + \varepsilon_t \quad [5]$$

Here, p is defined as the model order. In the MA model, the error is modelled as given in the following equation (Kaiser and Maravall, 2000):

$$x_t = \varepsilon_t + \beta_1 \varepsilon_{t-1} + \beta_2 \varepsilon_{t-2} + \cdots + \beta_q \varepsilon_{t-q} \quad [6]$$

If a time lag operator is defined as:

$$Lx_t = x_{t-1}$$

then

$$L^k x_t = x_{t-k} \quad [7]$$

AR and MA processes can be given as in the following equations (Kaiser and Maravall, 2000):

$$\left(1 - \underbrace{\sum_{k=1}^{p} \alpha_k L^k}_{AR\ process}\right) x_t = \underbrace{\left(1 + \sum_{k=1}^{q} \beta_k L^k\right)\varepsilon_t}_{MA\ process} \quad [8]$$

This equation is known as the autoregressive moving average (ARMA) process and is used in many areas such as TSA. ARIMA can be thought of as a kind of ARMA process. The only difference is the differencing operation, which is an indispensable part of TSA methods to eliminate trend components. The differencing operation can be represented as:

$$\Delta x_t = x_t - x_{t-1} = (1 - L)x_t$$
$$\Delta^2 x_t = (1 - L)^2 x_t \quad \ldots \quad [9]$$

Now the main equation for the ARIMA (p, d, q) model can be given as (Kaiser and Maravall, 2000):

$$\left(1 - \underbrace{\sum_{k=1}^{p} \alpha_k L^k}_{AR\ model}\right) \underbrace{(1 - L)^d}_{differencing}\ x_t = \underbrace{\left(1 + \sum_{k=1}^{q} \beta_k L^k\right)\varepsilon_t}_{MA\ model} \quad [10]$$

The only parameters to determine in this model are p, d and q, which represent the model degree of the AR process, the degree of differencing, and the model degree of the MA process, respectively.

Analysis methodology and evaluation criteria

The data taken from the six stations over a period of 56 days was used for modelling by ARIMA. For each station, different ARIMA models were tested and the best-suited model was recorded. Also, for all stations, a regression process was conducted for comparison. Here again, the best-suited regression line was found. A total of 50 data values were used for model foundation while the remaining six data values were used as validation data for the founded model. The comparison between ARIMA models and the best-suited regression model was done using the correlation coefficient (R^2) and predictive mean square error (PMSE: same as MSPE). The correlation coefficient can be calculated by the following equation:

$$R^2 = \frac{\sum_{k=1}^{m}(x_{k,i} - \bar{x_i})(y_k - \bar{y})}{\sqrt{\sum_{k=1}^{m}(x_{k,i} - \bar{x_i})^2 \sum_{k=1}^{m}(y_k - \bar{y})^2}} \quad [11]$$

Results

Results with ARIMA models

For the first station's data, which is termed data-1, five ARIMA models were tested using data from 50 days (deformation values in the Y directions). After testing the generated models with remaining six data groups, the correlation coefficient (R^2) and PMSE were recorded, and are shown in Table I. As shown in Table I, the best fit model is ARIMA (3,1,1), which represents a combination of a third-order AR process, first-order MA process, and one-degree differentiation. The obtained parameters of the best fit ARIMA model are seen in Table II.

Table I

The tested ARIMA models for station-1 data and the results obtained in validation data with these models

ARIMA model	R^2	PMSE
ARIMA(3,1,0)	0.99	0.1293
ARIMA(3,0,0)	0.99	0.0988
ARIMA(2,1,0)	0.99	0.0963
ARIMA(2,0,0)	0.99	0.0392
ARIMA(3,1,1)	0.99	0.0197

Table II

The obtained ARIMA parameters

Parameter	Value	Error
Constant	0.0132	0.0049
AR{1}	1.6872	0.2003
AR{2}	-0.8913	0.3558
AR{3}	0.1652	0.2195
MA{1}	-0.9999	0.1020

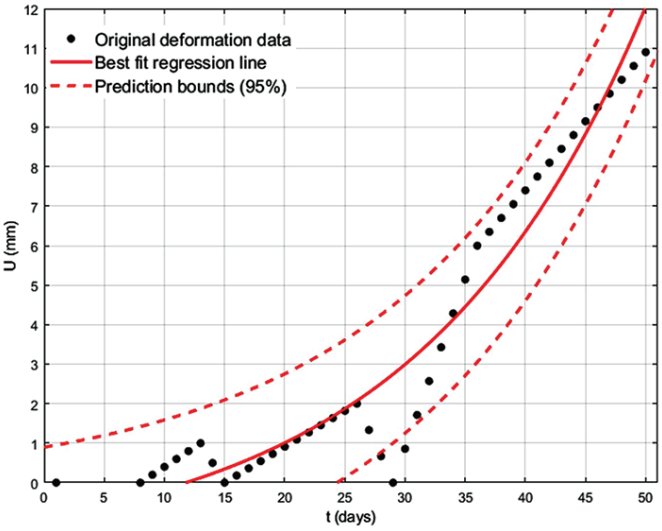

Figure 3—The regression line of the best fit equation (given in Equation [11]) for the deformation data obtained from station-1

To compare the success of ARIMA in modelling data-1, a regression procedure was also conducted for data-1. After some experimentation, the best fit equation for the 50 data values in data-1 was found to be:

$$U = -1.858 + e^{0.05265t} \quad [12]$$

Here, U is the deformation value in the Y-direction in millimetres and t is time in days. The regression line is shown in Figure 3 together with the original deformation data.

When six validation data groups were predicted by the best fit ARIMA model and best fit regression model, the consequences shown in Figure 4 were found. Also, the real and predicted values of validation data are given in Table III.

As shown in Figure 4 and Table III, there is an obvious difference between real data and predicted data for the regression model. However, when it comes to the ARIMA model, the consequences are less significant. The difference between the ARIMA and regression models with respect to the correlation

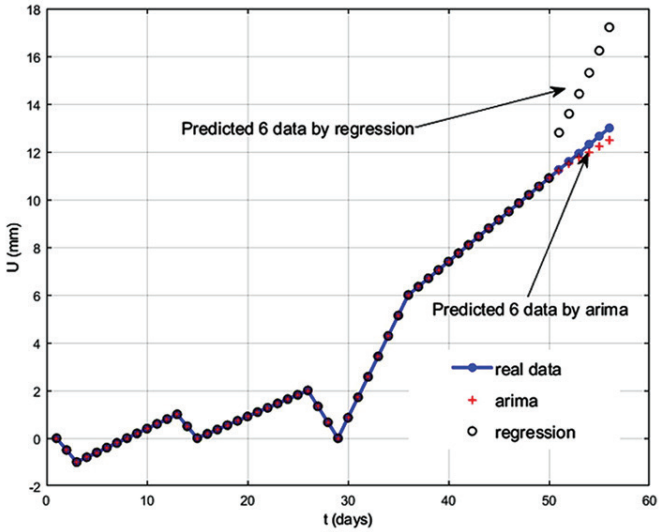

Figure 4—Prediction for validation data in best fit ARIMA and regression models

coefficient and PMSE for data-1 is given in Table IV. As can be seen, ARIMA presented a remarkably better performance with respect to the PMSE, which is a much more important factor in predicting unobserved data.

The same procedure was conducted for the remaining five stations. Again, several ARIMA models were tested for each station. The best fit ARIMA models are shown in Table V. Generally, except for one station, a third-order AR process was utilized in all models. This means that a new unobserved value will be predicted by using the last three data values in the current time series. When it comes to the MA process, which defines periodicity or 'seasonality' in a time series data, a first-order MA process was used in only two of the stations. This means that the deformation data in the stations has a generally non-repetitive trend component.

Table III

Real and predicted validation data by ARIMA and regression

Data	Real value	Predicted value by ARIMA	Predicted value by regression
1	11.25	11.21	12.80
2	11.60	11.49	13.59
3	11.95	11.75	14.43
4	12.30	12.00	15.31
5	12.65	12.24	16.24
6	13.00	12.48	17.22

Table IV

Correlation coefficient and PMSE of best fit regression and ARIMA models for validation data in station-1

Model	R^2	PMSE
Regression	0.99	8.7126
ARIMA (3,1,1)	0.99	0.0197

The regression models were also found for these stations. The regression lines and best fit regression equations for these five stations are shown in Figure 5. As shown, the best suited model was exponential regression equation.

Regression can be an appropriate choice for such problems, but it is a strict method because of its work strategy. Once a mathematical equation is determined from available data, all future values are predicted by that fixed equation. However, especially in mining, there can be sudden and unexpected changes and regression models cannot cope with that level of change. On the other hand, after determining model order in ARIMA, future values are predicted by previously observed data. Then, if there is a sudden change in data, subsequent future values are predicted such that they will also be affected by this

Table V

Best fit ARIMA models for six stations

Station-1 ARIMA(3,1,1):			Station-2 ARIMA(3,1,1):			Station-3 ARIMA(3,0,0):		
Parameter	**Value**	**Error**	**Parameter**	**Value**	**Error**	**Parameter**	**Value**	**Error**
Constant	0.0133	0.0049	Constant	0.0932	0.1226	Constant	0.4474	0.5630
AR{1}	1.6873	0.2003	AR{1}	0.3967	0.7501	AR{1}	1.7472	0.2010
AR{2}	-0.8914	0.3558	AR{2}	0.0129	0.5346	AR{2}	-0.9727	0.3975
AR{3}	0.1653	0.2195	AR{3}	-0.2693	0.1946	AR{3}	0.2137	0.2327
MA{1}	-0.9999	0.1021	MA{1}	0.2746	0.8249			
R^2 = 0.99 PMSE = 0.0197			R^2 = 0.99 PMSE = 0.0576			R^2 = 0.99 PMSE = 3.7663		
Station-4 ARIMA(3,0,0):			**Station-5 ARIMA(3,1,0):**			**Station-6 ARIMA(2,0,0):**		
Parameter	**Value**	**Error**	**Parameter**	**Value**	**Error**	**Parameter**	**Value**	**Error**
Constant	0.1916	0.2199	Constant	0.0859	0.0631	Constant	0.0371	0.7901
AR{1}	1.7559	0.2638	AR{1}	0.7695	0.2198	AR{1}	1.7648	0.5650
AR{2}	-0.9641	0.5241	AR{2}	-0.3207	0.2360	AR{2}	-0.7660	0.5025
AR{3}	0.1956	0.2885	AR{3}	0.0197	0.1791			
R^2 = 0.99 PMSE = 0.0007			R^2 = 0.99 PMSE = 0.7192			R^2 = 0.99 PMSE = 0.3222		

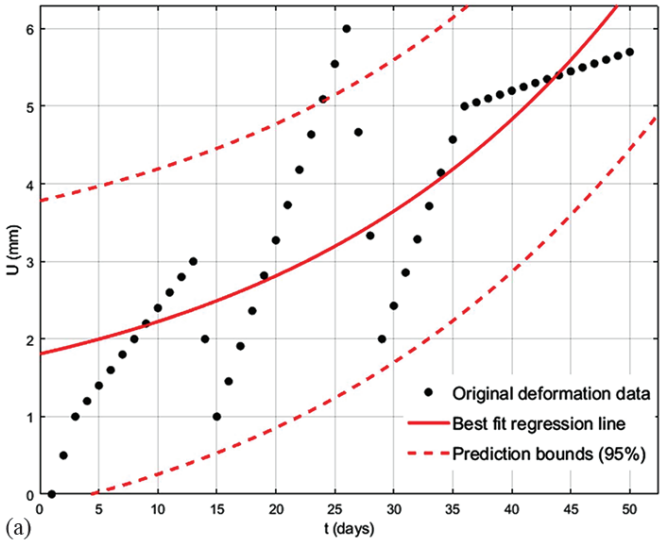

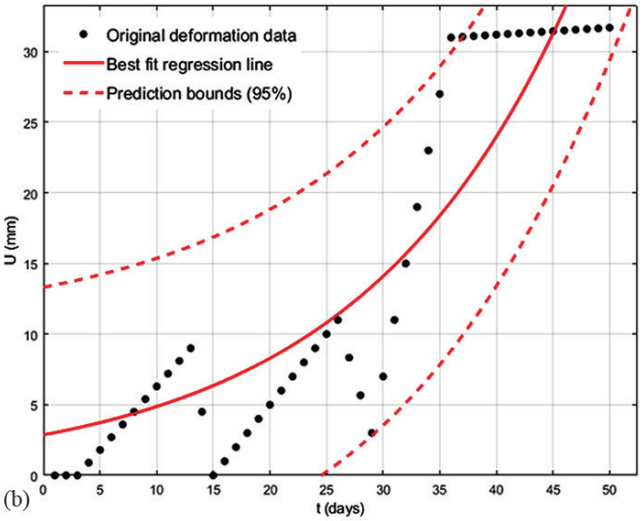

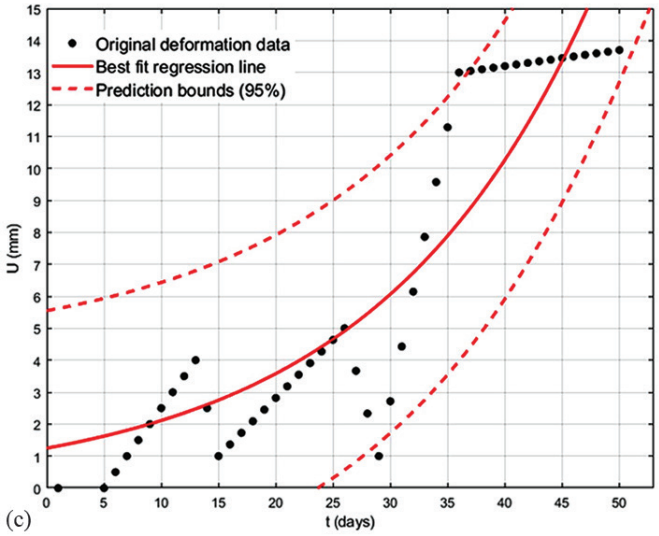

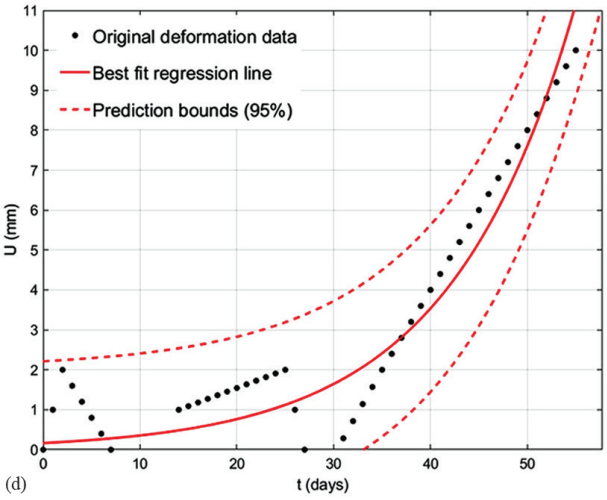

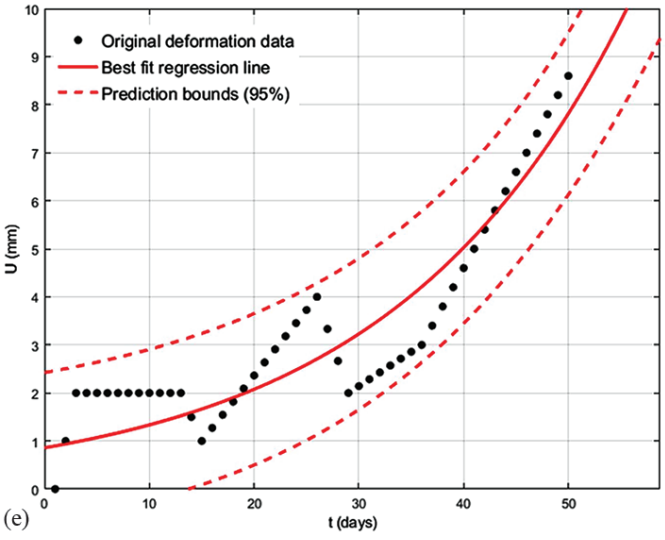

Station-2	Figure 5a	Best-fit regression model: $U=0.8084 + e^{0.03487t}$ Performance in validation: $R^2 = 0.99$ PMSE = 1.9932
Station-3	Figure 5b	Best-fit regression model: $U=2.866e^{0.05311t}$ Performance in validation: $R^2 = 0.99$ PMSE = 323.69
Station-4	Figure 5c	Best-fit regression model: $U=1.248e^{0.05268t}$ Performance in validation: $R^2 = 0.99$ PMSE = 53.84
Station-5	Figure 5d	Best-fit regression model: $U=0.07191e^{0.09497t}$ Performance in validation: $R^2 = 0.99$ PMSE = 8.6363
Station-6	Figure 5e	Best-fit regression model: $U=0.8586e0^{.04417t}$ Performance in validation: $R^2 = 0.99$ PMSE = 0.7250

Figure 5—Generated regression models for the remaining five stations *(continued)*

change. The is also known as the 'shock effect' in TSA, and the results of regression and ARIMA incorporating this situation are given in the next subsection. The other problem in using a strict mathematical model in regression is the determination of an appropriate model. For example, an exponential model can give similar results to a power model. The real relationships between independent and dependent variables are not known, but predictions are attempted *via* mathematical equations. Thus, error

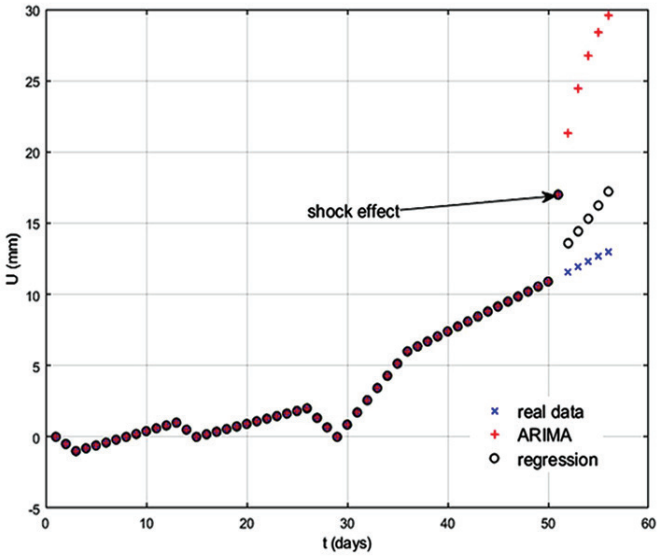

Figure 6—Simulation of shock effect: responses of ARIMA and regression methods to the validation data

margins for the regression can be large. In ARIMA, however, the only thing to select was the order of the model: p, d, and q. ARIMA uses the same equation for all data (Equation [10]).

Shock effect simulation of ARIMA and regression for the station-1 data

As briefly mentioned above, a shock effect in a time series data group is caused by a sudden or unexpected change in the data. In this case, because the recorded data did not include such a change, it was inserted manually for simulation. Station-1 data was used for this purpose and the value of the 51st data point, which was the first validation data, was changed manually. The prediction of regression and ARIMA for validation data including this shock effect is shown in Figure 6.

The first 50 data values were not changed and were used to find the best fit model both in ARIMA and regression. The 51st data value simulates a shock effect and the remaining five in the validation set were predicted using both methods. When the predicted data values are compared in Figure 4 (without shock effect) and Figure 6 (with shock effect); it can be seen that there is no change in the predicted data values of regression. That is, the shock effect doesn't have any influence on the regression method. However, ARIMA changed its new predicted values because it computed a new value by using previously recorded data. This situation is more suited to real cases because if an unexpected event happens, such as an earth tremor or a flood triggered by heavy rainfall, deformations could be more serious.

Conclusions

Prediction of slope failure is an important aspect in the prevention of possible accidents in open pit mines. Computational procedures have to be conducted for the safety of the area, but the prediction process is not easy and requires experienced personnel. Many methods have been used for this aim, and most of them depend on regression. Regression is the term given to methods used to find parameter values in a specific mathematical relationship between inputs and outputs. Thus, it supposes that there is a mathematical formula defining a process. However, in real life situations, this is affected by various factors such as floods, earth tremors, and landslides. Thus, there can be abrupt and unexpected changes in the likelihood of slope failure. This violates the strict mathematical definition of slope displacements. One alternative to regression-based methods is TSA. In TSA, an unobserved data event in the future is predicted by using a combination of available data.

In this study, ARIMA was used as a TSA method to predict slope failure as an alternative to regression. Deformation data from six stations at an open pit mine was used for this purpose. When ARIMA was used for the data, it was seen that ARIMA models with three AR coefficients were generally successful. This means that a new value will be predicted by the last three data values. The prediction ability of tested ARIMA models was examined using correlation coefficients and PMSE in validation data. According to the results, satisfactory values were obtained. In addition to this, to emphasize the success of ARIMA models and compare them with a general prediction method for such problems, regression methods were also applied to all data from six stations. The best regression lines were found by experimental procedures and it was noted that exponential mathematical forms gave the best results. When the correlation coefficients and PMSE values of these models obtained for validation data were compared with those from ARIMA, noticeably better results were recorded in favour of ARIMA.

The advantage of ARIMA over regression is that it has no strict mathematical formulation to define the data. In regression, a mathematical model is formulated to describe the behaviour of the data and it does not change with time, but unexpected changes may occur that violate the formed equations. In such cases, the formulation calculated with regression loses its validity. On the other hand, ARIMA uses its formulation only to predict a new value by using some previous observations. Thus, it is more suitable for the abovementioned changes. To simulate this, an artificial shock effect was applied to both the ARIMA and regression methods, and it was seen that ARIMA's performance was better than regression in coping with this shock effect.

Acknowledgements

The author is indebted to the administrative and technical personnel of TKI and the reviewers for their valuable contributions.

References

Carlà, T., Farina, P., Intrieri, E., Botsialas, K., and Casagli N. 2017a. On the monitoring and early-warning of brittle slope failures in hard rock masses: Examples from an open-pit mine. *Engineering Geology*, vol. 228. pp. 71–81.

Carlà, T., Intrieri, E., Farina, P., and Casagli, N. 2017b. A new method to identify impending failure in rock slopes. *International Journal of Rock Mechanics and Mining Sciences*, vol. 93. pp. 76–81.

Chen, H. and Zeng Z. 2013. Deformation prediction of landslide based on improved back-propagation neural network. *Cognitive Computation*, vol. 5. pp. 56–62.

Fuhrmann, T., Heck, B., Knöpfler, A., Masson, F., Mayer, M., Ulrich, P., Westerhaus, M., and Zippelt K. 2013. Recent surface displacements in the Upper Rhine Graben – Preliminary results from geodetic networks. *Tectonophysics*, vol. 602. pp. 300–315.

Gama, F.F., Cantone, A., Mura, J.C., Pasqualli, P., Paradella, W.R., dos Santos, A.R., and Silva G.G. 2017. Monitoring subsidence of open pit iron mines at Carajás Province based on SBAS interferometric technique using TerraSAR-X data. *Remote Sensing Applications: Society and Environment*, vol. 8. pp. 199–211.

Jibson, R.W. 2011. Methods for assessing the stability of slopes during earthquakes - A retrospective. *Engineering Geology*, vol. 122. pp. 43–50.

Kaiser, R. and Maravall, A. 2000. Notes on the time series analysis ARIMA models and signal extraction. Working paper, Banco de Espana, Madrid.

Khanlari, G.R., Heidari, M., Momeni, A.A., and Abdilor Y. 2011. Prediction of shear strength parameters of soils using artificial neural networks and multivariate regression methods. *Engineering Geology*, vol. 131-132. pp. 11–18.

Lian, C., Zeng, Z., Yao, W., and Tang, H. 2013. Displacement prediction model of landslide based on a modified ensemble empirical mode decomposition and extreme learning machine. *Natural Hazards*, vol. 66. pp. 759–771.

Liu, Z., Shao, J., Xu, W., Chen, H., and Shi, C. 2014. Comparison on landslide nonlinear displacement analysis and prediction with computational intelligence approaches. *Landslides*, vol. 11, no. 5. pp. 889–896.

Occhiena, C., Pirulli, M., and Scavia, C. 2014. A microseismic-based procedure for the detection of rock slope instabilities. *International Journal of Rock Mechanics & Mining Sciences*, vol. 69. pp. 67–79.

Özşen, H., Özkan, İ., and Mesutoğlu, M. 2019. An approach on modelling of in-situ deformations for unstable coal mine slopes. *Bulletin of Engineering Geology and the Environment*, vol. 78. pp. 3191–3203.

Özşen, H. and Özkan İ. 2013. Deformation monitoring and time dependent mathematical modeling of the tension cracks at the western slopes of TKI-GLI Ilgın open lignite mine. *Selcuk University Journal of Engineering, Science and Technology*, vol. 1, no. 3. pp. 37–44.

Song, Y., Huang, D., and Cen, D. 2016. Numerical modelling of the 2008 Wenchuan earthquake-triggered Daguangbao landslide using a velocity and displacement dependent friction law. *Engineering Geology*, vol. 215. pp. 50–68.

Tan, G., Liu, H., Cheng, Y., Liu, B., and Zhang, Y. 2011. Prediction method for the deformation of deep foundation pit based on neural network algorithm optimized by particle swarm. *Proceedings of the 2011 International Conference on Transportation, Mechanical, and Electrical Engineering*, Changchun, China, 16-18 December 2011. IEEE, Piscataway, NJ. pp. 1407–1410.

Vanneschi, C., Eyre, M., Francioni, M., and Coggan, J. 2017. The use of remote sensing techniques for monitoring and characterization of slope instability. *Procedia Engineering*, vol. 191. pp. 150–157.

Wu, H., Dong, Y., Shi, W., Clarke, K.C., Miao, Z., Zhang, J., and Chen, X. 2015. An improved fractal prediction model for forecasting mine slope deformation using GM (1, 1). *Structural Health Monitoring*, vol. 14, no. 5. pp. 502–512. ◆

Reliability and evaluation of point load index values obtained from different testing devices

D. Akbay[1] and R. Altındağ[2]

Affiliation:
[1]Çanakkale Onsekiz Mart University, Çan Vocational School, Çanakkale.
[2]Süleyman Demirel University, Department of Mining Engineering, Isparta.

Correspondence to:
D. Akbay

Email:
denizegeakbay@hotmail.com

Dates:
Received: 21 May 2019
Revised: 31 Nov. 2019
Accepted: 2 Dec. 2019
Published: March 2020

How to cite:
Akbay, D. and Altındağ, R. Reliability and evaluation of point load index values obtained from different testing devices. The Southern African Insitute of Mining and Metallurgy

DOI ID:
http://dx.doi.org/10.17159/2411-9717/759/2020

ORCiD ID:
D. Akbay
https://orcid.org/0000-0002-7794-5278

R. Altındağ
https://orcid.org/0000-0002-5397-7312

Synopsis

In some rock mass classification methods, the point load index (PLI) value is used as a parameter in the determination of the class of rock mass. The PLI value may be used as a design parameter such as uniaxial compressive strength (UCS) and tensile strength (TS), owing to its being simpler, faster, and cheaper and easier to prepare than the specimens for UCS and TS tests. It can also be carried out in both the field and the laboratory. Many researchers have investigated PLI testing and the effect of different loading configurations, sample size, and size correction factors.
Within the scope of this study, PLI tests were performed in 15 different point load index testing devices. The experiments were carried out on seven different rock types (three sedimentary, one metamorphic, three magmatic) by the same operator. The errors of the testing devices were investigated based on the experimental results, and a device was modified to avoid the errors identified. Additional experiments were carried out in the modified testing device to acquire more realistic values. The PLI values obtained from the modified device were found to be more reliable, with standard deviations lower than those obtained from other conventional testing devices.

Keywords
point load index, rock mass classification, measurement error, testing device.

Introduction

Classification of rock masses in engineering projects is important in terms of project planning and designing. There is little information about the rock mass in the feasibility and initial design phases of a project. Attempts have been made to acquire knowledge about the rock mass by using experimental, observational, and empirical methods. The experimental methods are carried out in accordance with rock mechanics standards, which are the most commonly used and most accurate methods to characterize the rock mass. It is sometimes costly and time-consuming to prepare the rock samples and to carry out the experiments. In such cases, the test methods which are simpler, faster, easier, portable, cheaper, and do not require specimen preparation are preferred. The most commonly used strength values for rock materials are the point load index (PLI) and uniaxial compressive strength (UCS). Such values are also used as input parameters in the classification of rock masses and rock excavatability for engineering structures both underground and on the surface.

PLI is used as a rated parameter as the strength value of intact rock in some rock mass classification systems. When rock mass classification systems in which PLI is directly used as a rated parameter are examined, it will be noticed that five classes are mostly formed of lower to higher strengths. Also, that the strength values in the first four classes range from zero to 4 MPa, whereas the fifth class comprises the values >4 MPa (Franklin, Broch, and Walton, 1971; Broch, Broch and Walton, 1971; Broch and Franklin, 1972; Edet and Teme, 1990; Ghosh and Srivastava, 1991; Pettifer and Fookes, 1994; Tsiambaos and Saroglou, 2010). However, UCS is the most commonly used parameter in the classification systems, whereas PLI is most commonly used in the indirect estimation of UCS. Several researchers have carried out studies to predict UCS as a function of PLI and more than 100 equations relating the two parameters have been proposed (Akbay, 2018). The PLI values of the rocks must be multiplied by a wide range of coefficients, from 3 to 71, to predict the UCS values (Akbay, 2018). However, there is no particular study which deals with the rock types and the shapes of specimen to which these coefficients apply. Although the PLI test is considered a field test, it is unclear whether the PLI data found in the literature was obtained in the laboratory or in the field. Within the context of the studies, it is understood that the tests were carried out in a laboratory. For this purpose, the current method of determining the PLI using a PLI device should be reviewed so that more accurate measurements, which are free from the current errors and associated disadvantages, can be obtained.

Reliability and evaluation of point load index values obtained from different testing devices

Several studies have been devoted to examining the relationship between PLI and some physical and mechanical properties of rocks. Topal (2000) studied the problems related to the PLI device and its application. Aston, MacIntyre, and Kazi (1991) investigated the effects of wear and rupture on the strength of the conical platens of the PLI testing device. Akbay and Altındağ studied the errors inherent to the PLI testing device and the errors caused by the operator (2018), and Akbay (2018) modified the conventional PLI testing device to avoid the errors. In addition, several other researchers have used PLI values to determine the UCS and tensile strength of rocks, to classify rocks according to their strength in terms of material properties (Guidicini, Nieble, and De, 1973; Bieniawski, 1975) in the RMR rock classification system (Bieniawski, 1989), to estimate the speed of a tunnel boring machine (McFeat and Tarkoy, 1979), and to classify rocks in terms of excavatability (Pettifer and Fookes, 1994). Karaman, Kaya, and Kesima (2015) estimated UCS by using the PLI for RMR classification. Broch and Franklin (1972) stated that the UCS value of rocks is 24 times the PLI value. Hawkins (1998) investigated the relationship between UCS and PLI using different rock types and found that the ratio between the two (UCS/PLI) varied from 7–68. Rusnak and Mark (2000) examined the ratio between UCS and PLI and found it to be between 20 and 22. Quane and Russel (2003) carried out UCS and PLI tests on hard and soft rocks, and observed that the relationship between UCS and PLI is linear in hard rocks and nonlinear in soft rocks. Singh, Kainthola, and Venkatesh (2012) studied the ratio between UCS and PLI using similar hard and soft rocks and observed that the ratio was between 21 and 24 in hard rocks and 14 and 16 in soft rocks. It is thus seen that the conversion coefficients (K) used to predict UCS from PLI vary between 3 and 71 (Akbay, 2018). The K value depends on many factors such as rock type, shape of the specimen, test method, *etc*. Table I presents a simplified list of K values for different rock strength classes.

There are several companies marketing PLI testing devices around the world, but very few manufacturers. There are also more than 100 different PLI testing devices. The general principles of the measurement technique and design are very similar; however, there are minor differences such as the hydraulic system, position of the hydraulic system (horizontal or vertical), loading arm, indicator (mechanical or digital), and specimen location (fixed or free). The most widely used PLI testing device consists of a loading system, load indicator, and conical platens (Figure 1).

In this study, problems related to the PLI testing device and the common errors generated by the operators are considered. Based on the experience of the researchers and a literature review, differences in loading speed and failure time, maintenance issues, dial gauge calibration, geometry of the conical platens, axis shift of the conical platens, length of the loading arm, and different operators are identified as sources of error. PLI tests were carried in 15 different testing devices using seven different rock types (three sedimentary, one metamorphic, three magmatic) by the same operator and the errors obtained were studied and described based on the results. In this study, a conventional PLI testing device was modified to eliminate the errors and disadvantages. For each rock type, seven different specimens of the same size were tested uniformly at constant loading speed and the PLI values were recorded. The differences between the conventional PLI testing device and the modified device were demonstrated.

Materials and method

Rock samples tested in this study were obtained from stone processing plants situated in different regions in Turkey (Table II)

Table I

K values for different rock strength classes

Rock strength class	Conversion coefficient (K)
Very low	11–71
Low	11–46
Medium	9–50
High	6–40
Very high	8–20

Table II

Geographical and geological origins of the rocks used in this study

Sample	Sample code	Type	Origin
Limestone-1	K-1	Sedimentary	Isparta
Limestone-2	K-2	Sedimentary	Isparta
Limestone-3	K-3	Sedimentary	Antalya
Marble	M	Metamorphic	Muğla
Andesite	A	Igneous	Isparta
Granite	G	Igneous	Aksaray
Diabase	D	Igneous	Kayseri

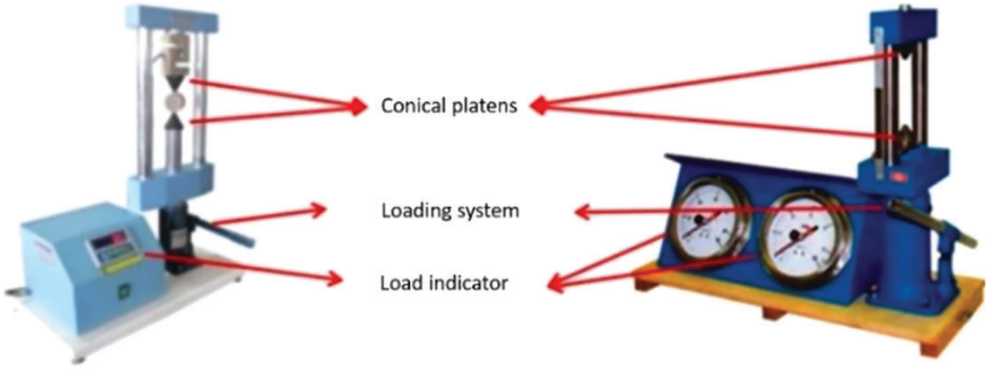

Figure 1—Appearance of conventional point load index testing devices

and were prepared in compliance with the standards suggested by ISRM (1985, 2007). Studies were performed in the Natural Stone Technology and Excavation Mechanics Laboratory of the Mining Engineering Department at Suleyman Demirel University. Specimens used in the tests were classified in such a way that a low to high strength scale was formed in order to be able to represent the rocks with different strength values.

Prismatic specimens 30 × 50 × 50 mm in size were prepared from rock types selected as being as homogeneous and isotropic as possible. In order to avoid differences due to depth, the test samples were prepared from 30 mm thick slabs cut horizontally from the same block. The block samples were examined for macroscopic imperfections so as to ensure standard testing samples free of cracks and weathering. In order to ensure the homogeneous distribution of the samples between the 15 different testing devices in terms of structural properties, samples with the same number of visible structural defects were classified and distributed equally on each testing device. For each testing device, 10 specimens were prepared from each rock sample. Diagonal lines were drawn on the prismatic specimens so that the operator could perform the loading operation at the exact midpoint of the specimen (Figure 2). During the laboratory work, more than 1500 specimens were tested.

The tests were carried out in 15 different PLI testing devices, by the same operator, according to the standards suggested in ISRM (1985, 2007). The PLI devices were of eight different brands. Six of the devices had mechanical dial gauges and nine had digital gauges. The conical platens used in the devices were of five different geometries.

Prior to the tests, the standards (ISRM, 1985, 2007, ASTM, 1995, 2008) relating to the PLI test were scrutinized. A preliminary study was performed and some observations were made (Figure 3). The available information from the literature regarding the problems and difficulties encountered were combined with the observations from the preliminary study. Some measurements were conducted before conducting the experiments, considering the issues specified in the standards (ISRM, 1985, 2007). These were:

- Calibration (load indicator) control: a load cell and an indicator were used to control the calibration of the testing devices
- Hardness value measurement of conical platen: A micro-hardness testing device was used.
- The angle of conical platens and spherical radius of the tip: Photographs of the conical platens were taken and examined digitally using autocad software package and the radii were calculated.
- Length of the loading arm: All loading arms were measured using a length measuring device.

All measured parameters of the PLI devices are given in Table III. The conical platens used in the devices had a spherical radius between 2.2 and 6.2 mm, and hardness values varying between 51 and 64 HRc. The loading arm lengths ranged from 35 cm to 51 cm.

Errors in point load index test

Loading speed and discrete loading

The loading process is performed manually in PLI devices, hence the magnitude and continuity of the applied force varies according to the operator As suggested by ISRM, the load should be steadily increased such that failure occurs within 10–60 seconds (ISRM, 1985, 2007). The failure load varied in a nonuniform manner according to the loading speed. The

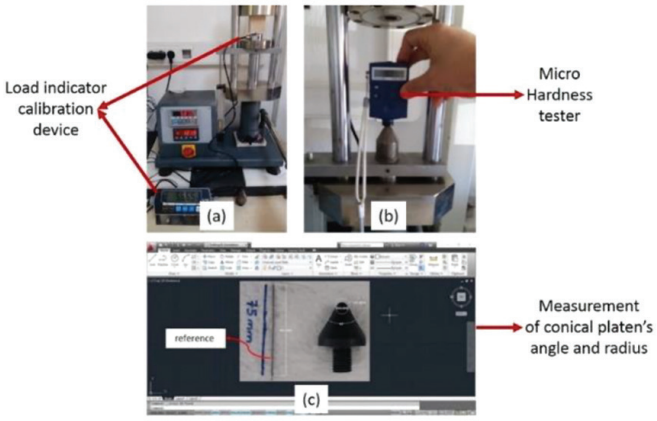

Figure 3—Pre-measurements on the testing devices. (a) Calibration control, (b) hardness test, (c) measurement of the angle of conical platen and platen radius

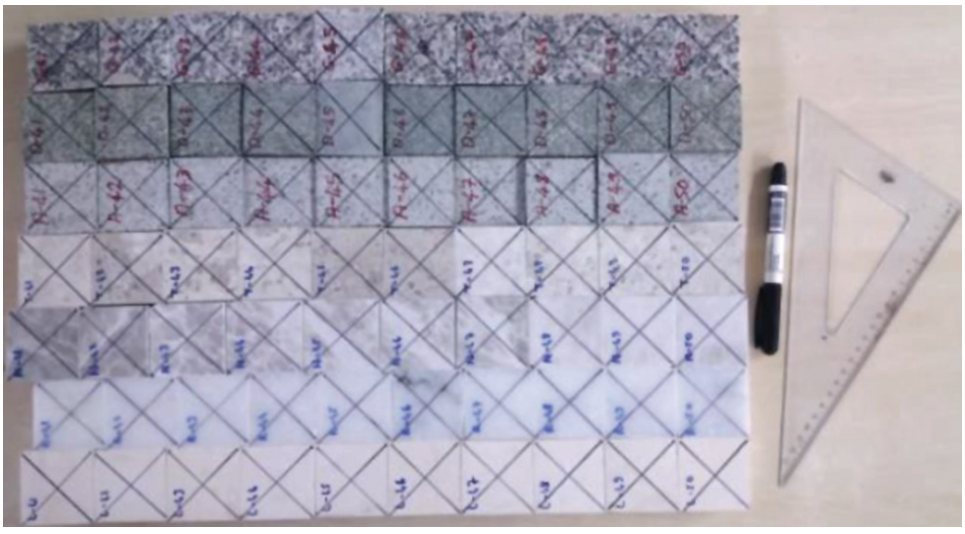

Figure 2—Specimens prepared for PLI tests

Table III

General information regarding the PLI testing devices

Device code	Production date (year)	HRc hardness of conical platens	Angle of conical platens (°)	Spherical radius of conical platens (mm)	Length of loading arm (cm)
1	2012	62.63	59.5	5.8	51.0
2	1995	63.59	60.0	6.1	45.0
3	1995	59.27	60.5	5.2	45.0
4	2007	53.37	59.5	2.2	39.5
5	1999	59.14	60.5	6.2	50.5
6	2011	55.95	63.0	4.4	44.5
7	2000	51.44	59.5	5.9	35.0
8	1995	63.74	59.5	5.6	45.0
9	2014	56.9	62.5	4.0	47.0
10	2013	60.64	59.5	5.6	40.0
11	1995	59.55	60.5	5.6	45.0
12	2016	58.45	60.0	5.0	43.5
13	2008	54.45	60.0	3.9	39.5
14	2016	63.25	59.5	3.9	36.5
15	1995	62.02	60.5	5.4	44.5
Reference values		>58	60.0	5.0	

loading speed should be kept constant during the entire test. If the loading process is too fast, the PLI load will be higher than normal, if too slow, lower.

Failure time

Many researchers do not pay attention to the failure time. If the test process is completed in less than 10 seconds or more than 60 seconds (*i.e.* the loading process is too fast or too slow), the 'failure load of the rock' is measured higher or lower than it is supposed to be. As such, the test process should be completed within 10 to 60 seconds. When the loading is too fast or too slow it will cause the rock to fail at higher or lower loads, respectively, than it would otherwise.

Lack of periodical maintenance

The maintenance of the testing devices was not carried out periodically. Non-calibrated load indicators (dial gauges), worn conical platens, and oil loss affect the PLI values.

Use of different types of jacking systems

PLI testing devices are not very expensive, so the device selected by the manufacturer is chosen from among the least expensive (but workable) equipment. This will lead to the use of devices that are not long-lasting, and which also lack quality and precision. In the different brands of PLI devices that are available in the market, the manufacturers use jacking systems supplied from other companies, which leads to the use of jacks with different characteristics (*e.g.* different loading capacities).

Dial gauge (indicator) errors

Precision readings of failure load cannot be performed on mechanical dial gauges. PLI testing devices with mechanical indicator have two dial gauges, one of which has a capacity of 5.5 kN and a sensitivity of 0.1 kN while the other has a capacity of 55 kN and a sensitivity of 1 kN. If the dial gauges are not calibrated to each other, they can indicate different values. Determination of the failure load may be up to the operator, *e.g.* the indicator is not automatically set to zero, so the two indicators may not be synchronized (Figure 4).

Conical platen geometry

According to the standards suggested by ISRM (1985, 2007), the conical platens should have an angle of $\alpha = 60°$ and the tip should have a sphericity of 5 mm (Figure 5). Use of non-standard conical platens will cause the results to differ from the true values. If the conical platen tip has a sphericity of more than 5 mm, the PLI load will be higher than normal, otherwise, lower.

Distortion of conical platens from axis

In the ISRM standards (1985, 2007), it is suggested that the platens should remain coaxial within ±0.2 mm throughout testing (Figure 6). In general, if this condition is not fulfilled, the test is not carried out under appropriate conditions. In this case, the test result will not be correct, and furthermore there is a risk to the operator that the specimen may be ejected from the device uncontrollably.

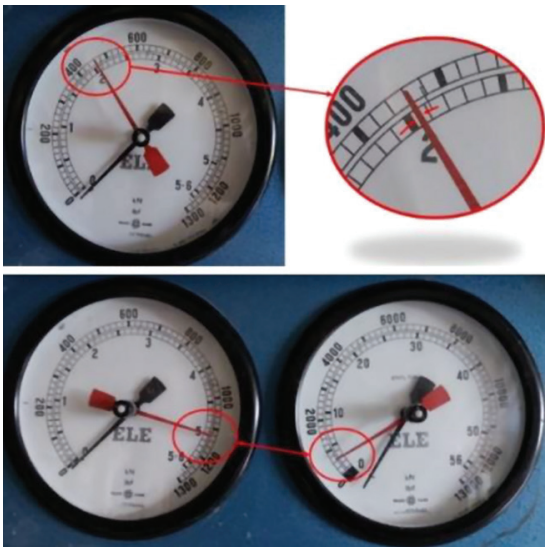

Figure 4—Some indicator errors

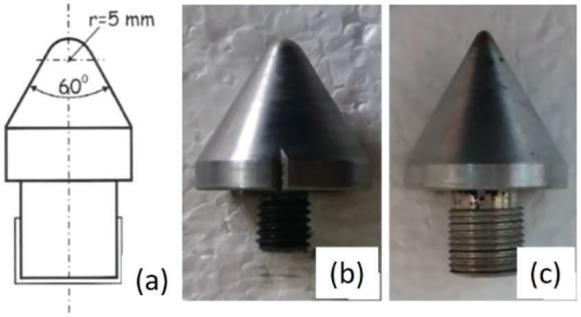

Figure 5—Standard (a) and non-standard (b) and (c) conical platens

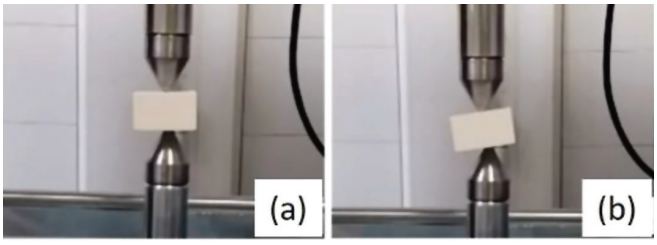

Figure 6—Distortion of conical platens from axis

Penetration of the conical platens into the specimen in the case of soft or weak rocks

When testing soft or weak rocks, the conical heads are allowed to penetrate into the sample (Figure 7), and compression is initiated after the heads have penetrated a certain distance, not as soon as the contact with the sample is established. Therefore, some researchers have suggested that the distance between the conical platens at the end of the test should be taken into account when PLI is calculated, instead of the measured thickness of the specimen.

Effect of the length of loading arm (jack)

ISRM (1985, 2007) and ASTM (1995, 2008) make no suggestions as to the length of the loading arm of the PLI testing device. Loading arms of various lengths are available in different testing devices (Figure 8).and hence the moment effect will vary. The loading process will be unbalanced if the loading arm is longer or shorter than it is required to be. In this case, the tests will not yield accurate results.

Effect of different operators

Determination of the PLI requires a laboratory experiment in which physical activity is needed. In case of the PLI test, the loading process is done manually, hence the magnitude and continuity of the applied force will vary depending on the operator. This means that there will be several factors such as age, level of experience, strength of the operator, different moods (calm, hasty, nervous, sad, preoccupied *etc*.) that may affect the performance in a positive or negative manner). This may result in different loading speeds, different failure times, and different dynamic situations for each test.

Modified point load index testing device

As outlined above, some of the errors or disadvantages of the device will cause the testing results to indicate higher or lower values than the true values. Some PLI testing devices embody all the errors and disadvantages stated above, while others have only a few of the shortcomings. In fact, It is difficult to predict how the measured values will deviate from the true values when all of those errors and disadvantages are combined. The 'operator factor' probably constitutes the most important factor since it is difficult to calculate its influence on PLI values. When the effect of the operator on the results is added, prediction of the changes in measured values will be impossible, but the influences of other factors can be corrected if the operator factor is eliminated. Hence, the truest value of the appropriate reading can be obtained.

A modification to the PLI testing device was made to eliminate the errors and disadvantages caused by the device and the operator (Figure 9). The device was modified to perform computer-controlled automatic loading in accordance with the standards recommended by ISRM (1985, 2007). The modification comprises two main parts: a hydraulic loading section and a control panel. Sensitive readings are acquired by a digital gauge. The loading process is controlled by a computer using 'X 34' software (Figure 10). The loading process can also be controlled manually from the control panel on the device. With the help of the software, the maximum load and the load-time graph can be displayed on the computer screen. In addition, data from up to 30 tests can be stored and transferred to the computer. Also, an instantaneous load-time graph can be displayed and the ultimate failure load read from the screen. The modified PLI testing device has a loading capacity of 200 kN. The conical platens of the modified device conform to ISRM standard (r = 5 mm and α = 60°) (Akbay, 2018).

Results

Determination of physical and mechanical properties

The physical and mechanical properties of the rocks tested in this study were determined according to the Turkish Standards Institution (TSE) and International Society for Rock Mechanics and Rock Engineering (ISRM). The unit volume weight (TS EN 1936, 2010), water absorption by weight and volume (TS EN 13755, 2014), apparent and total porosity (TS EN 1936, 2010), density (TS EN 1936, 2010), seismic velocity (TS EN 14579, 2006), wear resistance (TS EN 14157, 2017), Schmidt hammer (L-type) rebound number (ISRM, 2007), uniaxial compressive strength (TS EN 1926, 2013), indirect tensile strength (Brazilian tensile strength) (ISRM, 2007), modulus of rupture (TS EN

Figure 7—Penetration of the conical platens into the specimen

Figure 8—Loading arms of different lengths

Figure 9—The modified PLI testing device

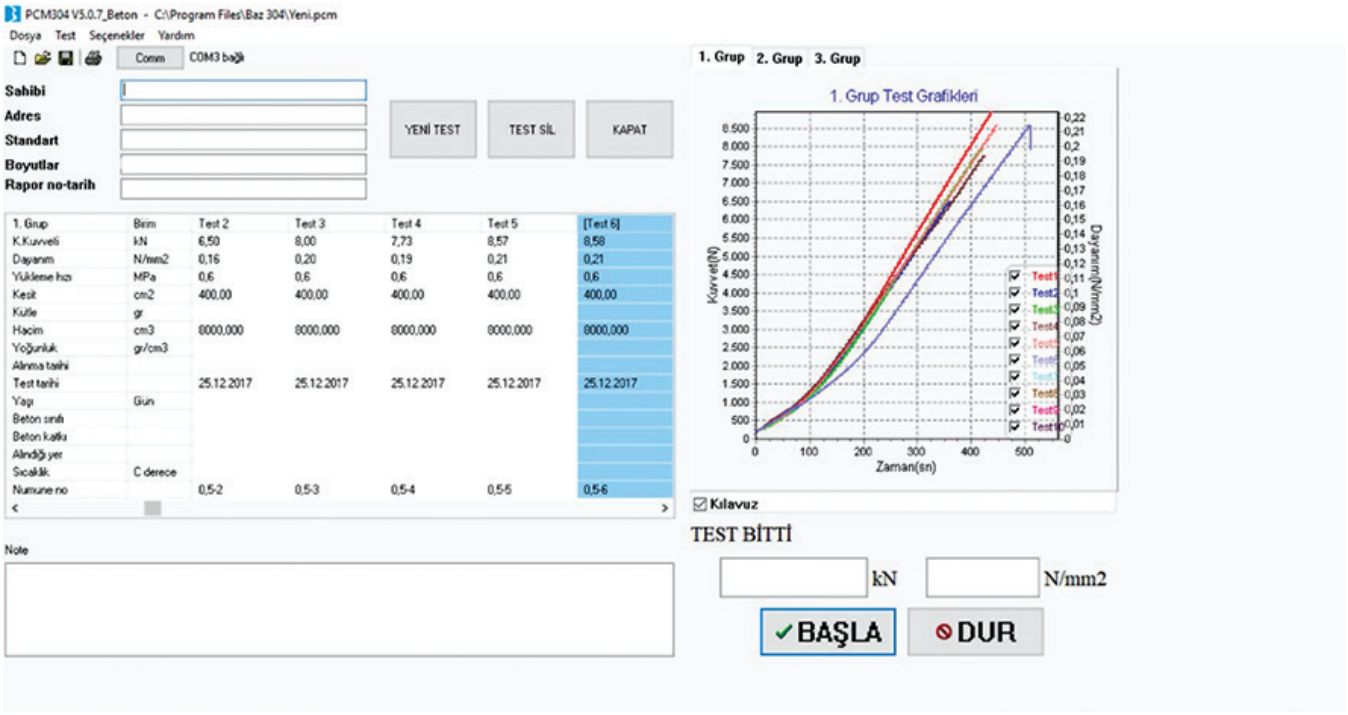

Figure 10—A screenshot from the 'X 34' software

Table IV

Physical properties of the specimens (Akbay, 2018)

Sample code	d_0 (kN/m³)		UW (kN/m³)		WAW (%)		AP (%)		TP (%)	Vp (km/h)	
	x̄	SD	x̄	SD	x̄	SD	x̄	SD	x̄	x̄	SD
K-1	27.7	0.07	27.6	0.16	0.124	0.053	0.343	0.148	0.484	6.62	0.03
K-2	28.5	0.09	27.1	0.09	1.173	0.119	3.183	0.313	4.788	5.45	0.68
K-3	27.3	0.05	25.6	0.12	2.375	0.290	6.081	0.720	9.311	5.03	0.45
M	27.3	0.02	27.1	0.01	0.076	0.015	0.206	0.040	0.440	6.14	0.72
A	26.1	0.02	23.0	0.19	3.281	0.297	7.552	0.632	11.704	4.87	0.09
G	6.7	0.05	26.4	0.02	0.218	0.004	0.576	0.011	1.082	5.36	0.15
D	30.0	0.12	29.0	0.30	0.656	0.076	1.902	0.204	3.011	5.10	0.15

d_0: density; UW: unit weight; WAW: water absorption percentage by weight; AP: apparent density; TP: total porosity; V_p: ultrasonic wave velocity; x̄: average; SD: standard deviation

12372, 2013), and flexural strength (TS EN 13161, 2014) tests were carried out. At least ten specimens were used for each test on each rock type. The summarized data is given in Table IV and Table V.

Tests with the modified PLI testing device and justification of the results

The loading speed was set so that all the specimens were broken within the time specified in the standard (ISRM, 1985, 2007). The loading speed is adjusted by the potentiometer on the control panel. Throughout the experiments, the failure time was observed to be around 60 seconds for the strongest rock and around 30 seconds for the weakest.

Table VI shows the average and standard deviations of the point load index values obtained using 15 different devices for seven different rock types. It can be seen that the difference between the minimum and maximum PLI values is almost 40% (Figure 11). The scatter of the PLI values appears to be high, which shows that it is not possible to determine the actual invariant PLI that represents the particular rock (Figure 11). It will be reasonable to use average PLI values obtained from 15 different PLI testing devices. Figure 12 shows that each testing device has its own characteristics, owing to the fact that

Table V

Mechanical properties of the specimens (Akbay, 2018)

Sample code	σc (MPa)		σ_t (MPa)	
	x̄	SD	x̄	SD
K-1	110.6	11.1	8.4	1.3
K-2	103.9	12.3	8.0	1.8
K-3	64.2	10.8	8.9	0.9
M	72.1	5.0	8.5	1.7
A	102.4	11.5	10.0	0.6
G	154.0	8.6	10.0	1.3
D	144.5	15.8	11.6	1.4

σc: uniaxial compressive strength; σt:: Brazilian tensile strength; x̄: average; SD: standard deviation

Table VI

Data obtained from experiments using 15 different PLI testing devices (Akbay, 2018)

Specimen code	Min. $I_{s(50)}$ (MPa)	Max. $I_{s(50)}$ (MPa)	$\bar{x}$ $I_{s(50)}$ (MPa)	SD
K-1	3.08	5.10	3.95	0.86
K-2	2.35	4.95	3.29	1.27
K-3	2.83	4.73	3.84	0.40
M	2.20	3.79	2.97	0.31
A	4.55	7.44	5.87	0.72
G	5.47	8.08	6.64	0.63
D	6.05	9.21	7.92	0.92

Is(50): point load index; x̄: average; SD: standard deviation

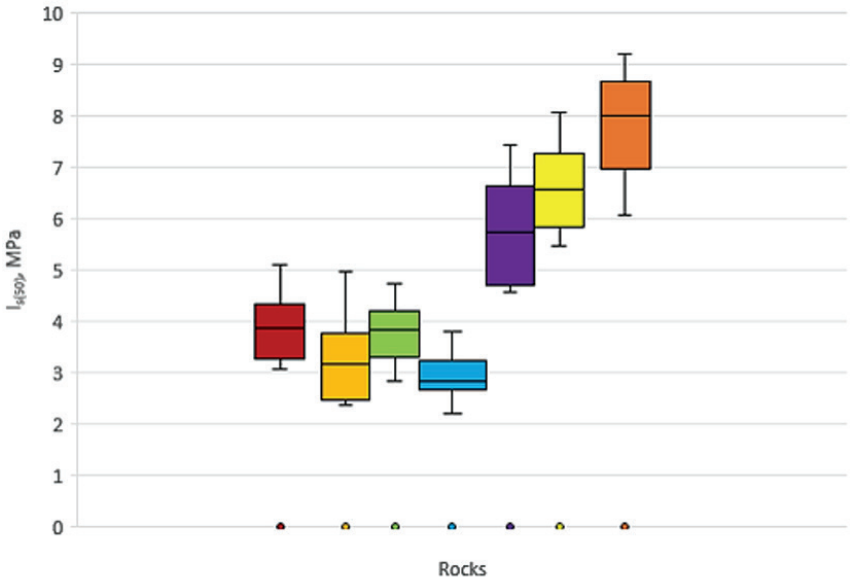

Figure 11—Box plot of PLI values of the rocks obtained using 15 different PLI testing devices

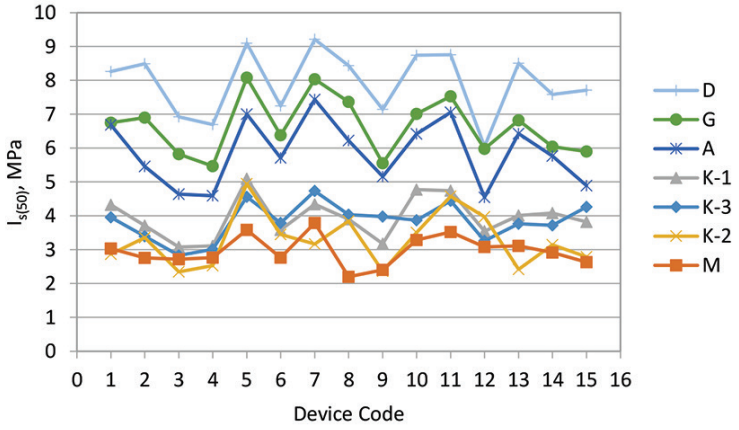

Figure 12—PLI values of the rocks tested using 15 different PLI testing devices

higher or lower PLI values are obtained in the same device. The fluctuations in PLI values may be explained by the different HRc hardnesses of conical platens, angles of conical platens, rounding radius of conical platens, and lengths of loading arm as shown in Table III. Although all the experiments were performed by the same operator, it appears that the standard deviations will be within acceptable limits.

If the experiments were carried out by different operators, in addition to the parameters stated above, operator-induced variations in the results (due to age, gender, physical fitness, stress level, nutrition, ergonomics, health situation, fatigue *etc.*) would also be relevant. Although the experiments were performed by the same operator, different conditions during the day may have caused the variations in PLI values. Therefore, the

relevance of all the factors, regardless of their origin, operator or the device, must be evaluated together. Hence, causes of the decrease in a PLI value for a particular specimen should not be explained by the rounding radius of the conical platens or any other factor in isolation.

It is obvious that the PLI values obtained as a result of the experiments performed on different devices by different operators on a more heterogeneous rock will have much wider range of scatter. Therefore, by using the point loading strength value, it is obvious that in the equations used in prediction of compressive strength of the rocks, very different strength values will be obtained. Likewise, it is obvious that this will lead to different values in the determination of rock mass classification systems where the PLI is used. With these considerations, as a result of the experiments carried out by different users in PLI testing devices with non-standard or different technical properties, the actual PLI of the rock cannot be determined. In this context, operator differences may cause different loading speeds. To eliminate the influence of loading speed on the PLI value, the modified testing device was designed in order to ensure uniform loading under computer control. When the same operator repeated the experiment on another PLI testing device for various testing durations between 10 and 90 seconds, the duration for failure was nearly the same (±5 seconds) as with the modified testing device. Also, standard deviations of failure loads were very small compared to other testing devices. Experiments were carried out on 10 specimens for each rock type in the modified PLI testing device. The results are given in Table VII. It can be seen that difference between minimum and maximum PLI values is almost 30%. Also, standard deviations of the PLI values from the modified testing device were significantly smaller than those from conventional devices. It is obvious that the PLI values obtained from the modified testing device are higher than those obtained from the averages of 15 different testing devices, except for 'K-2' and 'A' coded samples (Figure 13). Also, the PLI values were found to be close for both data groups. This implies that the PLI values of the rocks are represented by two data groups. In Figure 13, the standard deviations of the PLI values obtained from the modified PLI testing device are clearly lower than those obtained from a conventional PLI testing device. It is clear that the PLI values obtained from the modified device are more reliable.

Table VII

Data obtained from experiments using the modified testing device (Akbay, 2018)

Specimen code	Min. $I_{s(50)}$ (MPa)	Max. $I_{s(50)}$ (MPa)	$\bar{x}$ $I_{s(50)}$ (MPa)	SD
K-1	3.47	4.66	4.22	0.24
K-2	1.64	4.20	2.76	0.98
K-3	3.83	4.45	4.14	0.22
M	3.08	3.64	3.31	0.20
A	3.72	7.21	5.77	0.73
G	5.59	7.77	6.96	0.23
D	7.23	9.14	8.25	0.66

$I_{s(50)}$: point load index; Min.: minimum; Max.: maximum; $\bar{x}$: average; SD: standard deviation

Prediction of uniaxial compressive strength using point load index

Numerous studies have been conducted to estimate the UCS using the PLI value, and various equations have been proposed by means of statistical analyses and artificial intelligence (AI) methods utilizing experimental data. Researchers have determined conversion coefficients (K) and examined the problem by grouping the rocks according to geological origin, strength class, and porosity value to obtain more meaningful outcomes.

The conversion coefficients (K) were determined by graphical method (Table VIII). All the experiments were performed by the same operator on 15 different PLI testing devices, so the user effect can be eliminated. The average K values calculated from both the modified PLI testing device and the results from 15 different PLI testing devices are found to be very close. Conversion coefficients (K) obtained by averaging the results of 15 different testing devices vary between 17.44 and 25.49. Also, the correlation coefficients (r) were found to vary in a wide range (0.21–0.92). If the effects caused by different operators are taken into account, these values will spread in a wider range. The conversion coefficient (K) obtained from the modified device is 20.01 and is very close to the mean K value obtained from the average of the results of 15 different PLI testing devices. This may imply that PLI tests have to be performed on many different conventional testing devices in order to obtain a reliable result. This, however, also means that more samples must be prepared and more time spent on data acquisition. It can be seen in Table

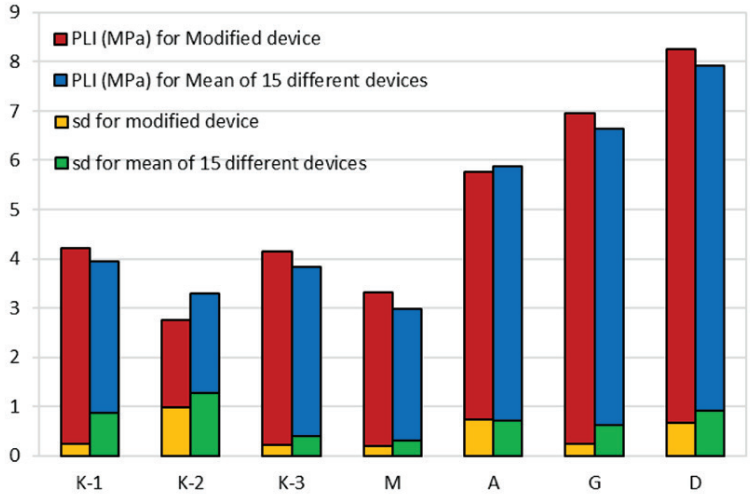

Figure 13—PLI values from modified testing device *vs.* average from 15 different testing devices

Table VIII

Conversion coefficients (*K*) for predicting the uniaxial compressive strength of rocks

	K	*r*
Modified PLI testing device	**20.01**	**0.58**
Average of 15 different PLI testing devices	**20.95**	**0.70**
***K* and *r* value range for 15 different PLI testing devices**	**17.44-25.49**	**0.21-0.92**
Device 1	19.81	0.53
Device 2	20.78	0.66
Device 3	24.94	0.60
Device 4	25.49	0.66
Device 5	17.44	0.85
Device 6	22.08	0.72
Device 7	17.44	0.48
Device 8	19.69	0.64
Device 9	23.61	0.28
Device 10	19.23	0.21
Device 11	18.11	0.79
Device 12	24.71	0.92
Device 13	19.90	0.35
Device 14	21.82	0.69
Device 15	22.34	0.53

K: conversion coefficient; *r*: correlation coefficient

Table IX

Conversion coefficients (K) for predicting uniaxial compressive strength of rocks

	K	
	$I_{s(50)}$ <5 MPa	$I_{s(50)}$ >5 MPa
Modified PLI testing device	23.51	19.06
Average of 15 different PLI testing devices	24.80	19.59
***K* value range for 15 different PLI testing devices**	15.51-37.64	17.52-22.13

K: conversion coefficient; $I_{s(50)}$: point load index

VIII that device 12 yielded the highest r value, and devices 9 and 10 the lowest. It will always be debatable as to which device should be used in the determination of the true PLI value.

Table VIII also suggests that some PLI testing devices may not be reliable, as seen in the wide range of results. It should be noted that *K* values found in this study are close to those published in the literature. It can also be observed that *K* values should be determined separately for each rock type (Table IX).

Discussion and conclusion

PLI is known as an engineering design value that is simple, quick, cheap, and easy to determine and requires less time to prepare test specimens than other tests. Moreover, the PLI value is used to estimate the uniaxial compressive strength of intact rock. However, PLI values obtained from conventional testing devices may be questionable owing to the errors arising from different devices and operators. Hence, in order to obtain more accurate and more sensitive results, conventional testing devices need modifying in line with the ISRM suggested methods (1985, 2007) to eliminate the errors and disadvantages related to conventional devices and different operators. This is extremely important to ensure that correct values of rock strength are determined for rock engineering design purposes, and for contractual information to avoid contract disputes.

In this study, PLI tests were performed on seven different rock types using 15 different PLI testing devices. The errors arising from conventional PLI testing devices are generally due to the following:

- Loading speed and discrete loading
- Time to failure (too long or too short)
- Lack of regular maintenance
- Use of different types of jacking system
- Indicator errors
- The geometry of the conical platens
- Distortion of conical platens from axis
- In soft or weak rocks, penetration of the conical platens into the specimen
- The effect of the length of loading arm (jack)
- The effect of different operators.

Seven different rock types were classified according to the strength classification suggested by Bieniawski (1974). For M-, A-, G-, and D-coded rocks, the strength class does not change for three different strength values. However, limestones coded K-1, K-2, and K-3 have been placed in a different rock class owing to the difference of ±0.22 MPa in the value of Is(50). This emphasizes the importance of how precisely $I_{s(50)}$ has to be determined. If there is 10 to 15% change in the specified $I_{s(50)}$ value this may not necessitate any class change if the strength of the rock is not too close to the limit/transition value. However, especially in weak and very weak rocks (<2 MPa) the changes in these ratios will cause the rock to be shifted into another class.

Hence, in this study, it is emphasized that determination of $I_{s(50)}$ values under constant load and speed and without operator effect is of great importance, especially for very weak and weak rock groups. Although the rocks used in this study were

intact and in the medium strength class, there are significant differences in the experimental method and the results. It is understood that these differences, and the effects thereof, will be more pronounced in weak or very weak rocks.

The mean PLI values obtained from 15 different PLI testing devices and the conversion coefficients (K) were very close to the values acquired from the modified PLI testing device. However, the correlation coefficients of the values obtained from 15 different devices were found to have a high degree of scatter. Although all the experiments were performed on the same samples by the same operator using the 15 different PLI devices, the standard deviations in the PLI values were higher than anticipated. The higher standard deviation values can therefore be ascribed to errors inherent in the conventional testing devices. On the other hand, standard deviations in the PLI values obtained from the modified testing device were lower, and the correlation coefficients were found to be high and very significant. Based on these facts, the modified PLI testing device can be recommended as yielding more reliable results than conventional testing devices.

PLI testing is used to estimate the strength of intact rock and can be applied in both the laboratory and in the field. As is well known, the distribution of the data obtained from laboratory and field tests may vary. The PLI testing method should be applied in a laboratory in cases where standard test specimens cannot be prepared to determine the uniaxial compressive strength of an intact rock. Hence, the PLI test becomes very useful for estimating the strength of intact rock. Several researchers have commented on the difficulties encountered in preparing specimens for the determination of UCS value in weak rocks. In such cases, the use of a PLI testing device will become invaluable for the determination of the strength of intact rocks. It has often been reported that care must be taken in the determination of the strength of weak rocks. The modified PLI testing device has the advantage of being able to appropriately test weak rocks. Conventional portable PLI testing devices can still be used to predict the strength of intact rocks, despite the known errors and disadvantages mentioned in this study.

This study has demonstrated that variations in PLI values depend on the test device and testing method. Hence, the reliability of the PLI values obtained may be questioned. In this investigation, a total of 154 scientific studies were examined in detail. Only four of the studies were seen to include the data of the PLI tests implemented in the field. In other words, only 2.5% of the studies conducted on PLI testing were actually carried out in the field.

Acknowledgment

This study was supported by the Scientific and Technological Research Council of Turkey (TUBITAK) Project 116R070 and Süleyman Demirel University OYP Coordination Unit Project OYP-05286-DR-13. The authors would like to thank TUBITAK and SDU OYP Project Coordination Unit.

References

Akbay, D. 2018. Designing a new testing apparatus for preventing the errors in point load index test. Doctoral thesis, Süleyman Demirel University, Isparta, Turkey. http://dspace.sdu.edu.tr/xmlui/handle/123456789/31140

Akbay, D. and Altindağ, R. 2018. Determination of the errors arising from apparatus and operator during applying the point load index. *Geomechanics and Geodynamics of Rock Masses. Proceedings of the 2018 European Rock Mechanics Symposium*. Taylor & Francis. pp. 181–188.

ASTM. 1995. Standard test method for determination of the point load strength index of rock. American Society for Testing and Materials, West Conshohocken, PA. pp. 1–9. doi: 10.1520/D5731-08.2

ASTM. 2008. Standard test method for determination of the point load strength index of rock and application to rock strength classifications. American Society for Testing and Materials, West Conshohocken, PA. pp. 1–11.

Aston, T.R.C., MacIntyre, J.S., and Kazi, H.A. 1991. The effect of worn and chipped points on point load indices. *Mining Science and Technology*, vol. 13. pp. 69–74.

Bieniawski, Z.T. 1974. Estimating the strength of rock materials. *Journal of the South African Institute of Mining and Metallurgy*, March. pp. 312–320. doi: 10.1016/0148-9062(74)91782-3

Bieniawski, Z.T. 1975. The point-load test in geotechnical practice. *Engineering Geology*, vol. 9, no. 1. pp. 1–11. doi: 10.1016/0013

Bieniawski, Z.T. 1989. Engineering Rock Mass Classifications. Wiley, New York.

Broch, E. and Franklin, J.A. 1972. The point-load strength test. *International Journal of Rock Mechanics and Mining Sciences*, vol. 9. pp. 669–697.

Broch, J.A., Broch, E., and Walton, G. 1971. Geological Society Working Party Report. The logging of rock cores for engineering purposes. *Quarterly Journal of Engineering Geology and Hydrogeology*, vol. 4, no. 2. pp. 131–132. https://doi.org/10.1144/GSL.QJEG.1971.004.02.04.

Edet, A.E. and Teme, S.C. 1990. Strength classification of some Nigerian limestones using the point load testing technique. *Bulletin of the International Association of Engineering Geology*, vol. 41, no. 1. pp. 97–106. doi: 10.1007/BF02590210

Franklin, J.A., Broch, E., and Walton, G. 1971. Logging the mechanical character of rock. *Transactions of the Institution of Mining and Metallurgy*, Section A, vol. 80(A). pp. 1–9.

Ghosh, D.K. and Srivastava, M. 1991. Point-load strength: An index for classification of rock material. *Bulletin of the International Association of Engineering Geology*, vol. 44. pp. 27–33. doi: 10.1007/BF02602707

Guidicini, G., Nieble, C.M., and De, C.A.T. 1973. Analysis of point load test as a method for preliminary geotechnical classification of rocks. *Bulletin of the International Association of Engineering Geology*, vol. 7, no. 1. pp. 37–52.

Hawkins, A.B. 1998. Aspects of rock strength. *Bulletin of Engineering Geology and the Environment*,vol. 57, no. 1. pp. 17–30. doi: 10.1007/s100640050017

ISRM. 1985. Suggested method for determining point load strength. pp. 53–60.

ISRM. 2007. The complete suggested methods for rock characterization, testing and monitoring: 1974–2006. *Suggested Methods Prepared by the Commission on Testing Methods*. Ulusay, R, and Hudson, J.A. (eds).

Karaman, K., Kaya, A., and Kesimal, A. 2015. Use of the point load index in estimation of the strength rating for the RMR system. *Journal of African Earth Sciences*, vol. 106. pp. 40–49. doi: 10.1016/j.jafrearsci.2015.03.006

McFeat-Smith, I. and Tarkoy, P.J. 1979. Assessment of tunnel boring machine performance. *Tunnels and Tunnelling*, vol. 11, no. 10. pp. 33–37.

Pettifer, G.S. and Fookes, P.G. 1994. A revision of the graphical method for assessing the excavatability of rock. *Quarterly Journal of Engineering Geology*, vol. 27. pp. 145–164.

Quane, S.L. and Russell, J.K. 2003. Ranking welding intensity in pyroclastic deposits. *European Journal of Mineralogy*, vol. 15. pp. 855–864. doi: 10.1007/s00445-004-0367-5

Rusnak, J. and Mark, C. 2000. Using the point load test to determine the uniaxial compressive strength of coal measure rock. *Proceedings of the 19th International Conference on Ground Control in Mining*, Morgantown, West Virginia, 8-10, August 2000. Peng, S.S. and Mark, C. (eds). College of Engineering and Mineral Resources, West Virginia University. pp. 362–371.

Singh, T.N., Kainthola, A., and Venkatesh, A. 2012. Correlation between point load index and uniaxial compressive strength for different rock types. *Rock Mechanics and Rock Engineering*, vol. 45, no. 2. pp. 259–264. doi: 10.1007/s00603-011-0192-z

Topal, T. 2000. Nokta yükleme deneyi ile ilgili uygulamada karşılaşılan problemler. *Jeoloji Mühendisliği*, vol. 24, no. I. pp. 73–86.

TS EN 14579. 2006. Natural stone test methods - Determination of sound speed propagation. Turkish Standards Institution, Ankara.

TS EN 1926. 2013. Natural stone test methods - Determination of uniaxial compressive strength. Turkish Standards Institution, Ankara.

TS EN 12372. 2013. Natural stone test methods - Determination of flexural strength under concentrated load. Turkish Standards Institution, Ankara.

TS EN 13161. 2014. Natural stone test methods -Determination of flexural strength under constant moment. Turkish Standards Institution, Ankara.

TS EN 13755. 2014. Natural stone test methods - Determination of water absorption at atmospheric pressure. Turkish Standards Institution, Ankara.

TS EN 14157. 2017. Natural stone - Determination of the abrasion resistance. Turkish Standards Institution, Ankara.

TS EN 1936. 2010. Natural stone test methods - Determination of real density and apparent density and of total and open porosity. Turkish Standards Institution, Ankara.

Tsiambaos, G. and Saroglou, H. 2010. Excavatability assessment of rock masses using the Geological Strength Index (GSI). *Bulletin of Engineering Geology and the Environment*, vol. 69, no. 1. pp. 13–27. doi: 10.1007/s10064-009-0235-9 ◆

Operator influence on the loading process at LKAB's iron ore mines

A. Gustafson[1], H. Schunnesson[1], J. Paraszczak[2], G. Shekhar[1], S. Bergström[3], and P. Brännman[3]

Affiliation:
[1]Luleå University of Technology, Sweden.
Université Laval, Quebec City, Canada.
Luossavaara Kiirunavaara AB, Sweden.

Correspondence to:
A. Gustafson

Email:
anna.gustafson@ltu.se

Dates:
Received: 12 Oct. 2018
Revised: 29 Oct. 2019
Accepted: 5 Dec. 2019
Published: March 2020

How to cite:
Gustafson, A., Schunnesson, H., Paraszczak, J., Shekhar, G., Bergström, S., and Brännman, P. Operator influence on the loading-process at LKAB's iron ore mines. The Southern African Insitute of Mining and Metallurgy

DOI ID:
http://dx.doi.org/10.17159/2411-9717/376/2020

Synopsis

The loading process in sublevel caving mines entails loading material from the drawpoint using load haul dump machines that transport the material to orepasses or trucks, depending on the mine conditions. When each bucket is drawn from the drawpoint, a decision must be made as to whether loading should continue or be stopped and the next ring blasted. The decision to abandon the drawpoint is irrevocable, as it is followed by the blasting of the next ring. Abandonment of the drawpoint too early leads to ore losses and inefficient use of ore resources. Loading beyond the optimal point increases dilution as well as mining costs.

The experience of the LHD operators is an important basis for manual drawpoint control. However, it has been difficult to establish which specific factors manual drawpoint control is based on. To try to shed more light on these factors we analysed the operators' experiences at LKAB's Kiirunavaara and Malmberget iron ore mines. The operators in the two mines completed a questionnaire on the current loading practices and the process of deciding to abandon 'normal' rings, opening rings, and rings with loading issues.

It was found that in both case study mines, most decisions on the abandonment of drawpoints are made by the operators. The more experienced operators tend to make more decisions themselves rather than rely on support from the existing support functions.

Keywords
loading process, operator influence, decision control, sublevel caving, load haul dump machine, draw control.

Introduction

The process of loading in the sublevel caving (SLC) mining method is difficult, as a large amount of material is loaded from a drawpoint with a small cross-section, while at the same time material flows down from the top of the drawbell, filling the void left by the material removed (Dunstan and Power, 2011) (Figure 1). Then, the loaded material is either hauled by load haul dump (LHD) machines to orepasses or dumped into trucks, depending on production conditions. Loading at the drawpoint begins after a production ring is blasted and clearance is given for loading.

The blasted material swells and fills the drawpoint to form a muckpile; the spread and angle of the muckpile's slope vary during loading. According to Kvapil (2008), for good extraction, an ideally blasted ring creates a muckpile which fills the drawpoint, as shown in Figure 2.

Sublevel caving includes a series of unit operations: drilling, blasting, loading, and transportation

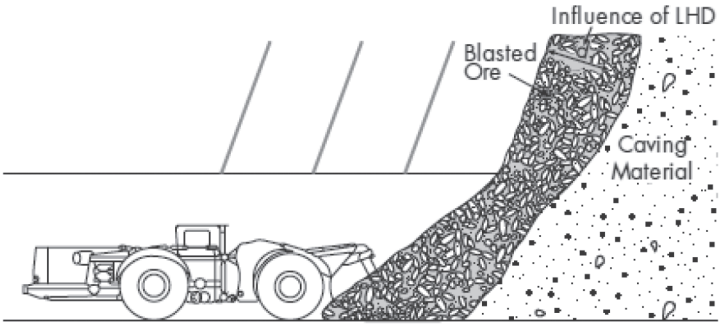

Figure 1—Loading at a drawpoint (Dunstan and Power, 2011)

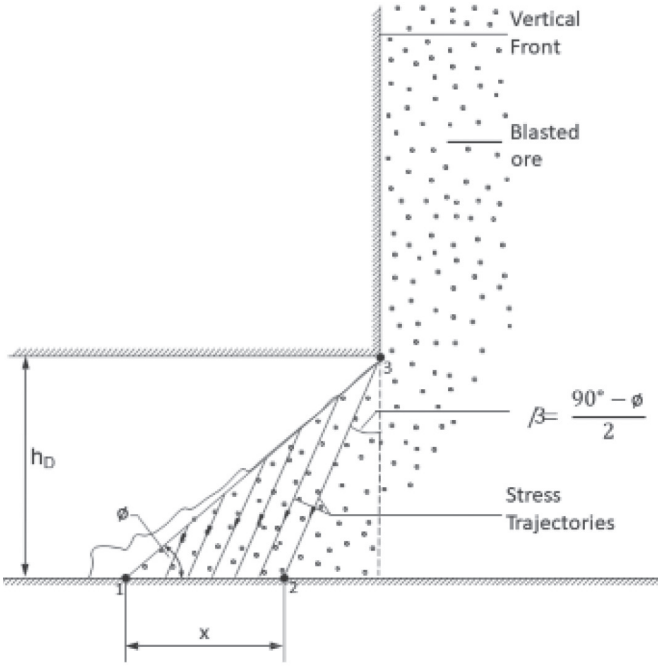

Figure 2—Muckpile spread for a vertical ring (Kvapil, 2008)

of material. Each unit operation generates a large amount of data that is used to plan the subsequent processes and monitor the mining operation. The systematic recording, storing, and delivering of mining-related information is vital for today's highly mechanized mining operations.

The ore recovery, dilution, and extraction rate are determined and controlled at the drawpoint. Here, the overall production plans depend on a fundamental decision – as each bucket is drawn, the operator must decide to either continue loading or to abandon the drawpoint. A decision to abandon the drawpoint is irrevocable, since it is followed by the blasting of the next ring. Premature abandonment of the drawpoint leads to ore losses and inefficient use of ore resources. Continuing to load beyond the optimum point, however, results in increased dilution and increased production costs. Decisions to stop or to continue loading must consider factors such as the current ore grade, extraction ratio, indication of remaining ore above the loading point, metal price, cut-off grades, processing costs, and the possibility of recovering the remaining ore at lower levels.

In other words, the SLC loading process depends on various mining, geological, and economic parameters. In order to balance these vastly different. but equally important parameters, a set of rules and guidelines must be established (Shekhar, Gustafson, and Schunnesson, 2016). This is generally termed the 'draw control strategy'. A draw control strategy incorporates the sequencing and scheduling of development, production, and material handling systems, with the dual objective of minimizing mining costs and dilution (Smith and Rahal, 2001). A good draw control strategy creates an optimal balance of ore dilution and ore recovery, balancing production demands with loading procedures and resource efficiency.

Table I

Loading issues in SLC (Shekhar, Gustafson. and Schunnesson, 2016)

Loading issue	Problem	Source of issue	Effect
Poor brow condition	Uneven material flow, scattered muck profile, difficulty approaching drawpoint	Blasting damage from development and/ or poor mine support (Bull and Page, 2000; Kvapil, 2008)	Poor ore recovery and increased dilution
Brow failure	Loading cannot be done, next set of rings re-drilled	Poor support and /or blasting damage from production blast (Baase, Diment' and Petrina, 1982; Bull and Page, 2000; Kvapil, 2008)	Poor ore recovery
Bridging	Preferential flow of dilution and eventual ring freezing	Toe left due to poor blasting, which grows (Bull and Page, 2000)	Poor ore recovery and increased dilution
Walls	Over-compaction of caved material	Overcharging or double ring blasting (Brunton, 2009)	Poor ore recovery
Ring freezing	No flow or interrupted flow of material	Over-burdening or over-consolidation of waste (Gustafsson, 1998; Bull and Page, 2000)	Poor ore recovery
Rib formation	Unbroken or partially broken ore around the side holes	Poor drilling and blasting or poor mine design (Bull and Page, 2000)	Poor ore recovery
Hangups	Uneven flow of material with premature dilution by fine waste material	Poor fragmentation (Kvapil, 2008)	Increased dilution
Wedge failures/ large-scale cave slides	Damage to pre-drilled production holes and underground infrastructure	Discontinuous caving or other stability issues (Bull and Page, 2000)	More support and re-drilling required
Overhangs	Damage to holes and structures	Delayed caving of material (Bull and Page, 2000; Gustafsson, 1998)	More support and re-drilling required
Blast-hole damage	Delay in blasting and loading	Blasting damage or poor geological conditions (Brunton, 2009)	Re-drilling required
Overcharging	Increased consumption of explosives and back-break	Cracks or openings in the holes (Brunton, 2009)	Increased explosive cost
Air blast	No material flow initially and damage to structures	Delayed caving (Bull and Page, 2000)	Increased support costs

Operator influence on the loading process at LKAB's iron ore mines

Loading at the drawpoint can be halted or delayed due to a variety of loading issues (Cokayne, 1982), adversely affecting the resource efficiency. These issues include poor mine design or poor drilling or blasting practices, as listed in Table I. At the Swedish mining company Luossavaara Kiirunavara AB (LKAB), loading at the drawpoint is sometimes stopped early because of loading issues such as hangups, brow failure, pillar failure, intrusions, poor fragmentation, or ring freeze (Shekhar, Gustafson, and Schunnesson, 2016).

Many decisions (how much to load from a drawpoint, the identification of different loading issues, and the action taken, *etc.*) are based on the LHD operator's personal experience and practical knowledge. This experience is today an important foundation for manual drawpoint control. However, it is difficult to define which factors manual drawpoint control is based on.

The purpose with this study is to investigate the experience of the LHD operators in in LKAB's Kiirunavaara and Malmberget mines to obtain a better understanding of current loading practices and the decision-making processes involved in abandoning 'normal' rings, opening rings, and rings with loading issues (*e.g.* brow failure, pillar failure, or ring freeze). Furthermore, in order to improve a draw control model it is important to include the operator's experience, since the operators can override any suggestion provided by the existing drawpoint control system.

Methodology

To understand how LHD operators influence the process of loading and decision-making, the LHD operators at LKAB's Kiirunavaara and Malmberget mines completed a questionnaire. Findings were combined with a study of the mine's internal documents and reports, and various scientific reports and articles.

Questionnaire study

The total number of questionnaire respondents was 59 in the Kiirunavaara mine and 62 in the Malmberget mine, corresponding to 74% and 100% of all LHD operators respectively. The lower number of respondents at Kiirunavaara can be explained by the fact that many of the operators were not working at the time of the study. However, the respondents still included operators from all shift teams in both mines and can therefore be seen as representative.

The questionnaire contained 34 questions; 24 were closed questions (with alternative answers) and 10 were open questions (the respondent composed the answer). The questionnaires were handed to the operators in person and answered right away in the presence of the interviewer. This ensured that a large number of questions were answered.

The questionnaire aimed at investigating:

- The organizational structure of the mines
- The general loading process
- The decision process in abandoning a normal ring
- The decision process in abandoning an opening ring
- The decision process in abandoning a ring with loading issues
- The person responsible for abandoning a ring with loading issues
- The differences between operators, depending on loading experience.

Mine site descriptions

The mines selected for this study were LKAB's two underground iron ore mines: Kiirunavaara and Malmberget. Both use sublevel caving (SLC) as the mining method.

LKAB uses different information systems to support the unit operations at these mines. The three support systems used for the loading operation are GIRON, the Wireless Loader Information System (WOLIS), and the Loadrite scoop weighing system. GIRON is an application tool which creates, stores, and displays mine-related data used during different unit operations (Adlerborn and Selberg, 2008). The application also communicates with other mine systems by sending and receiving data. WOLIS is used to transfer data from the LHDs to a database (Adlerborn and Selberg, 2008); it is a control, decision, and support system that provides automatically generated production data to the operator and to the mine control group. The Loadrite scoop weighing system is installed on the LHD machines to weigh the load of the bucket (Davison, 1996). It measures the hydraulic pressure in the lift cylinders of the LHD's arms connecting the bucket to the machine. It then converts this hydraulic pressure into a weight and a Fe grade (Davison, 1996) which is displayed for the operators inside the LHD through the WOLIS system.

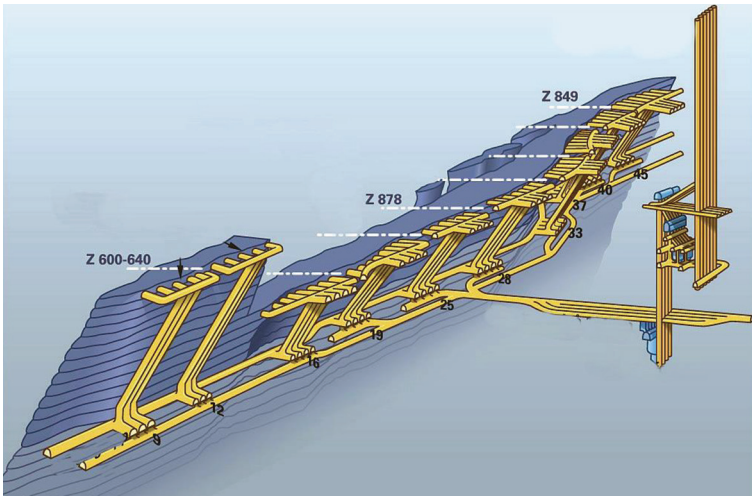

Figure 3—Current haulage system in the Kiirunavaara mine (Courtesy of LKAB)

LHD operation is not a continuous process, and the LHD machines operate only when needed. Loading is prohibited immediately after blasting because noxious gases are produced by the detonation of explosives. Loading cannot be resumed until the area has been adequately ventilated.

The Kiirunavaara mine

The Kiirunavaara orebody consists of a magnetite-rich magmatic intrusion. The orebody is about 4 km along the strike (N10°E) with an average width of around 80 m, dipping at about 60°SE towards Kiruna city (Nordqvist and Wimmer, 2014). The ore initially mined was pure magnetite, but the magnetite content has dropped to 65 to 70%, with the remainder consisting of impurities such as apatite, calcite, or phosphate minerals. The average iron content of the orebody is 64% (Nordqvist and Wimmer, 2014). The thickness of the orebody increases with depth, especially in the northern part where it can be up to 200 m (Rutanen, 2011).

The mine is divided into 10 main production areas (Figure 3). The key loading equipment for production is Sandvik LH625E electric LHDs with a bucket capacity of 25 t.

The LHDs load the ore from drawpoints and haul it to one out of seven orepasses located in each production block. Trains, operating on the main level, transport the ore from the orepasses to crushers, from where it is carried by belt conveyors to the hoisting system. To conform to mining restrictions, before mining moves to the subsequent block, the preceding one must maintain continuous production until all available ore is removed.

The Malmberget mine

The Malmberget mine consists of about 20 orebodies, of which 13 are currently being mined with varying rates of production (Savilahti and Jonsson, 2013). The orebodies consist of an apatite iron ore, and the country rock is metamorphosed and deformed volcanics of felsic to mafic composition, referred to at the mine as leptites. The deposit stretches 5 km in the EW direction and 2.5 km in the NS direction. The ore minerals comprise magnetite (95%) and haematite (5%), and the grade varies from 49% to 63% for different orebodies. The width of the orebodies varies from 20 to 100 m, and the tonnage of individual blocks varies from 5 Mt to 250 Mt.

The Malmberget mine uses 13 diesel-powered LHD machines with a loading capacity of 21 t. These machines, manufactured by Sandvik or Caterpillar, went into production between 2005 and 2013.

Organization

Loading of the fragmented ore from the drawpoint is a continuous process at LKAB and requires appropriate manpower and equipment utilization. The loading section controls the loading process at both mines and decides on the procedures and criteria to be employed for loading at the drawpoints.

The Kiirunavaara mine

The organizational chart for the loading section at the Kiirunavaara mine is shown in Figure 4. This paper focuses on the loading section, which is responsible for loading material at the drawpoint.

The involvement of mine personnel in loading is described below:

- ➤ Loading control
  - The loading control group provide information about which drawpoints should be loaded and which drawpoints should be closed (personal communications, 2016). They also deal with short-term mine sequencing and scheduling. They use the Giron and WOLIS systems to follow and control the loading operation. These systems provide information on which drawpoints should remain operational and which are to be abandoned. Loading control assists the loading team and the production team by updating and improving the different information systems used during loading.
- ➤ Loading
  - Production managers: Two production managers head the loading operation at Kiirunavaara mine. They are in charge of the LHD operators and assign them to different production areas (personal communications, 2016).

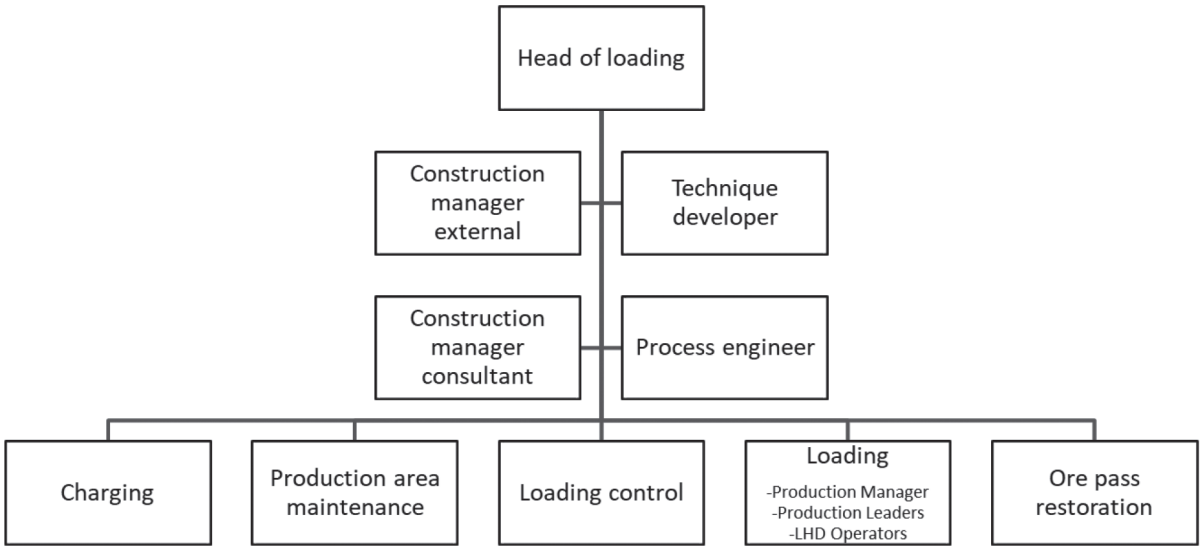

Figure 4—Organizational chart for the loading section at the Kiirunavaara mine (courtesy of LKAB)

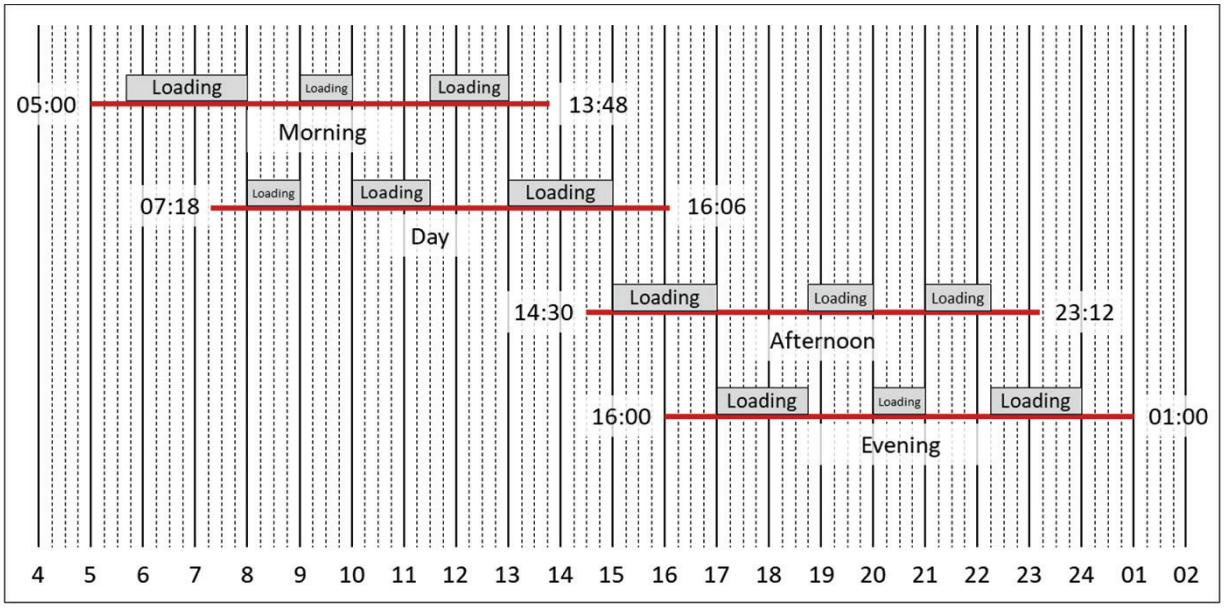

Figure 5—Shift design at the Kiirunavaara mine

- Production leaders: A total of three production leaders are deployed in the shifts with LHD operators and provide directions to operators based on information from the production manager and loading control (personal communications, 2016). The production leaders work in rotation with two people on and one off every week (all seven days).
- LHD operators: The Kiirunavaara mine has 81 LHD operators who load the material at drawpoints and transport it to dumping points (personal communication, 2016).

Figure 5 shows the shift roster for the LHD operators at the Kiirunavaara mine. The mine has a total of four shifts: morning (05:00-13:48), day (7:18-16:06), afternoon (14:30-23:12), and evening (16:00-01:00). The mine shifts overlap. In the morning and day shifts, each LHD is operated by two operators in turn so as to use it as effectively as possible. The duration of the loading periods varies between 1 hour and 2.3 hours, as shown in Figure 5 (personal communications, LKAB, 2016).

The morning shift commences at 05:00, but the LHD operator actually begins loading from the drawpoint at around 5:45 (due to the time needed to travel from the surface to production areas underground) and continues loading until 08:00. Thereafter, the LHD operator from the day shift takes over until 09:00 and the first LHD operator resumes the loading at 09:00, relieving the second operator who then takes a break. The evening shift runs at a slightly reduced manpower capacity, which means there is not always an overlap in personnel between the afternoon and evening shifts. Overall, the LHD operators are divided into seven groups. The first five groups are assigned to work in the morning, day, and afternoon shifts. The groups rotate in a morning/afternoon/week off/day/week-off pattern, so in any given week, three groups are at work and two others have time off. The remaining two of the seven groups work alternate weeks and operate the evening shift (personal communications LKAB, 2016).

The Malmberget mine

The organizational structure and manpower distribution in the Malmberget mine are slightly different from the Kiirunavaara mine. Figure 6 shows the organizational structure for the loading and transportation section at Malmberget.

The mine personnel involved in loading are organized as follows.

➤ Loading control
- Loading control provides information about which drawpoints should be loaded and which drawpoints are to be closed (personal communications, 2016). They also deal with short-term mine sequencing and scheduling. Loading control handles the loading criteria and the daily planning of the loading activities and uses Giron and WOLIS to follow up the loading. These systems provide information on which drawpoints should remain operational and which are to be abandoned. The loading control group consists of four production leaders who work in rotation, with three people working the morning, day, and afternoon shifts and one person with the week off.

➤ Loading areas 1 and 2
- Production manager: Loading is divided into two areas, area 1 and area 2, each with its own production manager. They are in charge of handling the LHD operators and assigning them to different production areas (personal communications, 2016).
- LHD operators: The Malmberget mine has a total of 59 LHD operators employed by LKAB (personal communication, 2016). They perform the loading of the material at the draw point. There are also a number of LHD operators working for an external contractor operating in one part of the mine. These operators were not included in this study.

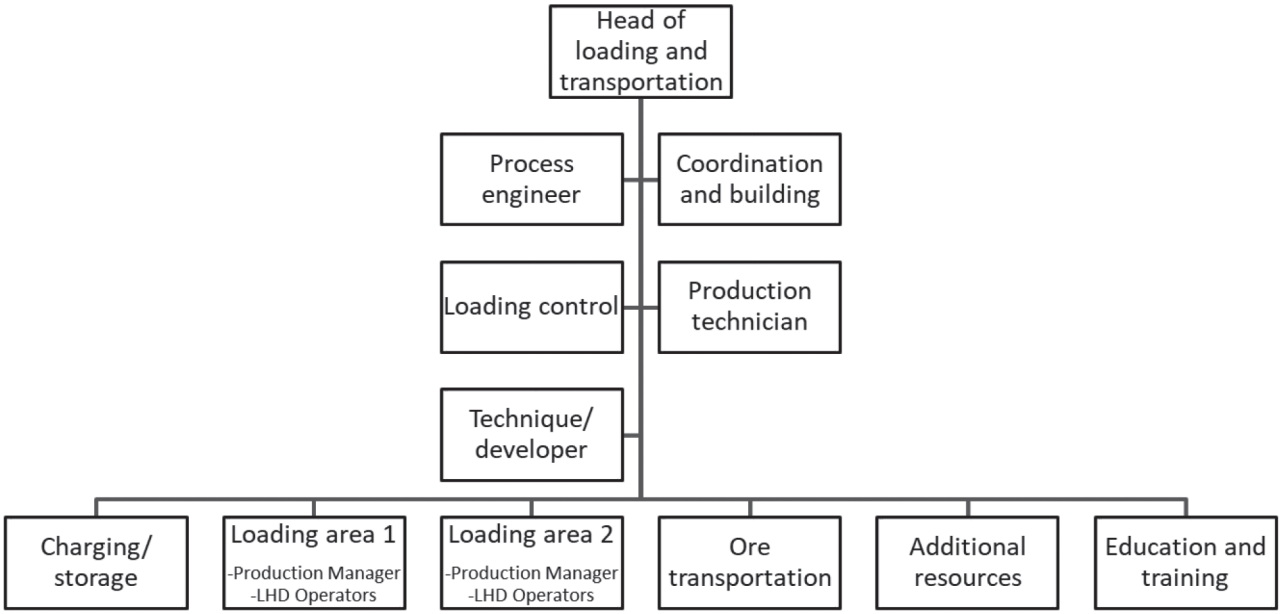

Figure 6—Organizational chart for the loading and transportation section at the Malmberget mine (courtesy of LKAB)

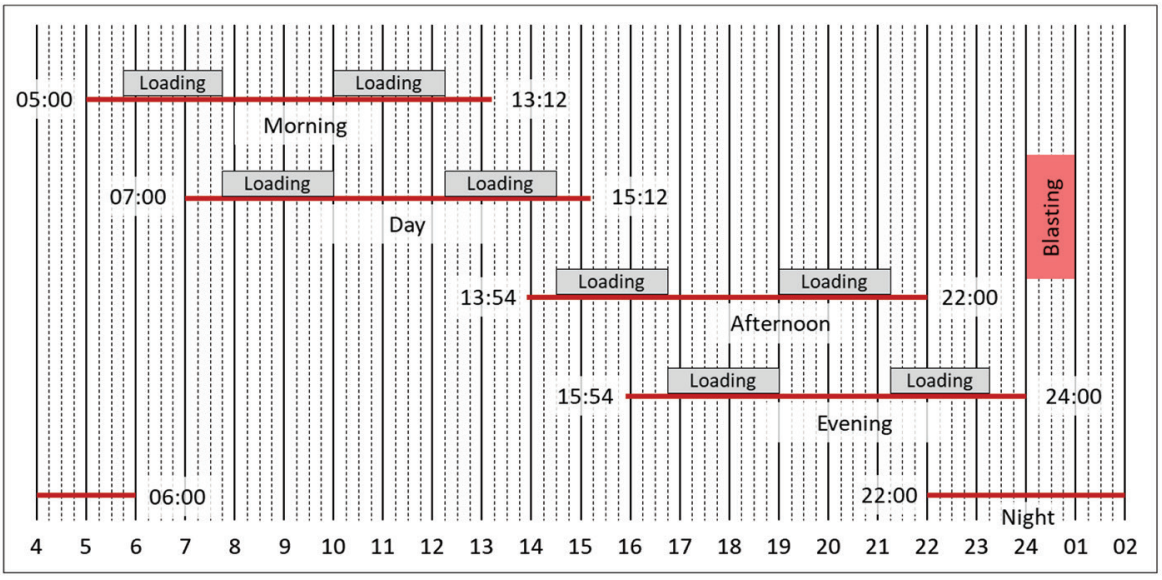

Figure 7—Shift design at the Malmberget mine

Figure 7 shows the Malmberget shift design. The mine has a total of five shifts: morning (05:00-13:12), day (07:00-15:12), afternoon (13:54-22:00), evening (15:54-24:00), and night (22:00-06:00). As in the Kiirunavaara mine, the shifts overlap, making the LHD utilization as efficient as possible. The duration of a loading period is constant (2 hours 15 minutes), except for the first and last loading periods (2 hours) of the day, as shown in Figure 7.

The morning shifts commences at 05:00, but the LHD operator actually begins loading from the drawpoint at around 5:45 (time taken to travel from surface to production areas underground) and continues loading until 07:45. Thereafter, the LHD operator from the day shift takes over until 10:00, and the first one resumes at 10:00 (personal communications, 2016), as in the Kiirunavaara mine. The practice is followed for the first four shifts, as shown in Figure 7. The fifth shift or the night shift has two operators working 23:15 to 06:00. The LHD operators are divided into eight groups. The first six groups are assigned to work the morning, day, afternoon, and evening shifts (personal communications LKAB, 2016). The groups rotate in a morning/afternoon/week-off/day/evening/week-off pattern, so in any given week, four groups are at work and two are off (personal communications LKAB, 2016). The remaining two of the eight groups work alternate weeks on the night shift (personal communications LKAB, 2016).

Loading procedures

There are 81 LHD operators in the Kiirunavaara mine and 62 in the Malmberget mine. The experience of the operators in terms of years worked on LHDs, is slightly different in the two mines

(see Figure 8). The Malmberget mine has a higher percentage of recently employed operators than the Kiirunavaara mine. However, 43% the operators at the Malmberget mine, and 50% at the Kiirunavaara mine, have been working 6 years or more.

In both mines, the operator's task is to move the broken ore from the drawpoint to the orepass. Loading should be performed in such a way that it enables a good flow of the caved ore, maximizes ore recovery, and minimizes dilution. During loading, the operator takes loads alternately from the right and the left sides of the face, if possible.

The daily work routine of the operators is as follows.

- Performing daily maintenance on the machine and in the workplace
- Loading ore, according to plan, either to orepasses or on trucks
- Handling boulders
- Deciding whether to change drawpoint;
- Reporting disturbances in WOLIS to the production coordinator.

Boulders in the Kiirunavaara mine are broken with a rock-breaker before being dumped in the orepass through a grizzly. The Malmberget mine has no grizzlies; boulders are broken by drilling and blasting in a nearby boulder drift.

Both mines use a draw control strategy based on bucket weights. The drawpoint monitoring system provides continuous ore grade information to the operator and to the managers for every loaded bucket (Nordqvist and Wimmer, 2014; Quinteiro, Larsson, and Hustrulid, 2001). Waste or ore percentage is plotted against the extraction ratio, and the resulting curve is displayed inside the LHD machine through WOLIS (Adlerborn and Selberg, 2008) (Figure 9). The bucket grade curve gives information on

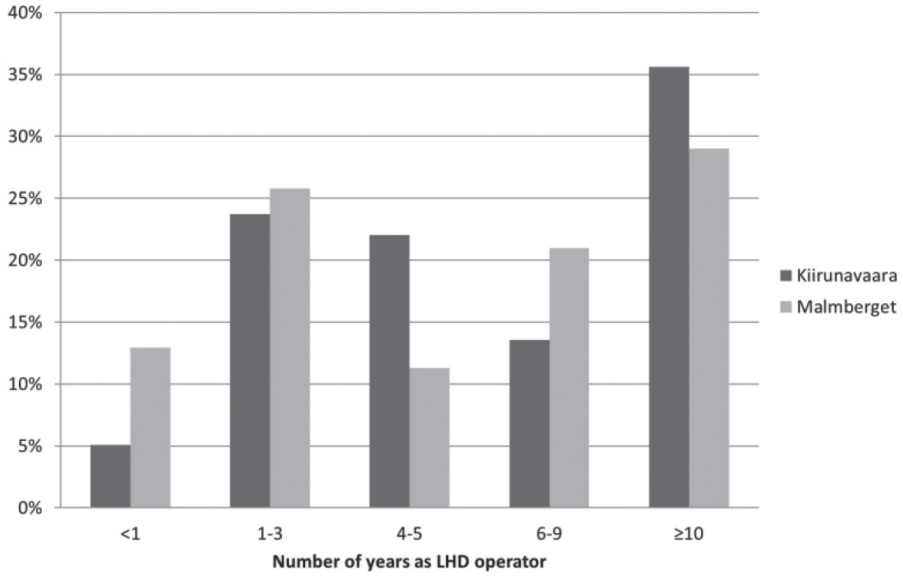

Figure 8—Number of years' experience loading for each operator

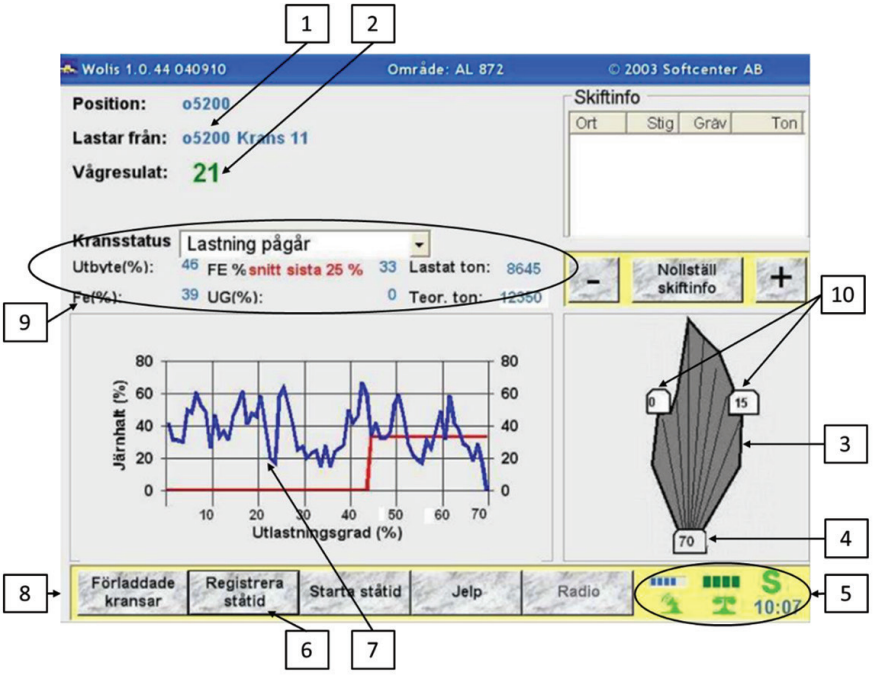

Figure 9—Waste *versus* bucket numbers (modified from Adlerborn and Selberg, 2008)

the grade of the ore being loaded, which assists the operator to decide when to stop loading (Adlerborn and Selberg, 2008). The bucket grade curve is smoothed by considering a moving average for the last 15 buckets (Nordqvist and Wimmer, 2014).

The loading information displayed on the WOLIS screen (Figure 9) consists of the following (Adlerborn and Selberg, 2008):

1. The location from where the material is taken, including the drift and ring number.
2. The last bucket weight recorded by the system.
3. A graphical representation of the current ring being loaded showing the drill-holes, along with the neighbouring rings.
4. The current extraction ratio of the ring being loaded, as a percentage.
5. Status indicators showing if the system is connected to the weighing system and if it is connected to the WLan, along with an indication of upload/download transfers.
6. A new window to register downtime, *i.e.* the duration and cause of the system being down or unusable.
7. A graphical representation of the total loading from the current ring. The system has four modes for graphical representation. The following can be plotted:
   (a) Iron percentage (Y axis) *vs* extraction ratio (X axis)
   (b) Waste percentage (Y axis) *vs* extraction ratio (X axis)
   (c) Bucket weight (Y axis) *vs* number of buckets loaded (X axis)
   (d) Waste percentage (Y axis) **vs** number of buckets loaded (X axis).

   In Figure 6, the blue line shows the moving average property (iron percentage or bucket weight) and the red line the iron percentage of the last 25% (by units) of the extraction ratio. These two lines guide the operator's decision to stop loading from a ring.
8. A new window showing if any charged holes are close to the current ring.
9. Additional data about the current ring displayed on the operator's screen includes the present status of the ring, the iron percentage for the last 25% of the extraction ratio, tonnage loaded, planned tonnage, and iron percentage for bucket.
10. The final extraction ratio of the neighbouring drifts in the level above the present drawpoint.

At LKAB, each LHD operator can see the information, such as the extraction ratio and ore grade for the last 15 buckets, total planned tonnage, and tonnage extracted from the ring, on the WOLIS screen installed in the LHD. The information is used by the operator to decide if loading should be continued or discontinued at a particular drawpoint based on the loading criteria. If the information on the screen indicates that loading should be continued, loading is pursued; otherwise, the drawpoint is closed. However, if loading cannot be continued because of loading issues such as hangups, brow failure *etc.*, the operator enters the reason for stopping loading in WOLIS and moves to the next active drawpoint for loading.

Loading of normal rings

The criteria guiding the loading process are called loading criteria and are part of draw control, along with loading procedures. Loading at the drawpoint is assisted by the WOLIS system in both the Kiirunavaara and the Malmberget mines; the system displays bucket weight and bucket grade, together with other ring properties. The extraction ratio is used as a loading criterion; this is the ratio of total tonnage of material loaded from the drawpoint to the planned tonnage of the ring.

In the Kiirunavaara mine, loading is normally continued to the fixed extraction ratio target communicated by the loading managers to the operators. In the Malmberget mine, three loading criteria must be met for a normal ring before the operator can/should stop loading and abandon the drawpoint: extraction ratio, Fe grade, and a negative trend on bucket weights.

When the decision is made to close a ring, the operator builds a catch wall to ensure the safety of the personnel who will charge the next fan in the drift. This wall must be approved by the charging personnel.

Loading of opening rings

The loading process and draw control of the opening rings near the hangingwall are guided by safety concerns. Drawpoints near the hangingwalls have an open cavern during the later stages of the draw; *i.e.* the hangingwalls have not yet caved or have just begun to cave, creating an open cavern above the drawpoint. Keeping this in mind, LHD operators load the material under the supported part of the drift. The current loading procedure dictates that no loading can be performed in an open cavern situation; *i.e.* loading is stopped when an opening is encountered at the drawpoint because of a gap between the muckpile and the supported part of the drawpoint. The final extraction ratio for rings near the hangingwall can vary from 35% to 70% in the Kiirunavaara mine.

Loading of rings with loading issues

Loading at the drawpoint is sometimes stopped early due to loading issues such as hangups, ring freeze, brow failure, *etc.* Poorly fragmented material at the drawpoint is still loaded, but the boulders are broken by a rock-breaker in the Kiirunavaara mine and by drilling and blasting in the Malmberget mine before being dumped into the orepass. The loading criteria are followed for drawpoints with poor fragmentation, but an inefficient filling of the bucket may cause inaccurate grade estimations. Loading issues, such as bridges, rib formation, walls, and overhangs, are difficult to detect during loading, and the only symptoms may be poor material flow, for which there are no separate loading criteria. The handling of hangups differs in the Kiirunavaara and Malmberget mines.

Decision process

The decision-making process for three types of situations was investigated, namely the abandonment of:

- 'Normal' rings
- Opening rings
- Rings with loading issues (hangups, brow failure *etc.*).

The decision-making process differs for each category of ring and for each mine.

With respect to the decision to stop loading a 'normal' ring and to blast the next fan, most operators in both mines said they make the decision themselves and inform the loading control group that they are abandoning the drawpoint (Figure 10). A slightly higher percentage of operators in the Malmberget mine discuss the closing of a draw point with the loading control group before a decision is taken, compared to Kiirunavaara mine. The

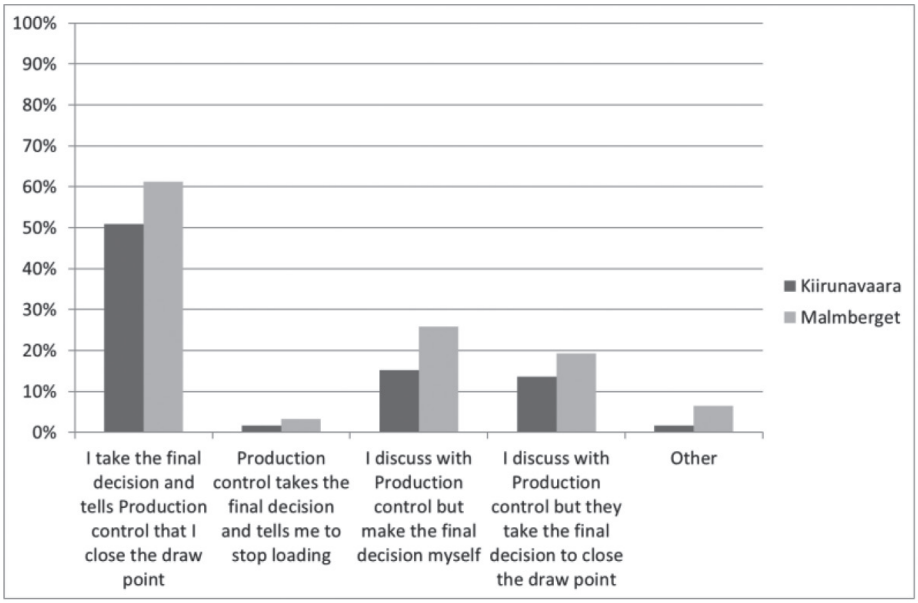

Figure 10—Who makes the final decision to abandon a 'normal' ring?

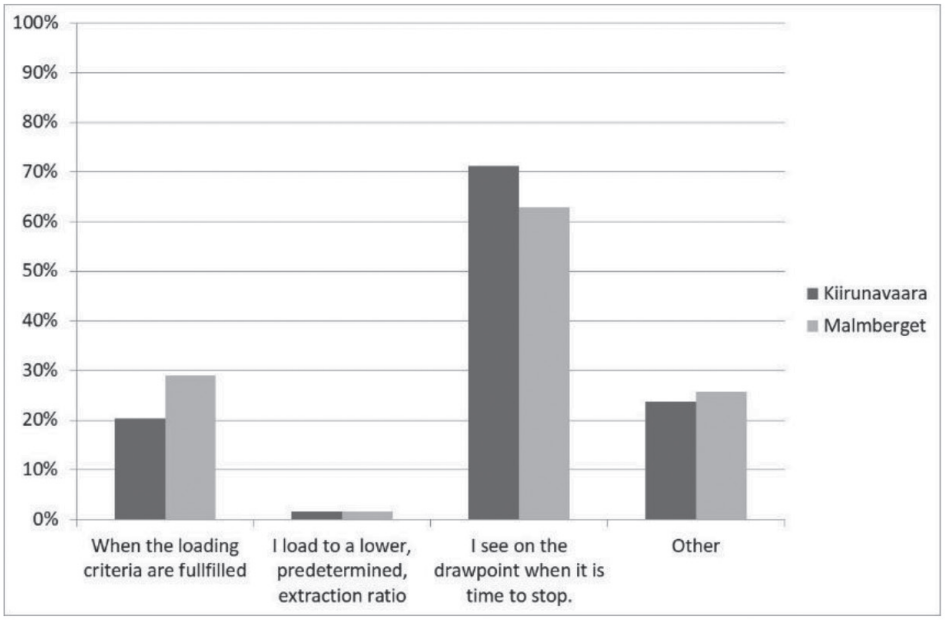

Figure 11—How do you know when it is time to abandon an opening ring?

decision to abandon the ring is then made either by the operator or by the loading control group. Only occasionally does the loading control group takes the final decision and instruct the operator to stop loading.

The decision to close an opening ring is different from the decision to close a normal ring. For opening rings, most operators said they can see at the drawpoint when it is time to stop loading (Figure 11). The majority of these answers (67% from the Kiirunavaara mine and 71% from the Malmberget mine) relate to seeing an open cavern above the drawpoint; this is an indication that it is time to stop loading and go on to blast the next ring. Note that these percentages also include the answers from the category 'other'.

The next question dealt with the decision to stop loading for rings with loading issues. The answers show that most operators make a visual inspection to decide if loading can be continued safely (Figure 12). Interestingly, the number of operators asking the loading control group to come and visually inspect the drawpoint before closing it is higher in the Malmberget mine.

Overall, it is mainly the operator, either with or without assistance from the loading control group, who decides when to abandon drawpoints with loading issues. The operators in the Kiirunavaara mine are more likely to do so than those in the Malmberget mine (Figure 13), while the loading control group in the Malmberget mine makes the decision to close drawpoints more often than its fellow group in the Kiirunavaara mine.

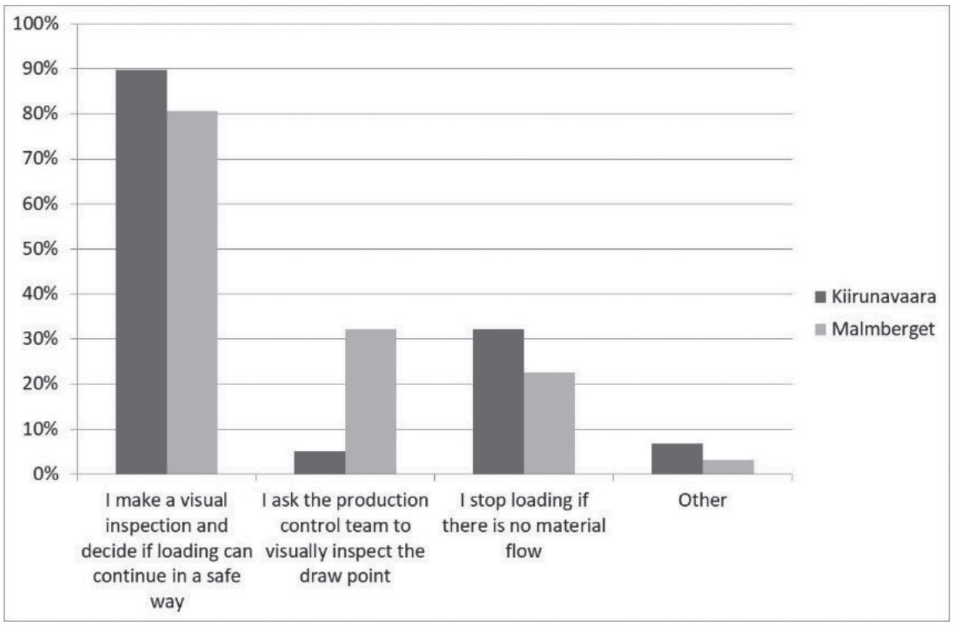

Figure 12—How is the decision to stop loading made for rings with loading issues (hangups, brow failure, *etc.*)?

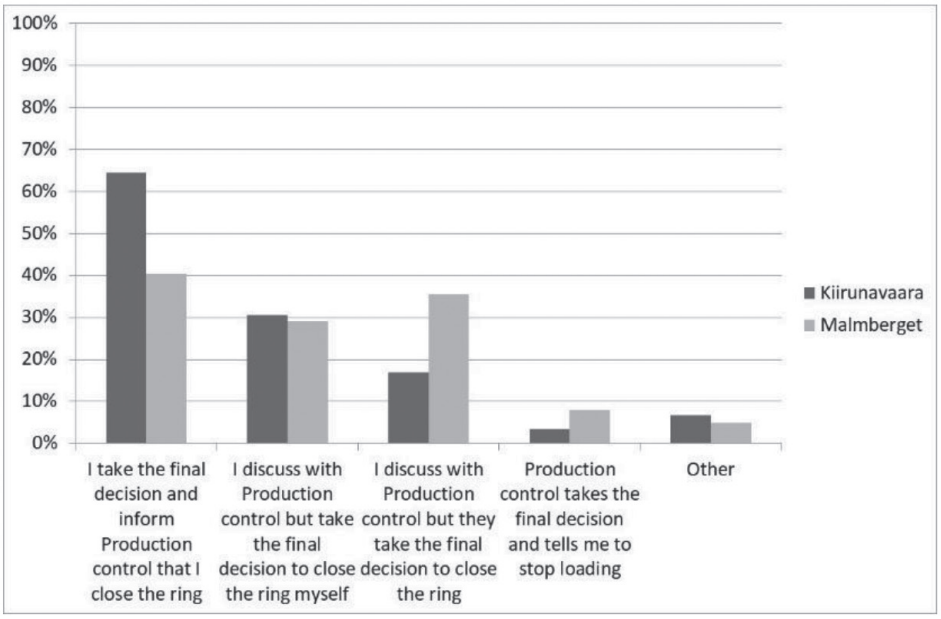

Figure 13—Who makes the final decision to abandon rings with loading issues (hang-ups, brow failure, *etc.*)?

Differences depending on loading experience

The study also compared the process of deciding to abandon a drawpoint with loading issues among operators with different levels of loading experience. Operators with more than 10 years of experience make more decisions themselves than those with less experience (<10 years), with the latter relying more on the loading control group (Figure 14). Operators with less experience have a tendency to discuss the situation more often with the loading control group before a decision is made. After discussions, the decision is made slightly more often by the loading control group than by the operator. For the more experienced operators, however, the decision is more often theirs after discussions with the loading control group. In Figure 14, the Kiirunavaara and Malmberget mines are assessed together.

In the Kiirunavaara mine, rings with loading issues are closed depending on the experience of the operator. All experienced operators make a visual inspection before they decide if loading can continue safely (Figure 15). Fewer of the less experienced operators visually inspect the drawpoint before abandoning it.

In the Malmberget mine, the less experienced operators visually inspect drawpoints to a greater extent than the more experienced ones (Figure 16), but the loading control group is also more involved with inspecting the drawpoint for the less

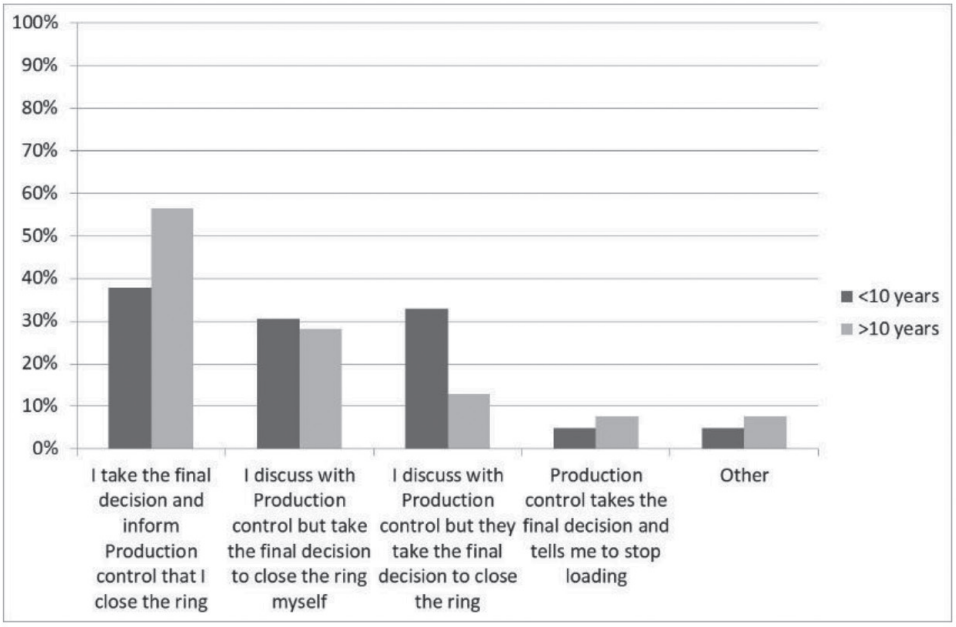

Figure 14—Who makes the final decision to abandon rings with loading issues (*e.g.* hang-ups, brow failure, *etc.*)?

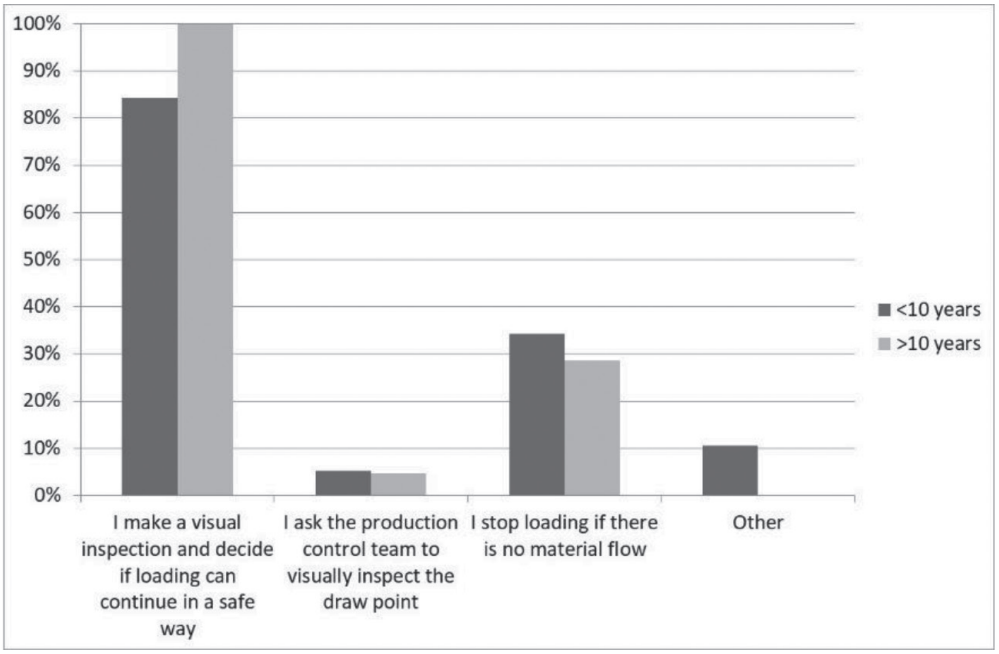

Figure 15—How is the decision to stop loading made for rings with loading issues (hangups, brow failure *etc.*) in the Kiirunavaara mine?

experienced operators. The more experienced operators tend to make a visual inspection of the drawpoint and then decide if loading can be continued safely or to stop loading if there is no material flow at the drawpoint.

Concluding remarks

The experience of the LHD operators in LKAB's Kiirunavaara and Malmberget mines was investigated to obtain a better understanding of current loading practices and the decision processes involved in abandoning 'normal' rings, opening rings, and rings with loading issues (*e.g.* brow failure, pillar failure, or ring freeze). The main findings from this study are as follows.

- In both mines, the operators make the majority of the decisions to close a drawpoint, so their experience is very important for the loading process. Operators can also override any suggestion made by the draw control system on when to close the drawpoints.
- The loading control groups are involved in decisions to close drawpoints, but the loading control group in the Malmberget mine is more involved than that in the Kiirunavaara mine.
- The more experienced operators tend to make more decisions themselves, while the less experienced operators rely more on support from the loading control group. There are more experienced operators at the Kiirunavaara mine

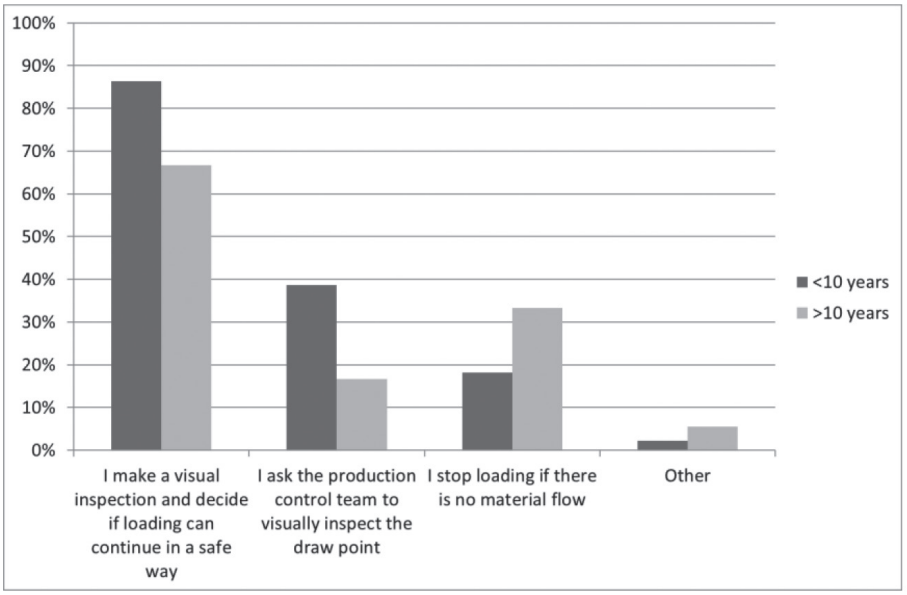

Figure 16—How is the decision to stop loading made for rings with loading issues (hangups, brow failure *etc.*) in the Malmberget mine?

than the Malmberget mine, which explains the greater role of the loading control group at the latter.

There is some debate in the mines as to whether the main responsibility for, *e.g.* abandonment of drawpoints or decisions on rings with loading issues, should rest with the operator or with the loading control group.

- The general consensus is that the loading control group should be in charge of prioritizing the drifts to be loaded, while abandoning the rings should be a joint decision.
- Although the loading control group should assist operators by providing a second opinion, the common view in the two mines is that operators should make the final decisions themselves since they likely have the most experience of different situations.
- For rings with loading issues, the common view is that the loading control group should assume more responsibility for the decision to stop or to continue loading, since the decision is irrevocable.

The results from this study will be used towards the development of a new model for draw control in sublevel caving mines. The model will be tested as future work in the Kiirunavaara mine.

Acknowledgements

The authors would like to acknowledge LKAB for its financial and infrastructural support. The authors are also grateful for the invaluable input and support from the staff and management of the Malmberget and Kiirunavaara mines. Agio System och Kompetens AB, Boliden Mineral AB, ABB AB, and RTC are thanked for their valuable input as well. Vinnova, the Swedish Energy Agency and Formas, is thanked for financing the project through the SIP-STRIM programme.

References

Adlerborn, B. and Selberg, M. 2008. GIRON and WOLIS - Two mine applications. *Proceedings of the 5th International Conference and Exhibition on Mass Mining 2008*, Luleå, Sweden, 9-11 June 2008. Schunnesson, H. and Nordlund, E. (eds). Division of Mining and Geotechnical Engineering, Luleå University of Technology. pp. 637–642.

Baase, R.A., Diment, W.D., and Petrina, A.J. 1982. Sublevel caving at Craigmont Mines Ltd. *Underground Mining Methods Handbook*. Hustrulid, W.A. (ed.). Society of Mining Engineers of the American Institute of Mining, Metallurgical and Petroleum Engineers, Inc., New York. pp. 898–915.

Brunton, I. 2009. The impact of blasting on sublevel caving material flow behaviour and recovery. Doctoral thesis, University of Queensland, Australia.

Bull, G. and Page, C.H. 2000. Sublevel caving–today's dependable low-cost 'ore factory'. *Proceedings of the 3rd International Conference and Exhibition on Mass Mining 2000*, Brisbane, Queensland, 29 October-2 November 2000. Australasian Institute of Mining and Metallurgy, Melbourne. pp. 537–556.

Cokayne, E.W. 1982. Sublevel caving. Chapter 1: Introduction. *Underground Mining Methods Handbook*. Hustrulid, W.A. (ed.). Society of Mining Engineers of the American Institute of Mining, Metallurgical and Petroleum Engineers, Inc., New York. pp. 872–879.

Davison, J. 1996. Assessment of the Loadrite scoop weighing system. Internal report, Kiirunavaara mine, Sweden. LKAB.

Dunstan, G. and Power, G. 2011. Sublevel caving. *Mining Engineering Handbook*. 3rd edn. Darling, P. (ed.). Society for Mining, Metallurgy and Exploration, Inc., Littleton, CO. pp. 1417–1437.

Gustafsson, P. 1998. Waste rock content variations during gravity flow in sublevel caving, Analysis of full-scale experiments and numerical simulations. Doctoral thesis, Luleå Tekniska Universitet, Luleå, Sweden.

Kvapil, R. 2008. Gravity flow in sublevel and panel caving – A common sense approach. *Special edition for 5th International Conference and Exhibition on Mass Mining 2008,* Luleå, Sweden, 9-11 June 2008. Division of Mining and Geotechnical Engineering, Luleå University of Technology.

Nordqvist, A. and Wimmer, M. 2014. Large scale field test of gravity flow at the Kiruna mine. *Proceeding of Aachen International Mining Symposia, Sixth International Symposium, High Performance Mining*. Institute of Mining Engineering, RWTH Aachen University, Aachen, Germany. pp. 621–636.

Quinteiro, C. R., Larsson, L., and Hustrulid, W. 2001. Theory and practice of very-large-scale sublevel caving. *Underground Mining Methods: Engineering Fundamentals and International Case Studies*. Hustrulid, W.A. and Bullock, R.L. (eds). Society for Mining, Metallurgy and Exploration, Littleton, CO. pp. 381–384.

Personal communications. 2016. Staff at the loading division and loading control at LKABs underground mines in Malmberget and Kiruna.

Rutanen, H. 2011. Kiirunavaara mine geology, PowerPoint presentation. Kiirunavaara mine, Sweden. LKAB.

Savilahti, T., and Jonsson. K. 2013. LKAB information (Sublevel caving). PowerPoint presentation. LKAB.

Shekhar, G., Gustafson, A., and Schunnesson, H. 2016. Draw control strategy and resource efficiency in sublevel caving: State-of-the-art. Research report, Luleå University of Technology.

Smith, M. and Rahal, D. 2001. Draw control optimization in the context of production scheduling. *Proceedings of the 17th International Mining Congress and Exhibition of Turkey*. Chamber of Mining Engineers of Turkey, Ankara. pp. 831–838. ◆

Au and Ag distribution in alloys produced from the smelting of printed circuit boards – an assessment using SEM-EDS, EPMA, and LA-ICP-MS analysis

C. Carelse[1], M. Manuel[1], D. Chetty[1], and A. Corfield[1]

Affiliation:
[1]Mintek, South Africa.

Correspondence to:
C. Carelse

Email:
candicec@mintek.co.za

Dates:
Received: 3 Apr. 2019
Revised: 3 Dec. 2019
Accepted: 5 Dec. 2019
Published: March 2020

How to cite:
Carelse, C., Manuel, M., Chetty, D., and Corfield, A. Au and Ag distribution in alloys produced from the smelting of printed circuit boards – an assessment using SEM-EDS, EPMA, and LA-ICP-MS analysis. The Southern African Insitute of Mining and Metallurgy

DOI ID:
http://dx.doi.org/10.17159/2411-9717/698/2020

Synopsis

Electronic waste such as printed circuit boards (PCBs) often contains important concentrations of precious metals such as Au and Ag, which are typically recovered using pyrometallurgical methods as a first step. Understanding the phase chemistry and distribution of precious metals in alloys is of value to the pyrometallurgist, as this gives information on phase partitioning in the furnace. In the present study we aimed at determining the contributions of different phases to the Au and Ag contained in the alloy, using a combination of mineralogical techniques.

Three alloy samples were first subjected to scanning electron microscopy (SEM) to distinguish the phases present. Electron probe microanalysis (EPMA) was then performed to determine the compositions of the different phases. Modal phase abundance was obtained, and laser ablation inductively coupled plasma mass spectrometry (LA-ICP-MS) was then used to quantify Au and Ag in the identified phases. The Au and Ag deportments were derived from these inputs.

The results show that Au and Ag partition into all identified alloy phases, but principally into Cu and Pb alloy phases. Cu-rich phases containing Sn are the major hosts of Au and Ag, with the Pb phase in one sample also being a major host. The study demonstrates the success of a combined mineralogical approach incorporating LA-ICP-MS as a method of choice for detecting low concentrations of precious metals in alloy phases, and contributes to our understanding of precious metal partitioning during smelting of waste PCBs.

Keywords
PCBs, e-waste, alloys, gold, SEM, LA-ICP-MS.

Introduction

With modern-day advances in technology, more electronic waste (e-waste) is being generated (Hadi *et al.*, 2015; Kim *et al.*, 2010) and needs to be dealt with in an environmentally safe and economical manner. E-waste is a fast-growing waste stream in South Africa, with more than 322 000 t being produced annually according to the e-Waste Association of South Africa (eWASA). A huge problem facing this country is access to e-waste, as most e-waste is not recycled and is still stored or locked up in offices, households, in landfills, *etc*. Proper e-waste management systems are also not in place, adding to the amount of e-waste being landfilled. Only 10% of e-waste is being recycled (DEA, 2012).

Urban mining involves the recycling of e-waste. One form of e-waste is printed circuit boards (PCBs), which are found in electrical and electronic appliances such as televisions, mobile phones and laptops (Khaliq *et al.*, 2014). These PCBs often contain considerable amounts of valuable metals, up to 40%, (Luda, 2011) including precious metals (PM) such as Au and Ag. Recycling of these PCBs is a profitable business in developed countries (Chatterjee and Kumar, 2009). The main economic driver for PCB recycling is the recovery of PM and copper, with more than 70% of the contained value in PCBs being contributed by the PM (Cui and Zhang, 2008). Not only is metal recovery from PCBs economically attractive; it reduces the amount of hazardous waste being landfilled and results in high savings in energy consumption compared to processing metal from ores (Cayumill *et al.*, 2016; Cui and Forssberg, 2003).

E-waste is recycled for its metal content using technologies in pyrometallurgy, hydrometallurgy, biohydrometallurgy, and mechanical processing (Kamberović *et al.*, 2009). E-waste recycling has been dominated by pyrometallurgical routes for the past three decades (Cui and Zhang, 2008). Large recycling and e-waste co-processing facilities such as Glencore's Horne Smelter in Quebec, Canada, Boliden's Rönnskär Smelter in Skelleftehamn, Sweden, and Umicore in Belgium all make use of pyrometallurgical processing for recycling of their e-waste. Umicore uses pyrometallurgy followed by hydrometallurgy, by smelting of the e-waste and concentrating the PM into a copper bullion and the rest of the metals into a lead slag. After leaching the copper, the residue is treated for its PM at a PM refinery (Hagelűken, 2006).

Au and Ag distribution in alloys produced from the smelting of printed circuit boards

Hydrometallurgy is extensively used in the downstream separation and refining of pyrometallurgical products. The emphasis has shifted in the last 10 years to hydrometallurgical techniques as a primary recovery method for PM (Cui and Zhang, 2008). Few companies globally, however, make use of this technique for direct recovery of PM.

Mintek in South Africa embarked on an urban mining research project employing pyrometallurgy, and subsequent hydrometallurgy, to recover PM and other metals from PCBs. The aim of the project was to develop a smelting process through which a wide range of e-wastes can be processed in a small DC arc furnace, recovering the valuable metals into an alloy which is amenable to downstream hydrometallurgical processing.

The present study applies a combined mineralogical approach to locate and quantify low concentrations of Au and Ag in alloys produced from the smelting of PCBs, and from this, to determine their deportment in the copper (Cu), iron (Fe), and lead (Pb) alloy phases produced. An initial assessment of the phases present, and their possible Au and Ag contents, was made using scanning electron microscopy (SEM) with standardless energy-dispersive spectrometry (EDS). These precious metals, however, were found to be below the detection capabilities of SEM. For this reason, laser ablation inductively coupled plasma mass spectrometry (LA-ICP-MS) was chosen to quantify these elements, given its much lower detection limits (typically in the ppm to ppb range).

Gold and silver were targeted as these metals are usually two of the most dominant PM in electronic PCBs and they add significantly to the potential value of PCBs (Szałatkiewicz, 2014). Moreover, the deportment of Au after smelting is of importance to the pyrometallurgist from a phase partitioning perspective. Federov and Volkov (2016), Lee, Oh, and Lee (1994), Martienssen (2007), and Predel (1991) describe the Au-Fe, Au-Cu, Au-Pb, Ag-Fe, Ag-Cu, and Ag-Pb binary systems. According to these authors, Au will preferentially partition between Cu and Pb phases, whereas Ag preferentially partitions into Pb phases, on the basis of density. Empirical data from mineralogical techniques such as SEM and LA-ICP-MS has great potential to validate such theories and may contribute value to the discipline.

LA-ICP-MS was considered due its lower detection limits, compared with routine electron probe microanalysis (EPMA, with detection limits typically in hundreds of ppm), and SEM, so as to detect trace concentrations of elements in a given matrix. This technique is increasingly used for detection of trace elements in a variety of mineral matrices (Chen and Simonetti, 2013; Gilbert *et al.*, 2014; Melcher *et al.*, 2008) with detection limits down to ppb levels often achieved.

Trace element distribution data can in turn be used to calculate the bulk concentration of the trace element if the modal proportions of the different phases are known. This is particularly useful if bulk trace element concentrations are low, which may pose challenges for detection limits with routine bulk chemical assays. Authors such as Devos *et al.* (2000), Devos, Moor, and Liedeman (1999, Dussubieux *et al.* (2008), Dussubieux and Williams (2007), Dussubieux and Zelst (2004), Guillaume, Gratuze, and Barrandon (2007), and McCurdy, Woods, and Scrimshire (2005) have developed analytical methods for the analysis of ancient copper, gold, silver, nickel, and iron alloys using LA-ICP-MS.

Latkoczy and Ghislian (2006) used LA-ICP-MS to analyse trace element content in industrial magnesium alloys as part of corrosion studies. In a similar vein, this paper looks at trace element analysis of Au and Ag as it applies to copper- and iron-base alloys generated from PCB smelting, and considers their distribution among the alloy phases.

Materials and methods

Alloy tap samples

Three tapped alloy samples (taps A, B, and C) from three different PCB smelting campaigns were selected for Au and Ag analysis to assess the PM distribution among the alloy phases. The three smelting campaigns were conducted to develop and illustrate a flexible smelting process to recover the PM contained in electronic waste into an alloy. The three tapped alloys were chosen based on their composition (copper-rich alloys) and also on the bulk Au, Ag, and Cu concentrations. Alloys with the highest Au, Ag, and Cu concentrations were chosen for this study, as these represented the best candidates for downstream recovery by leaching.

Tap A originated from a smelting campaign whereby pre-shredded (< 50 mm in size) PCBs were smelted together with copper oxide (malachite-rich) ore and limestone to collect the valuable metals into a Cu alloy phase. The copper ore acted as a collector source. Low-grade PCBs (< 40 ppm Au) were chosen to assess the effectiveness of the collection and therefore upgrading into the alloy phase. Approximately 2000 kg of PCBs were processed. The PCBs were manually fed to the furnace in 30 kg to 90 kg batches.

After the addition of each batch of feed, the metal and slag were tapped via the furnace tap-holes into refractory-lined ladles and allowed to solidify and cool before weighing and labelling. Tapped alloys with different bulk compositions were produced: those low in iron and high in copper, and alloys high in iron and low in copper. It was noted that for alloys low in iron, the solid iron phase may be dispersed in the copper matrix and flow out of the furnace together with the copper in a semi-homogenous alloy. The appearances of the three alloys are shown in Figure 1.

Taps B and C originated from two different smelting campaigns involving the smelting of PCBs without the addition of copper ore as a collector, since it was found in the first campaign (tap A) that the collector diluted the valuable material content in the alloy. Iron- and copper-rich alloys were produced.

Tap B was formed by the feeding of shredded PCBs to a molten metal bath produced by the melting down of a metal heel (copper alloy) together with a synthetic slag mixture (silica, limestone, and alumina). Tap C was formed by heating a heel of copper scrap and feeding the PCBs in batches together with the synthetic slag mix.

For assaying of the feed PCBs, the PCBs were shredded to < 10 mm, and crushed and milled to further reduce the particle

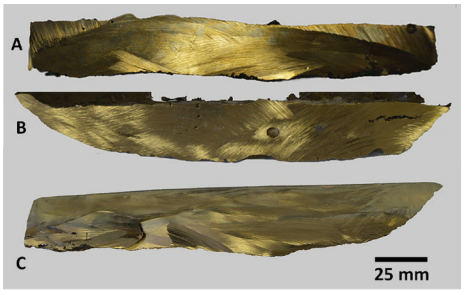

Figure 1—Appearance of alloy tap samples A, B, and C after solidification and cutting. All three alloy taps are high in copper with iron-rich inclusions

size. PCBs were taken directly from the conveyer belt underneath the feed hopper, milled, and screened. A typical bulk chemical assay of the feed PCBs is presented in Table I. For bulk chemical analysis of the alloy, sub-samples were taken from the alloy during each tap.

Physical inspection of the three tapped alloys shows great heterogeneity (Figure 1) in the alloy components, as well as the presence of admixed slag. Small pieces showing evidence of many phases at a visual scale were cut from the large ingots and prepared as polished sections for SEM, EPMA, and LA-ICP-MS analysis.

Polished section preparation

The cut pieces of each of the three tapped alloys were embedded in resin. The sample surfaces were initially ground using a 220 grit followed by grinding on 600 and 1000 grit grinding discs. The samples were then polished using diamond suspensions with particle sizes of 6 µm, 3 µm, and 1 µm. After polishing, the samples were cleaned with water followed by ethanol. For SEM and EPMA, the polished sections were coated with carbon by using an evaporative carbon coater.

Scanning electron microscopy

A metallographic investigation was conducted on the alloy phases in each of the three tapped alloys, using a Zeiss Evo MA15 scanning electron microscope with energy-dispersive spectroscopy (EDS). A voltage of 20 kV with a beam current of 3.3 nA was used. Typical detection limits for the SEM-EDS system are in the range 0.1–0.5 wt%. The study included identification of the different phases present, their textures and associations, inclusions, *etc*. This step is deemed important since it gives insight into what areas to target for LA-ICP-MS analysis and whether the alloy area targeted is representative of the overall structure (Meredith *et al.*, 2011).

Table I

Typical bulk chemistry of feed PCBs (mass%)

Element	Value
Ag	740.04*
Au	54.88*
Mg	0.21
Al	6.61
Si	5.33
Ca	2.4
Ti	0.28
V	b.d.l
Cr	0.065
Mn	0.97
Fe	10.43
Co	0.05
Ni	0.71
Cu	17.16
Zn	1.98
Pb	1.70
C	23.20
Sn	3.015
As	0.05
K	0.014
Sb	0.21
P	0.05
S	0.07
Pd	21.50*
Pt	22.16*

b.d.l below detection limit (0.05%), * ppm

Modal analysis of alloy phases

Modal proportions of alloy phases were obtained using the Olympus Stream Essentials image processing software, which integrates a detection method that uses thresholding to reliably separate objects (particles, mineral phases) from the background (resin). A series of backscattered electron (BSE) images of each tapped alloy sample was imported into the software. Thresholds were selected for each alloy phase and the background. The final threshold image was then segmented and the count and measure function applied to calculate the area of each alloy phase in the image. The modal abundance of each alloy phase was then calculated from the area of that phase and, using assigned densities for each phase, the mass abundance was calculated.

Electron probe microanalysis (EPMA)

Analyses were performed using a Cameca SX50 electron microprobe equipped with four wavelength-dispersive spectrometers (WDS) and an energy-dispersive spectrometer (EDS). An accelerating voltage of 20 kV and a beam current of 30 nA were used, with a beam spot size of 5 µm. Pure metal standards were used to calibrate the system for the analysis of the Al, Si, Ti, Mn, Fe, Ni, Cu, Zn, Sn, Sb, and Pb contents of selected phases.

EPMA was performed to not only determine the composition of the different phases identified by SEM but also to obtain the Cu, Fe, and Pb concentrations for internal standardization in the LA-ICP-MS process.

Laser ablation inductively coupled plasma mass spectrometry (LA-ICP-MS)

Analyses were performed using a NEW WAVE 193 nm ArF excimer laser coupled to a Thermo Element XR high-resolution ICP-MS. Identical ablation conditions were used for standards and samples. Alloy phases were ablated using two ablation modes: lines and spots. Spot size was 15 µm and for lines a width of 25 µm was used. Analyses were conducted in a He atmosphere within the ablation cell and mixed with Ar gas before entering the plasma.

^{65}Cu was used as an internal standard for the Cu-rich phases, ^{56}Fe for the Fe-rich phases, and ^{208}Pb for the Pb-rich phases to monitor instrument drift and to correct for differences in ablation yield. Scanned masses were ^{56}Fe, ^{65}Cu, ^{107}Ag, ^{197}Au, and ^{208}Pb. Data reduction was performed using the GLITTER laser ablation software.

The NIST 610 glass was used as calibration material for the Cu, Fe, and Pb alloy phases. Velasquez *et al.* (2018), using a femtosecond laser, showed that accurate results can be obtained for copper alloys using the NIST 610 as a calibration standard. A copper alloy standard, 39X 17868 (Brammer Standard Company) was used as reference material to assess the accuracy of Au and Ag determination in the Cu-rich phases. Accuracies of between 2% and 16% were achieved for Ag, and between 13% and 34% for Au. The poorer accuracy for Au can be ascribed to the heterogeneity of the 39X 17868 standard, as it was not manufactured specifically for LA-ICP-MS analysis and does not have good homogeneity on the finer micrometre scale.

In the absence of a suitable matrix-matched Fe alloy reference material containing Au and Ag, the BCR-2G glass standard was used. The BCR-2G contains about 9.63 wt% Fe; the Fe-rich samples, in comparison, contained between 60 and 87 wt% Fe. The BCR-2G contains no Au, therefore only the accuracy of Ag

determination was assessed. Accuracies of between 35 and 74% were obtained for Ag , which was expected given the non-matrix-matched character of the standards used.

A suitable matrix-matched lead alloy reference material containing Au and/or Ag could not be sourced. A tin/lead standard, NF43-2 (Brammer Standard Company) was analysed to check the accuracy for Au and Ag. Accuracies within 11% and 43 % were obtained for Ag and Au, respectively. The poorer accuracy on Au can be ascribed to the heterogeneity of this standard with respect to Au as it was also not manufactured for a microanalytical technique such as LA-ICP-MS.

The Pb phase of tap C was smaller than 5 µm, and could not be analysed with the laser, as insufficient energy reached the standards and samples at a spot size of 2 µm and 1 µm, resulting in no signal. The use of such small spot sizes (2 µm) requires further investigation.

Results

Bulk chemical assays

Table II lists the bulk chemical assay results for the three tapped alloys. Taps B and C are more enriched in Au and Ag compared to tap A. Tap C is the most enriched in Ag (2000 ppm) and tap B the most enriched in Au (190 ppm). Tap A is more enriched in Cu, Pb, and Sn than taps B and C. The lower Au and Ag contents of alloy tap A are a result of the compositional character of the feed PCBs used, which were low in Au.

Alloy phase characteristics

Phase distinction and textural characteristics

Metallographic investigation of the three tapped alloys indicated considerable heterogeneity, which is a direct result of the inherent heterogeneous nature of the feed PCBs. Table III lists the different phases present in each tapped alloy, together with their relative abundance in mass percentage. The latter was determined by means of point counting using the Olympus Stream Essentials image processing software.

Five alloy phases were identified based on EDS analysis, namely a Pb phase, a Fe-Si phase, a Fe-Cu phase, and two Cu-Sn phases. The two Cu-Sn phases, based on their Cu and Sn concentrations, are herein referred to as Cu-Sn (H) and Cu-Sn (L), where the former indicates a high Sn content (> 6 wt%) and the latter a low Sn content (< 6 wt%). Figure 2 to Figure 4 presents images illustrating the above-mentioned phases in each of the three tapped alloys.

Tap A is a Cu-Sn (L) matrix alloy with generally round globules of the Fe-Cu phase. Globules range from <10 µm to >100 µm in size. The Pb phase, present as randomly distributed droplets, is quite common and coarser (up to 50 µm in diameter) than in the other two taps. Tap B consists of a Cu-Sn (H) and Cu-Sn (L) matrix with generally small (< 25 µm in diameter) bleb-shaped inclusions of Pb and an octahedral Fe-Si phase. Tap C is a Cu-Sn (L) matrix alloy with round to irregular-shaped globules of Fe-Si (Figure 4). Pb is also present and is generally < 5 µm in size.

The different textures and alloy phases observed in the three tapped alloys can be linked to the different pyrometallurgical recipes used (variables such as temperature, collectors, fluxes, cooling rate, *etc.*). Tap A was formed by the addition of copper oxide ore as a collector, and taps B and C without copper ore a collector. For tap B, a metal heel (copper alloy) was melted down whereas in tap C, a heel of copper scrap was heated together with

Table III

Alloy phases present and their relative abundances (mass%) in the three tapped alloys

Tap	A	B	C
Alloy phases identified and abundance			
Cu-Sn (L)	76.4	56.4	89.1
Cu-Sn (H)	0.0	27.2	n.d
Fe-Si	0.0	16.0	10.9
Fe-Cu	22.9	n.d	n.d
Pb	0.7	0.4	<0.1

n.d not detected

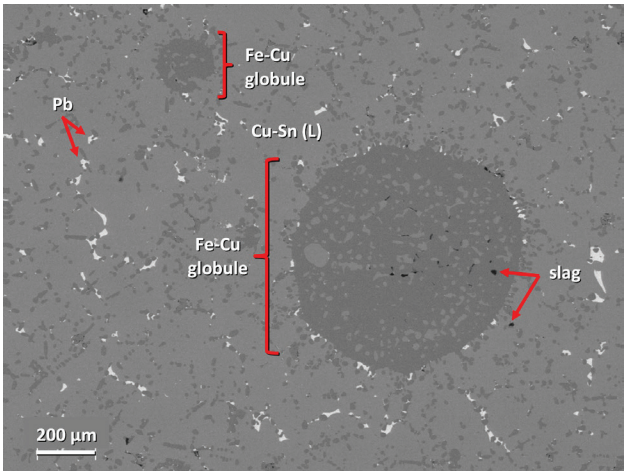

Figure 2—Backscattered electron image of tap A alloy illustrating the different alloy phases identified by SEM

Table II

Bulk chemical compositions (mass%) of the three tapped alloys

Tap	Al	C	Cr	Cu	Fe	Mn	Ni	Pb	S	Si	Sn	Ti
A	n.a.	0.04	b.d.l	89	4.93	b.d.l	0.69	1.99	0.18	b.d.l	6.81	b.d.l
B	3.24	0.17	0.44	46.2	27.75	1.1	1.8	0.28	0.01	12	5.38	0.37
C	1.84	0.09	0.21	69.3	15.2	0.63	1.01	0.24	0.01	6.69	4.78	0.1

Tap	Ag	Au	As	Ca	Co	P	Pd	Pt	Sb	Zn
A	450*	70*	n.a	n.a	0.244	0.039	31*	1.9*	n.a	0.16
B	1 300*	1 900*	0.004	0.1	0.07	0.03	50*	0.8	0.034	0.07
C	2 000*	1 400*	0.001	0.2	b.d.l	0.05	36*	3.5	0.027	0.12

n.a. not analysed, b.d.l below detection limit, detection limit (0.05%), *ppm unless otherwise stated

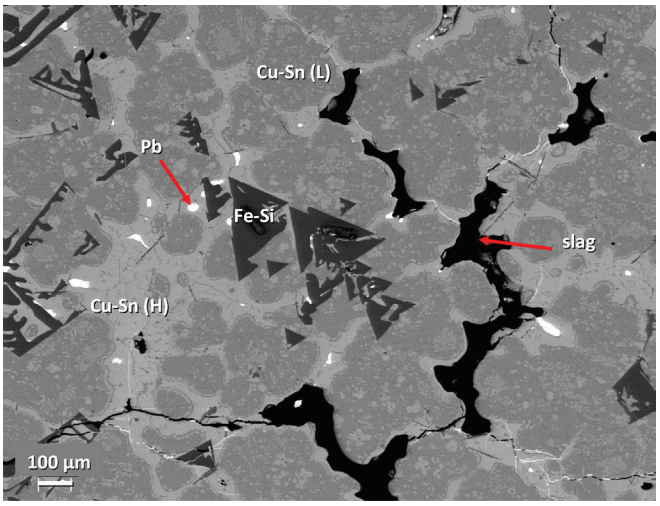

Figure 3—Backscattered electron image of tap B alloy illustrating the different alloy phases identified by SEM

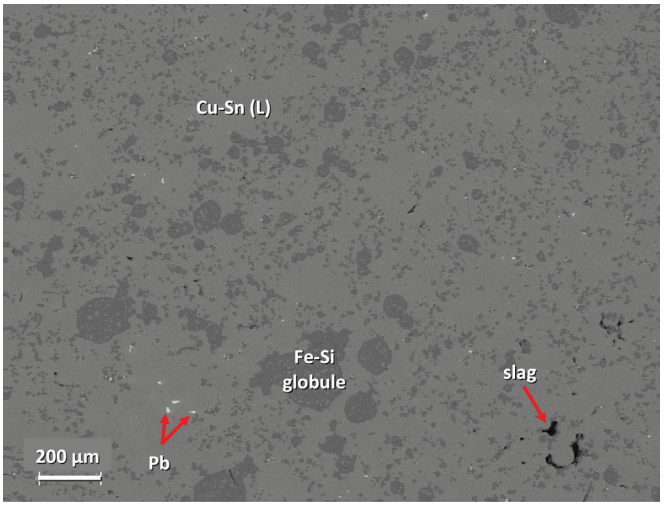

Figure 4—Backscattered electron image of tap C alloy illustrating the different alloy phases identified by SEM

the PCBs. The presence or absence of a collector can influence the different copper and iron alloy phases formed, as well as the copper and iron levels. Copper ore contains iron oxides and the raw PCBs also contain iron, resulting in iron in the formed alloys.

The varying and complex compositional characteristics of the feed PCBs also plays a significant role in the phases that can form. Although a typical composition of the feed PCB is provided (Table I), the relative enrichment in Pb of tap A relative to taps B and C (Table II) may point to compositional variability in the feed PCB batches used to generate each tap sample. Larger and more abundant Pb droplets formed in tap A compared to taps B and C (Figure 3 and Figure 4), in which much smaller and less abundant lead droplets formed. Tin and silica were also present in the feed PCBs and hence in the formed tapped alloys.

Quantitative phase chemistry

Table IV lists the average elemental compositions of the phases identified by SEM, as determined by EPMA. The full set of raw data is available on request. It is important to note that concentrations below detection were assigned a value of zero for the purpose of calculating the average concentrations, which will be underestimated as a consequence.

The Cu-Sn (L) phase, present in all three taps, has an average Cu content of between 85.27 and 93.04 wt%. Tin content is generally below 6.00 wt%. The Cu-Sn (H) phase, found only in tap B, has a Sn content of up to 22.10 wt%.

The Fe-Si phases of taps B and C have Fe contents of 63.00 wt% and 85.24 wt% respectively. The Fe-Si phase of tap B has a higher silica content of 32.63 wt% compared to tap C (9.41 wt%).

The Pb-rich phases of taps A and C contain some Cu (up to 6.73 wt%). whereas the Pb phase of tap B contains some Sb (1.46 wt%).

Gold and silver content in alloy phases

Gold and silver concentrations were quantified in the Cu-rich, Fe-rich, and Pb-rich phases of the three tapped alloys using LA-ICP-MS (Table V). As mentioned in the LA-ICP-MS method section, the Pb phase of tap C could not be analysed due to the laser providing insufficient energy at small spot sizes (< 2 µm). Full data-sets are available upon request.

Gold and silver were found to be most enriched in the Pb phase of tap A, with average Au and Ag contents of 2 802 ppm and 10% respectively. Silver is also most enriched in the Pb phase of tap B, with an average Ag content of 7 582 ppm.

The two Cu–Sn phases, Cu–Sn (L) and Cu-Sn (H), are more enriched in Au and Ag than the Fe phases (Fe-Si and Fe-Cu). The Cu-rich phases contain average Au contents in the order of 10 to 100 ppm, whereas the Fe-rich phases contain in the order of 1 to 10 of ppm Au.

The Cu-Sn (L) phase of tap B is more enriched in Au, with an average Au concentration of 257.8 ppm, and tap A the least enriched (39.9 ppm). The Cu-Sn (H) phase is more Au-enriched than the Cu-Sn (L) phase, with the Cu-Sn (H) phase of tap B having an average Au concentration of 329.3 ppm.

Silver concentrations in the Cu-rich phases are in the order of 1000 ppm. The Cu-Sn (L) phase of tap B has the highest average Ag content of 7 189 ppm.

The Fe-rich phases are the least enriched in Au and Ag, especially the Fe-Si phase of tap C. Gold and silver contents are in the low ppm ranges in these phases (3.9–23.8 ppm for Au, 9.2–358.3 ppm for Ag).

Analysis by LA-ICP-MS revealed the presence of Ag and Au in all identified alloy phases but one (the Pb phase of tap C). Gold and silver are heterogeneously distributed across the various alloy phases, with the Pb phase being the most enriched in Au and Ag followed by the Cu-rich phases. Au and Ag are heterogeneously distributed not only across the alloy phases, but also in a given alloy phase as indicated by the large standard deviations around the averages (Table V).

The partitioning of Au and Ag into Pb, Cu, and Fe can be explained by referring to the Au-Fe, Au-Cu, Au-Pb, Ag-Fe, Ag-Cu, and Ag-Pb binary phase diagrams of Federov and Volkov (2016), Lee, Oh, and Lee (1994), Martienssen (2007), and Predel (1991). According to these authors, Au will preferentially partition between Cu and Pb phases, whereas Ag preferentially partitions into Pb phases, on the basis of density.

Au and Ag deportment in alloy phases

Gold and silver deportment was calculated, using the LA-ICP-MS results, to determine the contribution of each alloy phase in terms of Au and Ag and to determine the total Au and Ag contained in each of the three tapped alloy samples. For tap C, the Au and Ag deportment does not include the contribution from the Pb phase as it could not be analysed with the laser. Deportment

Table IV

Average elemental composition (in wt%) of the different alloy phases in the three tapped alloys as determined by EPMA

Phase	Tap	n	Al	Si	Ti	Mn	Fe	Ni	Cu	Zn	Sn	Sb	Pb	Total
Fe-Si	B	12	0.93	32.63	b.d.l	1.11	63.00	2.03	0.35	0.04	b.d.l	b.d.l	0.09	100.15
	C	19	0.09	9.41	b.d.l	0.37	85.24	1.86	2.96	b.d.l	b.d.l	b.d.l	0.12	100.02
Fe-Cu	A	15	b.d.l	1.86	b.d.l	0.03	86.41	2.19	9.19	0.04	b.d.l	b.d.l	0.08	99.71
Cu-Sn (L)	A	38	b.d.l	0.05	b.d.l	0.03	1.03	0.54	93.04	0.22	5.00	0.40	0.10	99.95
	B	36	5.45	2.40	b.d.l	0.40	0.08	0.21	85.27	0.17	5.79	0.30	0.11	100.21
	C	50	0.50	0.50	b.d.l	0.35	2.02	0.35	91.82	b.d.l	4.09	0.27	0.15	100.01
Cu-Sn (H)	B	18	3.14	1.17	b.d.l	0.22	0.34	0.27	70.45	0.13	22.10	1.84	0.19	100.00
Pb	A	7	b.d.l	b.d.l	b.d.l	b.d.l	1.11	0.05	2.20	0.05	0.16	0.06	96.33	99.87
	B	10	b.d.l	b.d.l	b.d.l	0.03	0.04	0.03	0.69	b.d.l	0.77	1.46	96.36	100.33
	C	16	0.14	b.d.l	0.04	0.02	0.59	0.03	6.73	b.d.l	0.07	b.d.l	92.30	
DL		0.03	0.03	0.01	0.02	0.02	0.02	0.03	0.03	0.03	0.03	0.07		

b.d.l below detection limit, n total number of spots analysed, DL detection limit

Table V

Average Au and Ag concentrations and ranges (in ppm) of the different alloy phases in the three tapped alloys as determined by LA-ICP-MS

Phase	Tap no.	n	n*Au	n*Ag		Au	Ag
Fe-Si	B	30	12	23	Av.	24	358
					SD	86	819
					MDL	0.09	0.30
					r ange	b.d.l–455	b.d.l– 3 778
	C	30	30	30	Av.	4	9
					SD	4	16
					MDL	0.02	0.11
					range	1–18	0.3–80
FeCu	A	30	30	30	Av.	4	50
					SD	2	5
					MDL	0.05	0.16
					range	2–26	0.4–988
Cu-Sn (L)	A	30	30	26	Av.	40	1 646
					SD	17	1 728
					MDL	0.34	1.05
					range	11–66	663–9 626
	B	30	30	30	Av.	258	7 189
					SD	19	3 565
					MDL	0.11	0.35
					range	223–306	4 735–24 793
	C	30	30	30	Av.	99	1 224
					SD	16	416
					MDL	0.08	0.20
					range	71–130	603–2 611
Cu-Sn (H)	B	30	30	30	Av.	329	2 941
					SD	27	319
					MDL	0.10	0.35
					range	288–385	2 292–3 526
Pb	A	30	27	30	Av.	2 802	94 806
					SD	4 069	114 451
					MDL	7.53	121.09
					range	124–11 985	b.d.l–380 956
	B	20	20	20	Av.	80	7 582
					SD	210	4 663
					MDL	0.45	3.36
					range	2–946	3 474–22 435

Av. average concentration, SD standard deviation at 1 sigma, MDL average minimum detection limit, n total number of spots analysed, n*Au = total number of spots Au was detected in, n*Ag total number of spots Ag was detected in

calculations were done by using the average Au and Ag concentrations and the modal proportions of the different phases determined by image analysis.

Figure 5 and Figure 6 illustrate the contribution of each alloy phase, in ppm, in terms of Au and Ag for each of the three tapped alloys as well as the total Au and Ag for each alloy. Figure 7 and Figure 8 illustrate the Au and Ag deportment, in per cent, as pie charts.

For tap A, the majority of the Au (29.8 ppm) and Ag (1 153 ppm) is contributed by the Cu-Sn (L) phase (Figure 5 and Figure 6). This corresponds to 58.2% of the total Au and 60.9% of the total Ag (Figure 7 and Figure 8). The Fe-Cu phase hosts

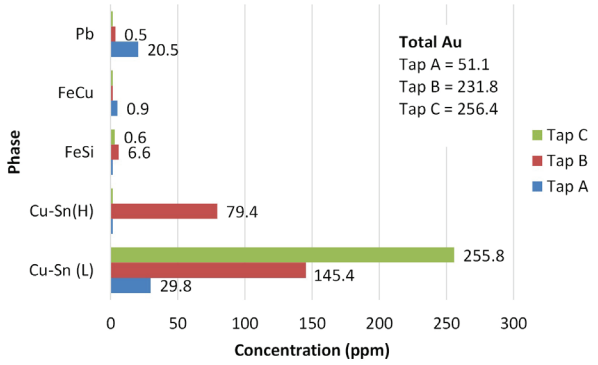

Figure 5—Au deportment (in ppm) for each of the three tapped alloys showing the contribution of each alloy phase

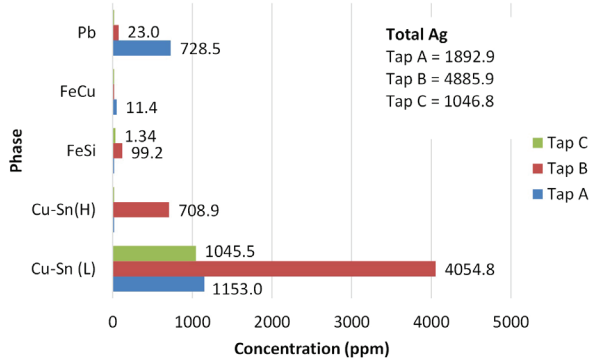

Figure 6—Ag deportment (in ppm) for each of the three tapped alloys showing the contribution of each alloy phase

the least Au and Ag (1.7% of the total Au and 0.6% of the Ag). Although the Pb phase contains the highest average Au and Ag concentrations (Table V), it makes up a small percentage of the total sample and hence its contribution is lower than that of the Cu-Sn (L) phase. Forty per cent of the total Au, and 38.5% of the total Ag, is contributed by the Pb phase. In total, tap A hosts 51.1 ppm of Au and 1 893 ppm of silver.

For tap B, the two Cu-Sn phases are the main hosts of gold and silver with 97.0% of the total Au and 97.5 % of the total Ag present (Figure 7 and Figure 8) in these phases. The Pb phase contributes the least Au (0.2%) and Ag (0.5%) to the total Au and Ag, owing to its low modal abundance in the alloy. The Fe-Si phase is also a minor contributor of Au and Ag with 2.8% of the total Au and 2.0% of the total Ag being hosted by this phase. In total, tap B hosts 231.8 ppm Au and 4 886 ppm Ag.

For tap C, a similar trend is visible with the Cu-Sn (L) phase hosting the majority of the Au and Ag. In terms of percentage contributions, 99.8% and 99.9% of the total Au and Ag are contributed by the Cu-Sn (L) phase respectively (Figure 7 and Figure 8). The Fe-Si phase is a minor contributor, with 0.24% and 0.13% of the total Au and Ag being contributed by this phase. The Au and Ag contribution of the Pb phase could not be determined due to this phase being too small to analyse. The modal abundance of the Pb phase is low (< 0.1 wt%) and hence its contribution will be minor. In total 256.4 ppm Au and 1 047 ppm Ag are hosted in tap C.

Deportment calculations show that the Cu-Sn (L) phase of each tapped alloy contributes the most to the total gold and silver budget. For tap B, the Cu-Sn (H) phase is also a dominant host. The Pb phase of tap A is also a major Au and Ag host. All three taps host more Ag than Au, which is as expected.

Bulk chemical assay results of the tapped alloys (Table II) show that tap A is less enriched in gold and silver than taps B and C. Gold deportment results are in agreement with the bulk chemical assay results in that taps B and C contain higher total Au than tap A. Bulk chemical assay results show that tap C contains the highest total Ag and tap A the lowest total Ag. Silver deportment, however, shows that tap B has the highest Ag and tap C the lowest. The reason for this discrepancy between bulk chemical assay results and deportment using LA-ICP-MS data is the heterogeneous nature of the tapped alloys, which in turn is due to the heterogeneous nature of the feed PCBs. Different sub-samples from the same tapped alloy were analysed by the two techniques and cross-checks of the total Au and Ag are therefore difficult.

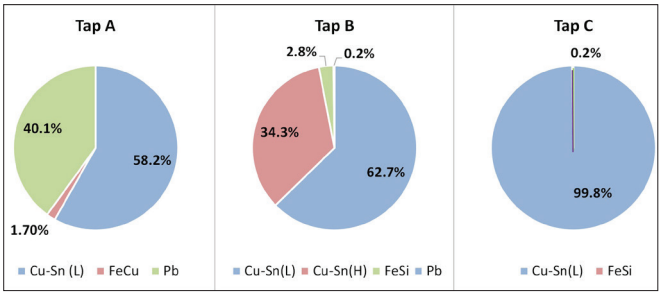

Figure 7—Au deportment (%)

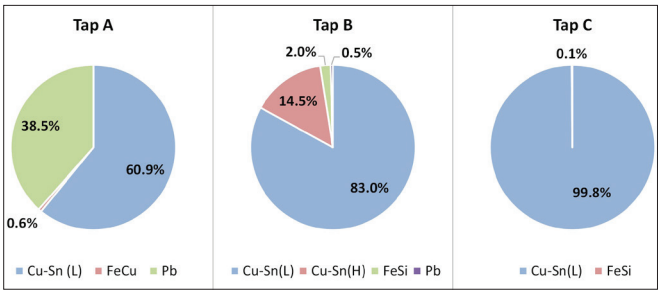

Figure 8—Ag deportment (%)

Discussion

The results have shown that all of the alloy phases in the three tapped alloys, except the Pb phase of tap C, are hosts of Au and Ag, *i.e.*, Au and Ag partitioned into all of the alloy phases but more dominantly into specific (Pb and Cu) alloy phases. Silver concentrations are generally higher than Au, which is to be expected since PCBs generally contain more Ag than Au (Khaliq *et al.*, 2014).

Results further indicate that Au and Ag migrated towards and partitioned mostly into the denser lead phase, and to a lesser extent into the Cu and Fe phases. Lead is used as solder in PCBs (Jha *et al.*, 2012) and Au and Ag were therefore not originally present in the Pb phase.

The LA-ICP-MS results confirm the Au-Fe, Au-Cu, Au-Pb, Ag-Fe, Ag-Cu, and Ag-Pb binary systems and thermodynamics identified by Federov and Volkov (2016), Lee, Oh, and Lee (1994), Martienssen (2007), and Predel (1991). The technique not only confirmed the thermodynamics of the binary diagrams; it also quantified the Au and Ag in these binary phases.

The Au and Ag deportments indicate that the Cu-Sn (L) phase of the three tapped alloys contributes the most Au and Ag to the total Au and Ag for each tapped alloy. The Pb phase of tap A is also a major contributor of Au and Ag, as well as the Cu-Sn (H) phase of tap B. For tap B, the Pb phase makes a small contribution to the total Ag, despite it having the highest Ag concentrations. This is due to its low modal abundance in the tapped alloy. The Fe phases make a minor contribution to the total Au and Ag for each tapped alloy. The Au and Ag deportment informs the pyrometallurgist on precious metals partitioning in the furnace.

Gold and silver vary in concentration in each alloy phase. The large standard deviations and wide concentrations ranges of Au and Ag further supports this heterogeneity in distribution.

Due to upgrades in the design and functions of electronic products, PCBs are constantly changing in composition (Chancerel *et al.*, 2009). Due to the heterogeneous and complex nature of a batch of PCBs obtaining a representative sample, as well as the chemical analysis of the sample itself, is challenging (Ogunniyi, Vermaak, and Groot, 2009).

The heterogeneous nature of the tapped alloys is a result of not only the heterogeneous nature of the feed PCBs, but also the different pyrometallurgical recipes (factors such as cooling rate, temperature, fluxes, collectors added, *etc.*) used in the smelting process. The composition of the feed PCBs and the pyrometallurgical recipe used, in turn determine the alloy phases that form and how much of these will form.

Electrorefining and leaching tests may be performed on the copper alloy for the recovery of Cu and Au. For electrorefining, a pure Cu metal will be produced and the PM (Au, Ag, PGM) and other metals (Pb, Sn, Sb) concentrated into the insoluble anode sludge. Leaching is then performed on the anode sludge in chloride media to recover the PM. Leaching efficiency/recovery

may be variable depending on the leach process, as well as host phase distribution, composition, and contribution to the PM budgets. Alloys with different compositions have different leaching behaviour/kinetics. A designed flow sheet should be flexible to accommodate the heterogeneous nature of the tapped alloys.

Conclusions and recommendations for further work

The results have shown that Au and Ag in alloys produced from the smelting of PCBs can be successfully located and quantified using a combination of SEM, EPMA, and LA-ICP-MS. Initial studies to detect and quantify gold using only SEM were unsuccessful due to the concentrations of Au being below the detection limit of the SEM. LA-ICP-MS however, with its much lower detection limits, were successful in locating and quantifying gold and silver. The data can be used to understand Au and Ag distribution in alloy phases, and the contributions of each phase to the total Au and Ag content in the alloy. Deportment studies of this type allow for improved pyrometallurgical (and subsequent hydrometallurgical) processing for precious metals recovery from PCBs. The heterogeneous nature of the alloys produced can be addressed through prudent sampling, *e.g.*, atomization to produce smaller particle sizes from which representative samples can be taken.

For the LA-ICP-MS method, suitable reference materials containing Au and/or Ag are needed to properly assess the accuracy of Au and Ag analyses of in the alloy phases. The use of smaller spot sizes (< 5 µm) also needs to be assessed further.

Acknowledgements

The authors are grateful to Mintek for financial support and permission to publish. We thank Mintek colleagues Markus Erwee, Rodney Jones, Derek Hayman, Roxanne Mottay, Thabiso Ntloko, Sello Tsebe, and Glen Denton for their inputs on the pyrometallurgical and hydrometallurgical processing.

References

Cayumill, R., Khana, R., Rajarao, R., Mukherjee, P.S., and Sahajwalla, V. 2016. Concentration of precious metals during their recovery from electronic waste. *Waste Management*, vol. 57. pp. 121–130

Chancerel, P., Meskers, C.E., Hagelüken, C., and Rotter, V.S. 2009. Assessment of precious metal flows during preprocessing of waste electrical and electronic equipment. *Journal of Industrial Ecology*, vol. 13, no. 5. pp. 791–810.

Chatterjee, S. and Kumar, K. 2009. Effective electronic waste management and recycling process involving formal and non-formal sectors. *International Journal of Physical Sciences*, vol. 4, no. 13. pp. 893–905

Chen, W. and Simonetti, A. 2013. In-situ determination of major and trace elements in calcite and apatite, and U-Pb ages of apatite from the Oka carbonatite complex: Insights into a complex crystallization history. *Chemical Geology*, vol. 353. pp. 151–172.

Cui, J. and Forssberg, E. 2003. Mechanical recycling of waste electric and electronic equipment: a review. *Journal of Hazardous Materials*, vol. 99. pp. 243–263.

Cui, J. and Zhang, L. 2008. Metallurgical recovery of metals from electronic waste: a review. *Journal of Hazardous. Materials*, vol. 158. pp. 228–256.

Department of Environmental Affairs. 2012. South African Environmental Outlook: A report on the state of the environment. Pretoria.

Devos, W., Moor, Ch., and Lienemann, P. 1999. Determination of impurities in antique silver objects for authentication by laser ablation inductively coupled plasma mass spectrometry (LA-ICP-MS). *Journal of Analytical Atomic Spectrometry*, vol. 14. pp. 621–626.

Devos, W., Senn-Luder, M., Moor, Ch., and Salter, C. 2000. Laser ablation inductively coupled plasma mass spectrometry (LA-ICP-MS) for spatially resolved trace analysis of early-medieval archaeological iron finds. *Fresenius Journal of Analytical Chemistry*, vol. 366. pp. 873–80.

Dussubieux, L. and Van Zelst, L. 2004. LA-ICP-MS analysis of platinum group elements and other elements of interest in ancient gold. *Applied Physics A, Material Science and Processing*, vol. A79, no. 2. pp. 353–6.

Dussubieux, L. and Williams, P.R. 2007. Elemental analysis of Peruvian copper-based artefacts using LA-ICP-MS. *Proceedings of the 2nd International Conference – Archaeometallurgy in Europe 2007*, Aquileia, Italy 17-21 June. Associazione Italiana di Metallurgia, Milan. pp. 489–497.

Dussubieux, L., Deraisme, A., Frot, G., Stevenson, C., Creech, A., and Bienvenu, Y. 2008. LA-ICP-MS, SEM-EDS and EMPA analysis of eastern north American copper-based artefacts: Impact of corrosion and heterogeneity on the reliability of the LA-ICP-MS compositional results. *Archaeometry*, vol. 50, no. 4. pp. 643–657

Fedorov, P.P. and Volkov, S.N. 2016. Au-Cu phase diagram. *Russian Journal of Inorganic Chemistry*, vol. 61. pp. 772–775.

Gilbert, S.E., Danyushevsky, L.V., Goemann, K., and Death, D. 2014. Fractionation of sulphur relative to iron during laser ablation ICP-MS analyses of sulphide minerals: implications for quantification. *Journal of Atomic Spectrometry*, vol. 29. pp. 1024–1033.

Guillaume, S., Gratuze, B., and Barrandon, J. 2007. Application of laser ablation inductively coupled plasma mass spectrometry (LA-ICP-MS) for the investigation of ancient silver coins. *Journal of Analytical Atomic Spectrometry*, vol. 22. pp. 1163–1167.

Hadi, P., Xu, M., Lin, C.S.K., Hui, C., and McKay.G. 2015. Waste printed circuit board recycling techniques and product utilization. *Journal of Hazardous Materials*, vol. 283. pp. 234–342

Hagelüken, C. 2006. Recycling of electronic scrap at Umicore Precious Metals Refining. *Acta Metallurgica Slovaca*, vol. 12. pp. 111–120.

Jha, M. K., Kumari, A., Choubey, P.K., Lee, J., Kumar, V., and Jeong, J. 2012. Leaching of lead from solder material of waste printed circuit boards (PCBs). *Hydrometallurgy*, vol. 121–124. pp. 28–34.

Kamberović, Z., Korać, M., Ivšić, D., Nikoliić, V., and Ranitoviić, M. 2009. Hydrometallurgical process for extraction of metals from electronic waste. Part 1: Material characterisation and process option selection. *Association of Metallurgical Engineers of Serbia*, vol. 15, no. 4. pp. 231–243.

Khaliq, A., Rhamdani, M. A., Brooks, G., and Masood, S. 2014. Metal extraction processes for electronic waste and existing industrial routes: A review and Australian perspective. *Resources*, vol. 3. pp. 152–179

Kim, E., Kim, M., Lee, J., Yoo, K., and Jeong, J. 2010. Leaching behaviour of copper using electro-generated chlorine in hydrochloric acid solution. *Hydrometallurgy*, vol. 100. pp. 95–102.

Latkoczy, C. and Ghislain, T. 2006. Simultaneous LIBS and LA-ICP-MS analysis of industrial samples. *Journal of Atomic Spectrometry*, vol. 21. pp. 1152–1160.

Lee, B.Z, Oh, C.-S., and Lee, D.N. 1994. Ag-Pb system. *Journal of Alloys & Compounds*, vol. 215. pp. 293–301.

Luda, M.P. 2011. Recycling of printed circuit boards. *Integrated Waste Management*. vol. 2. Kumar, S. (ed.). Intech. pp. 286–298.

Martienssen, W. (ed). 2007. Landolt-Börnstein. Numerical Data and Functional Relationships in Science and Technology, Group IV: Physical Chemistry, Volume 19. *Thermodynamic properties of Inorganic Materials compiled by SGTE Subvolume B, Part 5: Binary Systems Supplement 1*. Springer. pp. 30, 33, 93.

McCurdy, E., Woods, G., and Scrimshire, P. 2005. Laser ablation (LA)-ICP-MS for production control of nickel alloys. Agilent Technologies, Santa Clara, CA. pp. 1–6.

Melcher, F., Guapner, T., Henjes-Kunst, T., Oberthür, T., Sitnikova, M., Gäbler, E., Gerdes, A., Bratz, H., Davis, D., and Dewaele, S. 2008. Analytical fingerprint of columbite-tantalite (coltan) mineralisation in pegmatites – Focus on Africa. *Proceedings of the Ninth International Congress for Applied Mineralogy*, Brisbane, QLD, 8–10 September 2008. Australasian Institute of Mining and Metallurgy, Melbourne.

Meredith, C., Tromp, M., Peterson, D., Dudgeon, J., Gevorkyan, A., and Meliksetian, K. 2011. New standards in the analysis of archaeological metalwork using LA-ICP-MS: A case study from the South Caucasus Archaeometallurgy Project. Poster presentation, *Annual Meeting of the Society for American Archaeology*, Sacramento.

Ogunniyi, I.O, Vermaak, M.K.G., and Groot. D.R. 2009. Chemical composition and liberation characterization of printed circuit board comminution fines for beneficiation investigations. *Waste Management*, vol. 29, no. 7. pp. 2140–2146.

Predel, B. 1991. Landolt-Börnstein. Numerical Data and Functional Relationships in Science and Technology, Group IV: Physical Chemistry, vol. 5a. *Phase Equilibria, Crystallographic and Thermodynamic Data of Binary Alloys* · Ac-Au – Au-Zr. Springer.

Szałatkiewicz, J. 2014. Metals content in printed circuit board waste. *Polish Journal of Environmental Studies*, vol. 23, no. 6. pp. 2365–2369.

Velasquez, G., Borisova, A.Y.,Baron, S., and Robbiola, L. 2018. In situ analysis of copper alloys by femtosecond laser ablation inductively coupled plasma mass spectrometry: Constrains on matrix effects. *American Journal of Analytical Chemistry*, vol. 9. pp. 150–161. ◆

Extending the protection range in protective seam mining under the influence of gas drainage

L. Wang[1,2], X. Chen[2], Z. Wang[2], S. Xu[3], and Q. Xu[2]

Affiliation:
[1]Key Laboratory of Gas and Fire Control for Coal Mines, China University of Mining & Technology, Ministry of Education, China.
[2]Henan Polytechnic University, China.
[3]Guizhou Qianxi Energy Development Limited Company, Bijie, China.

Correspondence to:
X. Chen

Email:
cxjhpu@163.com

Dates:
Received: 4 Jul. 2017
Revised: 12 Jun. 2019
Accepted: 5 Nov. 2019
Published: March 2020

How to cite:
Wang, L., Chen, X., Wang, Z., Xu, S., and Xu, Q.
Extending the protection range in protective seam mining under the influence of gas drainage.
The Southern African Insitute of Mining and Metallurgy

DOI ID:
http://dx.doi.org/10.17159/2411-9717/17/115/2020

Synopsis

Both theoretical and field research have shown that protective layer mining with pressure-relief gas extraction in protected coal seams is an effective and economical way of controlling coal and gas outbursts in underground mines. Given the influences of coal seam angles, layer spacing, pressure-relief angles, coal pillars, and other factors in the protected areas of protected seams, the protection range is often smaller than the area of protective seam mining. This problem can be solved by using a gas drainage method based on coal seam geology and the conditions of coalbed methane (CBM) occurrence during protective layer mining. If a protective layer is prone to outbursts, crossing boreholes and bedding boreholes can be used to eliminate outburst hazards. The crossing boreholes should control the upper side of the roadway contour for at least 20 m and the lower side for at least 10 m. For other coal seams, the boreholes should control both sides of the roadway contour for at least 15 m. Crossing boreholes can not only extract CBM from the protective layer but can also extract from the protected coal seam, thus leading to a larger protection range in the protective layer than that predicted by the pressure-relief boundary, as well as expanding the protection range. The actual protection range of the protected layer was determined using an index of residual gas content. The results of the study indicate that the pressure-relief angle increased from 56° to 69° in the strike direction and from 75° to 90° in the inclination direction. The protection range was approximately equal to the mining area of the working face of the protective layer, thereby extending the protection range. One of the important reasons for protection range expansion was the influence of gas drainage via crossing boreholes. The protection range extension mitigated the outburst danger over a large area of the coal seam, thus enabling high efficiency and safe exploitation.

Keywords
protective seam mining, range extension technology, pressure-relief gas extraction, protective range, gas pre-extraction.

Introduction

China possesses abundant coal resources, and coal accounts for at least 70% of China's energy, supporting the rapid growth of the national economy. In 2015, coal production reached 3.69 Gt. The demand for energy will continue to increase with the rapid development of China's economy, and coal is projected to account for 50% of primary energy consumption through 2050.

Due to the continued exploitation of long-standing seams, coal mining depths have reached an average of 540 m and increase at an annual rate of 10–15 m, with portions of mines reaching 800 m or more (Wang *et al.*, 2012, 2013). As mining depth has increased, conditions have become increasingly complicated. 'Four high problems and one low problem' exist in coal seams, namely, high stress, high gas pressure, high gas content, high ground temperature, and low coal seam permeability. These issues result in difficulty controlling gas. Therefore, gas control technology requires constant research and development (Zhou, Xie, and Zuo, 2005; Li *et al.*, 2009).

Both theoretical studies and field observations have shown that protective layer mining based on pressure-relief gas extraction in protected coal seams is an effective and economical way of controlling coal and gas outbursts in underground mines. During the mining of the protective layer, stress is decreased, fractures develop, and adsorbed gas is desorbed, thus increasing coal permeability a hundredfold. Additionally, when coupled with pressure-relief gas drainage, the gas content can be effectively reduced, thus eliminating outburst hazards in protected coal seams.

Protective layer mining technology was first used in 1933 to control coal and gas outbursts in France. Since 1958, protective layer mining has been conducted in China, including field tests in the Beipiao, Tianfu, Nantong, Zhongliangshan, Songzao, Xishan, Huajin, Tiefa, Huaibei, and Huainan mining areas. These tests have yielded remarkable results and have resulted in highly efficient and safe coal exploitation. The document 'The Regulations of Coal and Gas Outburst Prevention' (State Administration of Work Safety, 2009) notes that an inspection of the effect and scope of the protective layer should first be performed when mining a protective layer. The protection range, including the

protection range in the strike direction and strip direction, is the effective range in which the protective layer can be mined using pressure-relief gas extraction. Therefore, this range does not include dangerous outburst areas. The protection range is determined from the inspection results.

The protection range in the protective layer is determined from the gas content, gas drainage volume, the gas pressure, and the relative deformation of the coal seam roof and floor. Wang *et al.* (2014) and Hu, Wang, and Fang (2010) obtained protection ranges on the basis of gas flow theory. Tian, Sun, and Wei (2013) confirmed the protection range by comparing gas flow observations and gas contents. Wu *et al.* (2010) discussed a method of determining the effective pressure-relief range in protective layer mining and studied the factors that affect the scope of protection. Additionally, scholars have studied the permeability distribution, rock deformation, and stress distribution in protected layers.

The geological conditions of a coal seam significantly affect the protection range of a protective layer. Although the layout parameters of protection layers are the same, the protection range and the effect on eliminating outbursts are notably different because coal seam conditions and gas drainage methods are different in each mine. Currently, the regulations for preventing coal and gas outbursts (State Administration of Work Safety, 2009) that apply to the pressure-relief angle are conservative, and the protection border has space to be expanded. The protection range of protected coal seams can be reasonably determined and expanded by designating a wide range of coal seams for safe exploitation in order to significantly reduce outburst incidents in mines. Therefore, reasonable protection boundaries must be delineated in protection layer mining.

General situation in the Qinglong coal mine

The Qinglong mine is in Bijie, Guizhou Province, China (Figure 1). The mine includes multiple coalbed formations, and the main coal seam has exhibited an increased tendency undergo coal and gas outbursts.

The Qinglong coalfield stretches 9.0 km in the strike direction and 1.6–5.0 km in the strip direction, encompassing an area of 21.79 km^2. The mine began operation in 2007, with a designed annual capacity of 1.2 Mt. The main mineable coal seams used for economic production are the no. 16 and no. 18 seams, which have an average dip of 12°.

The gas contents of the two coal seams are greater than 20 m^3/t. The gas pressure and gas content of seam no. 16 are 1.73 MPa and 21.51 m^3/t, respectively, and for seam no. 18, 1.5 MPa and 24.40 m^3/t, respectively. Coal seams no. 16 and no. 18 are both prone to outbursts. Although seam no. 17 has exhibited no tendency for coal or gas outburst, this layer is only partially mineable. Considering its proximity to seams no. 16 and 18, mining seam no. 17 will first destroy seam no. 16. Thus, we selected seam no. 16 as a protective layer.

Gas extraction mode

Gas extraction mode in a protective coal seam

The implementation of a gas drainage mode with the crossing

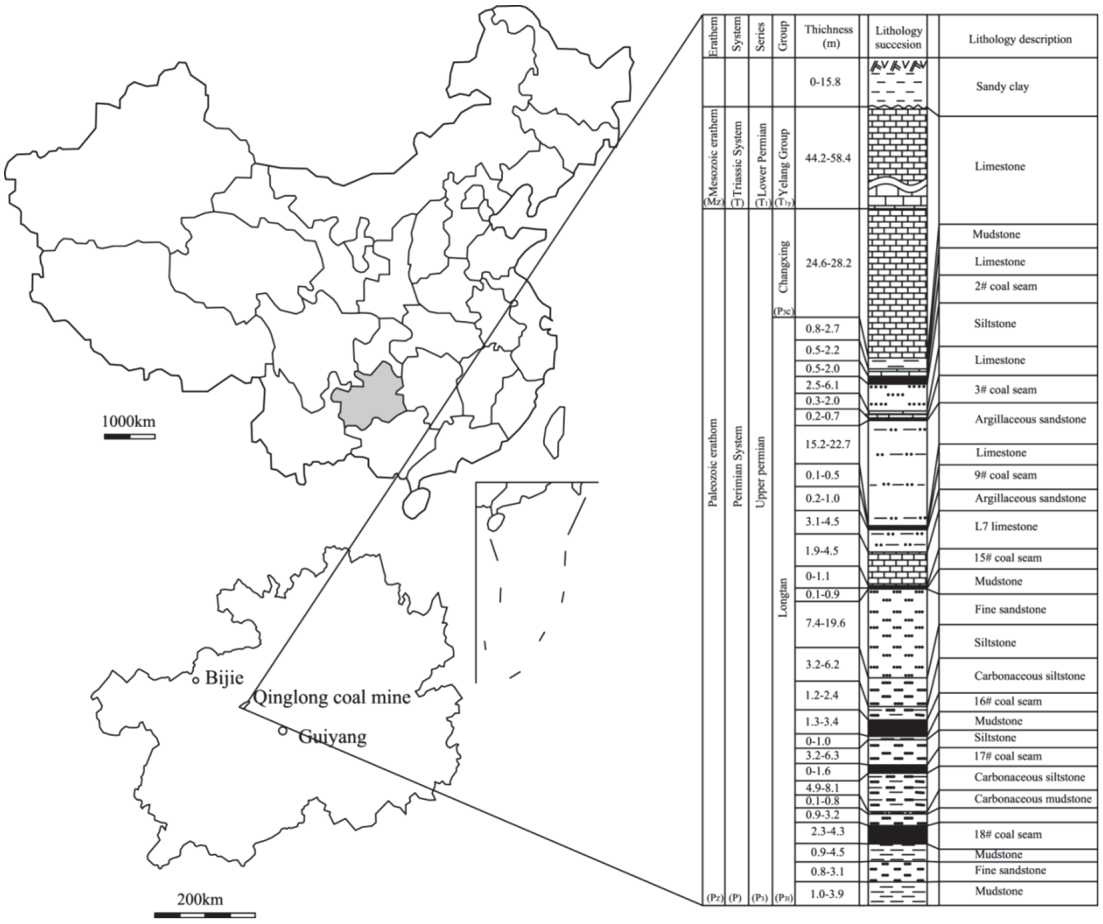

Figure 1—Location and stratigraphy of Qinglong coal mine

borehole extraction of coalbed methane (CBM) and the bedding borehole extraction of CBM comprised four steps. First, two rock floor roadways were constructed in the floor of the protected coal seam, corresponding to the protective layer roadway. The two roadways formed a negative pressure ventilation system (Figure 2).

Secondly, boreholes crossing the floor roadway were used to extract CBM from the roadway strip and eliminate outburst hazards. In the floor roadway, a drill site was excavated every 6 m with six crossing boreholes used to control both the roadway and a 15 m area outside the roadway contour line (Figure 2). The boreholes were 94 mm in diameter, and the distance between boreholes in the coal seams was 6 m. The negative pressure was greater than 25 kPa. The drainage time was longer than 10 months.

The transportation roadway and open cutting of the protective coal seam in the region eliminated the outburst hazards (Figure 3). During the third stage of implementation, a railway was constructed.

Finally, bedding boreholes within a certain distance were used to extract CBM from the workface to eliminate the outburst hazard in the protective seam. The boreholes were 108 mm in diameter, and the distance between boreholes in the coal seams was 3 m. The negative pressure was greater than 15 kPa. The drainage time was longer than six months.

A block diagram of the gas drainage pattern is shown in Figure 4.

Gas extraction mode in the protected coal seam

Mining the protective layer can relieve the stress in a protected coal seam, thereby increasing its permeability. We therefore performed pressure-relief gas extraction by using crossing boreholes (Figures 5 and 6). The boreholes were 108 mm in diameter, spaced 10 m apart. The negative pressure was greater than 25 kPa and the drainage time was longer than 10 months.

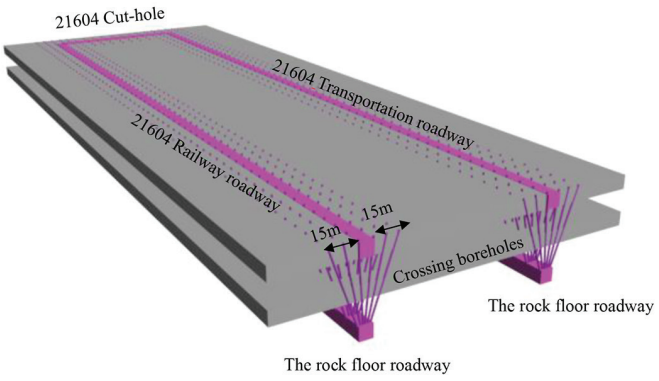

Figure 2—Diagram of the crossing borehole method used for gas pre-drainage in the roadway strip

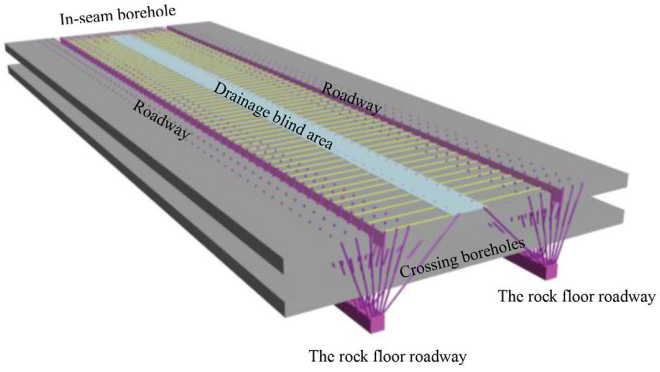

Figure 3—Diagram of the bedding borehole method used for gas pre-drainage in the workface

Numerical modelling

The inspection indexes used to determine the protection range include the gas pressure, gas content, and expansion deformation rate of the protected coal seam. The accuracy of these parameters is restricted by site conditions, and a full range of inspection cannot usually be achieved. Numerical simulation provides a method for determining the protection scope in protective layer mining. COMSOL Multiphysics software was used to simulate the protection range in protected layer mining to provide information for mines with similar mechanical parameters of coal and rock.

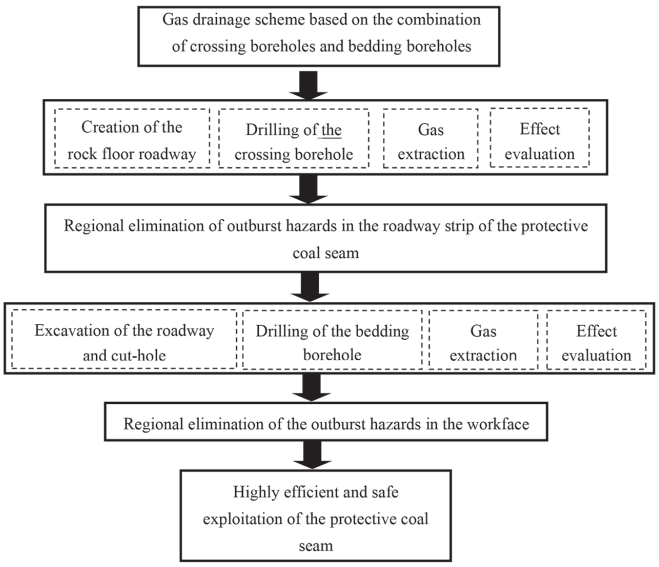

Figure 4—Block diagram of the gas drainage pattern

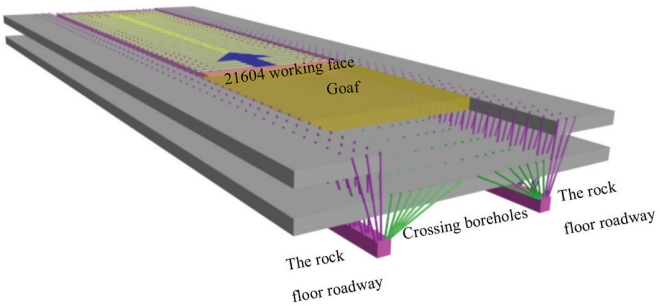

Figure 5—Sketch of pressure-relief gas extraction using crossing boreholes

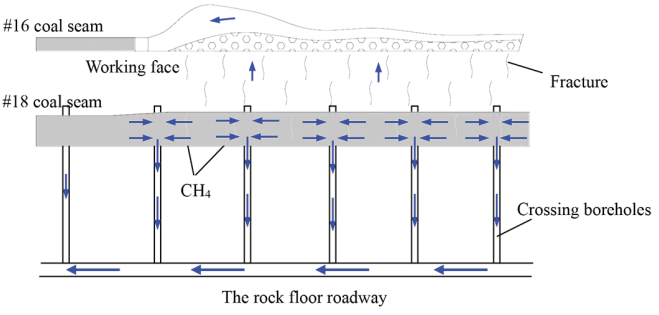

Figure 6—Schematic diagram of pressure-relief gas extraction and flow rules in the protected layer

Model creation

Creation of the geometric model

COMSOL Multiphysics software was used to simulate the stress and strain characteristics of the protected coal seam on the basis of data obtained during the mining of the working face of the no. 21604 protective layer. Thereafter, the protection range of protective layer mining was determined.

The model was built according to the geological conditions in the Qinglong coal mine. The length and width of the model were 260 and 120 m, respectively. The model is shown in the strike and strip directions in Figure 7.

Boundary constraints

The left, right, and bottom boundaries were established as fixed boundaries. A compressive stress of 1.9 MPa was imposed on the top of the model according to the model size and depth of the coal seam.

Yielding criteria

The expression of the Mohr-Coulomb (M-C) yielding criterion is:

$$F_{MC} = \sqrt{J_2}\left(\cos\theta_\sigma - \frac{\sin\theta_\sigma}{\sqrt{3}}\sin\phi\right) + \frac{1}{3}I_1 - c\cos\phi = 0 \quad [1]$$

where I_1 is first invariant of stress, J_2 is second invariant of deviator stress, and θ_σ is stress lode angle, $-\pi/6 \le \theta_\sigma \le \pi/6$.

The Drucker-Prager (D-P) yielding criterion is based on the Mises strength criterion, considering the equilibrium stress p or I_1, extending the Mises strength criterion in the following form:

$$F_{DP} = \alpha I_1 + \sqrt{J_2} - k = 0 \quad [2]$$

where α, k are the D-P criterion parameters.

$$\alpha = \frac{\sin\varphi}{\sqrt{3}\sqrt{3+\sin^2\varphi}} \quad [3]$$

$$k = \frac{3c\cos\varphi}{\sqrt{3}\sqrt{3+\sin^2\varphi}} \quad [4]$$

where c is cohesion and φ is the internal friction angle.

By transforming Equation [1], we obtain:

$$\frac{\sin\varphi}{3\left(\cos\theta_\sigma - \frac{1}{\sqrt{3}}\sin\theta_\sigma\sin\varphi\right)}I_1 + \sqrt{J_2} = \frac{c\cos\varphi}{\cos\theta_\sigma - \frac{1}{\sqrt{3}}\sin\theta_\sigma\sin\varphi} \quad [5]$$

If θ_σ is constant, comparison between Equations [2] and [5] shows that:

$$\alpha = \frac{\sin\varphi}{3\left(\cos\theta_\sigma - \frac{1}{\sqrt{3}}\sin\theta_\sigma\sin\varphi\right)} \quad [6]$$

$$k = \frac{c\cos\varphi}{\cos\theta_\sigma - \frac{1}{\sqrt{3}}\sin\theta_\sigma\sin\varphi} \quad [7]$$

Equations [6] and [7] are the unified expressions of the equivalent D-P transformation of the M-C criterion. They are related to θ_σ.

$$\theta_\sigma = a\tan\frac{2\sigma_2 - \sigma_1 - \sigma_3}{\sqrt{3}(\sigma_1 - \sigma_3)} \quad [8]$$

θ_σ can reflect the stress state of a point, that is, the proportional relationship between the main stress components.

Coal and rock mechanical parameters

The D–P failure criterion and matching M–Ccriteria were selected for the simulation. The initial properties of the rock mass are listed in Table I on the basis of the typical values in the Qinglong coal mine.

Protection range in the strike direction

Original stress state of the rock

Figure 8 shows the coal and rock stress pattern before working face no. 21604 was mined, *i.e.* influenced only by gravity.

Stress and deformation associated with 100 m of protective layer mining

Figure 9 shows the stress changes in the surrounding rock after working face no. 21604, the protective layer, was mined to

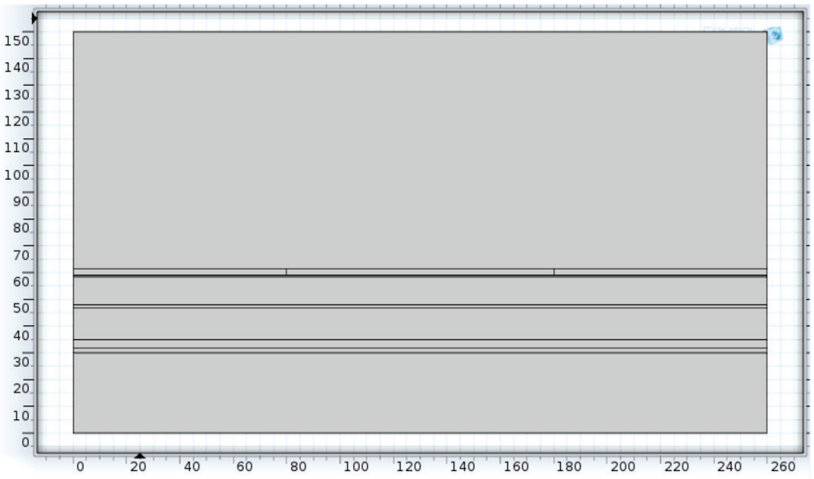

Figure 7—Model geometry in the strike and strip directions used in the numerical simulations

Table I

Mechanical parameters of coal and rock

Lithology	Density (kg/m³)	Friction angle (°)	Cohesion (MPa)	Tensile strength (MPa)	Bulk modulus (MPa)	Shear modulus (MPa)
Mudstone	2500	40	3	1.7	3333	1811
Limestone	2700	42	5	4.5	43 800	26 280
Siltstone	2700	40	4.2	2	8333	7895
Coal seam 16	1500	27	0.8	0.2	4167	1087
Mudstone	2500	40	3	0.7	3333	1811
Siltstone	2700	40	4.2	1.86	8333	7895
Fine sandstone	2800	36	9	3	12 821	8065
Coal seam 17	1500	27	0.8	0.2	4167	1087
Mudstone	3000	40	3	1.5	3333	1811
Fine sandstone	2800	36	9	3	12 821	8065
Siltstone	2500	40	4.2	2	8333	7895
Coal seam 18	1500	27	0.8	0.2	4167	1087
Sandy mudstone	2700	36	11.6	3	3804	2067

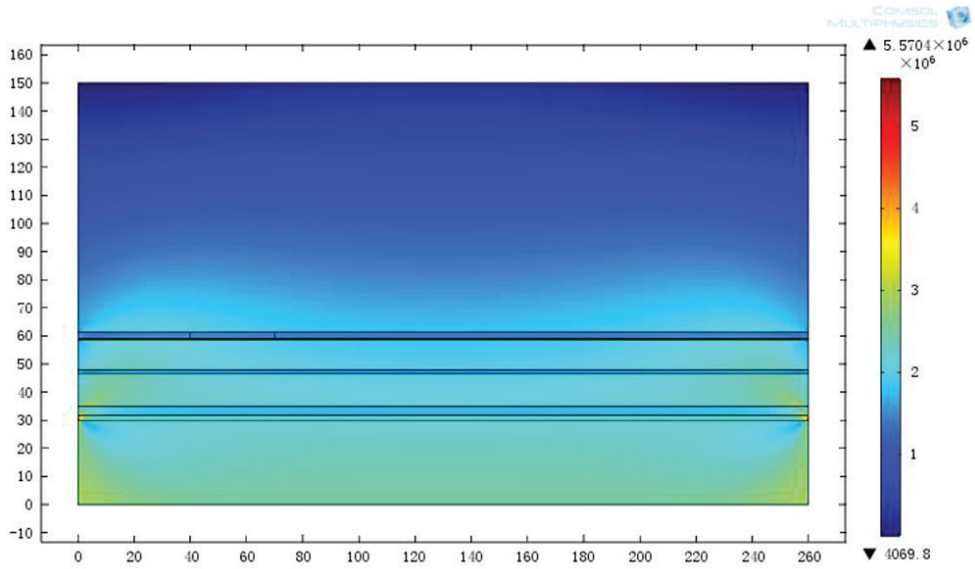

Figure 8—Original coal and rock stress pattern

100 m. The deformations in the roof and floor of the protected coal seam are shown in Figure 10.

Analysis of stress and deformation in the strike direction

As shown in Figures 9 and 10, stress concentrations appear at both ends of the goaf due to the mining of working face no. 21604. A stress concentration phenomenon also appears in the corresponding area of the protected coal seam, in which the roof and floor are both compressed and deformed. The roof compression/deformation in the protected layer is greater than the floor compression/deformation. Overall, the protected layer exhibits compressive deformation. Gas is more difficult to extract under this condition than in the initial state because of partial closure of fractures and a decreased permeability coefficient.

The coal and rock mass stress decreases in the upper and lower parts of the mining area. Additionally, a pressure-relief zone appears, and the roof stress in the protected layer decreases considerably. With continued mining of working face no. 21604, the stress decreases and eventually stabilizes. Correspondingly, expansion deformation occurs in the roof and floor. The roof expansion deformation in the protected layer is greater than the floor expansion deformation. Overall, the protected layer exhibits expansive deformation. Gas extraction in this state is easier than in the initial state because of the development of fractures and increased permeability.

Confirmation of the protection range

By using a protective layer mining length of 100 m as an example, we found that the maximum compression deformation in the protected layer was 9 mm, and the maximum relative compression deformation was 2.8‰. Additionally, the maximum swelling deformation was 18 mm, and the maximum relative expansion deformation was 5.6‰.

Combining these results with the protection criteria for seam deformation relief shows that if the relative expansive deformation in the protected layer is greater than 3‰, then the protective effect is satisfactory. Therefore, 3‰ was considered the critical value in the delineation of the protection scope. The relative expansion deformation reached 3‰ in 14 m of working face along the protected layer. Furthermore, the relative expansion deformation was greater than 3‰ along 14 m in the region. Combined with 24 m spacing between coal seams no. 16 and 18, the pressure-relief angle was approximately 60° in the strike direction.

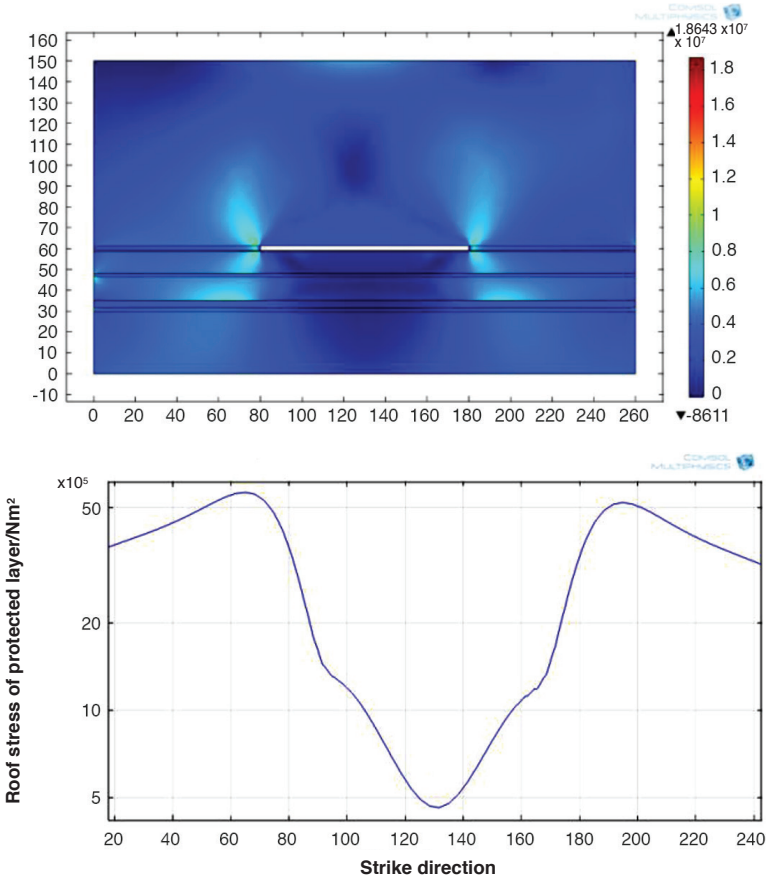

Figure 9—Goaf rock and protected seam roof and floor stress changes after 100 m of mining

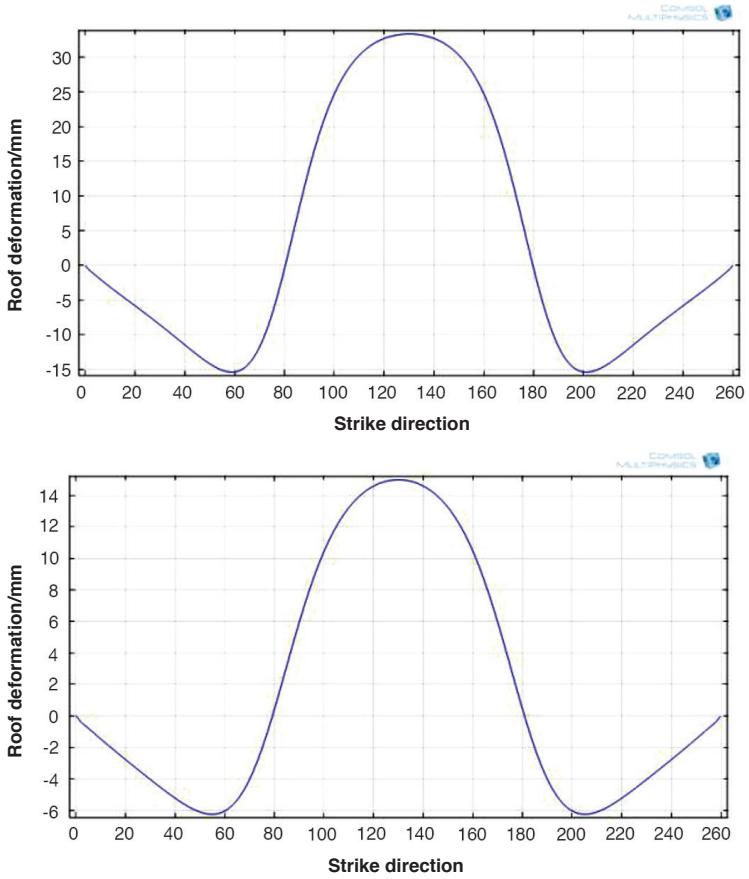

Figure 10—Deformation in the protected seam roof and floor after 100 m of mining

Protection range in the strip direction

Stress and deformation in the protected layer in the strip direction

The stress changes in the strip direction in the rock surrounding working face no. 21604 after mining began are shown in Figure 11. The roof and floor deformation in the protected coal seam are shown in Figure 12.

Confirmation of the protection range in the strip direction

Figure 12 illustrates that the maximum compression deformation in the protected layer was 15 mm. The maximum relative compression deformation was therefore 4.7‰. The maximum swelling deformation was 18 mm, and the maximum relative expansion deformation was 6.3‰.

Combining these results with the protection criteria for seam deformation relief shows that if the relative expansive

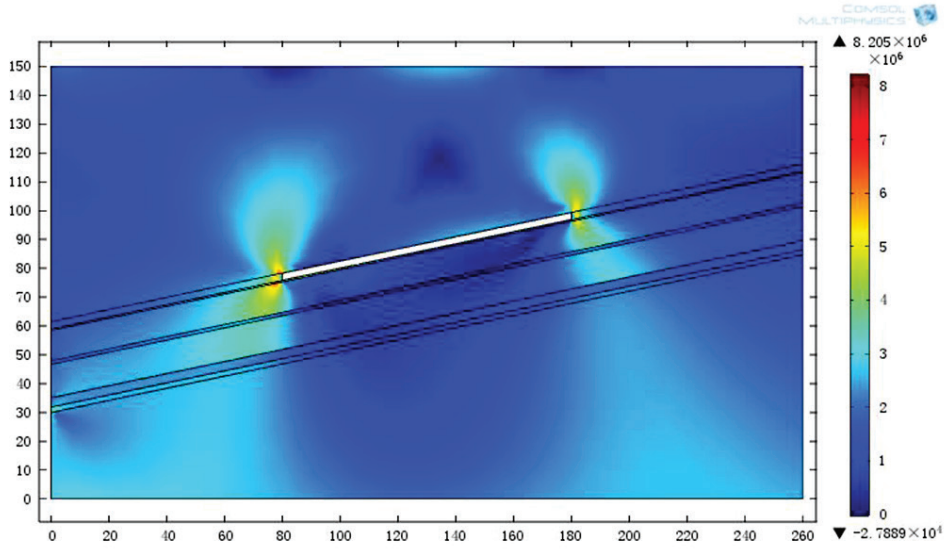

Figure 11—Stress changes in the strip direction goaf

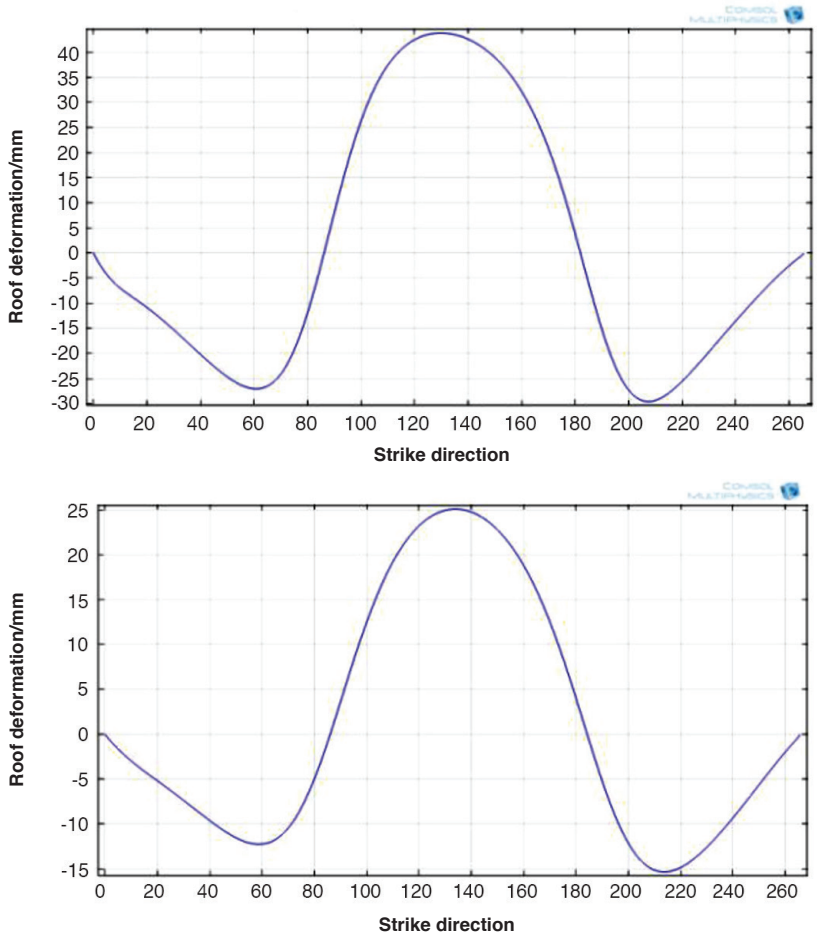

Figure 12—Roof and floor deformation in the protected seam

deformation in the protected layer is greater than 3‰, the protective effect is satisfactory. Therefore, 3‰ was considered the critical value in the delineation of the protection scope. The relative expansion deformation reached 3‰ along 13 m of the working face in the strip direction. Furthermore, the relative expansion deformation was greater than 3‰ along 13 m in the region in the strip direction. Combined with 24 m spacing between coal seams no. 16 and 18, the pressure-relief angle was approximately 62° in the strike direction.

Field measurements of protection scopes

Arrangement of drill-holes

If a protective layer is prone to outbursts, crossing boreholes and bedding boreholes can be used to eliminate outburst hazards. The crossing boreholes are used to extract CBM from the protective layer and protected coal seam. The yellow area in Figure 13 represents the area affected by gas extraction.

In designing the drilling locations and number of drill-holes, two boreholes were drilled in the area affected by gas extraction to determine whether the residual gas content was below 8 m³/t. Within the boundaries of the affected area, the unloading pressure was sufficient. Therefore, coupled with gas drainage, the residual gas content should have dropped below 8 m³/t. Two drill-holes were established to verify these expectations. Outside the affected area, the residual gas content may be high, therefore three drill-holes were established for further investigation.

The boreholes used to investigate the protection range were divided into six groups, each group consisting of seven holes, totalling 42 boreholes (Figures 13 and 14).

Analysis of the test results

The residual gas content test results are shown in Figure 15. The gas contents of boreholes no. 8 and 9 were 11.37 and 9.60 m³/t, respectively, which are both greater than 8 m³/t. However, the residual gas contents measured at the remaining points were less than 8 m³/t. By performing calculations that included a safety factor, the pressure-relief angle in the strike direction was determined to be 69° (Figure 16). The residual gas

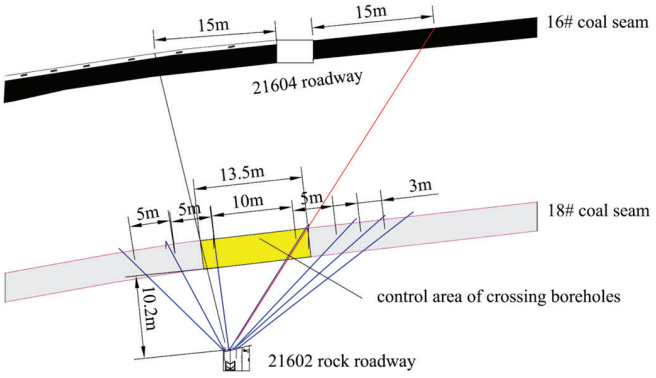

Figure 14—Profile of boreholes used to determine the protection range

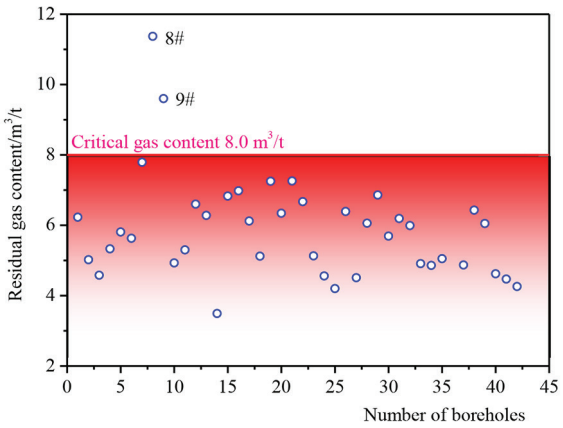

Figure 15—Test results of the residual gas content

contents in the drill-holes in the strip direction were less than 8 m³/t. Furthermore, calculations suggested that the pressure-relief angle was greater than 90°. For safety, we confirmed that the pressure-relief angle was 90°. The pressure-relief angle increased from 56° or 60° to 69° in the strike direction and from 75° or 62° to 90° in the strip direction; this finding illustrates the potential extension of the protection range.

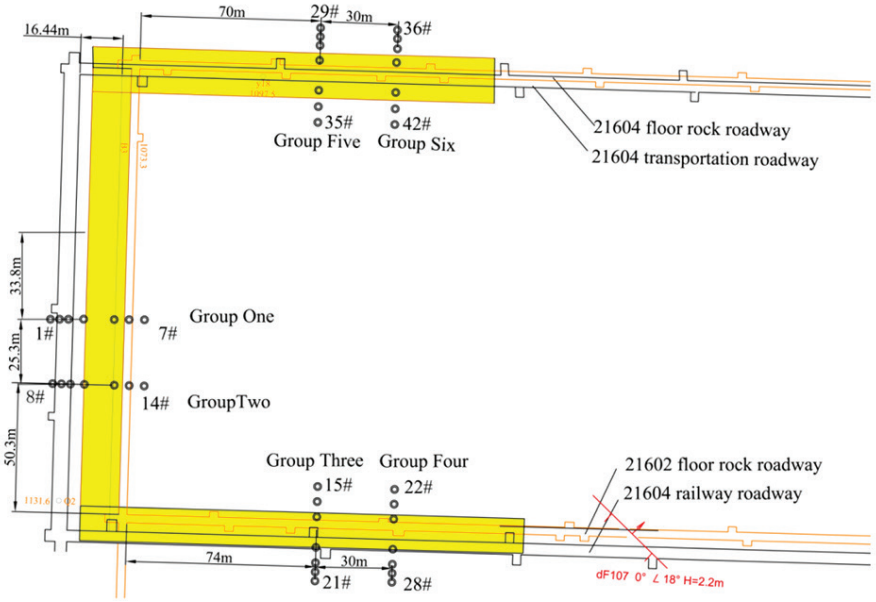

Figure 13—Layout of boreholes used to determine the protection range

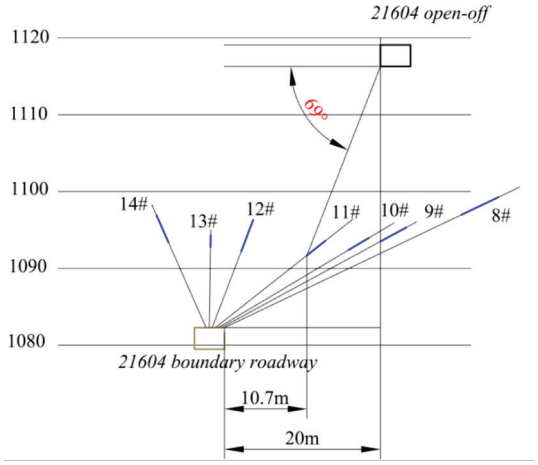

Figure 16—Profile of boreholes in the strike direction used to determine the protection range

Discussion

Table II shows the pressure-relief angles in the protection range based on the provisions of the prevention of coal and gas outbursts (China State Administration of Work Safety, 2019), the numerical simulation results, and the field measurements.

As shown in Table II, the pressure-relief angles in the strike and strip directions are 69° and 90°, respectively, which are greater than the angles noted in the outburst prevention regulations and those determined by numerical simulations. The protection range of the protective layer is approximately equal to the mining area of the working face of the protective layer; this result illustrates the potential extension of the protection range. One of the important reasons for the expansion observed in the protection range is the influence of gas drainage via crossing boreholes.

If a protective layer is prone to outbursts, crossing boreholes and bedding boreholes can eliminate outburst hazards. Crossing boreholes can extract CBM from the protective layer and protected coal seam.

China State Administration of Work Safety (2019) states that the outburst hazards in the roadway and within a certain range on both sides of the roadway must be eliminated before mining the roadway. The specific requirements are as follows. For inclined and steeply inclined coal seams, the borehole should control the upper and lower sides of the roadway contour for at least 20 and 10 m, respectively. For other coal seams, the borehole should control both sides of the roadway contour for at least 15 m. The dip angle of the coal seam in the Qinglong coal mine is 12°, thus suggesting that it belongs to the coal seam group with shallow inclines. According to the stated requirements, the pre-drainage boreholes control both sides of the roadway contour for at least 15 m, as shown in Figure 17.

As shown in Figure 17, the crossing boreholes extract CBM from the protective layer and the protected coal seam, thus leading to a larger protection range in the protective layer than that predicted by the pressure-relief boundary, as well as expanding the protection range. To obtain similar extensions of protection ranges in other working faces in the Qinglong coal mine or other coal mines, the boreholes should control the yellow area highlighted in Figure. 18.

Conclusions

Numerical simulations and field measurements were used to determine the actual protective range of the protected layer, with the goal of improving mining technology associated with the protective layer.

1. The stress and strain changes associated with 100 m of mining were simulated and analysed using COMSOL Multiphysics software. Given the exploitation of the working face of the protective layer, the protective layer covers a certain range. In this range, the stress in the protective layer decreases and the roof and floor expand. The combination of these results with the protection criteria for seam deformation relief shows that the pressure-relief angles in the strike and strip directions were 60° and 62°, respectively.

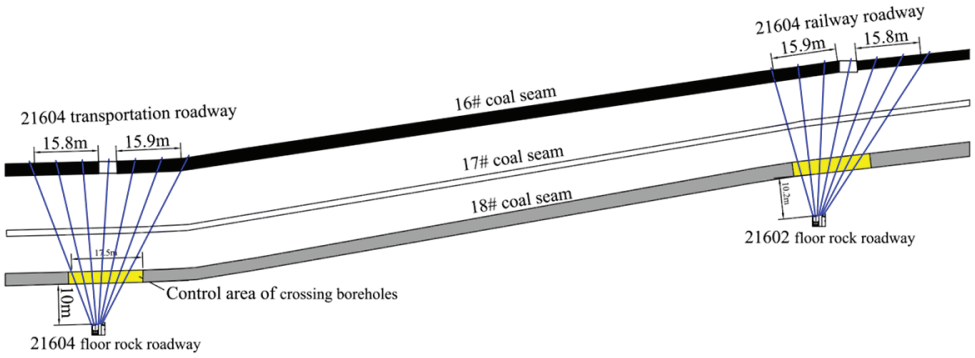

Figure 17—Profile of the crossing borehole method used for gas pre-drainage in a roadway strip

Table II

Comparison of pressure-relief angles

Inspection method	Strike direction	Strip direction	Remarks
Provisions of the Prevention of Coal and Gas Outburst	56°~60°	75°	(State Administration of Work Safety, 2009)
Numerical simulations	60°	62°	
Field measurements	69°	90°	

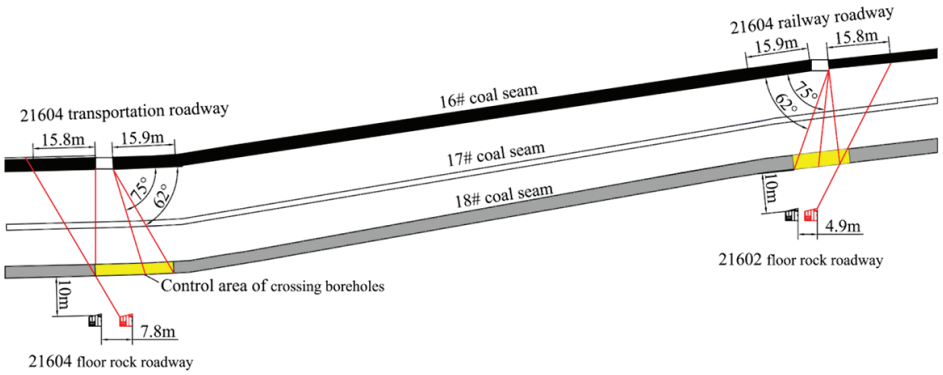

Figure 18—Area controlled by crossing boreholes

2. The actual protective range of the protected layer was determined on the basis of residual gas content. The pressure-relief angles in the strike and strip directions were 69° and 90°, respectively. The protection range was approximately equal to the mining area of the working face of the protective layer, thereby extending the protection range. One of the important reasons for protection range expansion was the influence of gas drainage via crossing boreholes.
3. Technology that is used for protection range expansion can be used in other working faces in the Qinglong coal mine or other coal mines by controlling the extension area with boreholes.

Acknowledgments

The authors are grateful for the financial support from the Natural Science Foundation for the Youth of China (No. 51404091), the China Postdoctoral Science Foundation (2014M561990) and the PhD Foundation of Henan Polytechnic University (B2015-08).

References

Chen, H.D., Cheng, Y.P., Ren, T.X., Zhou, H.X., and Liu, Q.Q. 20104. Permeability distribution characteristics of protected coal seams during unloading of the coal body. *International Journal of Rock Mechanics and Mining Sciences*, vol. 71. pp. 105–116.

Cheng, Y.P. and Yu, Q.X. 2003. Application of safe and high-efficient exploitation system of coal and gas in coal seams. *Journal of China University of Mining Technology*, vol. 32. pp. 471–476.

China State Administration of Work Safety. 2019. Detailed Rules for Prevention and Control of Coal and Gas Outburst. China Coal Industry Press, Beijing, China.

Díaz Aguado, M.B. and González Nicieza, C. 2007. Control and prevention of gas outbursts in coal mines, Riosa-Olloniego coalfield, Spain. *International Journal of Coal Geology*, vol. 69. pp. 253–266.

Hu, G.Z., Wang, H.T., and Fang, X.G. 2010. The law of methane gas leak flow in adjacent layer and its relief-pressure protection region. *Journal of China Coal Society*, vol. 35, no. 10. pp. 654–1659 [in Chinese].

Li, D.Q. 2014. Underground hydraulic mining of thin sub-layer as protective coal seam in coal mines. *International Journal of Rock Mechanics and Mining Sciences*, vol. 67. pp. 145–154.

Li, M., Zhang, X.P., Mao, S.J., and Liu, Q.S. 2009. Study on deep mining safety control decision making system. *Procedia Earth and Planetary Science*, vol. 1. pp. 377–383.

Liu, H.B., Cheng, Y.P., Song, J.C., Shang, Z.J., and Wang, L. 2009. Pressure relief, gas drainage and deformation effects on an overlying coal seam induced by drilling an extra-thin protective coal seam. *Mining Science and Technology*, vol. 19. pp. 724–729.

Liu, Y.K., Zhou, F.B., Liu, Y., Liu, C., and Hu, S.Y. 2011. Experimental and numerical investigation on the deformation of overlying coal seams above double-seam extraction for controlling coal mine methane emissions. *International Journal of Coal Geology*, vol. 87. pp. 139–149.

Noack, K. 1998. Control of gas emissions in underground coal mines. *International Journal of Coal Geology*, vol. 35. pp. 57–82.

State Administration of Work Safety. 2009. The Regulations of Coal and Gas Outburst Prevention. Coal Industry Press, Beijing.

Tian, K.Y., Sun, W.B., and Wei, E.J. 2013. Determination of protection range for mining upper protective layers and its numerical simulation. *Journal of Liaoning Technical University* (*Natural Science*), vol. 32, no. 1. pp. 7–13.

Wang, H.T., Huang, H.L., Yuan, Z.G., Shu, C., and Hu, G.Z. 2014. Model of gas leak flow coupled solid and gas for exploiting of steep-inclined upper-protective layer and its protection scope. *Rock and Soil Mechanics*, vol. 35, no. 5. pp. 1377–1383 [in Chinese].

Wang, L., Cheng, Y.P., Ge, C.G., Chen, J.X., Li, W., Zhou, H.X., and Wang, H.F. 2013. Safety technologies for the excavation of coal and gas outburst-prone coal seams in deep shafts. *International Journal of Rock Mechanics and Mining Sciences*, vol. 57. pp. 24–33.

Wang, L., Cheng, Y.P., Wang, L., Guo, P.K., and Li, W. 2012. Safety line method for the prediction of deep coal-seam gas pressure and its application in coal mines. *Safety Science*, vol. 50. pp. 523–529.

Wu, J., Sang, S.X., Fang, L.C., Huang, H.Z., Wu, D.G., and Yang, X.C. 2010. Protective seam mining released range and the site deployment of the released methane draining surface well in Huainan mine area. *Coal Geology & Exploration*, vol. 38, no. 3. pp. 10–14 [in Chinese].

Yang, W., Lin, B.Q., Qu, Y.A., Zhao, S., Zhai, C., Jia, L.L., and Zhao, W.Q. 2011a. Mechanism of strata deformation under protective seam and its application for relieved methane control. *International Journal of Coal Geology*, vol. 85. pp. 300–306.

Yang, W., Lin, B.Q., Qu, Y.A., Zhao, S., Zhai, C., Jia, L.L., and Zhao, W.Q. 2011b. Stress evolution with time and space during mining of a coal seam. *International Journal of Rock Mechanics and Mining Sciences*, vol. 48. pp. 1145–1152.

Yuan, L. and Xue, S. 2014. Defining outburst-free zones in protective mining with seam gas content-method and application. *Journal of China Coal Society*, vol. 39, no. 9. pp. 1786-1791 [in Chinese].

Zhou, H.W., Xie, H.P., and Zuo, J.P. 2005. Developments in researches on mechanical behaviors of rocks under the condition of high ground pressure in the depths. *Advances in Mechanics*, vol. 35, no. 1. pp. 91–99 [in Chinese]. ◆

Adaptive simultaneous stochastic optimization of a gold mining complex: A case study

Z. Levinson[1] and R. Dimitrakopoulos[1]

Affiliation:
[1]COSMO – Stochastic Mine Planning Laboratory, Department of Mining and Materials Engineering, McGill University, Montreal, Quebec, Canada.

Correspondence to:
Z. Levinson

Email:
zachary.levinson@mail.mcgill.ca

Dates:
Received: 15 Jul. 2019
Revised: 24 Nov. 2019
Accepted: 5 Dec. 2019
Published: March 2020

How to cite:
Levinson, Z. and Dimitrakopolous, R.
Adaptive simultaneous stochastic optimization of a gold mining complex: A case study.
The Southern African Insitute of Mining and Metallurgy

DOI ID:
http://dx.doi.org/10.17159/2411-9717/829/2020

ORCiD ID:
Z. Levinson
https://orcid.org/0000-0003-0489-1624

R. Dimitrakopolous
https://orcid.org/0000-0001-7329-2209

Synopsis

An innovative strategic mine planning approach was applied to a multi-mine and multi-process gold mining complex that simultaneously considers feasible capital investment alternatives and capacity management decisions. The simultaneous stochastic optimization framework determines the extraction sequence, stockpiling, processing stream, blending, waste management, and capital investment decisions in a single mathematical model. A production schedule branches and adapts to uncertainty based on the likelihood of purchasing a number of feasible investment alternatives that may improve mill throughput or blending, or increase the tailings capacity. Additionally, the mining rate is determined simultaneously by selecting the number of trucks and shovels required to maximize the value of the operation. The mining complex contains several sources – two open-pit gold mines and externally sourced ore – stockpiles, waste dumps, tailings, and three different processing streams. The simultaneous optimization framework integrates the blending of sulphates, carbonates, and organic carbon at the autoclave for refractory ore while managing acid consumption. The production schedule generated branches over an investment in the autoclave expansion; the first branch undertakes a capacity expansion at the autoclave resulting in a 6.4% increase in NPV, whereas the second branch results in a 27.5% increase in NPV without the investment. The adaptive approach is compared to a base case production schedule generated using a non-branching two-stage stochastic integer program.

Keywords
mining complex, simultaneous stochastic optimization, capital investments.

Introduction

Mining operations are capital-intensive ventures that require smart decisions to strategically time each investment and sustainably produce valuable products. The simultaneous stochastic optimization approach generates an optimal production schedule for a mining complex, using a single mathematical formulation (Del Castillo and Dimitrakopoulos, 2019; Montiel and Dimitrakopoulos, 2015, 2017, 2018; Goodfellow and Dimitrakopoulos, 2016, 2017). The optimized production schedule defines the extraction sequence, stockpiling, processing stream, blending, waste management, and capital investment decisions that maximize the net present value (NPV). These decisions are obtained by considering the interactions throughout the entire mining complex, which may consist of open pit and underground mines, several processing facilities, crushers, stockpiles, and waste destinations (Pimentel, Mateus, and Almeida, 2010). The stochastic approach also manages technical risk during the optimization by integrating a set of stochastic geostatistical simulations of the *in-situ* material supply, which reproduces the uncertainty and local variability of the material sourced from the mines. Selecting the appropriate time to undertake a capital investment during the life of mine is challenging due to a combination of supply uncertainty, high upfront costs, and prolonged payback periods for each investment. Nevertheless, investments in shovels, trucks, crushers, process plant upgrades, and waste facilities are critical for maximizing the NPV of the long-term production schedule.

The uncertain aspects of mine planning and forecasting, which arise from supply uncertainty, indicate there is large risk in undertaking capital investments (Ajaka, Lilford, and Topal 2018; Asad and Dimitrakopoulos, 2013; Del Castillo and Dimitrakopoulos, 2014; Dowd, 1994; Githiria and Musingwini, 2019; Khan and Asad, 2019; Groeneveld and Topal, 2011; Dimitrakopoulos, 2018; Groeneveld, Topal, and Leenders, 2012; Mai *et al.* 2018; Ravenscroft, 1992). In particular, supply uncertainty makes it challenging to produce an optimized production schedule with an investment plan that will satisfy the various futures that may unfold. The optimal investment decision for one future outcome may be very

different from another scenario. This gives rise to an interest in developing strategic mine plans that can adapt to uncertainty by considering feasible investment alternatives that directly impact the production rate of certain components in the mining complex and manage technical risk.

Del Castillo and Dimitrakopoulos (2019) present an adaptive simultaneous stochastic optimization approach that considers a number of feasible investment alternatives and determines the optimal time to branch the production schedule in order to manage the potential risk of supply uncertainty. A set of orebody simulations is generated for each mine to quantify supply uncertainty. Then, an adaptive approach considers the probability of undertaking an investment in different groups of scenarios. If the decision is counterbalancing, where a representative group of simulations takes on an investment and another representative group does not, the production schedule splits or branches into alternative mine plans based on these investments. Each of these branching alternatives is fully optimized based on the investment that is undertaken; however, decisions made prior to the investment cannot be changed once branching occurs. This prevents the optimization model from anticipating the investment decisions and changing the decisions that were made prior to choosing to invest, as the future investment choices remain uncertain until they are executed.

The adaptive optimization approach integrates non-anticipativity constraints into the optimization formulation. The non-anticipativity constraints ensure that the same decisions are taken unless there is an investment alternative that branches the mine production schedule. If branching occurs, the resulting mine plan of each branch should be distinguishably different based on the investment choice. Otherwise, the non-anticipativity constraints are enforced and the same decision is taken over all the simulated scenarios. The single production schedule generated with feasible investment alternatives provides an advanced method for determining the optimal time to invest and identifies the risk of investing in new equipment, plant improvements, and other infrastructure purchases (Dixit and Pindyck, 1994). Evaluating feasible alternatives and the resulting mine plan creates opportunities to delay, pre-plan, or undertake sizeable capital investments (De Neufville and Scholtes, 2011).

Boland, Dumitrescu, and Froyland (2008) also incorporate non-anticipativity constraints in a multistage optimization framework; however, this approach differs from the adaptive approach described above by Del Castillo and Dimitrakopoulos (2019). In the approach described by Boland and Dimitrakopoulos (2009), the simulated orebody scenarios are differentiated based on the spatial distribution of metal grades, which results in overfitting the production schedule to generate one mine plan per simulated orebody scenario. This method does not lead to an optimal production schedule, given that a single scenario does not represent the uncertainty and local grade variability of the deposit, thus resulting in erroneous production and financial forecasts that misrepresent reality. In contrast, in the case study presented herein, the adaptive approach leverages the ability to branch over several capital investments instead of each block's simulated grades, leading to a practical production schedule with feasible investment alternatives.

Similar multistage frameworks have been applied to strategically time the purchase of capital investments and expand the production capacity in other industries (Ahmed, King, and Parija, 2003; Gupta and Grossmann, 2017; Li *et al.*, 2008; Singh, Philpott, and Wood, 2009). These frameworks remain impractical for mine planning and design purposes as multistage frameworks lead to a production schedule with one plan per scenario, which misrepresents the ability to change capacities and is the major limitation of multistage approaches. Furthermore, when considering the execution of the long-term production schedule, operations cannot proceed without fixed guidance for the current year of production. Groeneveld, Topal, and Leenders (2012) suggest fixing the initial years of the mine production schedule to address this limitation, ensuring that operations have the appropriate production guidance and lead time to consider different mining and plant options for the future.

The adaptive simultaneous stochastic optimization approach manages technical risk and delivers a mine production schedule that can identify synergies between different components of the mining complex. For example, in a Nevada-type gold mining complex, the metal recovery from refractory ore is influenced by the sulphate and carbonate contents in the material that is delivered to an autoclave processing facility (Montiel and Dimitrakopoulos, 2018; Thomas and Pearson, 2016). Blending the material from several sources in the mining complex to maximize recovery may lead to a higher NPV over the operating life and capture value that is unidentifiable using traditional sequential optimization methods (Gershon, 1983; Hustrulid and Kutcha, 2006; Whittle, 1999). Additionally, waste management considerations such as the production of acid-generating waste and tailings can be integrated into the optimization to minimize detrimental environmental consequences and ensure permitting constraints are satisfied (Levinson and Dimitrakopoulos, 2019; Saliba and Dimitrakopoulos, 2018). These advances are achieved by maximizing the value of the products sold (Goodfellow and Dimitrakopoulos, 2017; Montiel and Dimitrakopoulos, 2015), instead of the traditional approach that considers the economic value of a block determined *a priori* and sequentially optimizes the extraction sequence, cut-off grade and transportation of materials downstream (Hustrulid and Kutcha, 2006).

Furthermore, the proceeding case study strategically determines the optimal production rate during the mine production scheduling process using an adaptive simultaneous stochastic optimization. Several frameworks directly integrate investments into the optimization to achieve a certain level of production and increase the value of the operation (Goodfellow, 2014; Groeneveld and Topal, 2011; Groeneveld, Topal, and Leenders, 2012). These integrative frameworks allows the optimizer to decide the most suitable time to invest in capital investment, overcoming limitations of defining the optimal mining and processing rates prior to optimizing the production schedule (Del Castillo and Dimitrakopoulos, 2014; Godoy and Dimitrakopoulos, 2004).

This work presents a major case study of a multi-mine and multi-process gold mining complex, where an adaptive simultaneous stochastic optimization approach strategically considers investment alternatives. The main contribution of this study is the ability to simultaneously consider investments in process plant upgrades and the tailings management area, while allowing the model to adapt to uncertainty based on the corresponding investment decisions. In the following sections, the adaptive simultaneous stochastic optimization approach is outlined, followed by a comprehensive case study at a gold mining complex containing two open-pit mines, twelve material types, twelve stockpiles, three external sources (including an

underground mine), and three processing stream alternatives. Subsequently, the conclusions and recommendations for future work are presented.

Method

This section summarizes the method used for the adaptive simultaneous stochastic optimization approach proposed by Del Castillo and Dimitrakopoulos (2019), which allows the production schedule to branch on a set of feasible investment alternatives. All sets, parameters, and decision variables are defined in the following subsections and can be reviewed in Appendix A.

Definitions and notation

A mining complex is designed to include a set of open pit and underground mines (M), stockpiles (S), processors (P), and waste facilities (W) (Goodfellow and Dimitrakopoulos, 2016, 2017; Montiel and Dimitrakopoulos, 2015, 2017, 2018). There can be many material types that are either extracted from the mine or generated through blending and processing. Each material has a set of attributes which can be transferred through the mining complex (*i.e.* mass, metal content, *etc.*). Attributes are further divided into two sub-categories; primary attributes that define the composition of the material passed between various locations in the mining complex, and hereditary attributes which are a derived through linear and nonlinear expressions. Hereditary attributes track important information in the model, including the costs incurred at different locations, revenues from the various processing streams, and metal grade. Two variables $v_{p,i,t,s}$ and $v_{h,i,t,s}$, quantify the value of primary ($p \in$ P) and hereditary ($h \in$ H) attributes at each location $i \in M \cup S \cup P \cup W$ in period $t \in$ T under scenario $s \in$ S, respectively. Hereditary attributes allow both nonlinear and linear functions to be incorporated into the model and are a function of the primary attributes, $f_h(p,i,k)$ for each primary attribute $p \in$ P at location $i \in M \cup S \cup P \cup W$ and considering each available capital investment $k \in$ K. The primary source of material for the mining complex is obtained by extracting a set of mining blocks $b \in B_m$ from mine $m \in$ M. Every block b has a set of simulated primary attributes $\beta_{p,b,s}$ (Goovaerts, 1997; Boucher and Dimitrakopoulos, 2009) which are inputs into the optimization model. The recovery of each attribute p at location i $\in$ P in each scenario s is defined as $r_{p,i,t,s}$ and is calculated using a nonlinear recovery function (Del Castillo, 2018; Farmer, 2016; Goodfellow, 2014).

Decision variables

Considering a life-of-mine of T time periods, the adaptive simultaneous stochastic optimization approach aims to maximize the NPV of a mining complex and minimize deviations from the annual production targets. This is accomplished by simultaneously determining the optimal decisions for four decision variables: (i) the mining block extraction sequence, (ii) destination policy, (iii) processing stream, and (iv) capital investment decisions. The method uses a set of binary decision variables $x_{b,t,s}$ that denote whether a block b is extracted in period t, in simulation s. The destination policy is then defined by discretizing the range of metal grades into a set of bins to determine the cut-off grade policy during the optimization process (Menabde *et al.*, 2007). Bins or groups $g \in$ G are defined using k-means++ clustering algorithm for the primary block attributes $\beta_{p,b,s}$ $\forall p' \subseteq$ P, b $\in B_m$, $m \in$ M, $s \in$ S of each material type (Goodfellow and Dimitrakopoulos, 2016). The destination policy decision variable $z_{g,j,t,s} \in \{0,1\}$ determines if the blocks in group g are sent to destination $j \in O(g)$ in period t, where $O(g)$ is the set of locations where the group of materials can be delivered in scenario s. After the material reaches the first set of destinations, based on the extraction sequence decisions, the downstream material flow is controlled by the processing stream decision variables $y_{i,j,t,s} \in [0,1]$. The processing stream variable defines the portion of product that is sent from destination $i \in S \cup P$ to destination $j \in O(i) \subseteq S \cup P$ in period $t \in$ T and scenario $s \in$ S. Lastly, the capital investment decision variable $\omega_{k,s,t}$ defines whether a capital investment $k \in K$ is executed in period $t \in$ T and scenario $s \in$ S. This is explained more fully in the following section.

Branching the production schedule

Two different sets are used to describe the different types of investments: branching (K^*) and non-branching (K^-), where $K^* \cup K^- =$ K. Branching alternatives are large capital investment decisions that are made only once during the life of the mining complex, for example, purchasing large crushers or constructing a new tailings facility. The non-branching investments may occur multiple times over the planning horizon, for instance truck and shovel purchases. The decision tree outlines the optimal timing of the branching investments and a new node n is created for each branching decision; this is defined as a stage. An optimized mine plan is produced for each branch that is created. The representative measure $R \in (0,0.5)$ is a user-defined parameter, which is used to describe the confidence interval for branching. R defines the probability threshold required to invest over all scenarios, branch the production schedule, or not invest in each capital investment (Equation [1]).

$$\begin{cases} \text{if the probability of investing in } k^* < R \;\rightarrow\; \text{do not invest in } k^* \text{ during } t^\omega \\ \text{if probability of investing in } k^* \in [R, 1-R] \;\rightarrow\; \text{branch during } t^\omega \\ \text{if the probability of investing in } k^* > 1-R \;\rightarrow\; \text{invest in } k^* \text{ during } t^\omega \end{cases} \quad [1]$$

The branching mechanism is described in the subsequent steps:

- Calculate the probability of investing in all alternatives $k^* \in K^*$ in each time period t.
- If there are a representative number of scenarios that choose to purchase the investment alternative, within an allotted time window, the solution branches and a new stage is created. However, if the probability of investing is less than the threshold then the optimization will not branch, and the investment is not purchased. On the contrary, if the probability is greater than (1–R) there is no branching and the investment is made over all scenarios. This is mathematically described in Equation [1].
- Given there are $S_n \subseteq$ S scenarios that belong to the root, these scenarios are partitioned into S_{n1} and S_{n2} when branching occurs. Therefore, when combined all the simulations from each branch are at the root ($S_{n1} \cup S_{n2} = S_n$), and when the simulations are partitioned each simulation can only report to one of the two partitions ($S_{n1} \cap S_{n2} = \varnothing$).

A time window, $\tau_\omega = \{t - \omega, t + \omega\}$, is used to stabilize the solution as often there may be a representative number of scenarios between one or two consecutive periods, making it more desirable to invest in one of those two years rather than completely ignore the investment opportunity. ω is set as an integer value that allows the model to expand the time window

of the branching mechanism. The branching or new stage will begin during the floor of the expected time period of investment k^* and is denoted as t^*. Lastly, N defines the minimum number of scenarios in a branch required to allow for further branching in periods $t + 1 \in T$.

Capital investments

Capital investments are critical decisions that require a lead time (τ_k) to assemble or construct. For each investment alternative $k \in K$ there is a life expectancy (λ_k) and a unitary increase in capacity ($\kappa_{k,h}$) that comes at a discounted purchase cost ($p^K_{k,t}$) for each period $t \in T$. The periodicity (ψ_k) of the investment decisions is also incorporated into the optimization model to simplify the optimization process and ensure a practical plan. The number of investments undertaken is denoted by $\sigma_{k,t,s}$ for each investment $k \in K$ in period $t \in T$ and scenario $s \in S$.

Objective function and constraints

$$\max \frac{1}{\|\mathbb{S}\|} \sum_{s \in \mathbb{S}} \sum_{t \in \mathbb{T}} \left\{ \underbrace{\sum_{i \in \mathcal{M} \cup \mathcal{S} \cup \mathcal{P} \cup \mathcal{W}} \sum_{h \in H} p_{h,t} v_{h,i,t,s}}_{\substack{\text{Profit of the mining complex} \\ \textbf{Part I}}} - \underbrace{\sum_{k \in K^=} p_{k,t} \sigma_{k,t,s}}_{\substack{\text{Cost of Truck and Shovel Investments} \\ \textbf{Part II}}} \right. \quad [2]$$

$$\left. - \underbrace{\sum_{k \in K^*} p^{K^*}_{k^*,t} \sigma_{k^*,t,s}}_{\substack{\text{Cost of One Time Capital Investments} \\ \textbf{Part III}}} - \underbrace{\sum_{i \in \mathcal{M} \cup \mathcal{S} \cup \mathcal{P} \cup \mathcal{W}} \sum_{h \in H} (c^+_{h,t} d^+_{h,i,t,s} + c^-_{h,t} d^-_{h,i,t,s})}_{\substack{\text{Penalties for Deviations} \\ \textbf{Part IV}}} \right\}$$

The objective function (Equation [2]) maximizes the expected profit obtained by summing the revenues generated from the metal produced and subtracting the various costs, for example, transportation, mining, processing, and refining costs (Part I). In addition, the objective aims to minimize the costs of investing in trucks and shovels (Part II), and one-time capital investments (Part III). Part IV minimizes the deviation from production targets, actively managing uncertainty. The adaptive optimization approach will purchase investments only when they lead to an increase in overall profitability and/or improve the capability to meet production targets in the mining complex.

Integrating the feasible investment alternatives into the optimization model changes the standard formulation of capacity constraints, from static upper ($U_{h,i,t}$) and lower ($L_{h,i,t}$) bounds in Equations [3] and [4], respectively, to dynamically changing capacities that are determined during the optimization. The capacities reflect changes in the corresponding investment decisions $\omega_{k,s,t}$. $\kappa_{k,h}$ represents the unitary increase in production capacity:

$$v_{h,i,t,s} - d^+_{h,i,t,s} \leq U_{h,i,t} + \sum_{k \in K;\ t > \tau_k} \sum_{t'=t-\lambda_k-\tau_k}^{t-\tau_k} \kappa_{k,h} \cdot \omega_{k,s,t'} \quad [3]$$

$$v_{h,i,t,s} - d^-_{h,i,t,s} \leq L_{h,i,t} + \sum_{k \in K;\ t > \tau_k} \sum_{t'=t-\lambda_k-\tau_k}^{t-\tau_k} \kappa_{k,h} \cdot \omega_{k,s,t'} \quad [4]$$

$$\forall\, h \in H, i \in \mathcal{M} \cup \mathcal{S} \cup \mathcal{P} \cup \mathcal{W}, t \in \mathbb{T}, s \in \mathbb{S}, k \in K$$

$$d^+_{h,i,t,s}, d^-_{h,i,t,s} \geq 0 \quad [5]$$

When investments are activated the capacity expansions and contractions can be explored, allowing for changes to the extraction rate, processing capacity, and storage of waste materials.

In addition, non-anticipativity constraints (Equations. [7], [8], and [9]) ensure that all scenarios within the same branch undertake the same decisions. The problem is initialized with the solution from a two-stage stochastic integer program and then non-anticaptivity constraints are enforced for the first period. Subsequently, the mechanism for branching iteratively solves a series of sub-problems to determine the optimal period to invest. The non-anticipativity constraints are then dynamically enforced over an iteratively increasing time frame T^α when a branching investment is undertaken. For example, once the first branching period is established non-anticipativity constraints become active for all periods up to t^*, the period in which a branching investment is undertaken. This ensures that the optimization framework will not change earlier decisions in anticipation of the investments made in future periods. A binary variable $u^n_{k^*,t}$ equals unity when the design branches over option $k^* \in K^*$ in node n in period $t \in T$ and zero otherwise. Therefore, the variable A determines whether the non-anticipativity constraints are activated (0) or not (1) for a given partition of scenarios in a single branch:

$$A = \left\lceil \frac{\sum_{k^* \in K^*} u^n_{k^*,t}}{|K^*|} \right\rceil = \{0,1\} \quad [6]$$

When there is no branching all decision variables must be the same for all scenarios. However, when branching occurs the scenarios partition $S_{n1}=\{s: w_{k^*,t^*,s} = 1, \forall s \in Sn\}$, $S_{n2} = S_n \setminus S_{n1}$. Examples of the non-anticipativity constraints are given below:

$$(1 - A)\left(x_{b,(t+1),s} - x_{b,(t+1),s'}\right) = 0, \quad \forall t \in T^\alpha; b \in M \quad [7]$$

$$(1 - A)\left(z_{g,j,(t+1),s} - z_{g,j,(t+1),s'}\right) = 0, \quad \forall t \in T^\alpha; g \in G;\ j \in \mathcal{M} \cup \mathcal{S} \cup \mathcal{P} \cup \mathcal{W} \quad [8]$$

$$(1 - A)\left(w_{k,(t+1),s} - w_{k,(t+1),s'}\right) = 0, \quad \forall t \in T^\alpha; k \in K \quad [9]$$

The destination policy, extraction sequence, and capital investment decisions are the same for all scenarios within each branch of the decision tree. Lastly, in order to ensure stochastic solution stability there must be a minimum number of simulated scenarios in each partition.

Solution method

A multi-neighbourhood simulated annealing metaheuristic is used to solve the optimization model. Metaheuristics are required as the number of decision variables is in the order of hundreds of millions when considering a multi-mine, long-term production schedule. The metaheuristic used in this work explores a neighbourhood or class of perturbations that are used to change decision variables and arrive at near-optimal solutions in a short period of time (Goodfellow and Dimitrakopoulos, 2016, 2017; Montiel and Dimitrakopoulos, 2015, 2017). Del Castillo (2018) introduces perturbations that change capital investment decisions, including adding or removing multiple investments in a period and swapping two investments between periods. The simulated annealing algorithm then uses an acceptance probability to determine whether the new solution is accepted or rejected to further explore the solution space (Kirkpatrick, Gelatt, and Vecchi, 1983). The modified simulated annealing approach, used in the subsequent case study, updates the probability of choosing a neighbourhood depending on its ability to improve the objective function (Goodfellow and Dimitrakopoulos, 2016).

Case study at a gold mining complex

The adaptive simultaneous stochastic optimization approach is applied to a gold mining complex that consists of two large open-pit mines with twelve different material types. These materials can be transported to a number of destinations: an autoclave processing facility, oxide mill, oxide leach, twelve stockpiles (one for each material type), waste facility, and a tailings management area. Each mine exploits a mixture of sulphide ores, which must be pretreated at the autoclave before processing, and oxide ores that can be sent to the oxide processor or oxide leach. The mining complex, including each of its component, and the allowable material routing, is presented in Figure 1. Sulphide materials, a refractory ore type, can be extracted from either of the open pit mines and sent to the autoclave, stockpile, or waste dump facility. Stockpiles are separated for each material type to provide accessibility to materials of certain chemical compositions, shown in Table I. Material that is sourced externally is used to supplement the ore feed that is produced at the two open pit mines and sent to the autoclave to help meet blending requirements. The optimizer seeks opportunities to increase value and more effectively blend materials to obtain a satisfactory product quality for effectively running the autoclave. Sulphide or refractory ores must be blended to achieve the permissible operating criterion for the autoclave, by controlling the grades of sulphide sulphur (SS), carbonate (CO_3), organic carbon (OC), and the SS/CO_3 ratio. Therefore, these deleterious attributes must be managed within the optimization framework to ensure blending requirements will be met. A constraint is added to the model to maintain the grades of SS and CO_3 between 3.8–4.2% and 4.5–6.5%, respectively. Deviations from these targets are penalized in the objective function to manage the risk similar to all the other production targets. Acid is used to pretreat the ore by neutralizing CO_3 and ensuring the appropriate SS/CO_3 ratio (0.8–1.2) enters the autoclave circuit. This becomes critical as there is variability in the material received from the different sources and often there are not enough materials with the desired qualities readily available. There is a maximum amount of acid (38 400 t) that can be used on an annual basis, which introduces a constraint in the optimization process. The autoclave's target production is 2.5 Mt/a. Oxide materials can report to either the oxide mill, leach, or stockpile and there are no constraints on the blending requirements for the oxide ore material. The oxide mill has a production target of 1.4 Mt/a and the leach pad is not constrained. After processing, the volumes of mine tailings that are generated from the processing facilities are continuously examined to ensure there is a large enough containment area to continue processing, which then introduces a constraint on the available tailings capacity. Stockpiling facilities are used as intermediate locations to assist with blending and can be extracted from throughout the mine life. Lastly, any material that does not positively contribute to the NPV of the mining complex is sent to the corresponding waste dump facility.

In this case study, there are three one-time feasible investment alternatives considered throughout the optimization process to test the adaptive optimization approach. First, the annual autoclave processing throughput may be expanded by investing in two additional positive-displacement piston-

Table I

Material classification for blending and material routing

Material	Chemistry			
Type	CO_3	SS	OC	Oxide
1	Med-low	Low	-	-
2	Med-low	High	-	-
3	Low	Med	-	-
4	Low	Low	-	-
5	Low	Med-high	-	-
6	High	-	-	-
7	Med-high	Low	-	-
8	Low	High	-	-
9	Very high	-	-	-
10	High	-	Med-high	-
11	-	-	High	-
12	-	-	-	High

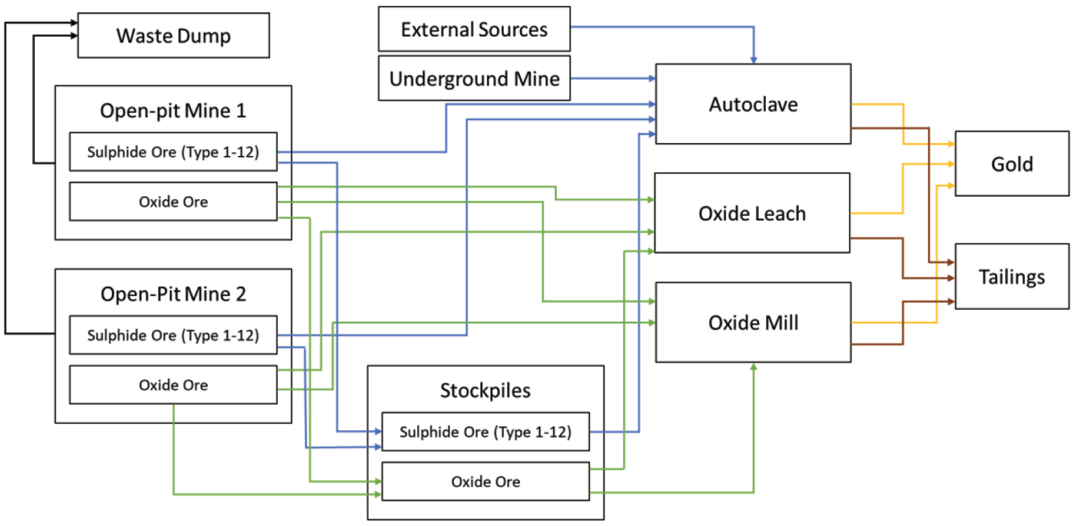

Figure 1—The mining complex and allowable material routing

Table II

Parameters and cost of capital investments

Parameters	Non-branching		Branching expansions		
	Shovel	Truck	Tailings	Autoclave	Acid
Lead time (years)	2	2	3	2	3
Capital cost ($ million)	10	1.6	200	1	0.2
Life of equipment (years)	7	7	13	13	13
Periodicity of decision (years)	3	3	13	13	13
Increase in capacity	Feed for 5 trucks/unit	1.4 Mt/unit	5.75 million m^3	925 kt	9.6 kt

diaphragm pumps (Eichhorn *et al.*, 2014). Secondly, an investment in the process plant autoclave circuit is evaluated to increase the allowable acid consumption and manage blending. Thirdly, an investment alternative that considers the construction of a new tailings storage area to increase the life of mine by allowing the processors to continue operating. The pump installation increases throughput at the autoclave by 25%. which allows for more refractory ore to be processed. The capital cost of this expansion is minimal; however, the cost of implementation and loss of production during the pump installation is also considered in the capital investment decision, resulting in a $1 million investment. Acid is ordered annually to satisfy production requirements, but storage areas and adaptations to the autoclave pretreatment circuit are required to safely utilize the additional acid. The expected investment is $0.2 million. The most significant investment decision is related to the addition of a new tailings containment area, which is expected to cost $200 million to construct completely. The new tailings area results in a 33% increase in tailings storage capacity for the mining complex. Once any of the three investments are purchased, they can be continuously used for the remainder of the mine life. Additionally, these three capital investment decisions can potentially allow the production schedule to branch. In this case study, a representativity measure $R = 0.3$ is used based on the acceptable risk of investing in capital at this mining operation. Therefore, the production schedule branches when a representative number of scenarios, between 30% and 70%, invest in one of these three feasible alternatives. The scenarios are then split, and further branching considerations are assessed in future periods. Further details on the parameters considered for each of the capital investments are described in Table II.

The mine initially begins with 30 haul trucks and six shovels that have two years remaining productive life before salvaging. The model dynamically considers the purchase of trucks and shovels throughout the thirteen-year production schedule. Truck and shovel purchases define the annual mine production rate. The cost per truck and shovel is $1.6 million and $20 million, respectively, which is accounted for in the annual cash flows, allowing for the optimizer to decide on the appropriate time to invest in trucks and shovels throughout the mine life. The mining operation has an ageing fleet and is planning to replace the originally purchased haul trucks with a new fleet. The ability to consider the purchase of new equipment during the optimization provides an opportunity to re-establish the optimal mining rate to satisfy the processor requirements and maximize the value of the operation. The trucks and shovels have a corresponding lead time of two years to provide a suitable amount of time for purchasing equipment from the manufacturer, shipping, and on-site assembly. In addition, they have an expected equipment life of seven years and a purchase can be made every three years, stabilizing the production rate.

Base case mine production schedule

A base case mine production schedule is defined here using a simultaneous stochastic optimization approach that considers capital investment decisions within the optimization framework

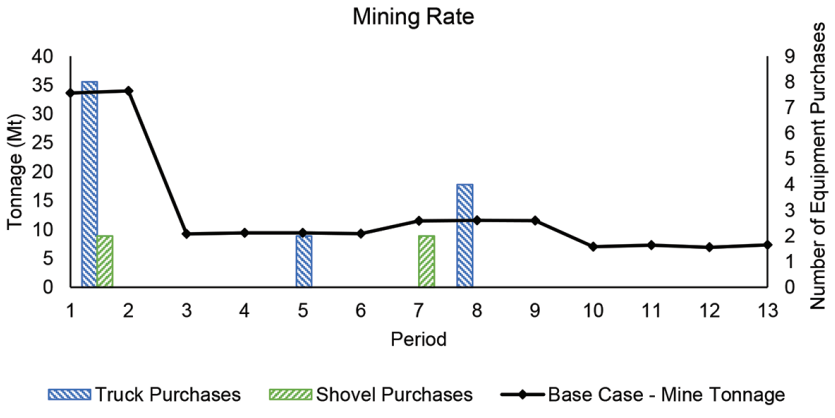

Figure 2—The mining rate and shovel/truck purchase plan for the base case production schedule with no branching

while managing uncertainty. Branching, however, is not considered. The base case mine production schedule can choose to invest in trucks, shovels, and the available expansions, but it cannot branch and adapt to uncertainty by considering alternatives; it must choose either to invest or not to invest. This is different from the adaptive simultaneous stochastic optimization that can be used to evaluate different alternatives and their corresponding value, as there is a fixed production schedule that must be executed in one way, which does not consider the value of having alternative options to manage uncertainty to a greater extent. The results from the base case mine production schedule are compared with the adaptive branching approach that considers feasible capital investment alternatives. Each method uses a set of multivariate stochastic simulations of the orebody for each open pit as input to the optimization model (Boucher and Dimitrakopoulos, 2009; Rossi and Deutsch, 2014). The external sources are simulated based on historical data associated with variability in the supply and quality of material received from other mines in the region. The variability and uncertainty of the material sources are accounted for directly in the optimization framework, unlike conventional frameworks that use a single estimated orebody model as input (Hustrulid and Kutcha, 2006). Lastly, the open pit mines have a block size of 30 m × 30 m × 20 m, representing the selective mining unit and contain 296 000 and 172 000 blocks in Mine 1 and Mine 2, respectively.

The results from the base case production schedule, including the extraction sequence, capital investments, stockpiling, blending, mining rate, and processing decisions, follow. Figure 2 defines the base case mining rate alongside the truck and shovel investment decisions. Noticeably, the amount of equipment that is required decreases as the mine life proceeds and as the older equipment approaches the end of its operational life, an opportunity arises to operate the two mines at a lower mining rate. Although a lower mining rate is utilized, the ability to satisfy the autoclave processor (Figure 3a) and oxide mill is fulfilled and a resulting NPV of $3.65 billion is achieved in the 50th percentile (P-50). The base case mine production schedule invests in both the expansion of the tailings management area and the additional acid storage facility. The investment in additional pumps does not contribute an increase to the mining complex's NPV when accounting for all scenarios, consequently the pumps are not purchased. The blending constraints are satisfied, between the upper (UB) and lower bounds (LB), in most years through the utilization of stockpiles and other available material (Figure 3b, 3c). However, during the first year, the blending constraints are unachievable as the material that can be extracted during that year does not have the appropriate properties to meet the blending requirements. As the production schedule proceeds, stockpiles are established to help with blending in future years. The operational costs of stockpiling these materials are integrated into the optimization to ensure that the stockpiling decisions contribute to the profitability of the mining complex and help manage the technical risk.

Lastly, the base case production schedule invests in a tailings storage expansion in year 7. This investment increases the

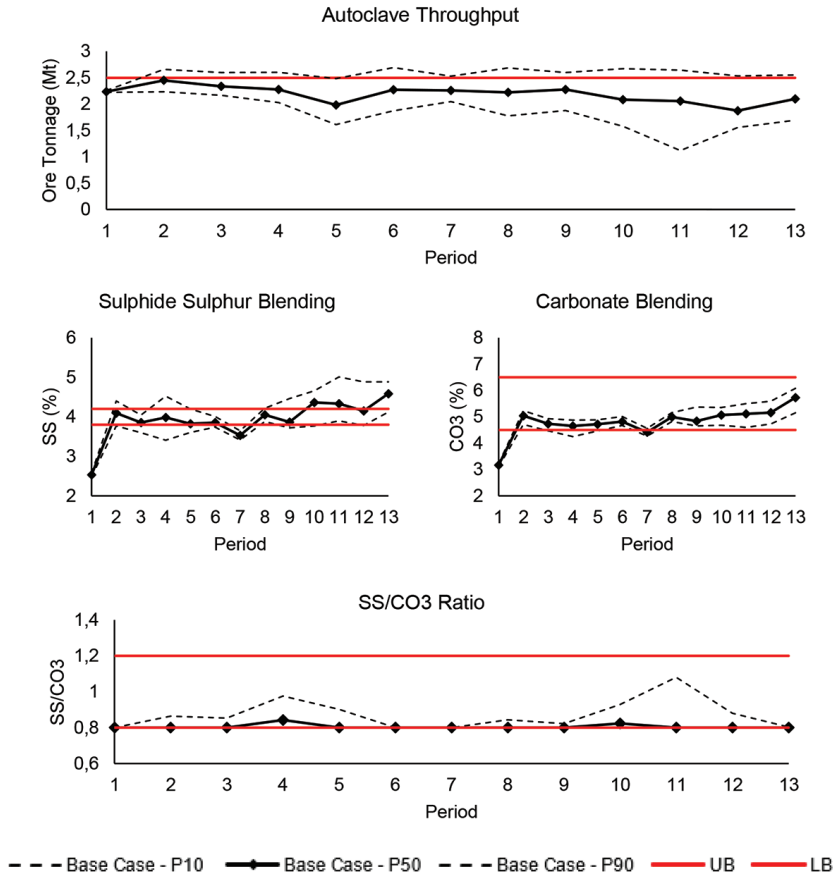

Figure 3—Base case autoclave throughput and blending: (a) no expansion taken in the optimization for additional throughput, (b) blending of SS, (c) blending of CO3, (d) maintaining the SS/CO3 ratio for ideal operating conditions

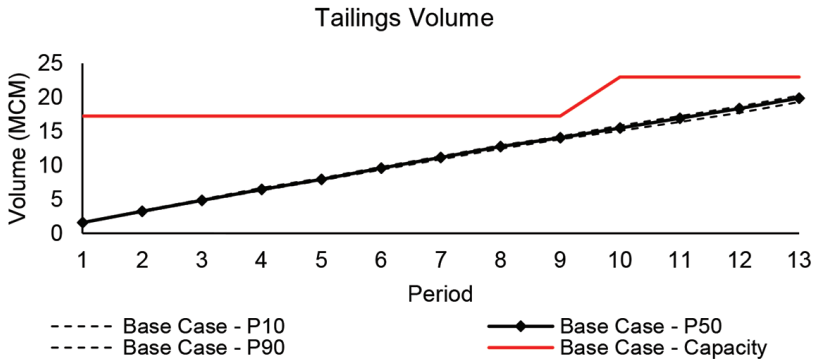

Figure 4—Tailings production over the long-term production schedule and the available capacity expanded in year 10

storage capacity and becomes available in year 10 (Figure 4). The increased tailings storage prolongs the mine life by three years and allows for 1 to 2 more years of gold production if the duration of this schedule is increased. This results in an additional $0.7 billion in discounted cash flows generated. It is important to optimize waste management considerations, such as tailings disposal, directly in the mine production scheduling process in order to generate feasible life-of-mine designs. Additionally, the processor upgrade that allows for additional acid consumption was purchased in year 3, allowing for a 20% increase in acid consumption in subsequent years Figure 5). This controls the blending requirements at the autoclave processing stream.

Adapting to supply uncertainty in a gold mining complex

The previously discussed results will be compared with the adaptive stochastic optimization that considers branching on feasible capital alternatives. During the adaptive simultaneous stochastic optimization, groups of scenarios are optimized to determine if there is a beneficial time to invest in any of the one-time capital investments alternatives described previously. The scenarios that lead to a branching decision are separated based on those that invest and those that choose not to invest in the time window. The scenarios that choose not to invest maintain the ability to invest in the capital investment in future years, while the scenarios that invest lock in that decision for that year, activating the non-anticipativity constraints. The scenarios are grouped into separate branches and optimized to produce a feasible alternative for both investing and not investing in the solution. A representative number (over 30%) of scenarios must undertake the same decision for the solution to consider branching or investing in these alternatives, which reduces the number of branches and prevents overfitting the decision tree to each scenario. It is important to note that the scenarios in each branch all undertake the same decisions until a new branching decision is made.

Based on the available capital investments, it was first determined that the additional acid capacity was a suitable investment for more than 70% of the scenarios leading to a non-branching investment decision. The first investment helped improve the ability to meet the quality requirements of the autoclave. After considering all the simulated scenarios (geostatistical simulations of each open pit mine and an uncertain external source) and the branching mechanisms criterion, the first branching decision is undertaken, allowing for the expansion of the autoclave throughput by installing two additional positive-displacement pumps. This separates the number of scenarios into a group of 115 scenarios in branch 1 (B1) that invest and 205 scenarios in branch 2 (B2) that do not invest. After the branching occurs, the optimizer also decides to invest in the additional tailings capacity in more than 70% of the scenarios, for both branches, preventing further growth of the scenario tree. The resulting feasible alternatives both produce a higher NPV than the base case production schedule, achieving a value of $3.89 billion in B1 and $4.66 billion in B2 (Figure 6). This accounts for a 6.4% and 27.5% increase in NPV when comparing the P-50 of each alternative to the base case production schedule. Each of the branches or feasible alternatives performs better than the base case production schedule; however, this may not always be the case as there could be a group of scenarios that underperforms the base case production schedule. The method prevents overfitting by ensuring that the number of scenarios

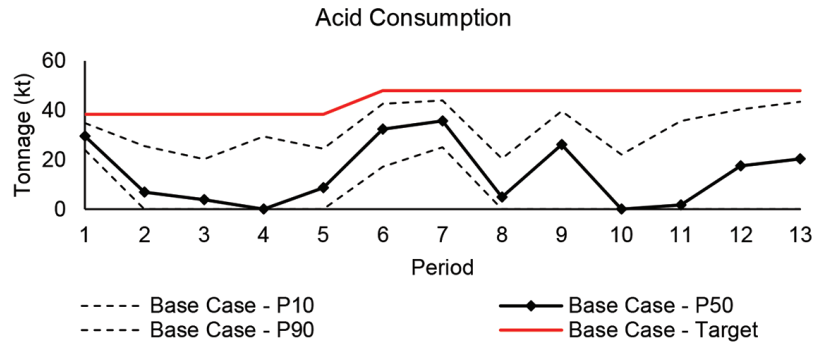

Figure 5—Annual acid consumption with additional capacity obtained in year 6

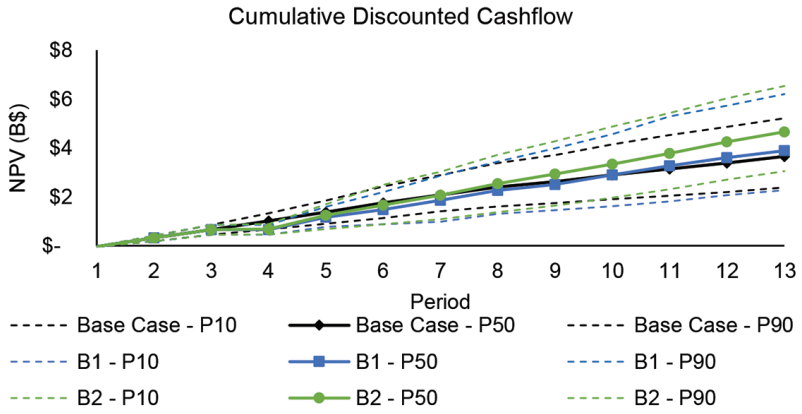

Figure 6—Comparison of the NPVs from the adaptive branching and base case production schedule

does not become too few within each branch and that there is a significant difference in the number of scenarios that either invest or maintain the same operating conditions, hence the representativity parameter which ensures between 30% and 70% of the scenarios will be split and not a small group of outliers. This substantially reduces the number of branches and ensures feasible, stable solutions. The changes in the investment decisions result in very different responses in the production scheduling process, as shown in Figure 7, when comparing the N-S cross-sections. The solution is exactly the same until branching occurs, and then the schedules change dramatically to take advantage of the new capital investments. There are a number of similarities between the base case and B2 in terms of the depth and extent of the mine. However, in B1 there is a large area in the north of the mine where extraction no longer occurs, compared to the other two mine plans. This implies that there is some high material variability and uncertainty in this section of the mine, which leads to large changes in the resulting mine plan.

B1 invests in the autoclave expansion (Figure 8), which can be fully utilized in year 6, and has the lowest mining rate over the long-term production schedule. A comparison of the mining rates is given in Figure 9, where the resulting production rates directly correlate to the number of trucks and shovels purchased. The autoclave expansion results in lower grade refractory ore material being processed and a higher throughput at the autoclave. Over the long-term production schedule, there is a 9% reduction in the number of gold ounces produced over the life of mine compared with the P-50 of the base case scenario. However, the reduction in mining costs due to the lower mining rate overcompensates the loss in revenue and results in a higher NPV. The lower mining rate is feasible as the throughput outweighs the grade of material through the autoclave, changing the

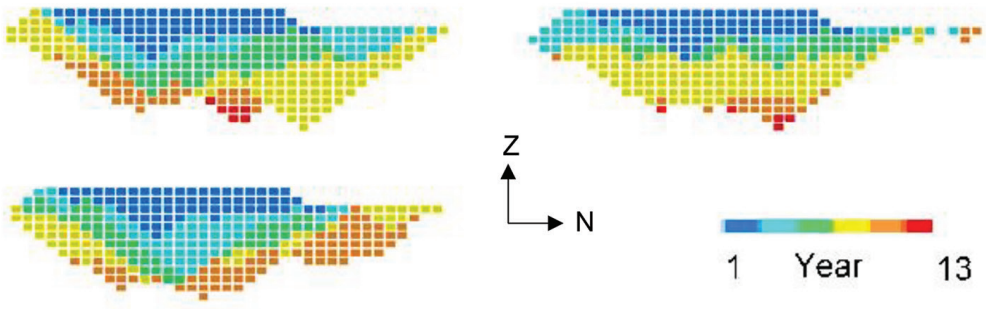

Figure 7—N-S cross-section of production schedule Mine 1: (a) base case (top left), (b) branch 1 (top right), and (c) branch 2 (bottom left)

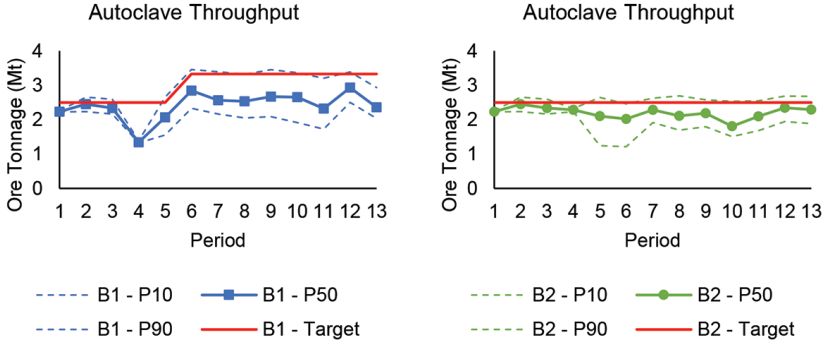

Figure 8—Autoclave throughput and targets (a) B1 and (b) B2 with investments

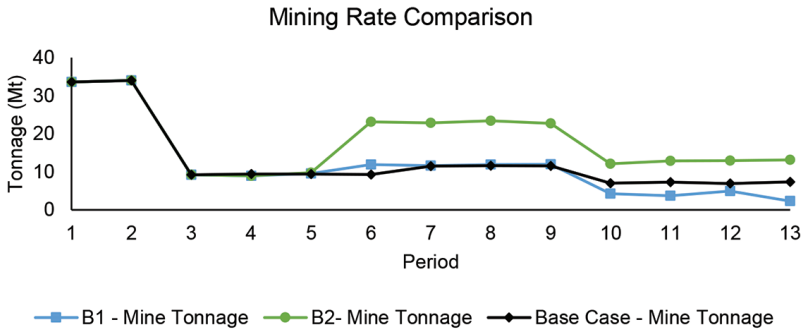

Figure 9—A comparison of the mining rates required to satisfy each production schedule

selectivity between ore and waste material. Lower utilization of the oxide processing facilities also decreases the operating costs. In B1, the optimizer has a challenging time meeting the blending constraints and is unable to provide the appropriate material to attain the blending targets, making the acid investment a critical decision for ensuring there is a suitable SS/CO_3 ratio.

B2 performs quite differently and instead increases the size of the truck and shovel fleet, which results in a higher extraction rate and ensures that higher-grade refractory ore is sent to the processor. The oxide processing streams are utilized far more in B2 than in B1 and their target production is maintained during most years. A higher stripping ratio is required to move the additional waste between years 5 and 9 (Figure 10), which is the reason for the additional truck and shovel requirements. Increasing the selectivity between ore and waste results in a substantially higher NPV, which B1 was unable to achieve even with the autoclave capacity expansion. The larger contribution in NPV is primarily due to the accessibility of oxide materials in the different groups of simulations and the uncertainty and variability in the gold, SS, CO_3, and OC grades. Here the adaptive approach is able to take advantage of understanding the inherent variability of the mineral deposits and indicates that there is an important investigation to be conducted. This includes more information with regards to the mineralization of oxide materials and stricter guidelines in terms of the quality of material received from external sources before deciding on the autoclave expansion. B2 produces 10% more gold by fully utilizing all the processing stream capacities and better satisfying the blending constraints. The increased utilization of the oxide leach and mill contribute significantly more gold ounces.

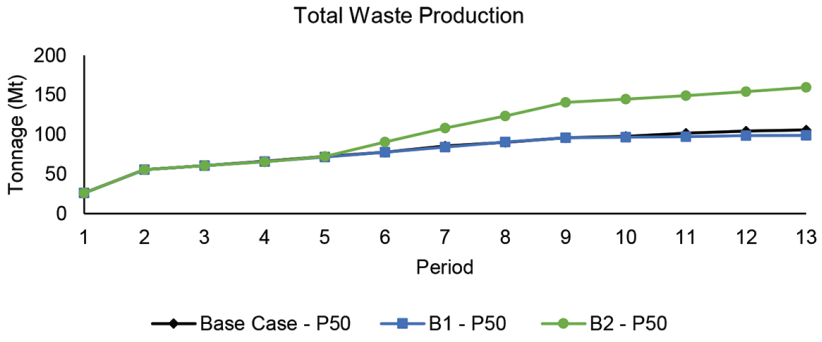

Figure 10—Total waste production over the long-term production schedule

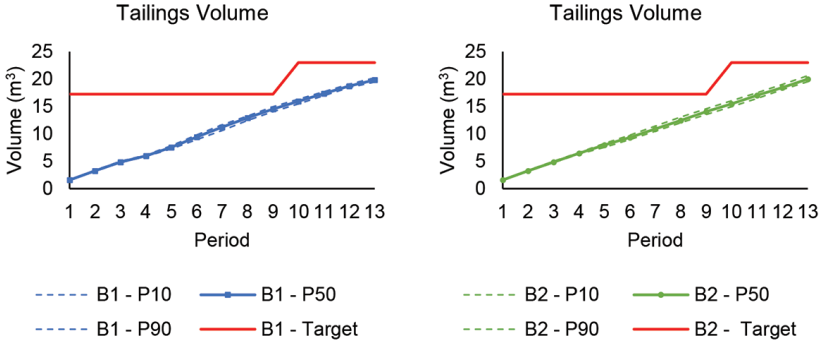

Figure 11—Total tailings production with investment decisions

The feasible alternatives B1 and B2 invest in the additional tailings containment area in year 7 and receive the capacity in year 10, similar to the base case. Had the tailings expansion not been considered during the optimization process, processing would have been required to stop in year 10 and a loss of $1 billion and $1.3 billion in additional cash flow would be incurred in B1 and B2, respectively. This would be a larger loss than the resulting $0.7 billion in the base case production schedule. The potential loss highlights the importance of simultaneously optimizing the entire mining complex to further understand the intrinsic value of each investment decision.

Conclusions

The simultaneous stochastic optimization of a gold mining complex was studied using an adaptive method that integrates feasible capital investment alternatives. The framework capitalizes on synergies and adapts to uncertainty, resulting in a 6.4% and 27.5% increase in NPV in branch 1 (B1) and branch 2 (B2) respectively, while satisfying a wide array of production targets and managing supply uncertainty. Investments in trucks and shovels define a new mining rate that minimizes capital expenditure and satisfies each processor's capacity. Additionally, an investment in a tailings facility expansion and additional acid consumption increase the life of the mining complex and manage variable material quality at the autoclave processor. Integrating tailings management into the optimization process increases the NPV by $0.7 billion in the base case production schedule and leads to an additional $1 billion in B1 and $1.3 billion in B2. This emphasizes the importance of considering waste and tailings management in the optimization process in order to capitalize on the available synergies. The optimizer chooses to branch the production schedule when the autoclave expansion is considered and identifies uncertainty and local variability associated with the supply of oxide and refractory ores sent to each processor. This leads to different mine plans and operating requirements for the processing streams and mining equipment, depending on whether the investment alternative is purchased. The feasible investment alternatives provide a high level of insight into the appropriate attributes to investigate, including highly variable areas of the deposit and large differences in the quantity of oxide materials mined. The optimized production schedule does not branch for the first three years and provides the appropriate lead time to evaluate each alternative decision and gather the required information to construct an informed final production schedule.

If either of the feasible alternatives are executed, the expected NPV increases substantially. The base case and adaptive approaches capitalize on the synergies that exist between the different components of the mining complex, helping to manage the challenging blending constraints and determine the appropriate size of the mining fleet directly in the optimization. The results from this case study emphasise the importance of modelling the entire mining complex in a single optimization process. In addition, the branching mechanism and adaptive ability of the optimizer provides a method to easily evaluate several feasible alternatives and further understand the variability and uncertainty associated with the mining complex.

Acknowledgements

This work is funded by the National Science and Engineering Research Council of Canada (NSERC) CRD Grant 500414-16, NSERC Discovery Grant 239019, the COSMO Stochastic Mine Planning Laboratory and mining industry consortium (AngloGold Ashanti, Barrick Gold, BHP, De Beers, IAMGOLD, Kinross, Newmont Mining, and Vale), and the Canada Research Chairs Program.

References

Ajaka, A.D., Lilford, E., and Topal, E. 2018. Application of predictive data mining to create mine plan flexibility in the face of geological uncertainty. *Resources Policy*, vol. 55. pp. 62–79 https://www.doi.org/10.1016/j.resourpol.2017.10.016

Ahmed, S., King, A.J., and Parija, G. 2003. A multi-stage stochastic integer programming approach for capacity expansion under uncertainty. *Journal of Global Optimization*, vol. 26. pp. 3–24. https://doi.org/https://doi.org/10.1023/A:1023062915106

Asad, M.W.A., and Dimitrakopoulos, R. 2013. Implementing a parametric maximum flow algorithm for optimal open pit mine design under uncertain supply and demand. *Journal of the Operational Research Society*, vol. 64, no. 2. pp. 185–197. https://doi.org/10.1057/jors.2012.26

Boland, N., Dumitrescu, I., and Froyland, G. 2008. A multistage stochastic programming approach to open pit mine production scheduling with uncertain geology. *Optimization Online*. http://www.optimization-online.org/DB_FILE/2008/10/2123.pdf

Boucher, A. and Dimitrakopoulos, R. 2009. Block simulation of multiple correlated variables. *Mathematical Geosciences*. vol. 41, no. 2. pp. 215–237. http://dx.doi.org/10.1007/s11004-008-9178-0

Dimitrakopoulos, R. (ed.). 2018. Advances in Applied Strategic Mine Planning. Springer Nature, Heidelberg. doi: 10.1007/978-3-319-69320-0

De Neufville, R. and Scholtes, S. 2011. Flexibility in Engineering Design. MIT Press, Cambridge, MA. 293 pp.

Del Castillo, F. 2018. Dynamic simultaneous optimization of mineral value chains under resource uncertainty. PhD thesis, McGill University, Montreal.

Del Castillo, F. and Dimitrakopoulos, R. 2014. Joint effect of commodity price and geological uncertainty over the life of mine and ultimate pit limit. *Mining Technology*, vol. 123, no. 4. pp. 207–219. https://doi.org/10.1179/1743286314Y.0000000069

Del Castillo, F. and Dimitrakopoulos, R. 2019. Dynamically optimizing the strategic plan of mining complexes under supply uncertainty. *Resources Policy*, vol. 60(C). pp. 83–93. https://doi.org/10.1016/j.resourpol.2018.11.019

Dixit, A. and Pindyck, R. 1994. Investment Under Uncertainty. Princeton University Press.

Dowd, P. 1994. Risk assessment in reserve estimation and open-pit planning. *International Journal of Rock Mechanics and Mining Sciences & Geomechanics Abstracts*, vol. 32, no. 4. pp. 148–154. https://doi.org/10.1016/0148-9062(95)97056-O

Eichhorn, M., Krumins, T., Zunti, L., and Ruff, F.C. 2014. Capacity enhancement at Newmont Mining Corporation's Twin Creek's whole ore pressure oxidation facility. *Canadian Instutute of Mining, Metallurgy & Petroleum: Hydrometallurgy,* vol. 1, no. 735–749. pp. 80–90.

Farmer, I. 2016. Stochastic mining supply chain optimization: A study of integrated capacity decisions and pushback design under uncertainty. MEng thesis, McGill University, Montreal. https://pdfs.semanticscholar.org/755d/38a5804034d03d393e93043aa90743a60f62.pdf

Gershon, M.E. 1983. Optimal mine production scheduling: evaluation of large scale mathematical programming approaches. *International Journal of Mining Engineering*, vol. 1, no. 4. pp. 315–329. https://doi.org/10.1007/BF00881548

Githiria, J. and Musingwini, C. 2019. A stochastic cut-off grade optimization model to incorporate uncertainty for improved project value. *Journal of the Southern African Institute of Mining and Metallurgy*, vol. 119. pp. 217-228. doi: 10.17159/2411-9717/2019/v119n3a1

Godoy, M. and Dimitrakopoulos, R. 2004. Managing risk and waste mining in long-term production scheduling of open-pit mines. *SME Transactions*, vol. 316, no. 3. pp. 43–50.

Goodfellow, R. 2014. Unified modelling and simultaneous optimization of open pit mining complexes with supply uncertainty. PhD thesis, McGill University, Montreal. http://digitool.library.mcgill.ca/webclient/StreamGate?folder_id=0&dvs=1575644597071~332

Goodfellow, R. and Dimitrakopoulos, R. 2016. Global optimization of open pit mining complexes with uncertainty. *Applied Soft Computing*, vol. 40. pp. 292–304. https://doi.org/10.1016/j.asoc.2015.11.038

Goodfellow, R. and Dimitrakopoulos, R. 2017. Simultaneous stochastic optimization of mining complexes and mineral value chains. *Mathematical Geosciences*, vol.49, no. 3. pp. 341–360. https://doi.org/10.1007/s11004-017-9680-3

Goovaerts, P. 1997. Geostatistics for Natural Resources Evaluation. Oxford University Press, New York

Groeneveld, B. and Topal, E. 2011. Flexible open-pit mine design under uncertainty. *Journal of Mining Science*, vol. 47, no. 2. pp. 212–226. https://doi.org/10.1134/S1062739147020080

Groeneveld, B., Topal, E., and Leenders, B. 2012. Robust, flexible and operational mine design strategies. *Mining Technology*, vol. 121, no. 1. pp. 20–28. https://doi.org/10.1179/1743286311Y.0000000018

Gupta, V. and Grossmann, I.E. 2017. Offshore oilfield development planning under uncertainty and fiscal considerations. *Optimization and Engineering*, vol. 18, no. 1. pp. 3–33. https://doi.org/10.1007/s11081-016-9331-4

Hustrulid, W. and Kutcha, M. 2006. Open Pit Mine Planning and Design. 2nd edn. Taylor & Francis, London.

Khan, A.,and Asad, M.W.A. 2019. A method for optimal cut-off grade policy in open pit mining operations under uncertain supply. *Resources Policy*, vol. 60. pp. 178-184. doi: 10.1016/j.resourpol.2018.12.003

Kirkpatrick, S., Gelatt, C., and Vecchi, M. 1983. Optimization by simulated annealing. *Science*, vol. 220, no. 4598. pp. 671–680. https://doi.org/10.1126/science.220.4598.671

Levinson, Z. and Dimitrakopoulos, R. 2019. Simultaneous optimization of an open-pit gold mining complex with waste management and cut-off grade optimization. *International Journal of Mining, Reclamation and Environment*. https://doi.org/10.1080/17480930.2019.1621441

Li, Y., Huang, G., Nie, S., and Liu, L. 2008. Inexact multistage stochastic integer programming for water resources management under uncertainty. *Journal of Environmental Management*, vol. 88. pp. 93–107. https://doi.org/10.1016/j.jenvman.2007.01.056

Mai, N. L., Topal, E., Erten, O., and Sommerville, B. 2018. A new risk-based optimisation method for the iron ore production scheduling using stochastic integer programming. *Resources Policy*. doi: 10.1016/j.resourpol. 2018.11.004

Menabde, M., Froyland, G., Stone, P., and Yeates, G. 2007. Mining schedule optimisation for conditionally simulated orebodies. *Orebody Modelling and Strategic Mine planning: Uncertainty and Risk Management Models.* Spectrum Series vol. 14. Australasian Institute of Mining and Metallurgy, Melbourne. pp. 379–384. https://doi.org/10.1007/978-3-319-69320-0_8

Montiel, L. and Dimitrakopoulos, R. 2018. Simultaneous stochastic optimization of production scheduling at Twin Creeks Mining Complex, Nevada. *Mining Engineering,* vol. 70, no. 12. pp. 12–20.

Montiel, L. and Dimitrakopoulos, R. 2015. Optimizing mining complexes with multiple processing and transportation alternatives: An uncertainty-based approach. *European Journal of Operational Research*, vol. 247, no. 1. pp. 166–178. https://doi.org/10.1016/j.ejor.2015.05.002

Montiel, L., and Dimitrakopoulos, R. 2017. A heuristic approach for the stochastic optimization of mine production schedules. *Journal of Heuristics,* vol. 23, no. 5. pp. 397–415. https://doi.org/10.1007/s10732-017-9349-6

Pimentel, B., Mateus, G., and Almeida, F. 2010. Mathematical models for optimizing the global mining supply chain. *Intelligent Systems in Operations: Methods, Models, and Applications in the Supply Chain*. Business Science Reference, Hershey, PA. pp. 133–163. https://doi.org/10.4018/978-1-61520-605-6.ch008

Ravenscroft, P. (1992. Risk analysis for mine scheduling by conditional simulation. *Transactions of the Institution of Mining and Metallurgy Section A: Mining Industry*, vol. 101. pp. 104–108. https://doi.org/10.1016/0148-9062(93)90969-K

Rossi, M. and Deutsch, C. 2014. Mineral Resource Estimation. Springer, Dordrecht, The Netherlands. https://doi.org/10.1007/978-1-4020-5717-5

Saliba, Z. and Dimitrakopoulos, R. 2018. Simultaneous stochastic optimization of an open pit gold mining complex with tailings management. *Mining Technology*, vol. 128, no. 4. doi: 10.1080/25726668.2019.1626169

Singh, K.J., Philpott, A.B., and Wood, R.K. 2009. Dantzig-Wolfe decomposition for solving multistage stochastic capacity-planning problems. *Operations Research*, vol. 57, no. 5. pp. 1271–1286. https://doi.org/10.1287/opre.1080.0678

Thomas, K. and Pearson, M. 2016. Pressure oxidation overview. *Gold Ore Processing*. Thomas, K. and Pearson, M.(eds). Elsevier. Chapter 21, pp. 341–358. https://doi.org/10.1016/B978-0-444-63658-4.00021-9

Whittle, J. 1999. A decade of open pit mine planning and optimization The craft of turning algorithms into packages. *APCOM'99: Proceedings of the 28th International Symposium on Computer Applications in the Minerals Industries*, Golden, CO, 20-22 October 1999. Dagdelen, K. (ed.). Colorado School of Mines. pp. 15–23. ◆

Appendix A

Adaptive simultaneous stochastic optimization sets, parameters, and decision variables

Sets and Parameters

M	Set of open-pit and underground mines
P	Set of processors
W	Set of waste facilities
S	Set of stockpiles
G	Set of groups or bins for different cut-off grades $g \in G$
T	Set of scheduled time periods $t \in$ T
S	Set of simulated orebody scenarios $s \in$ S where there are $S_n \subseteq$ S scenarios that belong to the root, these scenarios are partitioned into S_{n1} and S_{n2} when branching occurs therefore $S_{n1} \cup S_{n2} = S_n$ and $S_{n1} \cap S_{n2} = \varnothing$
P	Set of primary attributes $p \in$ P
H	Set of hereditary attributes $h \in$ H
K	Set of available capital investments $k \in$ K. There are two different subsets used to describe the different types of investments branching (K^*) and non-branching ($K^=$), where $K^* \cup K^= = K$
O(g)	Set of locations where the groups of materials g can be delivered
B_m	Set of mining blocks $b \in B_m$ from mine $m \in$ M
$\beta_{p,b,s}$	Parameter that defines the set of simulated primary attribute p for block b in scenario s
$r_{p,i,t,s}$	Parameter that describes the recovery of each attribute p at location $i \in P$ in each scenario s
R	Representativity measure that describes the confidence interval for branching $R \in (0, 0.5)$
t_ω	Time window used to stabilize solutions where ω represents the number of periods to search
N	Defines the minimum number of scenarios in a branch required for further branching periods $(t+1) \in$ T
τ_k	Lead time to assemble or construct a capital investment $k \in K$
λ_k	Life expectancy of each capital investment $k \in K$
$\kappa_{k,h}$	Unitary increase in capacity that each investment $k \in K$ leads to for each attribute $h \in$ H
$p^K_{k,t}$	Discounted purchase cost for each investment $k \in K$ for each period $t \in$ T
ψ_k	The periodicity of the investment $k \in K$
$L_{h,i,t}$, $U_{h,i,t}$	The static upper and lower bounds for each hereditary attribute $h \in$ H, location $i \in M \cup S \cup P \cup W$, and period $t \in$ T

Decision Variables

$v_{p,i,t,s}$, $v_{h,i,t,s}$	Quantify the value of primary (p) and hereditary (h) attributes at each location $i \in M \cup S \cup P \cup W$ in period t under scenario s, respectively
$x_{b,t,s}$	A set of binary extraction sequence decision variables that denotes if a block b is extracted in period t in scenario s as 1, otherwise 0
$z_{g,j,t,s}$	A destination policy decision variable that takes a value of 1 if blocks in group g are sent to destination $j \in O(g)$, in period $t \in$ T
$y_{i,j,t,s}$	A continuous processing stream decision variable that defines the portion of product that is sent from one destination $i \in S \cup P$ to destination $j \in$ O(i)$\subseteq S \cup$ P in period $t \in$ T and scenario $s \in$ S, $y_{i,j,t,s} \in [0,1]$
$\omega_{k,s,t}$	A capital investment decision variable that defines if a capital investment $k \in K$ is executed in period $t \in$ T and scenario $s \in$ S
$\sigma_{k,t,s}$	The number of investments undertaken for each investment $k \in$ K in period $t \in$ T and scenario $s \in$ S
$u^{n}_{k^*,t}$	A binary variable equals unity when the design branches over option $k^* \in K^*$ in node n in period $t \in$ T, otherwise 0
A	A binary variable that activates the non-anticaptivity constraints taking on the value 0, 1.

Measuring and modelling entrainment in rougher and cleaner batch flotation

N.V. Ramlall

Affiliation:
[1]South Africa.

Correspondence to:
N.V. Ramlall

Email:
nv.ramlall@gmail.com

Dates:
Received: 13 June 2019
Revised: 13 Oct. 2019
Accepted: 13 Dec. 2019
Published: March 2020

How to cite:
Ramlall, N.V.
Measuring and modelling entrainment in rougher and cleaner batch flotation.
The Southern African Insitute of Mining and Metallurgy

DOI ID:
http://dx.doi.org/10.17159/2411-9717/792/2020

Synopsis

A study was carried out to measure the recovery by entrainment from batch rougher and cleaner flotation tests. A non-floatable tracer component (ferrosilicon, FeSi) was added to milled Merensky ore in the flotation test work and used to measure the recovery by entrainment. Conventional entrainment models such as the linear model and the exponential probability model gave poor model fits. A new entrainment model is therefore proposed in this study. A three-parameter Weibull probability model was fitted simultaneously to the rougher and cleaner entrainment recovery data. The model gave a good fit and returned parameters that are a logical description of the recovery by entrainment in both rougher and cleaner batch flotation.

Keywords
entrainment measurement, entrainment modelling, batch flotation.

Introduction

In mineral flotation, the nonselective recovery of non-floatable minerals (typically termed gangue) is due to a process of entrainment. Entrainment is an undesirable process that reduces the flotation concentrate grade. Operational changes (physical and/or chemical) are required to reduce the recovery of gangue minerals by entrainment so that an acceptable concentrate grade can be obtained. Many authors have investigated entrainment at the bench scale, and these studies can be broadly categorized as measurement or modelling studies.

Measurement studies have been carried out by Trahar (1981), Warren (1985), and Ross (1989). Trahar (1981) proposed carrying out two batch flotation tests, one with frother only and another with frother plus collector. The mineral recovery data was plotted against water recovery. Recovery by entrainment was assumed to occur only in the frother test, and recovery by true flotation and entrainment in the frother plus collector test. The difference in mineral recovery between the two tests, at similar water recoveries, was assumed to be recovery by true flotation. This approach assumes that the recovery by entrainment is the same for both tests for similar water recoveries. However, conditions in the pulp and froth phase are different in each test. These differences influence the water content in the froth and ultimately the recovery by entrainment. Water is the medium responsible for transporting particles that are susceptible to entrainment. A brittle froth (typical of low solids concentration) has a loose froth structure with low bubble coalescence, and recovery by entrainment from this froth structure is greater than for a non-brittle froth. When a collector is added to the pulp, it causes hydrophobic minerals (in addition to naturally floatable minerals) to move towards the froth. The froth, having a higher solids content (lower water content), carries less entrained particles. According to the bubble swarm theory proposed by Smith and Warren (1989), the rising column of mineralized bubbles in the froth, which also contains solids suspended in the water interstitial to the mineralized bubbles, squeezes out the water and suspended solids. This froth structure promotes rejection of entrained particles. As a result, recovery by entrainment will be different in both tests because of the different froth structures. The method of Trahar was also restricted to batch rougher flotation, so there is no evidence that entrainment measurements made in rougher flotation are valid in re-flotation.

Warren (1985) carried out batch rougher flotation tests at different froth depths and removal rates. The final recoveries from all tests were plotted against the associated water recoveries. A linear model was fitted to the data; the intercept and slope were related to the recovery by true flotation and the degree of entrainment respectively. In this approach, several rougher flotation tests had to be carried out. This is time-consuming and the froth structure is different for each test. Hence, the recovery by entrainment will be different in each test and there will be some uncertainty about the parameters estimated. Also, it is not known if the parameters determined from rougher flotation apply to re-flotation.

Ross (1989) carried out a single batch rougher flotation test for measuring recovery by entrainment. Two transfer functions were defined, one for entrained solids and another for total solids to the flotation concentrate. It was assumed that the recovery towards the end of the rougher flotation test was mainly due to entrainment, therefore the transfer function for total solids towards the end of flotation was used to estimate the recovery by entrainment. The froth structure changes during batch flotation because of the varying solids concentration in the froth. Early in the test the froth solids concentration is high (*i.e.* low water content in the froth), and as the test progresses, the froth solids concentration decreases because of less floatable minerals being present. The transition of the froth structure, from a low water content (at the beginning) to high water content (towards the end), means that entrainment measurements made at the end of flotation may not necessarily apply to the batch flotation test over its entire duration. Wang *et al.*, (2015) cautioned on the use of this approach for re-flotation, since the higher concentration of floatable minerals in the cleaner stage means that the degree of entrainment measured towards the end of flotation may exceed unity. This is impossible if non-floatable gangue recovery is by entrainment only. This also implies that data-points at the end of flotation do not constitute a reliable measure for estimating entrainment.

Konopacka and Drzymala (2010) reviewed the graphical representation of entrainment and the models used to describe these representations. Figure 1 shows the five types of representations found by the authors. The representations vary from linear (Types 1, 2, and 5) to nonlinear (Types 3 and 4). According to the authors, the shapes of the entrainment curves are the result of the way the flotation test is carried out, the type of flotation machine used, kinetics of the process, froth collecting time, the concentration of frothers, collectors and modifiers, the amount of air, density of the pulp, and supplied water. For the representations, the entrainment recovery is defined as the cumulative mass recovery of the mineral to the concentrate by entrainment divided by initial mineral mass content in the pulp. This is then expressed as a percentage. Water recovery may be defined in several ways, such as percentage water recovery (cumulative recovery to concentrate relative to pulp initial water content), mass of water recovery (cumulative mass of water recovered to concentrate), volume of water recovered (cumulative volume of water recovered to concentrate), and water flow rate (cumulative mass flow rate of water recovered to concentrate,expressed in units of g·min^{-1} or similar). A brief discussion on each curve type, based on the paper of Konopacka and Drzymala (2010), is given below. It is recommended that the original work of these authors be read for more information.

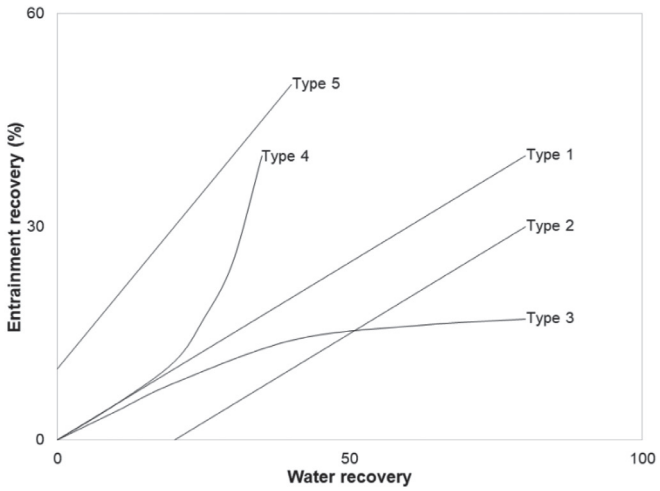

Figure 1—Shapes of the entrainment plots after Konopacka and Drzymala, (2010)

The Type 1 curve is a linear entrainment curve for which mineral entrainment is proportional to water recovery. Equation [1] is typically used to model this type of entrainment curve. R_{ent} is the cumulative recovery by entrainment, *ENT* is the degree of entrainment (which varies from 0 to 1), and R_{water} is the cumulative water recovery (typically expressed in per cent). There is one concern with the use of this model in batch flotation. Consider the situation of an *ENT* value close to unity, *e.g.* 0.85 reported by Warren (1985) for fine gangue. For batch flotation, the recovery of water can exceed 100% if water is continually added to maintain the pulp volume. Consequently, recovery by entrainment can exceed 100% mathematically, although this is impossible in practice. For *ENT* = 0.85, R_{ent} exceeds 100% when R_{water} is greater than 118%.

$$R_{ent} = ENT \times R_{water} \quad [1]$$

The Type 2 entrainment curve is a linear curve that is shifted down the abscissa of the plot. This may be attributed to the feed containing coarse particles and the froth height being low. A linear model was used to model this curve, but a correction factor ($R_{water,0}$) was added to water recovery to account for the downward shift. All other parameters have the same definitions as those given for Equation [1].

$$R_{ent} = ENT \times \left(R_{water} - R_{water,0}\right) \quad [2]$$

Type 3 is a nonlinear entrainment curve. The recovery by entrainment increases gradually and then approaches a plateau. Kirjavainen (1989) proposed Equation [3] to describe this curve. Here *P* is a dimensionless entrainment separation coefficient that varies between 0 and 1. All other parameters have the same definitions as for Equation [1].

$$R_{ent} = 100 \times \left[1 - e^{\left(-\frac{R_{water}}{100} \times P\right)}\right] \quad [3]$$

Type 4 is an entrainment curve that is parabolic. According to Konopacka and Drzymala (2010), this curve has been observed in studies carried out by Lynch *et al.* (1974), Engelbrecht and Woodburn (1975), and Bisshop and White (1976). Laplante (1980) presented Equation [4] for this type of curve. Here *Z* is called the classification entrainment coefficient and varies between 0 and 1. All other parameters have the same definitions as for Equation [1].

$$R_{ent} = \frac{100 \times Z \times R_{water}}{100 + R_{water}(Z-1)} \quad [4]$$

Type 5 is a linear entrainment curve that is shifted upwards along the ordinate of the plot. The upward shift is due to the occurrence of hydrophobic minerals (fully liberated or composite particles) that attach to ascending bubbles; these minerals are then recovered in the flotation concentrate. To account for this, Warren (1985) proposed the model given by Equation [5]. Here $R_{flotation}$ is the recovery by flotation; all other parameters have the same definitions as for Equation 1.

$$R_{ent} = ENT \times R_{water} + R_{flotation} \quad [5]$$

In summary, some drawbacks were observed regarding entrainment measurement and modelling studies:

- All studies were carried out using batch rougher tests, and there is no evidence that the entrainment measurements made in rougher flotation apply to re-flotation.
- The froth structure changes over the duration of the batch flotation test. Therefore, entrainment measurements made with particular data-points (such as data at the end of flotation) may not represent entrainment over the entire duration of flotation.
- There are a veritable plethora of entrainment models, each modelling entrainment for a particular flotation test methodology. This implies that no single model exists for representing the different types of entrainment curves that may be observed. Furthermore, these models were applied to rougher flotation and were not extended to re-flotation tests. Therefore it is not known if rougher fitted parameters apply to re-flotation.

In this study, a tracer component (FeSi) was used to investigate the recovery by entrainment. FeSi was added to milled Merensky ore conditioned with typical flotation reagents. The entrainment of FeSi from a naturally occurring ore and the observation of its recovery in both rougher and cleaner flotation leads to a more realistic study of entrainment. The primary objective of this study is to investigate and model entrainment changes between rougher and cleaner flotation.

Methods

Samples

Merensky ore was used in all flotation test work. The ore was crushed to –1.7 mm and split with the aid of rotary sample dividers (RSDs) into 2 kg aliquots for the test work. The sample had a Pt, Pd, plus Au (2PGE+Au) feed grade of 2.93 g·t^{-1}. Table I shows the mineral types and their distribution in the sample. The minerals are mainly paramagnetic (weakly magnetic) and diamagnetic (nonmagnetic). FeSi was used as a tracer component for measuring entrainment because of its ferromagnetic (strongly magnetic) properties. It can be recovered from the flotation products (concentrates and tails) using magnetic methods without recovering other minerals. Figure 2 shows the size distribution of the FeSi used in this study. A Rosin-Rammler particle size distribution model was fitted to the experimental data, which was obtained from laser sizing using a Fritsch Analysette 22. The specific density (SG) of FeSi was measured with a pycnometer and found to be 5.01.

Table I

Mineral distribution in the Merensky ore

Mineral	Concentration (%)
Pyrite	0.06
Pyrrhotite	0.24
Chalcopyrite	0.13
Pentlandite	0.15
Talc	5.57
Serpentine	1.39
Smectite	0.16
Pyroxene	75.29
Plagioclase	14.84
Muscovite	1.30
Chlorite	0.21
Olivine	0.18
Chromite	0.28
Ilmenite	0.01
Apatite	0.19
Other*	0.06

*Other refers to a group of minerals with trace concentration. The concentrations for these minerals were summed and shown as 'Other' in this table

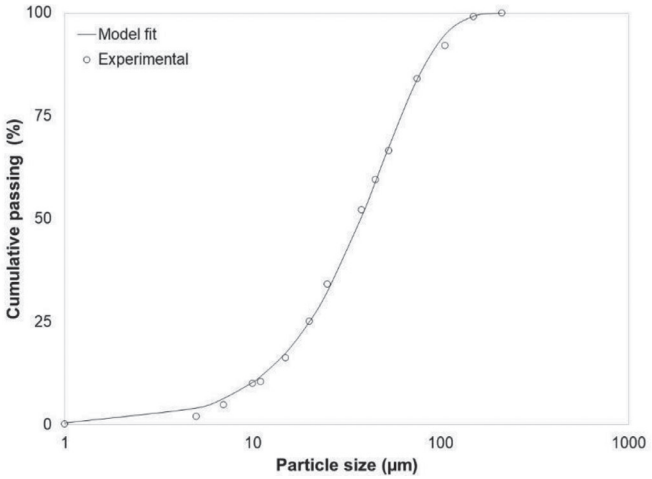

Figure 2—Particle size distribution for FeSi

Experimental

Figure 3 shows a schematic of the batch rougher and cleaner flotation test set-up. For the batch rougher flotation test, the Merensky ore was milled to 65% passing 75 µm using a rod mill. The milled ore was transferred into a 5 L flotation cell and tap water was added to the flotation pulp to give a solids concentration of 35% in the pulp. The pulp was conditioned with flotation reagents typically used in Merensky ore flotation. A Denver D-12 flotation machine and mechanism were used with the impeller speed set to 1500 r/min. After conditioning, FeSi was added into the flotation pulp, which was agitated for a further 30 seconds. Air was introduced into the flotation cell at a rate of 8.3 L·min^{-1}. The air flow rate was set to this value for better control of the froth since higher flow rates created a voluminous froth that was difficult to scrape at consistent intervals. This may be due to the ore containing a large amount of floatable material. The froth was allowed to build up naturally (allowing mineral separation to occur in the froth) and removed by hand-scraping every 15 seconds. The bottom edges of the scrapers were kept at a constant level of 5 mm above the froth/pulp interface. This is typical of most batch flotation test procedures, which use hand-scraping of the froth. Eight flotation concentrates were collected, ending at the cumulative flotation times of 1, 3, 7, 20, 30, 40, 50, and 60 minutes. Tap water was used to maintain the pulp level throughout the test. The flotation concentrates and the tails were weighed before filtration and again after drying. This made it possible to calculate the recovery of water.

For the cleaner tests, rougher flotation was first carried out as discussed above. The rougher concentrates collected over 60 minutes were combined and filtered. The undried rougher concentrate filter cake was transferred into a 2.5 L flotation cell and re-pulped to a suitable pulp height using the filtrate from rougher concentrate filtration. In re-flotation, the impeller speed was set to 1200 r/min, and the pulp was agitated for 2 minutes before the air was introduced at a rate of 4 L·min^{-1}. The froth was allowed to develop, and hand-scraping was used to remove the froth every 20 seconds. Six concentrates were collected, ending

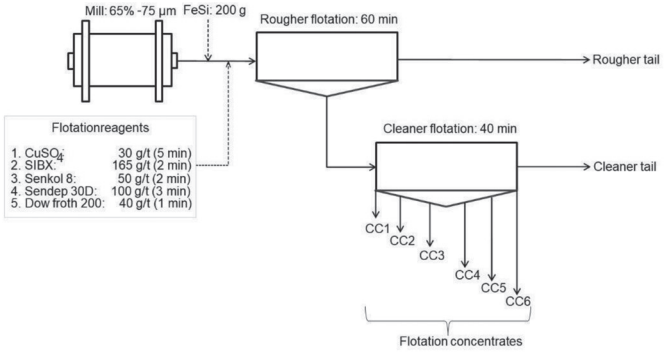

Figure 3—Schematic of the batch rougher and cleaner flotation methodology

at cumulative flotation times of 1, 3, 7, 20, 30, and 40 minutes. The filtrate from rougher concentrate and tails filtration was used to maintain the pulp level. The flotation concentrates and tails were weighed before filtration and again after drying so the water recovery could be calculated. No reagents were added to cleaner flotation so as not to introduce additional variables into the study.

FeSi was recovered from the rougher and cleaner flotation concentrates and tails using a Davis tube (Figure 4). This device is typically used to determine the amount of magnetic material in a sample. The solids were placed into the glass tube that contained water, and an electric current was introduced into the device. The current is related to a certain magnetic flux density. In this study it was 1000 gauss, which is sufficient for recovering ferromagnetic material only and not diamagnetic and paramagnetic material. The ferromagnetic material was held between the poles in the magnetic zone. Water was introduced into the tube at a rate of 1.5 L·min^{-1} using a peristaltic pump. The continuous flow of water into the tube, together with agitation of the tube, aids in the separation of paramagnetic and diamagnetic material (which exits at the discharge end of the tube) from the ferromagnetic FeSi material, which is held in the magnetized zone. A mass balance of material recovered to tube discharge and that held in the magnetized zone gave the distribution of FeSi in each flotation concentrate and tail. It should be noted that the mass introduced into the Davis tube should be small. Therefore, smaller masses had to be split out from the dried flotation rougher and cleaner tails before testing. For the rougher and cleaner tails, three 30 g sub-samples were split off using an RSD. Each was tested in the Davis tube and the average result used to determine the FeSi content in each flotation tail. An analytical mass balance was used to measure the mass of FeSi obtained from the Davis tube test.

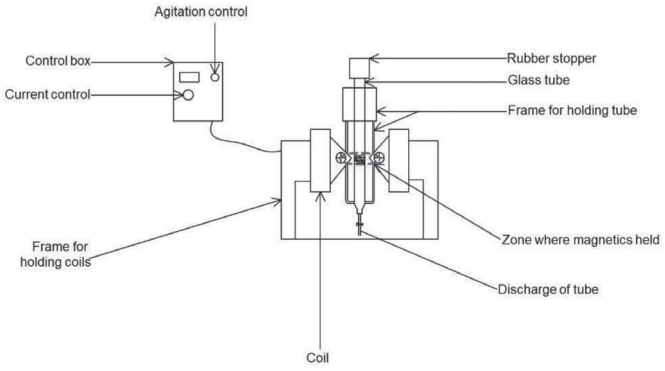

Figure 4—Schematic of Davis tube used to remove FeSi from flotation products

Results and discussion

Verification of FeSi as a tracer

Before the flotation test work, a sub-sample of milled (65% –75 µm) Merensky ore was passed through the Davis tube. No material was held in the magnetized zone at a magnetic flux density of 1000 gauss. This confirmed that the Merensky ore contained no ferromagnetic minerals. A sample of FeSi was also passed through the Davis tube. All the material was held in the magnetized zone at a magnetic flux density of 1000 gauss. This confirmed that FeSi can be used as a tracer since its distribution across the flotation concentrates and tails can be determined using a Davis tube.

The ferromagnetic material obtained from the Davis tube for each flotation product was subjected to X-ray diffraction (XRD) analysis. XRD analysis is a nondestructive test since the mass used can be recovered and reused after the test. This test was used to identify whether the magnetic material recovered by the Davis tube was FeSi. A FeSi sample was also introduced into this analysis as a standard for comparing the XRD patterns obtained for other samples. Figure 5 shows the results of the XRD analysis, confirming that the ferromagnetic material collected from each flotation product was FeSi and not another mineral.

The last step in verification was a mass balance of FeSi across the flotation products. After the XRD analysis, the samples were subjected to laser sizing using a Fritsch Analysette 22.

Table II and Table III show the mass distribution of water, total solids, and FeSi across the batch rougher and cleaner flotation tests respectively. Total solids include the mass of magnetic (FeSi) and nonmagnetic minerals. For the rougher test, the FeSi recovered from the three 30 g rougher tail sub-samples was 2.789, 2.808, and 2.730 g. For the rougher-cleaner test, the FeSi recovered from the three 30 g rougher tail sub-samples was 2.791, 2.781, and 2.861 g, and for the three 30 g cleaner tail sub-samples it was 0.969, 0.946, and 0.975 g. These values are comparable and show minimal variation across the triplicate testing. The average of the three was used to determine (by proportion) the FeSi content in the rougher and cleaner tails. A mass balance for FeSi shows that for 200 g introduced into each

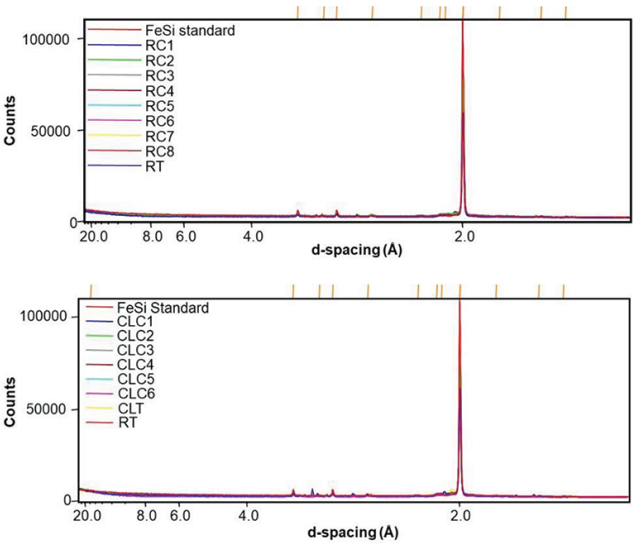

Figure 5—XRD analysis on ferromagnetic material collected from Davis tube test work for rougher and cleaner flotation products

Table II

Water, total solids, and FeSi recovery and sizing data for rougher flotation

Sample	Cumulative time (min)	Water recovery (g)	Total solids (g)	FeSi (g)	FeSi size distribution (%)		
					–5 µm	+5 µm –53 µm	+53 µm
RC1	1	138.1	32.0	3.09	3.5	78.8	17.7
RC2	3	177.1	33.5	3.07	5.2	78.9	15.9
RC3	7	445.9	37.3	2.45	6.3	79.2	14.5
RC4	20	1002.9	74.7	4.79	6.8	79.5	13.7
RC5	30	730.1	46.9	2.78	5.2	84.5	10.3
RC6	40	677.0	37.3	3.20	4.8	86.8	8.4
RC7	50	523.1	20.6	1.21	4.6	88.3	7.1
RC8	60	431.5	15.0	0.58	4.6	89.3	6.1
RT			1895.4	175.37	0.6	58.9	40.5

Table III

Water, total solids, and FeSi recovery and sizing data for cleaner flotation

Sample	Cumulative time (min)	Water recovery (g)	Total solids (g)	FeSi (g)	FeSi size distribution (%)		
					–5 µm	+5 µm –53 µm	+53 µm
CC1	1	86.0	32.3	3.40	2.7	66.5	30.8
CC2	3	168.9	26.8	3.21	3.3	78.2	18.59
CC3	7	261.4	30.8	2.93	4.7	86.9	8.4
CC4	20	511.0	48.8	3.54	5.4	86.0	8.6
CC5	30	443.4	23.9	1.31	5.9	85.0	9.1
CC6	40	426.3	16.3	0.69	5.9	84.4	8.7
CLT			115.1	3.70	9.0	88.7	2.3
RT			1900.3	178.06	0.8	68.3	30.9

flotation test, 196.54 g of FeSi was recovered from the rougher test and and 196.84 g from the rougher-cleaner test. The good agreement between the mass introduced and mass recovered supports the application of FeSi as a tracer.

Modelling recovery by entrainment

A mass reconciliation was carried out on the FeSi distribution across the rougher and cleaner flotation test work. It is necessary to use balanced data for linking entrainment measurements between rougher and cleaner flotation. Figure 6 shows a parity chart of the reconciled FeSi distribution and the experimental distribution as set out in Table II and Table III.

Figure 7 shows the total recovery of FeSi *versus* water recovery. FeSi recovery was determined with respect to the total amount added to the rougher feed. The recovery of water from rougher and cleaner flotation was determined with respect to the initial amount of water added to each stage. FeSi recovery does not follow the typical linear relationship expected between entrainment and water recovery. The relationship is nonlinear and resembles the Type 3 relationship reported by Konopacka and Drzymala (2010). Also, entrainment recovery appears to approach a plateau for each stage of flotation. This trend is not unusual and has been reported by other authors. Ekmekçi *et al.* (2003) investigated the effects of frother type and froth height on the entrainment behaviour of chromite from UG2 ore. They obtained a similar curve for the +45 µm chromite size fraction. The chromite recoveries at 30% and 50% water recovery (the last two data-points on their curve) were about 0.12% and 0.14% respectively, indicating that recovery approaches a plateau.

Kirjavainen (1989) investigated the entrainment of 1 µm chromite and silica in batch flotation. The entrainment recovery of both minerals also approached a plateau towards the end of flotation.

The approach of recovery by entrainment to a plateau suggests that the flotation operating conditions limit the recovery. For both rougher and cleaner flotation, the duration of flotation was much longer than that typically used in Merensky ore flotation. Flotation was deliberately prolonged to examine the behaviour of mineral entrainment at extended batch flotation

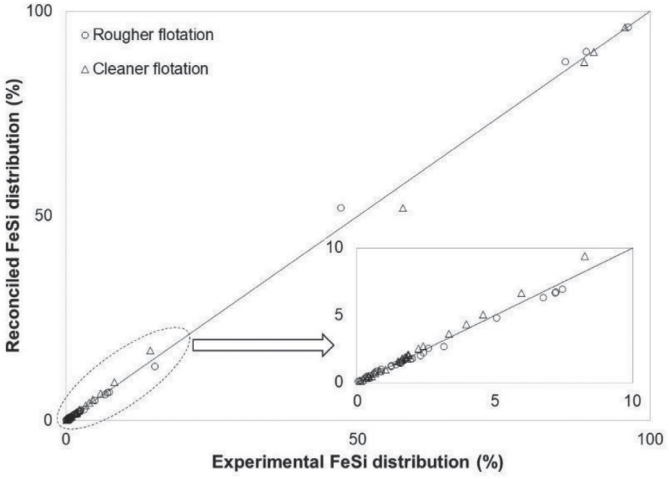

6—FeSi mass reconciliation across rougher and cleaner batch flotation

times. For the rougher stage, even at a water recovery of almost 89%, the entrainment recovery does not approach an absolute maximum of 100%. Instead, the recovery approaches a plateau of about 10%. This implies that entrainment recovery is constrained with respect to prevailing pulp conditions (*i.e.* air flow rate and impeller speed) as well as froth conditions (*i.e.* depth and scraping rate). Evidence for this reasoning can be found in a study by Zheng, Johnson, and Franzidis (2006), in which the entrainment of silica was measured for varying froth heights and air flow rates. The authors found that the degree of entrainment increased for increasing air flow rate and decreasing froth height. This observation suggests that entrainment recovery is constrained by prevailing flotation operating conditions (either in the pulp or the froth), therefore a particular maximum recovery by entrainment can be expected under these conditions.

The initial water content in the pulp is different for each stage, therefore simultaneous modelling of rougher and cleaner data is not possible. A new entrainment model is proposed for modelling the recovery by entrainment across batch rougher and cleaner flotation. The water flow rate was used instead of water recovery. The water flow rate is defined as the mass of water recovered per unit time for each flotation concentrate. This parameter is independent of the initial amount of water added to a batch flotation pulp. Therefore, rougher and cleaner entrainment measurements can be linked using the water flow rate. After assessing the profile of cumulative FeSi recovery with cumulative water flow rate for each flotation stage, a three-parameter Weibull model was suggested for modelling this curve. This gave a probabilistic model, defined as:

$$R_i^{Ent} = R_{Max,i}^{Ent}\left(1 - e^{\left[-\left(\frac{F}{\bar{F}_{i,j}}\right)^{n_i}\right]}\right) \quad [6]$$

where

R_i^{Ent} is recovery by entrainment for particles in size class i

$R_{Max,i}^{Ent}$ is a model-fitted parameter which describes the maximum amount that can be recovered by entrainment for particles in size class i

F is the experimental water flow rate (g·min^{-1})

$\bar{F}_{i,j}$ is a model-fitted parameter that describes the scale of the model. It is the water flow rate (g·min^{-1}) that results in 63.2% of maximum entrainment recovery being attained for particles in size class i in flotation stage j

n_i is a dimensionless model-fitted parameter that influences the shape of the Weibull probability distribution for particles in size class i

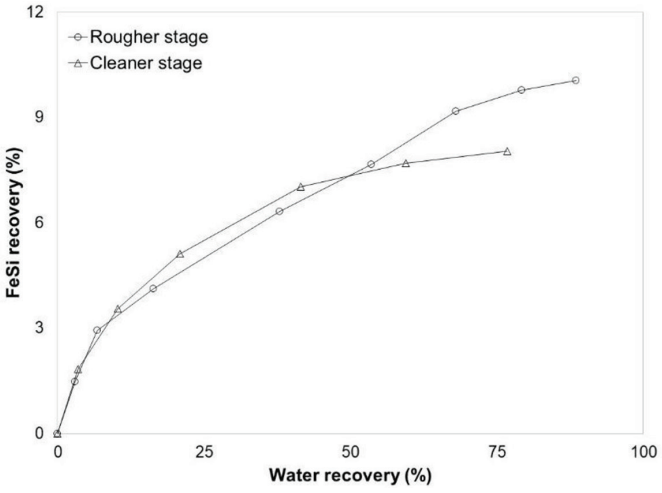

Figure 7—Recovery of FeSi *vs* water recovery

In Equation [6], the term $1-e^{\left[-\left(\frac{F}{\bar{F}_{i,j}}\right)^{n_i}\right]}$ represents a probability, so this quantity varies between 0 and 1. The probability (Pr) is influenced by the water flow rate, which changes over the duration of the flotation test because of depleting floatable mineral content and frother concentration in the flotation pulp. Therefore, Equation [6] can be expressed as follows:

$$R_i^{Ent} = R_{Max,i}^{Ent} Pr \quad [7]$$

The model was fitted simultaneously to the rougher and cleaner flotation data. There are 14 data-points for each size class. For each size class under examination, only four parameters had to be determined during model fitting, these were $R_{Max,i}^{Ent}$, $\bar{F}_{i,rougher}$, $\bar{F}_{i,cleaner}$, and n_i. The parameter $R_{Max,i}^{Ent}$ describes the maximum amount of material that can be recovered by entrainment from the rougher stage. The maximum amount that can be entrained in the cleaner stage can be determined as $R_{Max,i}^{Ent} \cdot Pr$, where Pr is the probability associated with the final concentrate collected from rougher flotation. $\bar{F}_{i,rougher}$ and $\bar{F}_{i,cleaner}$ describe the scale of the model, that is, the water flow rate that results in 63.2% of the maximum entrainment recovery being achieved for a stage. The value of 63.2% is obtained when $F_{i,rougher}$ and $\bar{F}_{i,cleaner}$ are equal to F for each flotation stage. At this value, $1-e^{\left[-\left(\frac{F}{\bar{F}_{i,j}}\right)^{n_i}\right]}$ is equal to 63.2%. The cleaner stage is more selective than the rougher stage due to the meticulous removal of the froth, that is, longer froth retention time (20 seconds *versus* 15 seconds for rougher flotation), and dilute pulp conditions. Hence, it was logical to define different model scale parameters for rougher and cleaner flotation. The parameter n_i controls the shape of the probability model. As n_i decreases, the shape of the curve produced by the model becomes more like the Type 3 curve reported by Konopacka and Drzymala (2010). For increasing n_i, the model becomes more vertical and linear about the scale parameter and appear like the Type 1 curve.

The probabilistic model was fitted to the recovery by entrainment data for particle size classes –5 µm, +5 µm – 53 µm, and +53 µm. Figures 9–11 show the model fit to these size classes. Also, the total FeSi recovery by entrainment was determined from the model-fitted parameters for each size class and the proportion of the particle size class in the flotation rougher feed. This fit is shown in Figure 8. The model gave a good fit to the experimental data for different particle size classes in the different flotation stages. The adjusted coefficient of determination (a statistic used to assess model fit to experimental data) was determined for a total of 56 data-points (14 per size class and 14 for total FeSi) and 12 model parameters (*i.e.* four model parameters per size class). A value of 0.9935 was obtained; this indicates a good model fit.

Table IV shows the parameters obtained from the fitting of the model to the experimental data. The maximum amount that can be recovered by entrainment ($R_{Max,i}^{Ent}$) decreases with increasing particle size. This parameter can be interpreted in a similar way as the *ENT* parameter for the linear entrainment model shown in Equation [1]. In that model, *ENT* decreases with increasing particle size. Similarly $R_{Max,i}^{Ent}$ decreases with increasing particle size. This is logical since larger particles tend to sediment in the flotation pulp and have low entrainment recovery. On the other hand, smaller particles tend to follow the fluid streamlines into the froth, due to their lower particle inertia, and have a higher

recovery by entrainment. Zheng, Johnson, and Franzidis (2006) carried out entrainment studies using a 3 m³ Outokumpu tank cell. In their study, the air flow rate and froth height were varied and the degree of entrainment for silica was measured. For an air flow rate of 1.10 $m^3 \cdot min^{-1}$ and froth height of 9.6 cm, the *ENT* values for particles with average sizes similar to this study were extracted from the graphical plots: *ENT* ≈ 0.56 (7 µm), 0.18 (25 µm), and 0.11 (88 µm). Therefore, the $R^{Ent}_{Max,i}$ parameter from this study is analogous to the *ENT* parameter and varies logically with particle size.

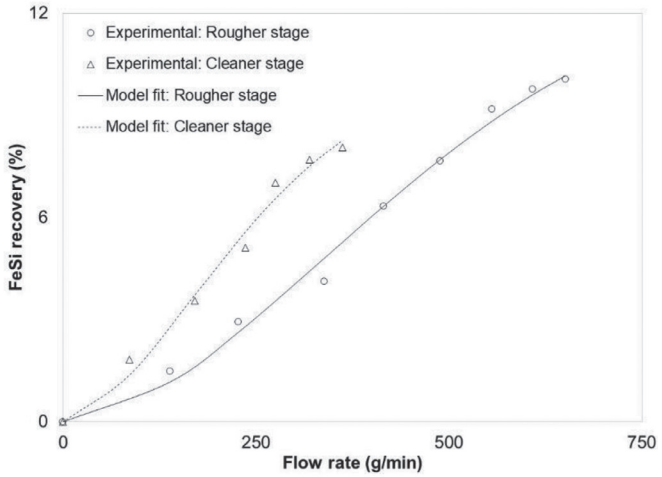

Figure 8—Overall FeSi recovery *vs* water flow rate

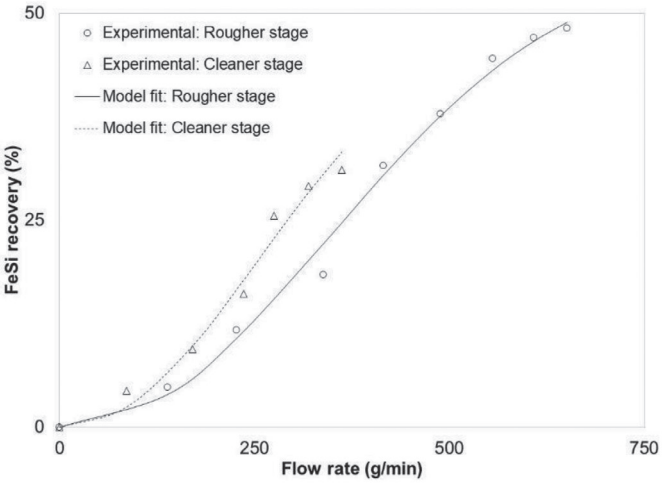

Figure 9—FeSi recovery for –5 µm particle size class *vs* water flow rate

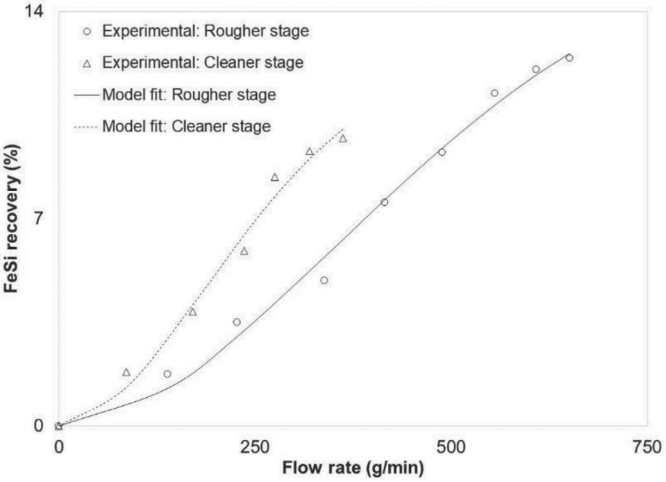

Figure 10—FeSi recovery for +5 µm –53 µm particle size class *vs* water flow rate

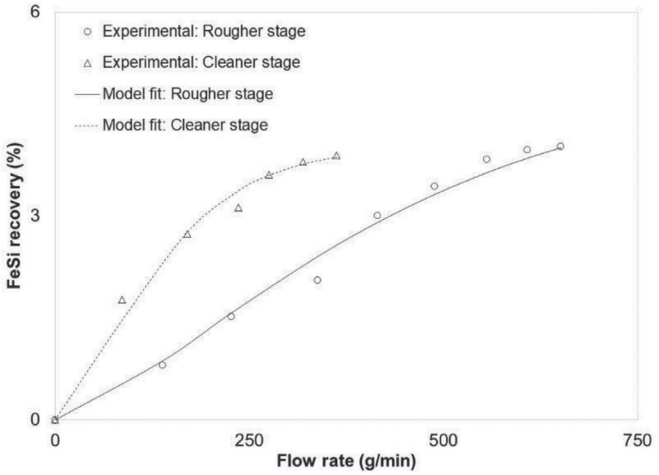

Figure 11—FeSi recovery for +53 µm particle size class *vs* water flow rate

The scale parameter ($\bar{F}_{i,j}$) for rougher flotation does not show a particular trend with particle size. This may be due to the nonselective operating conditions in rougher flotation. In rougher flotation, the set-up is designed for maximum mineral recovery. However, in cleaner flotation the longer froth scrapes, lower air flow rate, and dilute pulp conditions create a more selective environment. This may explain the decrease in scale parameter with increasing particle size in cleaner flotation. The lower model estimates for the scale parameter in cleaner flotation than the rougher flotation result in a horizontal shift in the probability model to the left. This indicates a lower probability of entrainment due to a more selective environment in the cleaner flotation stage.

The shape parameter (n_i) decreases with increasing particle size. This, together with decreasing estimates of the scale parameter, indicates that the probability of entrainment decreases with increasing particle size.

The shape of the entrainment curves (Figures 9–11) is unusual in comparison to curves reported in the literature. The use of water flow rate may be partially responsible. However, a closer examination of the curves shows features that may have a physical meaning. Consider the entrainment of fines (Figure 9). The curve shows three distinct parts; a slow recovery initially followed by a faster recovery and then a gradual slowing down of recovery. At the beginning of flotation, the pulp contains more floatable material and a higher frother concentration. This results in more material (in the form of mineralized bubbles) ascending towards the froth. Water interstitial to the mineralized bubbles contains suspended nonfloatable particles, which can only be recovered by entrainment. As the mineralized bubbles coalesce, the interstitial water and the suspended particles are squeezed out. The suspended particles then drain back into the pulp phase. As the floatable mineral content and frother concentration depletes, the froth contains fewer mineralized bubbles. Consequently, there is less coalescence of the mineralized bubbles. This results in a brittle froth with a higher water content and hence a higher amount of suspended particles. Therefore, entrainment increases during the intermediate period of batch flotation. Towards the end of batch flotation, there are barely any floatable minerals and the frother concentration is at its lowest. The entrainment recovery approaches a plateau at this stage of

Table IV

Model parameter estimates for entrainment recovery in rougher and cleaner batch flotation.

Size fraction	$R^{ENT}_{Max,i}$	$\bar{F}_{i,rougher}$ (g·min^{-1})	$\bar{F}_{i,cleaner}$ (g·min^{-1})	n_i
–5 μm	55.9	465.1	341.4	2.2
+5 μm –53 μm	16.5	537.8	281.6	1.9
+53 μm	5.0	456.8	152.1	1.4

flotation. This feature may be related more to the pulp conditions than the froth. The low number of ascending mineralized bubbles may not provide sufficient impetus for the transportation of entrainable particles to the froth. Changes to the pulp operating conditions, such as an increase in impeller speed to enhance particle suspension and air distribution, and an increase in air flow rate to drive more particles upwards, can force more particles to enter the froth, as seen in the study of Zheng, Johnson, and Franzidis (2006). However, the recovery by entrainment should logically approach a plateau if pulp operating conditions do not change.

Influence of density and particle size on entrainment

It could be argued that FeSi has a density atypical of most gangue minerals, and as such may not truly represent the entrainment behaviour of gangue. However, mineral density alone does not influence entrainment; the particle size, in addition to density, determines the mass of the particle and its propensity to be entrained. Evidence from the literature and the author's own view will be presented as justifications for using FeSi as a tracer.

From literature evidence, Wang *et al.* (2015) presented a review of factors influencing entrainment. The authors cited a study carried out by Maachar and Dobby (1992), who investigated the influence of density on the degree of entrainment. According to this study, the degree of entrainment was measured for two hydrophilic gangue minerals, silica (SG 2.6) and galena (SG 7.5). Figure 12 presents the results of this study. The degree of entrainment increased with decreasing particle size for both minerals. Furthermore, the degree of entrainment was greater for silica than galena for similar particle sizes, but the difference was minimal. At a particle size less than 5 μm, the degrees of entrainment for silica and galena were 0.74 and 0.70 respectively. According to Wang *et al.* (2015), particle density might interact with other factors which contribute to or affect entrainment in a flotation cell.

Kirjavainen (1989) carried out batch rougher flotation tests with hydrophilic quartz and chromite at a particle size less than 1 μm. Figure 13 shows the result for hydrophilic mineral recovery plotted against the volume of water recovered. The plot does not have the conventional water recovery units in per cent; nevertheless, it does show that both minerals have similar entrainment recovery profiles for similar water recovery, despite their different densities.

In summary, previous studies suggest that the conventional view – that entrainment is greater for minerals of lower density and lower for minerals of a higher density – is not completely correct. Other factors such as particle size must also be considered. Particle size and mineral density determine the mass of a particle, which in turn determines its susceptibility to being entrained. To expand on this, a brief explanation is given

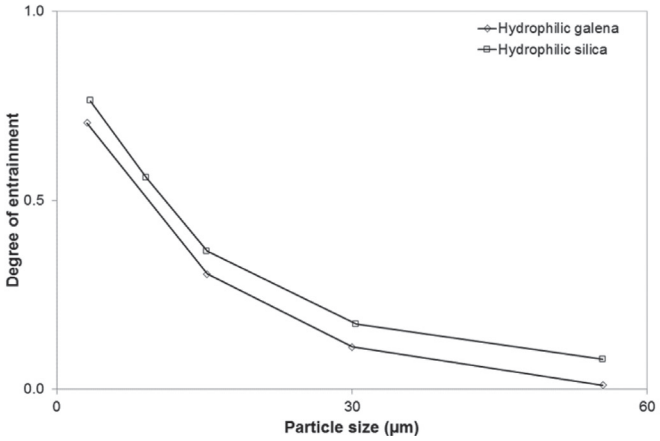

Figure 12—Effect of mineral SG on the degree of entrainment for different particle sizes (after Maachar and Dobby, 1992)

on particle motion in relation to a fluid. The purpose of this explanation is to show that mineral mass is the driving factor that influences entrainment.

The recovery of a particle by entrainment can be considered as a two-step process involving particle movement through the pulp phase into the froth, and then from the froth into the collected concentrate. In the pulp, an impeller is used to agitate the solids and provide suspension, as well as to disperse the air into smaller bubbles. Most particles that have a propensity to be entrained move towards the froth by following the streamlines of the ascending bubbles. The ability of these particles to follow the streamlines is related to the inertia of the particle. Wang *et al.* (2014) investigated solid-liquid separation by particle flow instability. The authors considered that when particles are sufficiently tiny they behave as an infinitesimal fluid element and follow the underlying fluid flow. However, when the particles size increases, the inertia of the particle prevents it from instantaneously matching its movement to that of the fluid. The authors then explained that the size and density of the particle moving in a fluid can be captured by the inertia number (σ):

$$\sigma = \frac{St}{R} \quad [8]$$

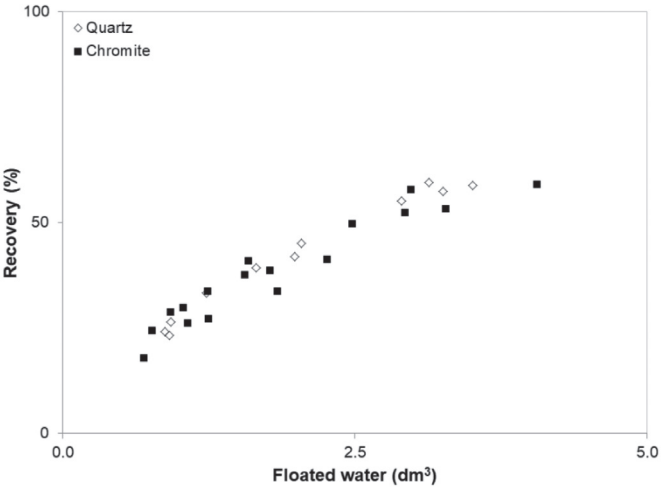

Figure 13—Recovery of chromite and quartz by entrainment (after Kirjavainen, 1989)

where St and R are the Stokes number and density ratio respectively. These are defined as:

$$St = \frac{2}{9}\left(\frac{a}{L}\right)^2 Re \quad [9]$$

$$R = \frac{1}{\frac{1}{2}+\frac{\rho_p}{\rho_L}} \quad [10]$$

Wang *et al.* did not define the type of Reynolds number used in their study. For this illustration, the Reynolds number will be defined for the pulp phase of flotation, and with respect to initial operating conditions.

$$Re = \frac{ND^2\rho}{\mu} \quad [11]$$

where

a is the radius of the particle (m)
L is the flow length scale (m), taken as impeller diameter by Wang *et al.* (2014)
Re is the Reynolds number
N is the impeller speed (s^{-1})
D is the impeller diameter (m)
ρ is the pulp density ($kg{\cdot}m^{-3}$)
μ is the viscosity of the pulp (Pa·s)
ρ_p is the particle density ($kg{\cdot}m^{-3}$)
ρ_L is the fluid density ($kg{\cdot}m^{-3}$)

Consider two particles, FeSi and silica, with ρ_p of 5010 and 2650 $kg{\cdot}m^{-3}$ respectively. Both particles are present in water with a ρ_L of 1000 $kg{\cdot}m^{-3}$. Using Equation [10], the density ratios for FeSi and silica were calculated as being 0.18 and 0.32 respectively. The Reynolds number for the flotation pulp was determined for N = 25 s^{-1} (*i.e.* 1500 r/min), D = 0.05 m, pulp density 1323 $kg{\cdot}m^{-3}$, and pulp viscosity 1.30 ×10^{-4} Pa·s. The pulp density was determined by using the initial mass fraction of each component (water, ore, and FeSi) and their respective densities. Cilek (2009) estimated the pulp viscosity using Equation [12], where μ_w is the water viscosity (8.90 ×10^{-4} Pa·s was used in this illustration) and φ is the fraction of the pulp occupied by solids; this was estimated from the initial mass fraction and density of each component in the pulp.

$$Re = \frac{ND^2\rho}{\mu} \quad [12]$$

The particle inertia number was estimated for a range of particle sizes using the pulp Reynolds number (which was calculated as 612 502) and the Stokes number. Figure 14 shows the results of this simulation. According to Wang *et al.* (2014), for $\sigma << 1$, the particle moves passively, that is, the particle matches its own velocity to that of the fluid. As σ increases, a particle becomes non-passive and its inertia (due to its higher mass) causes it to deviate from the fluid streamlines. So from Figure 14, the inertia numbers exhibited by FeSi and silica are similar up to a particle radius of 25 µm. The inertia number increases more rapidly for FeSi than for silica for a particle radius greater than 25 µm, but the number is still less than unity up to a particle radius of about 100 µm. The key point from this illustration is that fine material (particle diameters less than 50 µm for the purpose of this example) exhibits similar inertia numbers, which are much less than unity. This implies that irrespective of particle density, these fine particles will most likely follow the streamlines in the flotation pulp and travel towards the froth. Hence, the classification of particles in the flotation pulp

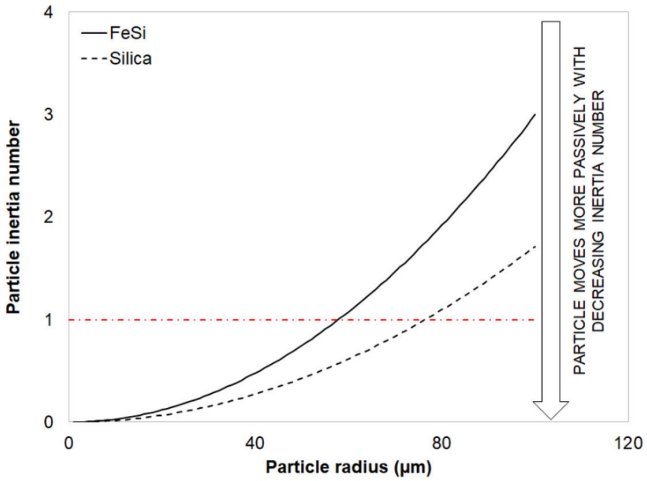

Figure 14—Influence of particle size on particle inertia for FeSi and silica in flotation pulp

(for entrainment) is strongly related to their inertia and ability to follow the fluid streamlines.

In the froth, a different entrainment classification process takes place. Here the particle settling rate plays a vital role in determining its recovery to the flotation concentrate. According to Kirjavainen (1992) and George, Nguyen, and Jameson (2004), a laminar flow regime may be assumed in the froth phase. Under this regime, the particle settling velocity under hindered conditions may be calculated using Equation [13].

$$v_{hs} = v_s(1-C_v)^m = \frac{(\rho_p-\rho_L)}{18\rho_L}\frac{gd^2}{\mu_L}(1-C_v)^m \quad [13]$$

where

v_s is the particle settling velocity in an unhindered environment ($m{\cdot}s^{-1}$)
g is the gravitational acceleration constant (9.81 $m{\cdot}s^2$)
d is the particle diameter (m)
ρ_p is the particle density ($kg{\cdot}m^{-3}$)
ρ_L is the fluid density ($kg{\cdot}m^{-3}$)
μ_L is the fluid viscosity (Pa·s)
v_{hs} is the hindered particle terminal settling velocity ($m{\cdot}s^{-1}$)
C_v is the the volumetric concentration of solids in the environment (dimensionless)
m is an empirical constant related to the Reynolds number. A value of 4.6 can be assumed for Reynolds numbers less than 0.2.

Figure 15 shows the results for the settling velocity of a FeSi and a silica particle at different particle sizes. In this illustration, particle densities for FeSi and silica were set at values given earlier, the fluid viscosity and density were as for water. C_v for the purpose of this illustration was calculated as 0.07 and was determined for the first concentrate collected from the rougher flotation test. The results from this analysis show that the settling velocities for both particles are similar up to a particle size of 20 µm. In addition to knowing the settling rate of a particle, the upward flow of water should be calculated since this will determine if a particle will settle out of the froth. The water velocity for the first rougher flotation concentrate was roughly estimated using the water collected in that time interval, the density of water, and the surface area at the top of the rougher cell. A value of 6.32 × 10^{-5} $m{\cdot}s^{-1}$ was calculated. The water velocity is much higher than the settling velocity for the particles at all sizes. This implies that if particles (fines up to coarse) enter

the flotation froth, there is a strong chance of these particles being recovered by entrainment.

In summary, the discussion shows that both particle size and density are crucial in determining the susceptibility of a particle to entrainment, since these factors determine the mass of a particle and hence its inertia in the pulp and settling rate in the froth. The lower the inertia of the particle, the greater chance of it following the fluid streamlines into the pulp-froth interface. These particles are pushed into the froth as more mineralized bubbles ascend. Should the particle enter the froth, the settling rate of the particle relative to the fluid velocity determines if the particle will settle out of the froth or be carried into the flotation concentrate.

Conclusions

Recovery by entrainment was measured in batch rougher and cleaner flotation tests using ferrosilicon (FeSi) as a tracer component. The tracer was added to Merensky ore flotation so entrainment could be examined in relation to the flotation of an actual ore and not as a mono-component test involving FeSi only.

The recovery by entrainment from rougher and cleaner flotation, for three different size classes, was not represented adequately by the typical linear and nonlinear entrainment models proposed in the literature. Therefore a three-parameter Weibull probabilistic model was proposed for modelling rougher and cleaner entrainment data simultaneously. The use of water flow rate, rather than water recovery, made it possible to link batch data from rougher and cleaner tests. The model gave a good fit to the experimental data, having an adjusted coefficient of determination of 0.9935. Also, the model-fitted parameters were a logical description of entrainment across rougher and cleaner flotation.

There may be some concern regarding the use of FeSi as a tracer due to its density being higher than that of most gangue minerals. However, evidence from the literature and an example are given to illustrate the influence of particle density and size on entrainment. Both these parameters determine the mass of a particle, which in turn determines the particle inertia in the flotation pulp and settling rate in the froth.

Recovery by entrainment is more dominant for fine particles. For fine particles, the recovery by entrainment appears to be the same (refer to Figure 12) irrespective of particle density. Hence, FeSi can be used as a proxy to measure entrainment, but it is recommended that a size analysis be performed so that the FeSi entrainment parameters determined by particle size (particularly fines, <5 µm) can be applied to entrainment measurements of other non-floatable minerals.

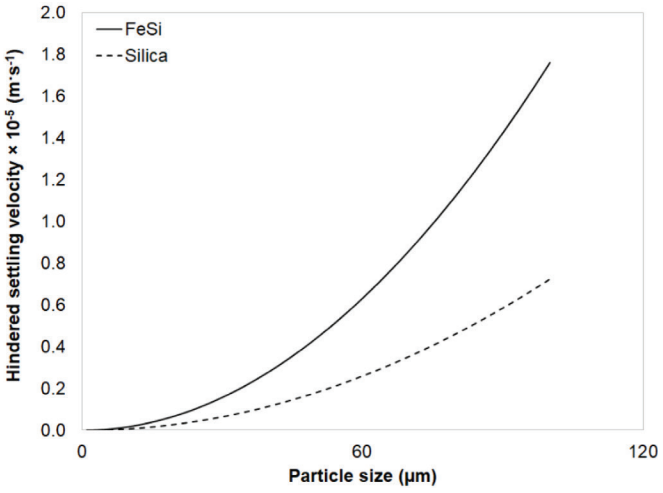

Figure 15—Influence of particle size on settling velocity of FeSi and silica particles in flotation froth

Recommendations

Further work should be carried out to investigate the application of the proposed model to modelling entrainment data from continuous and batch flotation tests. In addition, a more rigorous examination of the influence of particle density should be carried out to supplement the illustrative assessment presented.

Acknowledgements

This study was carried out by the author in his own capacity and does not reflect the views of SGS South Africa on the subject. The author would like to thank SGS for the use of their facilities.

References

Bisshop, J.P. and White, M.E. 1976. Study of particle entrainment in flotation froths. *Transactions of the Institution of Miningl and Metallurgy*, *Section C*, vol. 85. pp. C191–194.

Cilek, E.C. 2009. The effect of hydrodynamic conditions on true flotation and entrainment in flotation of a complex sulphide ore. *International Journal of Minerals Processing*, vol. 90. pp. 35–44.

Ekmekçi, Z., Bradshaw, D.J., Allison, S.A., and Harris, P.J. 2003. Effects of frother type and froth height on the flotation behaviour of chromite in UG2 ore. *Minerals Engineering*, vol. 16. pp. 941–949.

Engelbrecht, J.A., and Woodburn, E.T. 1975. The effects of froth height aeration rate and gas precipitation on flotation. *Journal of the South African Institute of Mining and Metallurgy*, vol. 76, no. 3. pp. 125–132.

George, P., Nguyen, A.V., and Jameson, G.J. 2004. Assessment of true flotation and entrainment in the flotation of submicron particles by fine bubbles. *Minerals Engineering*, vol. 17. pp. 847–853.

Kirjavainen, V.M. 1989. Application of a probability model for the entrainment of hydrophilic particles froth flotation. *International Journal of Minerals Processing*, vol. 27. pp. 63–74.

Kirjavainen, V.M. 1992. Mathematical model for the entrainment of hydrophilic particles in froth flotation. *International Journal of Minerals Processing*, vol. 35. pp. 1–11.

Konopacka, Z. and Drzymala, J. 2010. Types of particle recovery-water recovery entrainment plots useful in flotation research. *Adsorption*, vol. 16. pp. 313–320.

Laplante, A.R. 1980. The effect of air flow rate on the kinetics of flotation. PhD thesis, University of Toronto, Canada.

Lynch, A.J., Johnson, N.W., McKee, D.J., and Thorne, G.C. 1974. The behaviour of minerals in sulphide flotation process with reference to simulation and control. *Journal of the South African Institute of Mining and Metallurgy*, vol. 74, no. 9. pp. 349–360.

Maachar, A. and Dobby, G.S. 1992. Measurement of feed water recovery and entrainment solids recovery in flotation columns. *Canadian Journal of Metallurgy and Materials Science*, vol. 31, no. 3. pp. 167–172.

Ross, V.E. 1989. Determination of the contributions by true flotation and entrainment during the flotation process. *Proceedings of the International Colloquium: Developments in Froth Flotation*. Southern African Institute of Mining and Metallurgy, Johannesburg. https://www.saimm.co.za/Conferences/FrothFlotation/005-Ross.pdf

Smith, G. and Warren, L.J. 1989. Entrainment of particles into flotation froths. *Mineral Processing and Extractive Metallurgy Review*, vol. 5, no. 1–4. pp. 123–145.

Trahar, W.J. 1981. A rational interpretation of the role of particle size in flotation. *International Journal of Minerals Processing*, vol. 8. pp. 289–327.

Wang, S., Metcalfe, G., Stewart, R.L., Wu, J., Ohmura, N., Feng, X., and Yang, C. 2014. Solid–liquid separation by particle-flow-instability. *Energy & Environmental Science*, vol. 7, no. 12. pp. 3982-3988. https://doi.org/10.1039/C4EE02841D

Wang, L., Peng, Y., Runge, K., and Bradshaw, D. 2015. A review of entrainment: Mechanism, contributing factors and modelling in flotation. *Minerals Engineering*, vol. 70. pp. 77–91

Warren, L.J. 1985. Determination of the contribution of true flotation and entrainment in batch flotation tests. *International Journal of Mineral Processing*, vol. 14, no. 1. pp. 33–44.

Zheng, X., Johnson, N.W., and Franzidis, J.-P. 2006. Modelling of entrainment in industrial flotation cells: water recovery and degree of entrainment. *Minerals Engineering*, vol. 19. pp. 1191–1203. ◆

Work stress of employees affected by skills shortages in the South African mining industry

M. Thasi[1] and F. van der Walt[1]

Affiliation:
[1]Central University of Technology, Bloemfontein, South Africa.

Correspondence to:
F. Van Der Walt

Email:
fvdwalt@cut.ac.za

Dates:
Received: 13 Mar. 2019
Revised: 15 Oct. 2019
Accepted: 21 Nov. 2019
Published: March 2020

How to cite:
Thasi, M. and van der Walt, F. Work stress of employees affected by skills shortages in the South African mining industry. The Southern African Insitute of Mining and Metallurgy

DOI ID:
http://dx.doi.org/10.17159/2411-9717/666/2020

ORCiD ID:
F. Van Der Walt
https://orcid.org/0000-0001-6110-0716

Synopsis

Skills shortages in core occupational categories in the South African mining industry have reached crisis proportions. The reason for this is that the demand for qualified individuals exceeds the supply. The result is that available employees are overburdened with duties and responsibilities. To curb the current exodus of qualified employees, such as artisans and engineers, mining companies need to consider the wellbeing of these individuals. This study investigated the work stress of employees affected by skills shortages at selected gold mines in South Africa. A descriptive quantitative research design was employed. Convenience sampling was used, and the final sample consisted of 188 artisans and engineers. The respondents indicated that they do experience work-related stress. Occupational aspects that were statistically significantly related to work stress were the physical work environment, career-related issues, and HR policy, especially pertaining to remuneration and fringe benefits. The findings of the study deepen the understanding of work stress of employees employed in occupational categories where skills shortages exist. The findings suggest that mining companies nationwide need to place increased focus on the wellbeing of their employees, so as to prevent further skills shortages in this industry.

Keywords
work stress, skills shortages, mining industry, artisan, engineer.

Introduction

Skills shortages are widely regarded as a key factor preventing economic growth rate targets in South Africa from being achieved (Erasmus and Breier, 2009). One industry that makes a significant contribution to the national economy, as well as the economy of the African continent, is South Africa's mining industry (Chamber of Mines of South Africa, 2013). Unfortunately, this industry is currently experiencing critical skills shortages in occupational categories which form part of the core business, such as engineers (Khalane, 2011) and artisans (Oberholzer, 2010). Employees working in occupations affected by skills shortages are often burdened with additional duties and responsibilities, and thus may be more prone to work stress, which could possibly adversely affect their mental health and optimal functioning. Masia and Pienaar (2011) refer to research that has confirmed that role overload, role ambiguity, and role conflict are indicative of work stress. Work stress is a complex and dynamic phenomenon, in which various factors, or stressors, and modifying variables interact (Siegrist, as cited in Ogińska-Bulik, 2005). It is possible that employees working in occupational categories affected by skills shortages are experiencing work stress, due to the overburdening of their internal and/or external resources. Therefore, the current study represents an attempt to contribute to managers' understanding of skills shortages, which will assist them to address human resource issues more effectively.

Skills shortages have been scientifically investigated in sectors such as construction (Bennett and McGuinness, 2009) and information technology (Wickham and Bruff, 2008), but the topic has not yet been adequately studied within the context of the mining industry. A study conducted by Paten (2006) in the construction industry found that stress levels of respondents were attributed to inadequate staffing, leading to role overload, which was one of the major causes of occupational health issues. Furthermore, previous studies investigating skills shortages have focused mainly on the economic impact (*e.g.* Bennett and McGuinness, 2009; Razzak and Timmins, 2008). Apart from the economic impact of skills shortages, however, one needs to ask the question 'Where do skills shortages leave employees who need to do the work in occupational categories affected by these shortages?' It is important to ask this question, as the mental health of individuals working in male-dominated industries, such as mining, has received increased interest due to the high incidence of suicide in

these industries (Considine *et al.*, 2017). Therefore, from a mental health perspective, there is a need to extend the current literature on work stress in occupations where skills shortages are experienced.

Research aim, objectives, and hypotheses

The research objective of the study was to determine whether the occupational aspects of organizational functioning, job-related tasks, the physical work environment, career-related issues, social issues, and HR policy influence the experience of work stress by employees in occupational categories where skills shortages are prevalent. The research hypotheses for the study are that the following factors have statistically significant relationships to the experience of work stress.

H1: Organizational functioning
H2: Job-related tasks
H3: The physical work environment
H4: Career-related issues
H5: Social issues
H6: HR policy.

The study addresses the current dearth of empirical research focusing on stress within the context of the mining industry. Apart from the theoretical contribution of the study, the findings regarding the experience and causes of work stress can be useful to mining companies for redesigning current retention strategies and wellness programmes. Retaining competent employees and increasing their mental health and happiness increases productivity and reduces costs (Carmichael *et al.*, 2016), which is currently much needed in the South African mining industry.

Literature survey

Stress

South Africans from all walks of life experience abnormally high stress levels compared to the rest of the world, and these high stress levels often manifest in emotional behaviour (van Zyl and Bester, as cited in Oosthuizen and van Lill, 2008). Del Fabbro (2012) asserts that high stress levels cause employees to be less able to manage their emotions and to deal with pressure, and to be more likely to act destructively. Furthermore, problem-solving and decision-making skills are impaired, and the immune system is negatively affected, leading to more illnesses and prolonged recovery periods, which all have an adverse impact on productivity (Del Fabbro, 2012). Notwithstanding these negative outcomes associated with severe stress, stress is a natural part of everyday living, and it has become an integral part of jobs in every sector. However, if not managed effectively, work stress can have a negative effect on the physical and the emotional wellbeing of an individual (Hasnain, Naz, and Bano, 2010). Although some circumstances may have a detrimental effect on the wellbeing of an individual, the individual's perception of the situation will determine whether the situation will be stressful or not (Hasnain, Naz, and Bano, 2010). Furthermore, potential stress will become actual stress only if the outcome is both uncertain and important (Robbins *et al.*, 2009). Thus, although stress is often regarded as negative, it can also be a positive force, enabling individuals to reach their full potential.

Work stress

Stress in the workplace is a growing concern in the current state of the global economy, where employees increasingly face conditions of overwork and job insecurity, low levels of job satisfaction, and a lack of autonomy. Work stress manifests in harmful physical and emotional responses that occur when job requirements do not match the employee's capabilities, knowledge, skills, resources, and needs, and also the expectations of the employer (Negi, 2014). Furthermore, work-related stress occurs when there is a mismatch between the demands of the job and the resources and capabilities of the individual worker. Work stress has been shown to have a detrimental effect on the health and wellbeing of employees, as well as on workplace productivity and profits (Bickford, 2005). A number of factors can lead to stress reactions in the workplace, and these factors are often referred to as stressors. Stressors can be categorized as extra-organizational stressors, organizational stressors, group stressors, and individual stressors (Luthans, 2002; Velnampy and Aravinthan, 2013). In combination or individually, these stressors may impinge upon employees at every organizational level, and in every type of organization (Velnampy and Aravinthan, 2013).

Problems outside of the work environment can also contribute to stress and make it difficult for the individual to cope with the pressures of work, and can prevent optimal performance (Gibbens, 2007). Various factors within an organization can cause a person to experience stress, such as task demands, physical demands, role demands, and interpersonal demands (Robbins *et al.*, 2009). Group pressures, in contrast, include aspects such as pressure to increase or to limit output and pressure to conform to the group's norms (Griffin and Moorhead, 2012). If the individual's expectations differ from those of the group, they may experience high levels of stress, because they will often be excluded from group interactions or they will not experience group acceptance and support (Coopmans, 2007). On a personal level, individual dispositions also tend to moderate the effect that stressors have on an individual's health (Luthans, 2011; Quick and Nelson, 2009). Examples mentioned of such individual dispositions are Type A and Type B personalities, learned helplessness, self-efficacy, psychological hardiness, and optimism.

Schutte, Edwards, and Milanzi (2012) assert that the South African mining industry is rife with stress and difficult working conditions, despite the strategic drive to reduce injuries and ill-health. These difficult working conditions include challenging physical and cognitive job demands and the presence of hazardous materials, which have the potential to cause workplace accidents, injuries, and fatalities, making the mining industry one of the most dangerous and hazardous occupational settings in South Africa (Smit, de Beer, and Pienaar, 2016). However, despite the stressful nature of this industry, there is a dearth of research studies focusing on stress in this context (Schutte, Edwards, and Milanzi, 2012). Therefore, it is necessary to further investigate work stress in the South African mining industry. For the purposes of this study, experiences of work stress and work-related causes of stress were measured. The following work-related causes of stress were considered (Schaap and Kekana, 2016):

- Organizational functioning, which refers to employees' contribution to decision-making and strategy creation, supervisory or managerial trust, an effective organizational structure, a positive management climate, recognition, and the degree of openness in communication between employees and supervisors or managers.

- Job-related tasks, or task characteristics, which comprise the extent to which employees can control their work, adequate rewarding of executing work challenges, the quality of instruction received for a task, the level of autonomy given to employees, reasonable deadlines, utilization of employees, and work variety.
- Physical working conditions, which are aspects such as (in)adequate lighting, the temperature and the cleanliness of the work area, the availability of adequate office equipment, and the distance to and the condition of the bathrooms.
- Career opportunities, which refers to employees' expectations regarding further training and development, utilization of skills and talents, and job security.
- Social issues, which include employees' experience of social interaction at work, expectations with regard to job status, positive relationships with others, and reasonable social demands.
- HR policy, especially pertaining to remuneration and fringe benefits. Remuneration expectations refer to a fixed, a commission-based or a piece-rate salary, and a fair HR policy on remuneration. Fringe benefits include any tangible or intangible rewards that a company offers its employees.

From the mentioned research findings, one may expect that the challenging physical working conditions evident in the South African mining industry will be the main predictor of the prevalence of work stress in this industry.

Skills shortages

'Skills shortages' seems to be a somewhat vague concept, involving many specific components, but the core issue is that the demand for certain skills exceeds the supply of such skills (Daniels, 2007). Authors are not all in agreement on the definition of skills shortages, and therefore the concept has been defined differently, seemingly depending on the individual authors' areas of interest. For example, economists focus mostly on skills shortages and their relationship to productivity (Sebusi, 2007), while South Africa's Department of Labour does not make reference to this relationship (South Africa, 2006). The Department of Labour defines skills shortage as a situation in which employers are unable to fill, or experience difficulty in filling, vacancies in a specific occupation or field of specialization, due to an insufficient number of workers with the required qualifications and experience (John, 2006). For the purposes of this study, the latter definition will be used.

Core skills are applicable to occupations that form part of the core production and operations of an organization. These core skills, or core positions, are essential to an organization, and without them the organization cannot function (South Africa, 2008). Currently, critical skills shortages in South Africa's mining industry are experienced in the occupational categories of engineer and artisan (Oberholzer, 2010; Toni, 2009). Only a limited number of qualified engineers and artisans are currently available to occupy these positions, which may potentially have an adverse impact on their work experiences and organizational performance. Because engineers and artisans are part of the core business of the mining industry, shortages in these occupational groups are a burden. Not only do such shortages affect the performance of the industry and the country's economic growth rate, but they may also potentially have a detrimental impact on individuals working in occupational categories where skills shortages are experienced. Therefore, it is important to investigate how stressed individuals are within occupational categories affected by skills shortages, in order to deal with potential wellness issues before the problem of skills shortages worsens.

Methodology

Research design

A descriptive quantitative research design was used. The study was cross-sectional in nature because the research was carried out at a specific point in time on a sample from two mining companies.

Population and sampling strategy

Two mining companies agreed to participate in the study. A sample was drawn from two core mining-sector occupational categories, namely artisans and engineers, because these occupational categories are severely affected by skills shortages. A total of 43 engineers and 1015 artisans were employed at these mining companies at the time the data was collected. Only readily accessible respondents could participate in the study, and therefore the convenience sampling method was used to draw a sample from the target population. The final sample consisted of 188 artisans and engineers. A description of the sample is presented in Table I.

From the information presented in Table I, the sample may be described as mostly male, black African, falling within the age category of 20–39 years, having a Grade 12 or higher qualification, and having worked for 1–15 years in their current positions and at the current organization. Although the sample is skewed towards the position of artisan, the population included 43 engineers and 1015 artisans, and the sample may therefore be regarded as representative of the population.

Data collection procedure

Primary data was collected by means of self-administered questionnaires. The questionnaires were personally distributed and collected by the researcher at a pre-arranged time on a pre-arranged day. Attached to the research questionnaire was an introductory letter, in which the purpose of the study was clearly stated. The questionnaire consisted of three sections. The first section consisted of a self-constructed biographical questionnaire which was designed to solicit relevant demographic information from respondents regarding their gender, race, age, work experience, highest academic qualification, and their occupation, in order to describe the sample. The second section consisted of an abridged version of the Work and Life Circumstances Questionnaire (WLQ) (van Zyl and van der Walt, 1991). This section of the questionnaire consisted of 100 items, and was aimed at measuring the levels of stress that an employee may be experiencing, and identifying the causes of stress within the work situation (van Zyl and van der Walt, 1991). The following causes of stress within the work situation were investigated: the functioning of the organization, the characteristics of the tasks to be performed, the physical working conditions and the job equipment, social and career issues, and HR policy, especially pertaining to remuneration and fringe benefits. A sample item is 'How often in your work do you feel worried?' The respondents were required to rate how often at work they experience each item, where the possible responses range from 1 ('virtually

Table I

Profile of the respondents (n = 188)

Variable	Level of variable	N	%
Gender	Male	163	86.7
	Female	25	13.3
Race	Black African	111	59.4
	White	73	39.0
	Coloured	3	1.6
	Indian/Asian	0	0
Age	20–39 years	103	54.8
	40–59 years	85	45.2
	60+ years	0	0
Number of years in current position	1–15 years	123	65.4
	16–30 years	54	28.7
	31–45 years	11	5.9
Total number of years working in the current organization	1–15 years	123	66.8
	16–30 years	55	29.9
	31–45 years	6	3.3
Highest qualification	Grade 10–11	40	21.3
	Grade 12	60	31.9
	Post-matric certifcate	47	25.0
	National diploma/degree	41	21.8
Position	Artisan	178	94.7
	Engineer	10	5.3

never') to 5 ('always'). The third section consisted of an open-ended question to gain insight into engineers' and artisans' perceptions of the impact of skills shortages on their experience of work stress. This question gave respondents the opportunity to articulate their perceptions of the impact of skills shortages on work stress.

Instrument validation and piloting

Regarding validity, content validity was considered. Content validity was ensured by assessing the questionnaire to establish whether the questions posed were clearly formulated and concise. Two experts, an industrial psychologist and a human resource management specialist, evaluated the statements in the questionnaire to establish whether they were appropriate to measure work stress. A research psychologist also reviewed the questionnaire in terms of its content, format, and layout. Note should be taken that the WLQ is classified as a psychometric test by the Health Professions Act, Act 56 of 1974, Notice 155 of 2017 (South Africa, 2017). This implies that the psychometric properties of the test have been confirmed for a South African sample.

Before the final questionnaire was distributed to the sample, a group of 10 individuals participated in a pilot study. The individuals were requested to complete the questionnaire and to provide critical feedback, general comments, and/or advice, to ensure that the wording of the questionnaire was understandable and that the layout was appropriate. In addition, feedback was given on the time it took to complete the questionnaire. All the pilot study questionnaires were returned, comments were considered, and amendments were made.

Ethical considerations

Ethical clearance was obtained from the hosting university. Furthermore, in order to obtain informed consent from those parties that would be affected by the study, the following criteria were met, in accordance with the suggestions of Welman, Kruger, and Mitchell (2005). Written permission was requested from the respective mining companies to conduct the research study. In order to obtain informed consent from the respondents, an introductory letter explaining the purpose of the research project was composed and attached to the final questionnaire. The introductory letter made specific reference to respondents' right to confidentiality, anonymity, and voluntary participation. At the end of the questionnaire, respondents were requested to provide their contact details if they wanted to receive a copy of the results.

Data analysis

To test the hypotheses, a variance-based approach to structural equation modelling (SEM), namely partial least squares structural equation modelling (PLS-SEM), was used. The statistical software program used was SmartPLS version 3.2.8. Variance-based structural equation modelling software such as SmartPLS provides robust results in complex models assessed using small sample sizes (Hair, Ringle, and Sarstedt, 2011). In this study, the six independent variables were measured using 50 items, while the sample size was 188 respondents. Before testing the hypotheses, the measurement model was assessed for internal consistency and construct validity (Hair *et al.*, 2006). The assessment of internal consistency reliability entailed calculating the Cronbach's alpha value and the composite reliability (CR) value for each construct. The Cronbach's alpha value represents the 'conservative' estimate of reliability, and the CR value represents the 'liberal' estimate of reliability. Therefore, the true reliability of a scale lies between the Cronbach's alpha and the CR value of the scale. For evidence of internal consistency reliability, the Cronbach's alpha value and the CR value should be 0.7 or higher. Hair *et al.* (2006) assert that Cronbach's alpha values of 0.6 to 0.7 are deemed the lower limit of acceptability. To assess convergent validity, the outer loadings must be 0.7 or higher and must be statistically significant ($p \leq 0.05$ [two-tailed]). Also, the average variance extracted (AVE) for each construct must be 0.5 or higher. However, items with loadings between 0.4 and 0.7 should be considered for removal only when the removal of the item(s) would increase the reliability values and/or the AVE of the associated construct above the minimum values. To assess discriminant validity, the Fornell-Larcker criterion was applied. The Fornell-Larcker criterion entails comparing the square roots of the AVEs of two constructs with the correlation between the two constructs. For evidence of discriminant validity, the square root of the AVE of each of the two constructs forming a pair must be higher than the correlation between the two constructs.

To test the hypotheses, the bias-corrected accelerated bootstrapping procedure was used to calculate t-values and p-values (two-tailed) (Hair *et al.*, 2006). Acceptance of a hypothesis was based on the following decision criteria: (1) The sign of the path coefficient must be in the hypothesised direction, and (2) the p-value (two-tailed) must be equal to or less than 0.05.

Findings

Assessment of the measurement model

In line with the data analysis procedure described in the previous

section, the original measurement model of the independent variables was assessed for reliability and validity. However, although the assessment of the measurement model confirmed internal consistency reliability, the AVE of the six independent variables did not exceed 0.5. To achieve acceptable convergent validity, followed by discriminant validity, items with a low outer loading were systematically removed until the AVE of each factor exceeded 0.5 and discriminant validity could also be proved. In Table II the measurement model results are presented for the modified measurement model, which met the requirements for internal consistency and convergent validity.

Next, the discriminant validity of the measurement model was assessed. As seen in Table III, the square root of the AVE of each construct forming a pair is higher than the correlation between the two constructs. Thus, based on the results presented in Table III, it can be concluded that the modified measurement model also exhibits adequate discriminant validity, and the hypothesis testing can thus be performed.

Testing of the hypotheses

In Figure 1 the results of the testing of the hypotheses are summarized. As seen in Figure 1, the six independent variables explain 41.5% of the variance in the dependent variable (experience of work stress). Of the six independent variables, three variables have a statistically significantly influence on the experience of work stress – two factors exerted a negative influence, and one factor exerted a positive influence. Thus, H1, H4, and H5 are rejected, and H2, H3, and H6 are accepted. According to the results reported in Figure 1, remuneration, benefits, and policy had the strongest negative statistically significant influence on experience of work stress (–0.312; p = 0.001 [two-tailed]). Job-related tasks also had a negative statistically significant influence (–0.263; p = 0.002 [two-tailed]. In contrast, physical work environment was the only factor that had a statistically significant positive influence (0.233; p = 0.042 [two-tailed]) on experience of work stress.

Table III

Discriminant validity results

Factor	CI	JRT	OF	PWE	RBP	SI
CI	0.762					
JRT	0.684	0.745				
OF	0.723	0.620	0.809			
PWE	0.692	0.512	0.687	0.746		
RBP	0.719	0.595	0.602	0.663	0.751	
SI	0.694	0.630	0.790	0.560	0.562	0.814

CI: Career-related issues; JRT: Job-related tasks; OF: Organizational functioning; PWE: Physical work environment; RBP: Remuneration, benefits, and policy; SI: Social issues
Note: On the diagonal are the square roots of the AVEs and below the diagonal are the correlations between the factors

Perceived relationship between work stress and skills shortages

In order to determine the perceptions of respondents employed in core occupational categories (*i.e.* artisans and engineers) regarding the impact of skills shortages on their experience of work stress, the following question was posed: 'How would you describe the impact of skills shortages on your stress levels?' The responses to this question show that 13% (n = 24) indicated that

Table II

Measurement model results

Factor	Item	Outer loading	p-value (two-tailed)	Cronbach's alpha	CR	AVE
Career-related issues	CI2	0.702	0.000	0.763	0.847	0.581
	CI6	0.768	0.000			
	CI7	0.747	0.000			
	CI9	0.827	0.000			
Job-related issues	JRT15	0.703	0.000	0.732	0.832	0.555
	JRT4	0.701	0.000			
	JRT6	0.751	0.000			
	JRT7	0.819	0.000			
Organizational functioning	OF3	0.886	0.000	0.743	0.849	0.654
	OF6	0.737	0.000			
	F7	0.797	0.000			
Physical work environment	PWE3	0.875	0.000	0.819	0.859	0.557
	PWE4	0.878	0.000			
	PWE5	0.737	0.000			
	PWE6	0.559	0.000			
	PWE7	0.624	0.000			
Remuneration, benefits, and policy	RBP2	0.669	0.000	0.609	0.794	0.564
	RBP6	0.784	0.000			
	RBP7	0.793	0.000			
Social issues	SI2	0.716	0.000	0.830	0.886	0.662
	SI6	0.756	0.000			
	SI7	0.894	0.000			
	SI8	0.874	0.000			

CI: Career-related issues; JRT: Job-related tasks; OF: Organizational functioning; PWE: Physical work environment; RBP: Remuneration, benefits, and policy; SI: Social issues

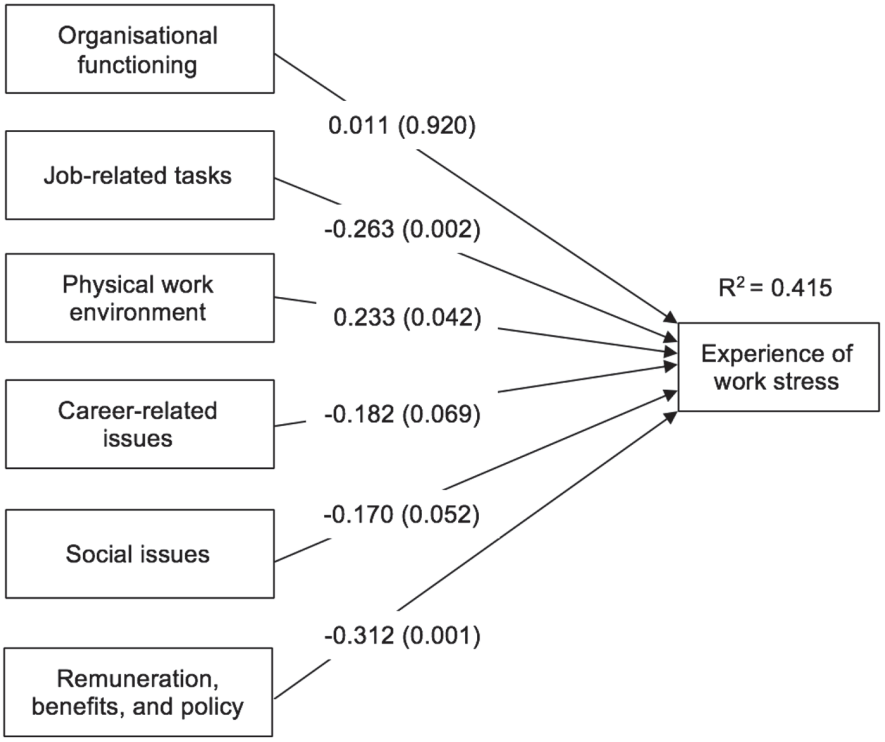

Figure 1—Structural model results

skills shortages did have an impact on their stress levels, 51% (n = 97) indicated that they were not sure, and 34% (n = 64) indicated that skills shortages did not have an impact on their stress levels. A total of three respondents (2%) did not answer the question. The responses indicate that many (34%) of the artisans and engineers included in the sample held the opinion that skills shortages do not have an impact on their levels of stress, while some (13%) indicated that skills shortages do have an impact on their levels of stress.

From the data collected with the open-ended question regarding the impact of skills shortages on work stress, the following themes emerged: coping mechanisms, work-related characteristics, work-life balance, and the physical work environment. The emerging themes regarding the impact of skills shortages on work stress levels of artisans and engineers included in the sample can be divided into individual, extra-organizational, and organizational factors. On an individual level, it seems that some of the respondents struggle to cope with the work stress they are exposed to. Regarding extra-organizational factors, the theme of work-life balance emerged. From the responses, it is clear that some of the respondents are experiencing work stress and non-work-related stress. Organizational factors included the themes of job-related characteristics and the physical work environment. Most of the responses listed under job-related characteristics made reference to work overload. The themes that emerged support previous research findings reported for a South African sample, which indicate that work load issues are the greatest cause of stress, followed by people or relationship issues, and then work-life balance (Nelson, as cited in Coetzee and de Villiers, 2010).

Discussion of results

As is evident from the results presented in Figure 1, the physical work environment had a positive and statistically significant influence on the experience of work stress. This finding is unexpected, and it contradicts previous research findings which indicate that the physical work environment of the mining industry is the main cause of work stress (*e.g.* Schutte, Edwards, and Milanzi, 2012). The physical work environment subsection of the questionnaire measured specifically the availability of job equipment, such as stationery, tools, and electronic and laboratory equipment, and their working order, as well as being allowed to function in inadequate physical working conditions (*e.g.* inadequate lighting, temperature, and office space). Thus, the more positively these aspects were evaluated, the more work stress the respondents reported. However, the reality is that employees in the mining industry are exposed to harsh working conditions, long working hours, sometimes unsafe working conditions, highly unionized environments, and enormous pressure to perform (Brand-Labuschagne *et al.*, 2012). Furthermore, mine workers in general are exposed to various safety hazards, such as falling rocks, dust, intense noise, fumes, and high temperatures (Badenhorst, 2006). It is possible that these industry-specific issues were not covered by the items in the questionnaire. It is also possible that the respondents did not perceive their physical work environment as a cause of stress, although it can potentially be the main cause of work stress. Furthermore, as was indicated previously, potential stress will become actual stress only if the outcome is both uncertain and important (Robbins *et al.*, 2009). Therefore, it is possible that the respondents did not perceive the physical work environment as important, and also, their familiarity with this environment may reduce their uncertainty in this regard.

HR policy, especially pertaining to remuneration and fringe benefits, was negatively and statistically significantly related to

the experience of work stress. This finding is supported by the argument offered by van der Walt *et al.* (2016), who state that in occupational categories where skills shortages exist, employees are likely to do more work but are not necessarily being remunerated or rewarded for the additional work they perform. The latter authors further suggest that mining companies should mindfully and continuously consider the structuring of remuneration packages and HR policy pertaining to occupational health and safety, in order to improve the job satisfaction levels of employees affected by skills shortages.

The findings of the study further revealed that job-related tasks were negatively and statistically significantly related to the experience of work stress. Consistent with the findings of the current study, Robbins (2005) asserts that employees prefer jobs that afford them the opportunity to apply their skills and abilities, that offer them variety and freedom, and that provide them with constant feedback on their performance. Furthermore, employees who find their work interesting are likely to be more satisfied and motivated than employees who do not enjoy their jobs. Ongori and Agolla (2008) came to a similar conclusion, and identified the following job-related causes of work-related stress: work overload, time pressure, role ambiguity, long working hours, and shift work. Supporting this finding, some respondents mentioned in their response to the open-ended question that work overload is a cause for concern. It is possible that due to the shortage of employees in the artisan and engineer categories, incumbents may feel that they are given too many tasks, which may leave them feeling that they are not in control of their work and that they cannot meet strict production deadlines. The finding that task characteristics influence work-related stress is of paramount importance to mining companies, and therefore they need to consider whether employees affected by skills shortages are overloaded, whether employees are fairly rewarded for executing additional responsibilities, whether proper instructions are given, and whether reasonable deadlines are set. It is further necessary that appropriate HR policies are developed and continuously updated in order to ensure equity and mental health. By considering these aspects, mining companies can prevent artisans and engineers from being 'poached' by international mining companies, thereby exacerbating the current skills shortages in these occupational categories.

Conclusion

Despite the theoretical and practical contribution of the study, it was not without limitations. Firstly, the study was limited to mining engineers and artisans employed on two gold mines in South Africa. Although the ideal would have been to include a random sample of artisans and engineers working in the South African mining industry, this was not possible due to the wide geographical distribution of mines in the country. This implies that the findings of the current study cannot be generalized to other populations, provinces, and countries. Furthermore, the fact that the study is restricted to the mining industry means that the findings are not generalizable to employees in other occupations and industries where skills shortages are experienced, due to prevailing dissimilar conditions which could yield different findings from those of this study. However, the findings of the study can be used by mining companies to retain artisans and engineers in their employment, rather than promoting the exodus of these employees employed in core occupational categories. Also, although the engineers included in the study were representative of the target population, the number was not sufficient to make meaningful comparisons possible between artisans and engineers.

It is recommended that empirical studies continue to investigate the impact of skills shortages on work behaviour. By understanding the behaviour and experiences of employees affected by skills shortages, mining companies will be in a position to improve the mental health of their workers, which will hold many positive outcomes for this industry. It is further recommended that the study of work stress be extended to include a more representative sample of South Africa's mining industry, in particular people from different occupational groups affected by skills shortages. Thus, it will be interesting to see how the findings of the current sample compare with those of a national and/or international sample. Further research on work stress in South Africa's mining industry should be encouraged. Due to the unique nature of this industry, it seems important that work stress is investigated further, to inform organizational leaders and wellness workers when they create new initiatives. In addition, stress management programmes can be tailored to meet the needs of different occupational groups, focusing on different life skills and coping techniques.

The findings of the current study show that mining companies need to consider interventions to reduce work-related stress, thus ensuring the wellbeing of engineers and artisans. It is proposed that mining companies should place increased emphasis on stress management training and counselling programmes, and that they should improve stress awareness programmes. Furthermore, by developing managerial capacity through effective leadership training programmes, organizational leaders will become more knowledgeable about work-related stressors and employee wellbeing. It is also proposed that artisans and engineers should be provided with work that is carefully structured. This will enhance their autonomy and responsibility, enabling them to utilize their skills. In addition, appropriate recognition should be given to artisans and engineers for their inputs.

The findings of the current study deepen the understanding of work-related stress of employees in occupational categories where skills shortages are experienced. In addition, the findings indicate that it is important for mining companies to consider human resource interventions to reduce work stress, thus ensuring the wellbeing of engineers and artisans in the mining industry. Should mining companies decide to ignore work-related stressors that employees are exposed to, particularly those employed in occupational categories where skills shortages are experienced, skills shortages may worsen, which may be detrimental to the future of the South African mining industry.

References

Badenhorst, C.J. 2006. Occupational health risk assessment: Overview, model and guide for the South African mining industry towards a holistic solution. PhD thesis, North-West University, Potchefstroom.

Bennett, J. and McGuinness, S. 2009. Assessing the impact of skill shortages on the productivity performance of high-tech firms in Northern Ireland. *Applied Economics*, vol. 41, no. 6. pp. 727–737.

Bickford, M. 2005. Stress in the workplace: A general overview of the causes, the effects, and the solutions. Canadian Mental Health Association, Newfoundland and Labrador Division.

Brand-Labuschagne, L., Mostert, K., Rothmann, S., Jr., and Rothmann, J.C. 2012. Burnout and work engagement of South African blue-collar workers: The development of a new scale. *Southern African Business Review*, vol. 16, no. 1. pp. 58–93.

Carmichael, F., Fenton, S.-J.H., Pinilla-Roncancio, M.V., Sing, M., and Sadhra, S. 2016. Workplace health and wellbeing in construction and retail: Sector specific issues and barriers to resolving them. *International Journal of Workplace Health Management*, vol. 9, no. 2. pp. 251–268. doi: 10.1108/IJWHM-08-2015-0053

Chamber of Mines of South Africa. 2013. Annual Report 2012/2013. https://commondatastorage.googleapis.com/comsa/annual-report-2012-2013.pdf [accessed 9 April 2018].

Coetzee, M. and de Villiers, M. 2010. Sources of job stress, work engagement and career orientations of employees in a South African financial institution. *Southern African Business Review*, vol. 14, no. 1. pp. 27–58.

Considine, R., Tynan, R., James, C., Wiggers, J., Lewin, T., Inder, K., Perkins, D., Handley, T., and Kelly, B. 2017. The contribution of individual, social and work characteristics to employee mental health in a coal mining industry population. *PLoS ONE*, vol. 12, no. 1. e0168445. doi: 10.1371/journal.pone.0168445

Coopmans, J.W.M. 2007. Stress related causes of presenteeism amongst South African managers. MBA dissertation, University of Pretoria, Pretoria.

Daniels, R.C. 2007. Skills shortages in South Africa: A literature review. Development Policy Research Unit, University of Cape Town, Cape Town.

Del Fabbro, G. 2012. High degrees of stress threaten workplace productivity. http://www.skillsportal.co.za/page/human-resource/1440174-High-degrees-of-stress-threaten-workplace-productivity [accessed 30 June 2013].

Erasmus, J. and Breier, M. (eds). 2009. Skills shortages in South Africa: Case studies of key professions. Human Sciences Research Council, Pretoria.

Gibbens, N. 2007. Levels and causes of stress amongst nurses in private hospitals: Gauteng Province. MSocSc dissertation, University of the Free State, Bloemfontein.

Griffin, R.W. and Moorhead, G. 2012. Organizational Behavior: Managing People and Organizations. 10th edn. South-Western Cengage Learning, Mason, OH.

Hair, J.F., Black, W.C., Babin, B.J., Anderson, R.E., and Tatham, R.L. 2006. Multivariate Data Analysis. 6th edn. Pearson Prentice Hall, Upper Saddle River, NJ.

Hair, J.F., Ringle, C.M., and Sarstedt, M. 2011. PLS-SEM: Indeed a silver bullet. *Journal of Marketing Theory and Practice*, vol. 19, no. 2. pp.139–152.

Hasnain, N., Naz, I., and Bano, S. 2010. Stress and well-being of lawyers. *Journal of the Indian Academy of Applied Psychology*, vol. 36, no. 1. pp. 165–168.

John, D. 2006. The impact of skills shortages on client satisfaction at Stewart Scott International in KwaZulu-Natal. MBA dissertation, University of KwaZulu-Natal, Pietermaritzburg.

Khalane, S. 2011. Nationalisation will worsen brain drain. *Free State Times*, June. pp. 24–30.

Luthans, F. 2002. Organizational Behavior. 9th edn. McGraw-Hill Irwin, Boston.

Luthans, F. 2011. Organizational Behavior: An Evidence-Based Approach. 12th edn. McGraw-Hill Irwin, New York.

Masia, U. and Pienaar, J. 2011. Unravelling safety compliance in the mining industry: Examining the role of work stress, job insecurity, satisfaction and commitment as antecedents. *South African Journal of Industrial Psychology*, vol. 37, no. 1. pp. 1–10.

Negi, K.R. 2014. Study of work stress in employees of business organizations of Matsasya Industrial Area, Alwar District, Rajasthan. *International Journal of Management and International Business Studies*, vol. 4, no. 2. pp. 169–174.

Oberholzer, C. 2010. South Africa has critical shortage of mining skills. www.solidaritysa.co.za/Home/wmprint.php?ArtID=2377 [accessed 12 January 2012].

Ogińska-Bulik, N. 2005. Emotional intelligence in the workplace: Exploring its effects on occupational stress and health outcomes in human service workers. *International Journal of Occupational Medicine and Environmental Health*, vol. 18, no. 2. pp. 167–175.

Ongori, H. and Agolla, J.E. 2008. Occupational stress in organizations and its effects on organizational performance. *Journal of Management Resources*, vol. 8, no. 3. pp. 123–135.

Oosthuizen, J.D. and van Lill, B. 2008. Coping with stress in the workplace. *South African Journal of Industrial Psychology*, vol. 34, no. 1. pp. 64–69.

Paten, N. 2006. Construction workers stressed. *Occupational Health*, vol. 58, no. 5. p. 8.

Quick, J.C. and Nelson, D.L. 2009. Principles of Organizational Behavior: Realities and Challenges. 7th edn. South-Western Cengage Learning, Florence, KY.

Razzak, W.A. and Timmins, J.C. 2008. A macroeconomic perspective on skill shortages and the skill premium in New Zealand. *Australian Economic Papers*, vol. 47, no. 1. pp. 74–91.

Robbins, S.P. 2005. Essentials of Organizational Behavior. 8th edn. Pearson/Prentice Hall, Upper Saddle River, NJ.

Robbins, S., Judge, T.A., Odendaal, A., and Roodt, G. 2009. Organisational Behaviour: Global and Southern African Perspectives. 2nd edn. Pearson Education, Cape Town.

Schaap, P. and Kekana, E. 2016. The structural validity of the Experience of Work and Life Circumstances Questionnaire (WLQ). *South African Journal of Industrial Psychology*, vol. 42, no. 1. a1349. http://dx.doi.org/10.4102/sajip.v42i1.1349

Schutte, P.C., Edwards, A., and Milanzi, L.A. 2012. How hard do mineworkers work? An assessment of workplace stress associated with routine mining activities. *Proceedings of the Mine Ventilation Society of South Africa Conference*, Emperors Palace, Kempton Park, 28-30 March 2012. http://researchspace.csir.co.za/dspace/bitstream/handle/10204/5855/Schutte_2012.pdf?sequence=1&isAllowed=y [accessed 6 March 2019].

Sebusi, I.E. 2007. An economic analysis of the skills shortage problem in South Africa. MCom dissertation, University of Johannesburg, Johannesburg.

Smit, N.W.H., De Beer, L.T., and Pienaar, J. 2016. Work stressors, job insecurity, union support, job satisfaction and safety outcomes within the iron ore mining environment. *South African Journal of Human Resource Management*, vol. 14, no. 1. a719.

South Africa. Department of Labour (DoL). 2006. National Skills Development Strategy: Implementation Report, 1 April 2004 – 31 March 2005. Department of Labour, Pretoria.

South Africa. Mining Qualifications Authority. 2008. A guide for identifying and addressing scarce and critical skills in the mining and minerals sector. http://mqa.org.za/sites/default/files/MQA%20Scarce%20Skills%20Guide.pdf [Accessed 30 November 2009].

South Africa. 2017. Health Professions Act, Act 56 of 1974, Notice 155 of 2017. Government Printer, Pretoria.

Toni, T. 2009. Causes and consequences of the shortage of electrical artisans at Eskom. MBA dissertation, Nelson Mandela Metropolitan University, Port Elizabeth.

Van der Walt, F., Thasi, M.E., Jonck, P., and Chipunza, C. 2016. Skills shortages and job satisfaction – insights from the gold-mining sector of South Africa. *African Journal of Business and Economic Research*, vol. 11, no. 1. pp. 141–181.

Van Zyl, E.S. and van der Walt, H.S. 1991. Manual for the Experience of Work and Life Circumstances Questionnaire (WLQ). Human Sciences Research Council, Pretoria.

Velnampy, T. and Aravinthan, S.A. 2013. Occupational stress and organizational commitment in private banks: A Sri Lankan experience. *European Journal of Business and Management*, vol. 5, no. 7. pp. 243–267.

Welman, J.C., Kruger, S.J., and Mitchell, B. 2005. Research Methodology. 4th edn. Oxford University Press, Cape Town.

Wickham, J. and Bruff, I. 2008. Skills shortages are not always what they seem: Migration and the Irish software industry. *New Technology, Work and Employment*, vol. 23 no. 1–2. pp. 30–43. ◆

SAIMM ADVERTISING OPPORTUNITIES

RATE CARD 2020

SAIMM
THE SOUTHERN AFRICAN INSTITUTE OF MINING AND METALLURGY

ADVERTISING RATES FOR THE SAIMM JOURNAL

SAIMM Journal Publication Rates 2020

Advert Size	Casual Bookings	2–5 Bookings
Outside front cover This includes outside front cover picture, plus full page inside front cover, plus small replica of the front cover on the contents page	R33 976	R32 687

	Casual Bookings	2–5 Bookings	6–12 Bookings
Outside back cover	R28 313	R27 283	R26 252
Inside back cover	R22 667	R21 877	R21 108
Double page spread*	R30 883	R30 374	R29 856
Full page	R16 987	R16 472	R15 959
Half page	R13 449	R12 933	R12 416
Third page	R10 615	R10 099	R9 589
1/4 page horizontal	R9 910	R9 394	R8 879

So much more to offer
Online and Article Placements:
Super Tower • Super Button • Leaderboard
Skyscraper • Vertical Banner • Button

Material should be supplied in a press-optimised PDF format—colours converted to CMYK. Material should be made up in Bureau software (*e.g.* Quark, InDesign, Freehand, Illustrator) before converting to PDF. Screen ruling 133 mm. *NOTE: Material made up in MS Word and PowerPoint is not acceptable.*

- All prices quoted are per insertion and are excluding VAT
- Special colours, positions and contracts will be priced on application
- DPS—Please allow a 20 mm gutter in the centre of the page to allow for binding

Website: http://www.saimm.co.za

Fifth Floor, 5 Hollard Street
Marshalltown 2107, South Africa
Tel: 27-11-834-1273/7
E-mail: journal@saimm.co.za
Website: http://www.saimm.co.za

ADVERTISEMENT BOOKINGS
Barbara Spence · Avenue Advertising
Tel: 011 463 7940 · Cell: 082 881 345
E-mail: barbara@avenue.co.za
Website: http://www.avenue.co.za

UNIVERSITY STUDENT BODIES

The SAIMM YPC Career and Leadership Conference is aimed at enhancing students' leadership skills and to provide them with an opportunity to interact with various stakeholders. The conference fulfils a need for students to acquire additional soft skills that will serve them well in their future career paths. These student bodies organise the conference on a rotational basis.

UNISA	UNISA	**UNISA Mining Society (UMS)** is a structure which exists within the University of South Africa (UNISA). UMS which is an acronym for UNISA Mining Society acknowledges its existence as an autonomous substructure of Science Engineering and Technology Student Association (SETSA). UMS represents students in Mining Engineering and Mine Survey.
UP	MYNBOU TUKS MINING	**The Tuks Mining Society (TMS)** is a student led society and the sub-house of mining department; which forms part of Engineering Built-Environment and Information Technology (EBIT). It is under the supervision of the mining department and aims not only at enhancing students social and leadership skills, but also creates a platform for students to network with other students, lecturers, alumni members and industry professionals. It was founded in the 1990's with the initial purpose of addressing the social needs of its members.
	Metallurgical Engineering	The **Metallurgical Sub-house** is a student organisation of the Department of Material Science and Metallurgical Engineering at the University of Pretoria. The main objectives of the Sub-House are to serve as a communication link between students in the Department of Materials Science and Metallurgical Engineering and the staff members, to assist in organizing academic, social and other events for the department and to assist in marketing Metallurgical Engineering as a career and a study field.
WITS	SCHOOL OF CHEMICAL AND METALLURGICAL ENGINEERING	The **CHMT (Chemical and Metallurgy) School Council** is an extension and operates under the governance of the SRC. We are here to voice out our students' concerns, interests and suggestions.
	SCHOOL OF MINING ENGINEERING	The **Mining Engineering Student Council (MESC)** is committed to exemplary student leadership in defining competent Mining Engineer that the Wits School of Mining Engineering is producing for the mining industry and the country at large. To this end, it aims to encourage academic excellence and promote equality of opportunity through effective, accountable and transparent student leadership.
	S.M.E.S	The **Student in Mining Engineering Society (SMES)** is a student body recognised by Wits University with the main objective to represent and address the social needs of its members (mainly consisting of Wits Mining Engineering Students). It is concerned with linking students to the school, alumni and the industry through different events.
UJ	MINING FORUM	We, the school of mines students of the University of Johannesburg, drawn from various cultural, religious, social, economic and political backgrounds, conscious of the historic disparities within the South African mining industry in general; and committed to the building and sustenance of a non-racial, non-sexist and democratic institution.
	Metallurgical Engineering Student Organisation MESO EXTRACT AND CAST YOUR FUTURE	**MESO** is an organisation concerned with the holistic development of its constituents. Academic excellence combined with social development is a goal that is to be reached. MESO seeks to create an environment that will allow for an improved relationship between students and the Metallurgical department. Our aim is also to build a bridge between students and the institution (University of Johannesburg) and industry.
	UJ 2016 WOMEN IN MINING	**Women in Mining** of the University of Johannesburg is a constituency of female students in mining related courses (namely; Mining Engineering, Mineral Surveying and Metallurgical Engineering). We are the flowers of our nation, springing from different roots of cultures, religion and race. In unity, we stand through our diversity with the main aim to empower each other.

NATIONAL & INTERNATIONAL ACTIVITIES

2021

23–25 June 2021 — **ROLLS6 2020**
London, UK, Website: http://www.rolls6.org/home

9–11 June 2021 — **Diamonds – Source to Use — 2020 Conference**
The Birchwood Hotel & OR Tambo Conference Centre
Contact: Camielah Jardine
Tel: +27 11 834-1273/7
Fax: +27 11 838-5923/833-8156
E-mail: camielah@saimm.co.za
Website: http://www.saimm.co.za

13–16 July 2021 — **Copper Cobalt Africa The 10th Southern African Base Metals Conference**
Avani Victoria Falls Resort, Livingstone, Zambia
Contact: Camielah Jardine
Tel: +27 11 834-1273/7
Fax: +27 11 838-5923/833-8156
E-mail: camielah@saimm.co.za
Website: http://www.saimm.co.za

29–30 July 2021 — **5th Mineral Project Valuation Colloquium**
Glenhove Events Hub, Melrose Estate
Contact: Gugu Charlie
Tel: +27 11 834-1273/7
Fax: +27 11 838-5923/833-8156
E-mail: gugu@saimm.co.za
Website: http://www.saimm.co.za

18–20 August 2021 — **WorldGold Conference 2021**
Misty Hills Conference Centre, Muldersdrift
Johannesburg, South Africa
Contact: Camielah Jardine
Tel: +27 11 834-1273/7
Fax: +27 11 838-5923/833-8156
E-mail: camielah@saimm.co.za
Website: http://www.saimm.co.za

29 August–2 September 2021 — **APCOM 2021 The next digital transformation in mining**
Misty Hills Conference Centre, Muldersdrift,
Johannesburg, South Africa
Contact: Camielah Jardine
Tel: +27 11 834-1273/7
Fax: +27 11 838-5923/833-8156
E-mail: camielah@saimm.co.za
Website: http://www.saimm.co.za

3–6 October 2021— **Massmin 2020 Eight International Conference on Mass Mining**
Santiago, Chile, Contact: J.O. Gutiérrez
Tel: (56-2) 2978 4476
Website: www.minas.uchile.cl

2022

17–24 June 2022 — **NAT2020 North American Tunneling Conference**
Philadelphia
Website: http://www.natconference.com

Due to the current COVID-19 pandemic our 2020 conferences have been postponed until further notice.

We will confirm new dates in due course.

Company affiliates

The following organizations have been admitted to the Institute as Company Affiliates

3M South Africa (Pty) Limited
AECOM SA (Pty) Ltd
AEL Mining Services Limited
African Pegmatite
Air Liquide (PTY) Ltd
Alexander Proudfoot Africa (Pty) Ltd
AMEC Foster Wheeler
AMIRA International Africa (Pty) Ltd
ANDRITZ Delkor(pty) Ltd
Anglo Operations Proprietary Limited
Anglogold Ashanti Ltd
Arcus Gibb (Pty) Ltd
ASPASA
Atlas Copco Holdings South Africa (Pty) Limited
Aurecon South Africa (Pty) Ltd
Aveng Engineering
Aveng Mining Shafts and Underground
Axiom Chemlab Supplies (Pty) Ltd
Axis House Pty Ltd
Bafokeng Rasimone Platinum Mine
Barloworld Equipment -Mining
BASF Holdings SA (Pty) Ltd
BCL Limited
Becker Mining (Pty) Ltd
BedRock Mining Support Pty Ltd
BHP Billiton Energy Coal SA Ltd
Blue Cube Systems (Pty) Ltd
Bluhm Burton Engineering Pty Ltd
Bond Equipment (Pty) Ltd
Bouygues Travaux Publics
CDM Group
CGG Services SA
Coalmin Process Technologies CC
Concor Opencast Mining
Concor Technicrete
Council for Geoscience Library
CRONIMET Mining Processing SA Pty Ltd
CSIR Natural Resources and the Environment (NRE)
Data Mine SA
Digby Wells and Associates
DRA Mineral Projects (Pty) Ltd
DTP Mining - Bouygues Construction
Duraset
Elbroc Mining Products (Pty) Ltd
eThekwini Municipality
Ex Mente Technologies (Pty) Ltd
Expectra 2004 (Pty) Ltd
Exxaro Coal (Pty) Ltd
Exxaro Resources Limited
Filtaquip (Pty) Ltd
FLSmidth Minerals (Pty) Ltd
Fluor Daniel SA (Pty) Ltd
Franki Africa (Pty) Ltd-JHB
Fraser Alexander (Pty) Ltd
G H H Mining Machines (Pty) Ltd
Geobrugg Southern Africa (Pty) Ltd
Glencore
Hall Core Drilling (Pty) Ltd
Hatch (Pty) Ltd
Herrenknecht AG
HPE Hydro Power Equipment (Pty) Ltd
Immersive Technologies
IMS Engineering (Pty) Ltd
Ingwenya Mineral Processing (Pty) Ltd
Ivanhoe Mines SA
Joy Global Inc. (Africa)
Kudumane Manganese Resources
Leco Africa (Pty) Limited
Leica Geosystems (Pty) Ltd
Longyear South Africa (Pty) Ltd
Lull Storm Trading (Pty) Ltd
Maccaferri SA (Pty) Ltd
Magnetech (Pty) Ltd
Magotteaux (Pty) Ltd
Malvern Panalytical (Pty) Ltd
Maptek (Pty) Ltd
Maxam Dantex (Pty) Ltd
MBE Minerals SA Pty Ltd
MCC Contracts (Pty) Ltd
MD Mineral Technologies SA (Pty) Ltd
MDM Technical Africa (Pty) Ltd
Metalock Engineering RSA (Pty)Ltd
Metorex Limited
Metso Minerals (South Africa) Pty Ltd
Micromine Africa (Pty) Ltd
MineARC South Africa (Pty) Ltd
Minerals Council of South Africa
Minerals Operations Executive (Pty) Ltd
MineRP Holding (Pty) Ltd
Mintek
MIP Process Technologies (Pty) Limited
MLB Investment CC
Modular Mining Systems Africa (Pty) Ltd
MSA Group (Pty) Ltd
Multotec (Pty) Ltd
Murray and Roberts Cementation
Nalco Africa (Pty) Ltd
Namakwa Sands(Pty) Ltd
Ncamiso Trading (Pty) Ltd
New Concept Mining (Pty) Limited
Northam Platinum Ltd - Zondereinde
Opermin Operational Excellence
OPTRON (Pty) Ltd
Paterson & Cooke Consulting Engineers (Pty) Ltd
Perkinelmer
Polysius A Division Of Thyssenkrupp Industrial Sol
Precious Metals Refiners
Ramika Projects (Pty) Ltd
Rand Refinery Limited
Redpath Mining (South Africa) (Pty) Ltd
Rocbolt Technologies
Rosond (Pty) Ltd
Royal Bafokeng Platinum
Roytec Global (Pty) Ltd
RungePincockMinarco Limited
Rustenburg Platinum Mines Limited
Salene Mining (Pty) Ltd
Sandvik Mining and Construction Delmas (Pty) Ltd
Sandvik Mining and Construction RSA(Pty) Ltd
SANIRE
Schauenburg (Pty) Ltd
Sebilo Resources (Pty) Ltd
SENET (Pty) Ltd
Senmin International (Pty) Ltd
Smec South Africa
Sound Mining Solution (Pty) Ltd
SRK Consulting SA (Pty) Ltd
Time Mining and Processing (Pty) Ltd
Timrite Pty Ltd
Tomra (Pty) Ltd
Ukwazi Mining Solutions (Pty) Ltd
Umgeni Water
Verni Speciality Construction Products (Pty) Ltd
Webber Wentzel
Weir Minerals Africa
Welding Alloys South Africa
Worley

cerium (Ce), dysprosium (Dy), erbium (Er), europium (Eu), gadolinium (Gd), holmium (Ho), lanthanum (La), lutetium (Lu), neodymium (Nd), praseodymium (Pr), promethium (Pm), samarium (Sm), scandium (Sc), terbium (Tb), thulium (Tm), ytterbium (Yb) and yttrium (Y)

SOUTHERN AFRICAN RARE EARTHS

INTERNATIONAL CONFERENCE 2021

18-20 OCTOBER 2021

SWAKOPMUND HOTEL AND ENTERTAINMENT CENTRE,
SWAKOPMUND, NAMIBIA

Driving the future of high-tech industries

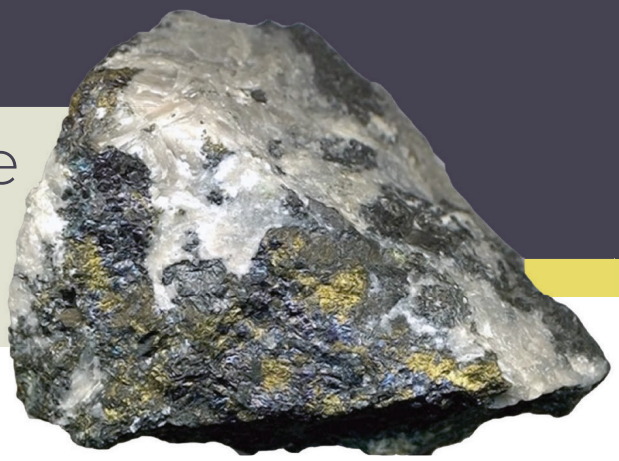

ABOUT THE CONFERENCE

The global demand for rare earth elements (REEs) and their alloys has increased enormously in the last few decades. REEs are critical materials in high-technology applications due to their unique chemical, catalytic, electrical, magnetic, and optical properties. In particular, REEs are used in emerging and niche technologies such as medical devices, electric vehicles, energy-efficient lighting, wind turbines, rechargeable batteries, catalytic converters, flat screen televisions, mobile phones. and disk drives. In fact, the 4IR-driven digital revolution will not be possible without the critical rare REEs.

The supply security of rare earth metals is of global concern. The need to diversify the supply of REEs thus creates significant opportunities for southern Africa to contribute to the global supply. In fact, as one of the regions with large REE resources, southern Africa can exploit this window of opportunity and significantly contribute to the sustainable supply of these high-tech materials.

PLEASE NOTE THAT SPONSORSHIP OPPORTUNITIES AND EXHIBITION SPACE IS AVAILABLE.

The need to fully participate along the REE value chain has also inspired interest in developing downstream capacity for refining, through the Southern African Centralized Rare Earth Refinery (SACREF). Thus, in order to maximize value from the REEs industry in the region, further discussions on optimizing the REE value chain are needed. This conference, focusing on the optimization of the primary production and refining of rare earth metals, is designed to stimulate debate on growth, creating opportunities for the southern African rare earths industry.

FOR FURTHER INFORMATION, CONTACT:

Camielah Jardine,
Head of Conferencing

E-mail: camielah@saimm.co.za
Tel: +27 11 834-1273/7
Web: www.saimm.co.za

SAIMM
THE SOUTHERN AFRICAN INSTITUTE OF MINING AND METALLURGY
125 YEARS 1894 - 2019

APCOM 2021

MINERALS INDUSTRY 4.0

The next digital transformation in mining

29 AUGUST - 2 SEPTEMBER 2021

MISTY HILLS CONFERENCE CENTRE
MULDERSDRIFT, JOHANNESBURG,
SOUTH AFRICA

APCOM (Applications of Computers and Operations Research in the Minerals Industries) is a series of well-established, high-quality international scientific conferences which was started in the early 1960s with the aim of sharing technological advances by engineers and computer scientists in all fields relevant to the mining industry. The APCOM events have evolved to become a major driver of innovation in the minerals industry, and over the years, many breakthrough innovations, such as geostatistics and mining process optimization, have been initially discussed at or originated from the APCOM conferences. One of the success factors of APCOM is the intensive, high-quality dialogue that it promotes between industry and academia. Thanks to the personal commitments of APCOM's loyal participants and supporters, the symposia continue to be a thriving success.

The APCOM 2021 Conference, the 40th in the series, will be held at Misty Hills, Muldersdrift, South Africa from 29 August – 2 September 2021. Nestled in the foothills of the Swartkop Mountains on the threshold of the beautiful Kromdraai Valley in Muldersdrift, Misty Hills is one of the most popular hotel and conference venues in Johannesburg. This charming stone-built hotel embodies the ethos of Africa. Set in more than 60 acres of lush botanical gardens, Misty Hills is the ideal venue for functions, conferences, exhibitions, product launches, team-building, getaways, and events. Come and experience the splendour of rich African hospitality in the heart of Gauteng. Johannesburg. An optional tourist visit is planned to the nearby Pilanesberg National Park which presents an opportunity to view the 'Big Five'.

FOR FURTHER INFORMATION, CONTACT:

Camielah Jardine,
Head of Conferencing

E-mail: camielah@saimm.co.za
Tel: +27 11 834-1273/7
Web: www.saimm.co.za

SAIMM
THE SOUTHERN AFRICAN INSTITUTE OF MINING AND METALLURGY
125 YEARS 1894 - 2019